A Virtual Conference organized by the

The University of Danang – University of Science and Technology

Co-Sponsored by

Kogakuin University of Technology and Engineering

Southern Taiwan University of Science and Technology

University of the Philippines

University of the Philippines Los Banos

Edited by

21st International Symposium on Advanced Technology

Published by

Kogakuin University of Technology & Engineering, Japan

ISSN 2434-4273

The 21st International Symposium on Advanced Technology (ISAT-21)

November 24-25, 2022

The University of Danang – University of Science and Technology, Vietnam

Table of Contents

Welcome Message from the Symposium Chairperson

I am Doan Quang Vinh, Rector of University of Science and Technology – The University of Danang or DUT. Since its establishment in 1975, DUT has predicated its leading position in the system of higher education in Vietnam and in Southeastern Asia. DUT is not only a center for training highly-qualified human resources in various engineering fields, but also a hub for scientific research, innovation, and technology transfer for Central Vietnam and for the whole country. In that spirit, DUT is very proud to be host of the International Symposium on Advanced Technology (ISAT) this year. This annual symposium is a valuable forum aiming to promote scientific and technologic exchange between leading scientists, researchers for the purpose of resolving pressing national and social issues.

The 21st ISAT, which will be organized online from 24 to 25 November 2022, sets its main theme as "Engineering Innovation for Sustainable Future" in which many specific topics will be covered, including more than 12 fields of research. I truly believe that the technical program, with a broad range of specific discussion topics and with participants' positive contributions, will make the ISAT-21 most productive and fruitful. I also truly believe that successful outcomes from ISAT-21 will certainly contribute to the continuous success of the symposium.

As the chairperson of the symposium, I would like to express my sincere thanks to the organizing committee members, all the participants and wish you a pleasurable and rewarding ISAT-21.

Sincerely Yours,

Prof. Doan Quang Vinh
Rector, The University of Danang – University of Science and Technology

General Information of ISAT-21

1. Main theme of ISAT-21: Engineering Innovation for Sustainable Future

Topics of ISAT-21 include, but not limited to:

1. Biochemistry and Food Science
2. Synthetic Chemistry and Medicinal Chemistry
3. Information and Communications Technology (ICT)
4. Energy and Transportation
5. Advanced Functional Materials
6. Architectural and Civil Engineering
7. Intelligent and Secure Systems
8. Education and Human Studies
9. Environmental Chemistry and Chemical Engineering
10. Simulation Science, Measurement Science, Computational Science
11. Electric Engineering and Electronic Engineering
12. Mechanical Engineering

The symposium program will consist of key-note lectures, oral presentations, and lightning talk sessions.

Language: English will be the official language during the conference
Venue: The conference will be held by online
Website: http://dut.udn.vn/ISAT21

2. Presentation Guidelines

Presentation Type	Presentation Time
Keynote Sessions	35 minutes (LIVE)
Oral Sessions	15 minutes (LIVE)
Lightning Talk Sessions	5 minutes (pre-recorded)

Live Keynote and Oral Presentations Sessions:

The time allocated to each presentation will be:

Key-note: 35 minutes talk and 5 minutes for discussion
Oral Session: 15 minutes talk and 5 minutes for discussion.

Lightning Talk Sessions:

5 minutes pre-recorded presentation will be open to the conference website.
The presenters are required to communicate with attendees via online.

Organization

Advisory Committee members
Organizing committee
Chairperson:

Prof. Doan Quang Vinh	Rector, The University of Danang - University of Science and Technology (DUT), Vietnam

Co-chairperson:

Prof. Shinichiro Ito	President, Kogakuin University of Technology and Engineering (KUTE), Japan
Prof. Deng-Maw Lu	President, Southern Taiwan University of Science and Technology (STUST), Taiwan
Dr. Jose V. Camacho, Jr.	Chancellor, University of the Philippines Los Baños (UPLB), Philippines

Vice-chairperson:

Dr. Tao Quang Bang	Head of Science, Technology and International Cooperation Department, The University of Danang - University of Science and Technology (DUT), Vietnam
Prof. Yasushi Nozawa	Vice President, School of Architecture, Kogakuin University of Technology and Engineering (KUTE), Japan
Prof. Miyuki Kamachi	Vice President, Faculty of Informatics, Kogakuin University of Technology and Engineering (KUTE), Japan
Prof. Ming-Shyan Wang	Department of Electrical Engineering, Southern Taiwan University of Science and Technology (STUST), Taiwan
Prof. Sheng-Chang Wang	Department of Mechanical Engineering, Southern Taiwan University of Science and Technology (STUST), Taiwan
Prof. Zong-Xian Yin	Department of Computer Science and Information, Southern Taiwan University of Science and Technology (STUST), Taiwan
Prof. Rossana Marie C. Amongo	Dean, College of Engineering and Agro-industrial Technology University of the Philippines Los Baños (UPLB), Philippines

Executive committee

Dr. Vo Tuan Minh	Deputy Head of Science, Technology and International Cooperation Department, The University of Danang - University of Science and Technology (DUT), Vietnam
Dr. Nguyen Thanh Binh	Deputy Head of Science, Technology and International Cooperation Department, The University of Danang - University of Science and Technology (DUT), Vietnam
Ms. Nakamura Yoko	Kogakuin University of Technology and Engineering (KUTE), Japan

Technical Program committee
Chairperson:

Dr. Tao Quang Bang	Head of Science, Technology and International Cooperation Department, The University of Danang - University of Science and Technology (DUT), Vietnam

Members:

Dr. Pham My	The University of Danang - University of Science and Technology
Dr. Nguyen Van Quang	The University of Danang - University of Science and Technology
Dr. Ho Viet Thang	The University of Danang - University of Science and Technology
Dr. Pham Anh Duc	The University of Danang - University of Science and Technology
Dr. Vo Nhu Thanh	The University of Danang - University of Science and Technology
Dr. Huynh Nhat To	The University of Danang - University of Science and Technology
Dr. Hoang Van Thanh	The University of Danang - University of Science and Technology
Dr. Phan Tran Dang Khoa	The University of Danang - University of Science and Technology
Dr. Huynh Thanh Tung	The University of Danang - University of Science and Technology
Dr. Nobuhiro Aburai	Department of Chemistry and Life Science, School of Advanced Engineering, KUTE
Dr. Hideki Hashimoto	Department of Applied Chemistry, School of Advanced Engineering, KUTE
Dr. Hiroki Nagai	Department of Applied Physics, School of Advanced Engineering, KUTE
Dr. Koji Hasegawa	Department of Mechanical Engineering, Faculty of Engineering, KUTE
Dr. Masakazu Mukai	Department of Electrical and Electronic Engineering, Faculty of Engineering, KUTE
Prof. Yusuke Nakajima	Department of Urban Design and Planning, School of Architecture, KUTE
Dr. Yukihiro Kudoh	Department of Information and Communications Engineering, Faculty of Informatics, KUTE
Dr. Kanta Tachibana	Department of Information System and Applied Mathematics, Faculty of Informatics, KUTE
Prof. Morio Yoshida	Division of Global and Carrier Education, Center for Promotion of Higher Education, KUTE
Prof. Hong-Ru Lin	Department of Chemical and Materials Engineering, STUST, Taiwan
Prof. Po-Ting Chen	Department of Biotechnology and Food Technology, STUST, Taiwan
Prof. Jeng-Han Li	Department of Electrical Engineering, STUST, Taiwan
Prof. Nai-Shang Liou	Department of Mechanical Engineering, STUST, Taiwan
Dr. Kevin F. Yaptenco	University of the Philippines Los Baños (UPLB), Philippines
Dr. Roger A. Luyun, Jr	University of the Philippines Los Baños (UPLB), Philippines
Dr. Monet Concepcion M. Detras	University of the Philippines Los Baños (UPLB), Philippines
Dr. Butch G. Bataller	University of the Philippines Los Baños (UPLB), Philippines
Dr. Marion Lux Y. Castro	University of the Philippines Los Baños (UPLB), Philippines

General Schedule

November 24th

Japan (JST)	Taiwan, Philippines (TST/PTS)	Vietnam (ICT)						
10:15	9:15	8:15	LOG-IN AND ROLL CALL https://zoom.us/j/97697160354 Passcode: isat21					
10:30	9:30	8:30	OPENING CEREMONY **Prof. Doan Quang Vinh** Rector, The University of Danang - University of Science and Technology **Prof. Lu, Deng-Maw** President, Southern Taiwan University of Science and Technology **Prof. Shinichiro Ito** President, Kogakuin University of Technology and Engineering **Prof. Jose D. Camacho, Jr.** Chancellor, University of the Philippines Los Baños Master of Ceremony: Dr. Quang Bang Tao, DUT						
11:00	10:00	9:00	KEYNOTE PRESENTATION 1 Exploring the repressive impacts of pomegranate peels on urinary bladder urothelial carcinoma **Prof. Ting-Feng Wu** **Department of Biotechnology and Food Technology** **Southern Taiwan University of Science and Technology, Taiwan**						
11:45	10:45	9:45	KEYNOTE PRESENTATION 2 Synthesis of MoS2 nanosheets and their electrochemical evaluation as cathode materials for aqueous Zn-ion Batteries **Dr. Ba Kien Nguyen,** **Faculty of Mechanical Engineering,** **University of Science and Technology – The University of Danang**						
12:30	11:30	10:30	BREAK						
			ORAL PRESENTATION, PARALLEL SESSION						
			Breakout Room	1	2	3	4	5	6
12:40	11:40	10:40	**ORAL1**	ACE1	ACE5	AFM1	ME1	ME4	EEE1
13:00	12:00	11:00	**ORAL2**	ACE2	ACE6	AFM2	ME2	ME5	EEE2
13:20	12:20	11:20	**ORAL3**	ACE3	ACE7	AFM3	ME3	ME6	EEE3
13:40	12:40	11:40	**ORAL4**	ACE4		AFM4			EEE4
14:00	13:00	12:00	**ORAL5**						EEE5

November 25th

Japan (JST)	Taiwan, Philippines (TST/PTS)	Vietnam (ICT)	
13:45	12:45	11:45	LOG-IN AND ROLL CALL https://zoom.us/j/97697160354 Passcode: isat21

14:00	13:00	12:00	KEYNOTE PRESENTATION 3 Solid Oxide Fuel Cell Technology and Its Application to Shrimp Farming **Assoc. Prof. Yusuke Shiratori, Department of Mechanical Science and Engineering** **School of Advanced Engineering, Kogakuin University, Japan**					
14:45	13:45	12:45	KEYNOTE PRESENTATION 4 The role of Engineering Technologies in the advancement of agricultural development in the Philippines **Dr. Rossana Marie C. Amongo** **Dean, College of Engineering and Agro-industrial Technology** **University of the Philippines Los Banos**					
15:30	14:30	13:30	BREAK					
			LIGHTNING TALK SESSION, PARALLEL SESSION					
			Breakout Room	1	2	3	4	5
15:40	14:40	13:40	**LIGHTNING1**	ECCEL 1-6	EHSL 1-6	ICTL 1-6	AFML 1-6	EEEL 1-6
16:20	15:20	14:20	**LIGHTNING2**	ECCEL 7-13	EHSL 7-12	ICTL 7-12	AFML 7-12	EEEL 7-13
16:50	15:50	14:50	BREAK					
17:00	16:00	15:00	AWARDING CEREMONY - Honorary Membership to Prof. Lu, Deng-Maw, STUST Awarding from Prof. Doan Quang Vinh Rector, The University of Danang - University of Science and Technology - Presentation Award Awarding from Prof. Doan Quang Vinh Rector, The University of Danang - University of Science and Technology Master of Ceremony: Dr. Tao Quang Bang, DUT					
17:30	16:30	15:30	CLOSING CEREMONY CLOSING REMARKS **- Prof. Prof. Doan Quang Vinh** Rector, The University of Danang - University of Science and Technology **- Next Host: Prof. Sheng-Chang Wang** Chair of Department of Mechanical Engineering, Southern Taiwan University of Science and Technology Master of Ceremony: Dr. Tao Quang Bang, DUT					

Oral Presentation (November 24th from 12:40 to 14:20 (JST))

Breakout Room #1
Architectural and Civil Engineering
Chairperson: Dr. Pham My, DUT

Presentation No.	Title	Author	Page
ACE1.	Seismic Performance of an Irregular School Building Based on Incremental Dynamic Analysis	Carla Mae B. Pilapil, Carmina B. Borja, Richelle G. Zafra	24
ACE2.	Development of Seismic Vulnerability Curves of Reinforced Concrete Buildings of the University of the Philippines Los Baños using Computational Methods	Gabriel Antonio I. Pimentel, Richelle G. Zafra, Carmina B. Borja, Bien Dave B. Papasin	29
ACE3.	Comparative Analysis on the Use of Low-Impact Development (LID) Practices and Flood Rerouting for Flood Mitigation using EPA-SWMM in San Isidro, Batangas City, Batangas, Philippines	Celwyn Joseph A. de Roxas, Kale Ashley P. Carurucan, Perlie P. Velasco, Ma. Hazel T. Castillo	34
ACE4.	Geostatistical Modeling of Standard Penetration Test Data to Determine the Minimum Required Number of Boreholes for Geotechnical Investigations	Roel Nikko T. Magno, Andre C. Cruz, Jedidiah Joel C. Aguirre, Ron Gabriel O. Navarro	40

Breakout Room #2
Architectural and Civil Engineering
Chairperson: Dr. Nguyen Van Quang, DUT

Presentation No.	Title	Author	Page
ACE5.	Electrical Resistivity of Concrete Containing Ceramic Tile Waste as Partial Replacement for Fine Aggregate	John Ezekiel D. Mateo, Marish S. Madlangbayan, Marloe B. Sundo, Richelle G. Zafra, Maricel A. Eneria	47
ACE6.	Feasibility Study of Rooftop Rainwater Harvesting System for Flushing Demand in Different Philippine Climate Types	Ricahlee R. Sabilla, Kale Ashley P. Carurucan, Richelle G. Zafra, Perlie P. Velasco	52
ACE7.	Sorptivity of Concrete with Ceramic Tile Waste as Partial Replacement for Fine Aggregate	Yusaine R. Maon, Marish S. Madlangbayan, Marloe B. Sundo, Richelle G. Zafra, Maricel A. Eneria	58

Breakout Room #3
Advanced Functional Materials
Chairperson: Dr. Ho Viet Thang, DUT

Presentation No.	Title	Author	Page
AFM1.	Twin-Free α-Ga2O3 Films Grown by Mist CVD On (0001) - Al2O3 Substrates	R. Yamada, A. Kobayashi, K. Ueno, A. Sekiguchi, T. Onuma, T. Honda, H. Fujioka, T. Yamaguchi	65
AFM2.	Physicochemical Properties of Chitosan-Acrylic Acid Hydrogel Prepared Using Atmospheric Pressure Plasma	Kathrina Lois Taaca, Eloise Prieto, Magdaleno Vasquez Jr.	66
AFM3.	Investigation of Fracture Behavior of Self-Healing Ceramics Using Acoustic Emission	Toyoki Agata, Koji Hasegawa, Masaki	68

		Hiratsuka, Tetsuro Yanaseko	
AFM4.	Label-Free Electrochemical Immunosensor for Detection of Mycobacterium Tuberculosis Culture Filtrate Antigen	Resmond L. Reaño, Glenson R. Panghulan, Clydee Anne T. Hernandez, Joseph P. Ortenero, Jeffrey P. Tamayo	69

Breakout Room #4
Mechanical Engineering
Chairperson: Dr. Pham Anh Duc, DUT

Presentation No.	Title	Author	Page
ME1.	Fabricating CuCr1Zr Parts by Using Laser Powder Bed Fusion Process – Simulation and Experimental Approach	Vi-Long Vo, Hong-Chuong Tran	73
ME2.	Fundamental Study on Nondestructive Estimation Of Three-Dimensional Creep Strain Using Surface Displacement	Satoshi Fujii, Ryota Iwasawa, Masaru Ogawa	74
ME3.	A Numerical Study on the Motion of a Moored Semisubmersible in Irregular Waves	Thua T. Nguyen, Long T. Phan, Thai Q. Pham	75

Breakout Room #5
Mechanical Engineering
Chairperson: Dr. Vo Nhu Thanh, DUT

Presentation No.	Title	Author	Page
ME4.	Aerodynamic Performance of Footballs with Different Complex Panel Surface Geometries	Kaito Tada, Kazuya Seo, Shinichiro Ito, Masaki Hiratsuka	82
ME5.	Directional Control of Jets Near A Boundary Using Coander Secondary Flow	Hiroki Tezuka, Minoru Nakagawa, Qiang Zhang, Kotaro Sato	84
ME6.	Effect Of the Frequency of Jet Excitation on The Symmetric Flow Field	Takumi Ito, Kotaro Sato	85

Breakout Room #6
Electric Engineering and Electronic Engineering and Information and Communications Technology (ICT)
Chairperson: Dr. Huynh Nhat To, DUT

Presentation No.	Title	Author	Page
EEE1.	Automatic Font Generation System Reflecting Emotions in Voice Based on Adversarial Generative Network	Keita Tsuchiya, Takuto Nonaka, and Qiu Chen	87
EEE2.	A Study on Skin Modeling Based on Monte Carlo Simulation for Skin Health Diagnosis	Duc D. D. Luu, Khanh D. Phan, Phuong T. Kieu, Nhan T. Nguyen, Thien T. Nguyen, Minh T. Nguyen, Tuan P. Van, Thu T. A. Nguyen	88
EEE3.	Vision Aid for Drones with Precise Positioning of Landing Targets	Jia-Shing Shih, Hsuan-Hsin Wu, Chun-Chieh Tsai, Guan-Yu Lin, Cheng-Dian Zhan	93
EEE4.	A Genetic Algorithm-Based CNN Approach for Ceramic Tile Defects Classification	Nhat-To Huynh	94

EEE5.	Verification Of Low Voltage Ride-Through Requirement for A Large-Scale Wind Farm	Cheng-Ting Hsu	96

Lightning Talk Session (November 25th from 15:40 to 16:50 (JST))

Breakout Room #1

Environmental Chemistry and Chemical Engineering & Advanced Functional Materials

Chairperson: Dr. Nguyen Thanh Binh, DUT

Presentation No.	Title	Author	Page
ECCEL1.	Dependence Of The Cuo Layer On Photocatalytic Properties Of Tio2/Cuo Thin Films	Katsuyuki Takeda, Ichiro Takano	101
ECCEL2.	XPS Analysis Of The Binding States In Nitrogen-Doped Snox Thin-Films Deposited By RF Magnetron Sputtering In N2 Atmosphere	Takuma Kawaguchi, Kotaro Watanabe, Shinya Aikawa	102
ECCEL3.	Crystal Growth Of Cu3N By Mist CVD With Ethylenediamine	Shogo Yoshida, Hiroki Nagai, Tomohiro Yamaguchi, Takeyoshi Onuma, Tohru Honda	105
ECCEL4.	Deposition Of Nitrogen-Doped Titanium Dioxide Thin Films Via Rf Magnetron Sputtering	Melanie M. Martinez, Takeyoshi Onuma, Hiroki Nagai, Tohru Honda, Shinya Aikawa, Tomohiro Yamaguchi, Magdaleno R. Vasquez Jr	106
ECCEL5.	Growth Of Zno Thin Films Via Magnetron Sputtering Using A Custom-Made Sintered Target	Rozen Grace B. Madera, Hiroki Nagai, Takeyoshi Onuma, Tohru Honda, Tomohiro Yamaguchi, Magdaleno R. Vasquez Jr	108
ECCEL6.	Study For Composition Control In Mist CVD Growth Of α-GIO Alloys	Kai Yamada, Tomohiro Yamaguchi, Takeyoshi Onuma, Tohru Honda	110
ECCEL7.	Investigation on the Stability of Source Solution for the a-In2O3 Growth by Mist CVD	T. Yamamoto, A. Taguchi, R. Yamada, H. Nagai, T. Onuma, T. Honda, T. Yamaguchi	112
ECCEL8.	Roles Of In Doping In Rocksalt-Structured Mgzno Films Grown By Mist CVD Method	Masaki Matsuda, Kotaro Ogawa, Yuichi Ota, Tomohiro Yamaguchi, Kentaro Kaneko, Shizuo Fujita, Tohru Honda, Takeyoshi Onuma	113
ECCEL9.	Realization Of High Mobility In α-In_2O_3 Film Grown By Mist CVD With Different Concentration Of In_2O_3 Powder As Source Precursor	Akito Taguchi, Takeyoshi Onuma, Tohru Honda, Tomohiro Yamaguchi	115
ECCEL10.	Electrochemical Preparation Of Copper Complex Aqueous Solution For Complex Reduction Method	K. Kumagai, T. Suzuki, P. Hishimone, M. Sato, H. Nagai	116
ECCEL11.	Analysis Of Traditional Wood Roofing Materials And Surface Protection Agents By Color Value Analysis Estimation Of Deterioration Properties	Hideto Takeuchi, Masaki Tamura	118
ECCEL12.	Room-Temperature Deposited Flexible B-Doped In2O3 Transparent Conductive Film	Shun Mori, Kanta Kibishi, Shinri Yamadera, Ayumu Nodera, Kotaro Watanabe, Ichiro Takano, Shinya Aikawa	119

ECCEL13.	Partial Reduction Of Weakly-Bonded Oxygen In Snox Thin Films By Dissociated Nitrogen Atoms	Kotaro Watanabe, Takuma Kawaguchi, Shinya Aikawa	121

Breakout Room #2

Education and Human Studies & Architectural and Civil Engineering

Chairperson: Dr. Hoang Van Thanh, DUT

Presentation No.	Title	Author	Page
EHSL1.	A Study On Vehicle Body Acceleration And Body Motion Of A Rider During Riding A Bicycle	Rintaro Omiya, Motoki Tsukada, Yusuke Kurasaki, Satoru Kizawa, Ayuko Saito	124
EHSL2.	Research On The Acceleration And Trunk Posture While Riding A Bicycle	Motoki Tsukada, Rintaro Omiya, Yusuke Kurasaki, Satoru Kizawa, Ayuko Saito	125
EHSL3.	A Study On Gaze Control While Riding A Bicycle	Yusuke Kurasaki, Rintaro Omiya, Motoki Tsukada, Satoru Kizawa, Ayuko Saito	126
EHSL4.	A Research On The Development Of Walking For A Healthy Toddler	Ryu Katsuhara, Kei Hoshino, Ayuko Saito, Shinichiro Morichi, Satoru Kizawa	128
EHSL5.	A Study On Estimation Of Lower Limb Muscle Forces During Squatting	Kazuya Inoshita, Shinichiro Morichi, Yoshikazu Kobayashi, Satoru Kizawa, Ayuko Saito	129
EHSL6.	A Study On Gaze In Passing A Ball	Takato Abe, Wataru Ichikawa, Satoru Kizawa, Ayuko Saito	130
EHSL7.	A Study On Person Dependency In Person Identification By Acceleration	Yoshihaya Takahashi, Takeshi Kamiyama, Masato Oguchi, Saneyasu Yamaguchi	131
EHSL8.	Research On Inter-Joint Coordination In Abnormal Gait	Kei Hoshino, Ryu Katsuhara, Shinichiro Morichi, Satoru Kizawa, Ayuko Saito	132
EHSL9.	A Proposal For Adaptive Advertising Media Using Viewers' Preferences And Person Recognition	Miho Mizutani, Yoshio Miki	134
EHSL10.	Relationship Between Plaster Density And Mechanical Properties By Unit Water Content Of Plaster Mixture	Aoba Sakai Kentaro Oka, Masaki Tamura	135
EHSL11.	Analysis Of Concentration During Reading By Saccadic Amplitude And Blink	Ryota Shimizu, Hisaya Tanaka	138
EHSL12.	Will Blockchain Technology Create A Leap Forward In The Construction Industry?	Anh-Tuan Nguyen	139

Breakout Room #3

Information and Communications Technology (ICT) & Intelligent and Secure Systems

Chairperson: Dr. Phan Tran Dang Khoa, DUT

Presentation No.	Title	Author	Page
ICTL1.	Study on a Trunk Reservation Control Method with Waiting Queue for Priority Calls in Emergency Situation	Yoichiro Arii, Katsunori Yamaoka, Kenichi Baba	145
ICTL2.	Method of Quantitative Assessment of Media Influence on Twitter	Yuki Sakurai, Aki Kobayashi	146

Breakout Room #4

Advanced Functional Materials & Mechanical Engineering

Chairperson: Dr. Huynh Thanh Tung, DUT

AFML9.	Study On Acceleration Coordination During Dribbling In Soccer	Wataru Ichikawa, Takato Abe, Satoru Kizawa, Ayuko Saito	181
AFML10.	Research On Exercise Support By Auditory Information Using Spatial Audio	Kota Yamamoto, Daigo Misaki	182
AFML11.	Preparation of the Side-chain Modified Peptides as Lysine-specific Demethylase 1 Inhibitors	Masaki Asakawa, Ayumu Agarie, Taeko Kakizawa, Takayoshi Suzuki	183
AFML12.	Synthesis of Short Peptides as Lysine-specific Demethylase 1 Inhibitors	Ren Inoue, Taeko Kakizawa, Takayoshi Suzuki	184

Breakout Room #5

Electric Engineering and Electronic Engineering

Chairperson: Dr. Vo Tuan Minh, DUT

Presentation No.	Title	Author	Page
EEEL1.	Analysis Malware Infection Of IOT Devices On Zero Trust Networks	Yudai Sakurai, Osamu Mizuno	186
EEEL2.	A Study Of Dynamic Routing Method In ICN-Based Wireless Sensor Networks	Kohei Yamamoto, Takafumi Taya, Eishin Nagaoka, Osamu Mizuno	187
EEEL3.	Affect Of Lorawan Network Parameters On The Performance Of The Network In Frequency Band In Vietnam	Tran Van Lic, Fang Yi Lee, Meng-Hsun Tsai	188
EEEL4.	Mutual Authentication Scheme In ICN-Based Wireless Sensor Networks	Takafumi Taya, Eishin Nagaoka, Osamu Mizuno	194
EEEL5.	Frequency Utilization Efficiency Improvement By Spectrum Suppressed Transmission With 16QAM	Teppei Kanke, Takatoshi Sugiyama	195
EEEL6.	A Study On Performance Of CPU Clock Rate Control Based On Application Monitoring	Kota Kumakura, Takeshi Kamiyama, Masato Oguchi, Saneyasu Yamaguchi	196
EEEL7.	A Study On A Modified Vision Transformer Model For Image Processing	Tatsuhiko Ikeda, Hidetoshi Saito	197
EEEL8.	A Study On Deletion Of Snis For Service Identification	Ryo Asaoka, Akihiro Nakao, Masato Oguchi, Saneyasu Yamaguchi	198
EEEL9.	A Study On Mutual Interference With Islanding Detection Function In Inverters With Inertia Function	Dehui Li, Yasuhiro Noro	199
EEEL10.	CO2 Gas Sensing By In2O3-Based Thin-Film Transistors	Ayumu Nodera, Shun Mori, Shinya Aikawa	200
EEEL11.	Electrical Property And Valence Band Offset In Conductive Mgnio On Sapphire Substrates	M. Murayama, A. Ishikawa, T. Yamaguchi, T. Honda, K. Sasaki, A. Kuramata, T. Onuma	203
EEEL12.	Growth And Characterization Of Algan And Multiple Quantum Wells With Varying III/V Ratios By RF-MBE	Mahiro Hayasaki, Tomoya Yamaguchi, Tomohiro Yamaguchi, Tohru Honda, Takeyoshi Onuma	204
EEEL13.	Structural Analysis In Epitaxial Growth Of Gainn By RF-MBE Using XRD-RSM	J. Takeuchi, T. Sasaki, H. Yokoyama, T. Onuma, T.	205

		Honda, T. Yamaguchi	

Keynote Presentation

Exploring the repressive impacts of pomegranate peels on urinary bladder urothelial carcinoma

Ching-Ping Chang[1], Yu-Yi Chan[2], Chien-Feng Li[1], Lan-Hsiang Chien[1], Song-Tay Lee[2] and Ting-Feng Wu[2,*]

[1]Department of Medical Research, Chi Mei Medical Center, Taiwan

[2]Department of Biotechnology and Food Technology, Southern Taiwan University of Science and Technology, Taiwan

E-mail: wutingfe@stust.edu.tw

Abstract

Pomegranate (*Punica granatum L.)* fruit has demonstrated its repressive effectiveness to many tumors. In this investigation, In this study, the data from the MTT assay illustrated that the ethanol extract of pomegranate peel showed better repressive efficacy to aggressive human bladder cancer J82 and T24 cells compared to the pulp. The ethyl acetate portion of peel ethanol extract has the best repressive impacts on bladder cancer cells. PEPE2 fraction, one of the eight segments eluted from the ethyl acetate portion with Diaion HP-20 chromatography, exhibited the best oppressive effects in bladder cancer cells. The flow cytometry and apoptotic pathway exploration results implicated the inhibitory efficiency of PEPE2 fraction attributed to the UBUC cell apoptosis. Xenograft-evoked bladder tumors in nude mice demonstrated that the ethyl acetate layer (2, 5, 10, and 100 mg/kg) feed could decrease the volume and weight of T24 tumors. Meanwhile, the extract could induce xenografted tumor apoptosis.

Urothelial carcinoma is the most encountered lesion among various bladder tumor types, contributing to more than 90% of bladder cancer cases [1]. Pomegranate peel is a rich resource of phenolics, flavonoids, ellagitannins, and proanthocyanins [2]. In this study, the pulps and peels of fresh pomegranate fruits were soaked with ethanol to produce pulp extract (PEG) and peel extract (PEP). MTT measurement indicated that PEP showed better oppressive capability than PEG to UBUC cells. Thus, PEP was extracted consecutively between EtOAc/H2O and n-BuOH/H2O, respectively, to give three portions of H_2O, n-BuOH, and EtOAc. IC_{50} of EtOAc, butanol, and water layers from PEP were 5, 10, and 50 μg/mL, respectively, toward the T24 cells, while toward the J82 cells, IC_{50} of these three layers were 20, 50, and 50 μg/mL. Because of the best activities, the EtOAc portion was fractionated into eight parts by Diaion HP-20 column chromatography. Findings in Figure 1 showed that the PEPE2 fraction revealed the best suppressive impacts on human T24 and J82 cells and the minor harmful effects on normal-like human E7 urothelial cells

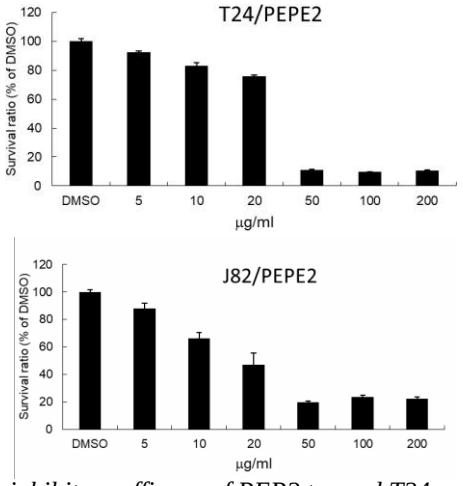

Fig. 1. The inhibitory efficacy of PEP2 toward T24 and J82 cells.

In order to further confirm the UBUC-cell-line-associated results, we injected T24 cells into nude mice to provoke xenografted tumors and investigate the EtOAc extract's inhibitory effects on tumor growth *in vivo*. As indicated in Fig. 2, T24 tumors of the EtOAc extract-cured group (2, 5, 10, and 100 mg/kg) developed slower than the control tumors. On week 10, tumor volumes of the control animals had reached 600 mm^3 on average, while those of 5 and 10 mg/kg of extract-consumed counterparts only had 200 mm^3 on average, respectively.

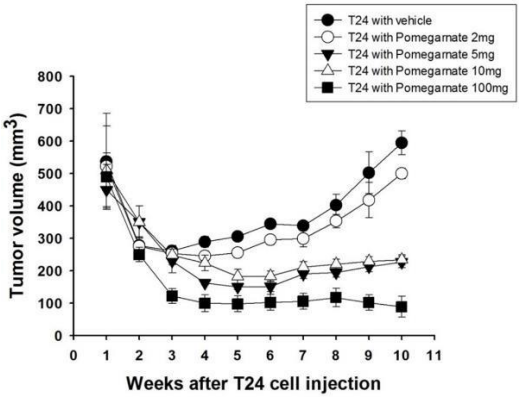

Fig. 2. The curb of the xenografted UBUC growth in nude mice by EtOAc extract therapy.

References:

[1] R. L. Siegel, K. D. Miller, A. Jemal, *CA Cancer J. Clin.*, **6**, 7–30 (2017).

[2] P. Sharma, S. F. McClees, F. Afaq, *Molecules*, **22**, 177 (2017).

Synthesis of MoS_2 nanosheets and their electrochemical evaluation as cathode materials for aqueous Zn-ion Batteries

Kien Nguyen-Ba[a*], Huy Le-Quoc[b], Tran Anh-Vo[a], Trang Nguyen-Thi-Thu[b], Vu-Truong-Son Le[c], Ngoc-Dat Trinh[c]

[a]Faculty of Mechanical engineering, University of Science and Technology - The University of Danang, Danang, Vietnam

[b]Faculty of Advanced Science and Technology, University of Science and Technology - The University of Danang, Danang, Vietnam

[c]Faculty of Physics, University of Science and Education - The University of Danang, Danang, Vietnam

*E-mail: nbkien@dut.udn.vn

Abstract

Aqueous rechargeable Zn-ion batteries (AZIBs) have recently attracted considerable attention, due to their intrinsic safety, environmentally benign, and low-cost. However, finding suitable cathode materials is still challenging and attracting much research. Layered MoS_2 has been considered a promising cathode candidate. Herein, we report a facile hydrothermal synthesis of MoS_2 at different reaction temperatures and investigation of their electrochemical properties as cathode material for AZIBs. We found that the as-prepared MoS_2 at the highest temperature 200°C achieved the highest specific capacity of 160 mAh/g at the charge/discharge rate of 100 mA/g. While the MoS_2 synthesized at medium temperature 180°C showed better stability and initial columbic efficiency. The MoS_2 synthesized at the lowest temperature 160°C suffered poor stability and significant fluctuation in columbic efficiency.

1. Introduction

Lithium-ion batteries (LIBs) have been widely used to power electronic devices, military equipment, and electric vehicles. However, safety concerns, and high-cost and environmental issues of LIBs have hindered their possible use for large-scale storage applications [1-3]. The aqueous zinc-ion battery appears as one of the most promising candidates, because of its high theoretical specific capacity (820 mAh/g). Combined with the advantages of high abundance, eco-friendly, and low cost, it may be widely used for large-scale stationary energy storage in the future [4]. Molybdenum disulfide (MoS_2), with a well-defined layered structure, has been considered as a promising cathode material for AZIBs [5].

Here, we report a facile hydrothermal synthesis to prepare the MoS_2 nanosheets at different reaction temperature and investigate their electrochemical properties as cathode materials for aqueous rechargeable Zn-ion batteries.

2. Experimental section

2.1. Materials synthesis

All chemicals were of analytical grade and directly used without further purification. Firstly, 1 mmol of ammonium paramolybdate and 30 mmol of thiourea were added into 35 mL D.I water. Then the mixture was sonicated for 30 min. and transferred into a 100 mL Teflon-lined stainless-steel autoclave. The autoclave was maintained at 160°C for 24h in an oven. After cooling naturally, the black powder was then collected and washed repeatedly with water and absolute ethanol, followed by drying at 60°C for 12h. The preparation procedure of other MoS_2 were similar with the MoS_2-160°C except for the different reaction temperatures, 180 °C and 200 °C.

2.2. Material characterizations

The crystal structure and morphology of all powders were characterized by an X-Ray diffractometer (Bruker D8 advanced, Germany) with Cu-Kα radiation (λ = 1.5418 Å) at 40 kV and by scanning electron microscopy (SEM, JEOL, JSM-IT200), respectively.

2.3. Electrochemical characterizations

To prepare the cathode electrodes, as-prepared MoS_2, carbon black (Super-P), and PVDF binder were mixed by a weight ratio of 6:3:1. Then, a certain amount of NMP solvent was added to the mixture and ground on a mortar for 30 minutes until a homogeneous slurry was obtained. After that, the slurry was uniformly cast on the carbon foil and dried in air at 60°C for 1 h and then dried in a vacuum oven at 80°C for 10 h. Finally, the carbon foil was cut into 12 mm in diameter disc electrodes with the active materials mass loading 1–2.5 mg/cm2. Commercial zinc foil was cut into 12 mm in diameter disc electrodes used as the anode. Aqueous 3M Zn(CF3SO3)2 solution was used as the electrolyte, and the glass microfiber membrane was used as the separator. A CR2032-type coin cell was fabricated in the air atmosphere to evaluate the electrochemical properties. Galvanostatic constant current charge/discharge of batteries was caried-out by a LAND CT2001 battery cycler. All tests were carried out at room temperature (Scheme 1).

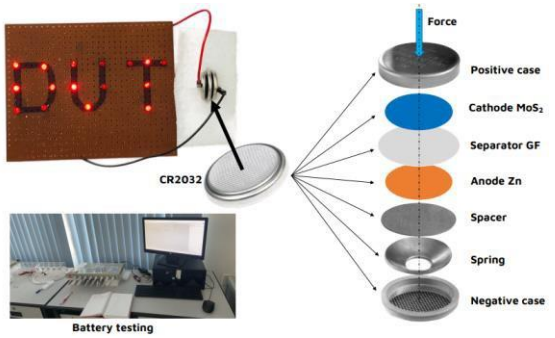

Scheme 1. Battery asembling and electrochemical characterization.

3. Results and discussion

Fig.1 shows typical XRD pattern of the MoS_2 nanosheets synthesized at 160ºC. The diffraction peaks at around 32.6º, 35.5º, and 57.5º, assigning to the (100), (102), (110) planes, are matched well to the hexagonal 2H-MoS_2 structure (JCPDS 37-1492) [6]. Moreover, a (002) peak shifts to the low-angle region of 13.3º, due to the slight increase of interlayer spacing. Broaden and low intensity of characteristic peaks suggest the disorder arrangement and low crystallinity of the as prepared MoS_2, which could facilitate the interlayer diffusion of Zn^{2+} ions during charging and discharging.

Scanning electron microscopy (SEM) was used to investigate the morphology of the as-prepared MoS_2. As shown in Fig.2 The SEM image of the MoS_2 synthesized at exhibits flower-like morphology.

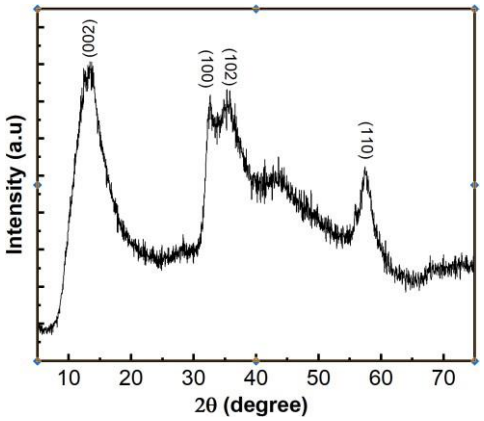

Fig. 1. XRD pattern of MoS_2 synthesized at 160ºC

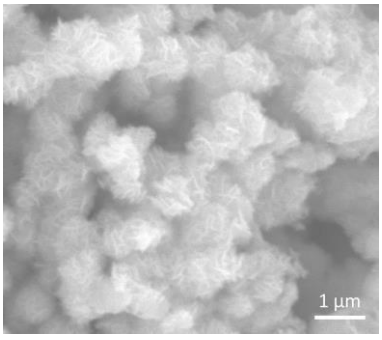

Fig. 2. SEM image of MoS_2 synthesized at 160ºC

The galvanostatic charge/discharge profiles of the as prepared MoS_2 at the current rate of 100 mA/g in the potential window of 0.3–1.3 V (vs Zn^{2+}/Zn) are displayed in Fig.3. As can be clearly seen the as-prepared MoS_2 synthesized at 200ºC achieved the highest capacity of 160 mAh/g. While the MoS_2 synthesized at 180ºC showed better stability and initial columbic efficiency. The MoS_2 synthesized at 160ºC suffered poor stability and significant fluctuation in columbic efficiency.

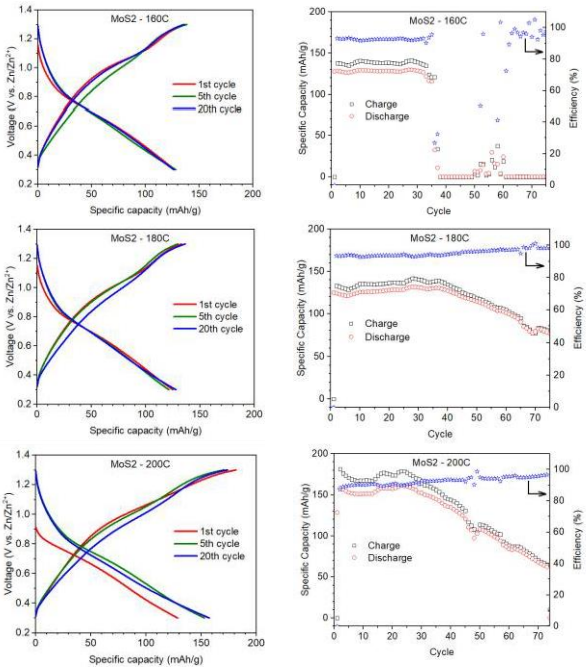

Fig.3. Galvanostatic charge/discharge of MoS_2 prepared at different temperatures at the current rate 100 mA/g.

4. Conclusions

In summary, we successfully synthesized MoS_2 nanosheets at different temperatures and investigated their electrochemical properties as cathode materials for rechargeable aqueous Zn-ion batteries. All prepared materials have high capacity but exhibit significant fluctuation of stability and columbic efficiency between different reaction temperatures. Further systematic studies will be needed to improve the performance of the materials.

Acknowledgement

This study was supported by Danang University of Science and Technology – The University of Danang under the Research Grant. Number T2021-02-31. Authors would like to thank researchers from the Faculty of Physics of Danang University of Science and Education – The University of Danang for supports with materials characterization.

References:

[1] N.S. Choi, Z. Chen, S.A. Freunberger, X. Ji, Y.K. Sun, K. Amine, G. Yushin, L.F. Nazar, J. Cho, P.G. Bruce, Challenges facing lithium batteries and electrical double-layer capacitors, Angew. Chem. Int. Ed. 51 (2012) 9994–10024.

[2] P. Yu, Y. Zeng, H. Zhang, M. Yu, Y. Tong, X. Lu, Flexible Zn-ion batteries: recent progress and challenges, Small 15 (2019) e1804760.

[3] X. Zeng, J. Hao, Z. Wang, J. Mao, Z. Guo, Recent progress and perspectives on aqueous Zn-based rechargeable batteries with mild aqueous electrolytes, Energy Storage Mater. 20 (2019) 410–437.

[4] G. Fang, J. Zhou, A. Pan, S. Liang, Recent Advances in Aqueous Zinc-Ion Batteries, ACS Energy Lett. 3 (2018) 2480–2501.

[5] S. Huang, F. Wan, S. Bi, J. Zhu, Z. Niu, J. Chen, A self-healing integrated all-in-one zinc-ion battery, Angew. Chem. Int. Ed. 58 (2019) 4313–4317.

[6] J. Shin, D.S. Choi, H.J. Lee, Y. Jung, J.W. Choi, Hydrated intercalation for highperformance aqueous zinc ion batteries, Adv. Energy Mater. 9 (2019) 1900083.

Solid Oxide Fuel Cell Technology and Its Application to Shrimp Farming

Yusuke Shiratori

Department of Mechanical Science and Engineering, School of Advanced Engineering, Kogakuin University, Japan
E-mail: shiratori@cc.kogakuin.ac.jp

Abstract

Highly-efficient solid oxide fuel cell (SOFC) is promising distributed power generator. This technology fueled by biogas will be applied to shrimp farming for the sustainable development of Mekong Delta.

Rapid economic growth in ASEAN countries has resulted in two issues, the increase in organic wastes and the unstable electric power supply. In Vietnam, fisheries industry including aquaculture is one of the major industries. Spread of the intensive shrimp farming using small ponds (500-1000 m^2) with a high shrimp stocking density brings a serious impact on the ecosystem of Mekong Delta. Sludge accumulation can cause water quality degradation, resulting in shrimp disease outbreak.

In the Science and Technology Research Partnership for Sustainable Development (SATREPS) program supported by the Japan International Cooperation Agency (JICA) and the Japan Science and Technology Agency (JST), under the collaboration with Institute for Nanotechnology (INT), Vietnam National University-Ho Chi Minh city (VNUHCM), it was found that the shrimp pond sludge can be utilized for biogas production, because it can act not only as a media to make biomass slurry but also the source of methanogenic bacteria for anaerobic fermentation to produce biogas [1].

In Vietnam, annual growth rate of electricity demand of recent years is around 10 % higher than economic growth rate [2]. To supplement the shortage of power supply, the number of coal-fired power plant continues to increase, and its share is expected to be 50% by 2030. For the sustainable development of local society, highly-efficient distributed power generator fueled by biogas is strongly desired to install.

Generating electricity without fuel burning is the key to increase power generation efficiency. In the conventional heat engine systems, chemical energy of a fuel is converted to thermal energy whose utilization is restricted by Carnot efficiency. Moreover, chemical energy is sequentially converted to thermal energy, kinetic energy and finally electrical energy including various irreversible losses. Unlike heat engine, fuel cell based on electrochemical process can convert chemical energy of a fuel directly into electricity, not through the conversion to sensible heat, resulting in elevated efficiency.

Among various types of fuel cells, solid oxide fuel cells (SOFCs) composed of ceramic materials operated at high temperature (600-900ºC) exhibit highest power generation efficiency (η_e) over 50% due to its rapid reaction kinetics and effective heat recovery concept [3]. Our 1 kW SOFC system developed for the biogas power generation recorded η_e of 53.1% LHV for the feed of 5.5 NL min^{-1} biogas (CH_4: 55%, CO_2: 45%) at a cell stack temperature of 700°C and fuel utilization of 69.0% (current: 30 A, stack voltage: 32 V) [4].

Based on the above findings and knowledge, Yuko-Keiso Co., LTD., Japan, starts a new project supported by New Energy and Industrial Technology Development Organization (NEDO) to demonste the next-generation shrimp farming (see Fig. 1) with biogas-fueled SOFC controlled by IoT aiming at the spread of this integrated technology for the sustainable development of Mekong Delta.

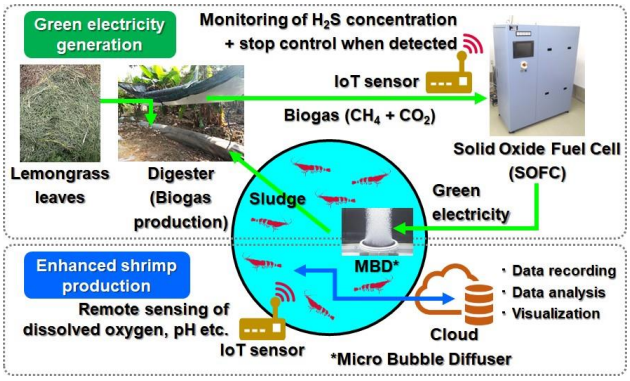

Fig. 1. Concept of the next-generation shrimp farming with biogas-fueled SOFC and IoT.

[1] Y. Shiratori, T. Yamakawa, M. Sakamoto, H. Yoshida, T. Kitaoka, Q.T. Tran, D.C.T. Doan, M.C. Dang, *Frontiers in Environmental Science*, **5**, Article 25 (2017).
[2] Vietnam electricity 2018, JETRO Hanoi (2019).
[3] N.Q. Minh, *J. Am. Ceram. Soc.*, **76**, 563–588 (1993).
[4] Y. Shiratori, M. Sakamoto, T. G.H. Nguyen, T. Yamakawa, T. Kitaoka, H. Orishima, H. Matsubara, Y. Watanabe, S. Nakatsuka, T.C.D. Doan, C.M. Dang, *Fuel Cells*, **19(4)**, 346–353 (2019).

Oral Presentation (November 24th from 12:40 to 14:20 (JST))

Breakout Room #1

Architectural and Civil Engineering

Chairperson: Dr. Pham My, DUT

Presentation No.	Title	Author	Page
ACE1.	Seismic Performance of an Irregular School Building Based on Incremental Dynamic Analysis	Carla Mae B. Pilapil, Carmina B. Borja, Richelle G. Zafra	24
ACE2.	Development of Seismic Vulnerability Curves of Reinforced Concrete Buildings of the University of the Philippines Los Baños using Computational Methods	Gabriel Antonio I. Pimentel, Richelle G. Zafra, Carmina B. Borja, Bien Dave B. Papasin	29
ACE3.	Comparative Analysis on the Use of Low-Impact Development (LID) Practices and Flood Rerouting for Flood Mitigation using EPA-SWMM in San Isidro, Batangas City, Batangas, Philippines	Celwyn Joseph A. de Roxas, Kale Ashley P. Carurucan, Perlie P. Velasco, Ma. Hazel T. Castillo	34
ACE4.	Geostatistical Modeling of Standard Penetration Test Data to Determine the Minimum Required Number of Boreholes for Geotechnical Investigations	Roel Nikko T. Magno, Andre C. Cruz, Jedidiah Joel C. Aguirre, Ron Gabriel O. Navarro	40

Seismic Performance of an Irregular School Building Based on Incremental Dynamic Analysis

Carla Mae B. Pilapil*, Carmina B. Borja, and Richelle G. Zafra

Department of Civil Engineering, College of Engineering and Agro-Industrial Technology, University of the Philippines Los Baños, Philippines
E-mail: cbpilapil@up.edu.ph

Abstract

The University of the Philippines Los Baños (UPLB), located in the province of Laguna, is a constituent university of the Philippine's national university. To reduce seismic-related disasters in the campus, a study was conducted in 2015 to seismic vulnerability prioritization of UPLB buildings based on the structural vulnerability, importance, and hazard. It showed that the NCAS building – a highly irregular structure - is among the buildings that need to be prioritized for seismic assessment. This paper aims to determine the seismic performance of NCAS building through Incremental Dynamic Analysis (IDA) using spectrally-matched time histories. Structural nonlinearity in beams and columns were modeled using fiber section with distributed plasticity. The maximum interstory drift ratio (MaxISDR) was used as a damage measure while the spectral acceleration as the intensity measure. IDA curves were generated. The base shear of the structure and demand/capacity ratios of each structural member were also determined. The result showed that all beams and columns passed the Life Safety Performance Level in terms of plastic rotation. The MaxISDR at Life Safety Performance Level ranges from 2.3% to 2.6%. Building collapse is expected to be reached between 1.75g to 2.7g spectral acceleration. The IDA results were used to generate the fragility curves for the Life Safety and the Collapse Prevention performance levels. Fragility curves showed that the NCAS building has the probability of 85% and 5% of reaching Life Safety and Collapse Prevention, respectively. The results of the study may help in post-earthquake damage assessment in the campus.

UPLB, a constituent university of the Philippine's national university, is in the province of Laguna. There are three active fault lines surrounding Laguna: West Valley Fault (WVF), Infanta Fault on the east, and Lubang Fault on the south. Of these three, the nearest is the WVF at 20 kilometers and it is also expected to produce the strongest earthquake among the three active faults near the province. The fault distance indicates that the anticipated earthquake to be produced by the WVF is a far-fault earthquake (fault distance > 15 km). A far-fault earthquake has a long period which is the reason why resonance might occur for buildings with high periods (e.g. tall buildings). Resonance will result in higher response and greater building damage. However, school buildings, being short buildings, do not guarantee a short-period behavior because it is typically made of frame systems.

Strong ground motion is anticipated at the site which might result in structural and nonstructural damages to the UPLB buildings. As part of the disaster prevention of UPLB, the buildings need to be seismically evaluated. A previous study identified the vulnerability of UPLB buildings through a semi-quantitative approach[1]. The academic buildings were arranged based on their level of priority using the parameters such as the building's structural vulnerability, importance, and hazard. The UPLB buildings were ranked according to a scoring system where the higher-ranked buildings are at medium risk. A higher ranking means that it must be prioritized in conducting a seismic evaluation. The study identified the NCAS Building – which houses the offices of the University Registrar, the Animal Biology Division of the Institute of Biological Sciences, and the Department of Humanities – as a high priority for seismic analysis.

The NCAS building is a four-story reinforced concrete structure with a lot area of about 2100 m2 and a total floor area of about 6300 m2. Fig. 1 and Fig.2 show the front and top views of the UPLB NCAS building, respectively. The structure is not parallel to or symmetric about the major orthogonal axis of the lateral force-resisting systems. The building shows a nonparallel systems irregularity based on NSCP 2015[2]. Vertical geometric irregularity can also be observed in the building. The horizontal dimension of the second story is more than 130% of the 3rd story.

Fig. 1. Top view of NCAS Building. (Source: Google Earth)

The building was constructed in 1997 and was designed based on NSCP 1992. The current code version during the conduct of this study is the NSCP 2015. There are significant differences between the two versions when it comes to seismic analysis and design parameters.

Fig. 2. Front view of NCAS Building. (Source: Google Earth)

The incremental dynamic analysis (IDA) is also a nonlinear dynamic procedure but is conducted with a suite of ground motion records. Unlike the conventional nonlinear time history analysis that is conducted once per ground motion record, IDA conducts a series of nonlinear time history analyses per ground motion record using the incrementally increasing scaling factors. Each ground motion is scaled with incrementally increasing scaling factors to ensure that the entire structural response is covered: from elastic to yielding, and finally to global instability. The advantage of scaling the ground motion records is that the evaluation will not be limited to the demand and capacity of each structural member. It also allows the determination of structural damage measures (in this case the MaxISDR) at different intensity measures (in this case the spectral acceleration). This is significant in generating fragility curves. A conventional nonlinear time history analysis does not have sufficient data to generate fragility curves unlike with the IDA. However, the main disadvantage of using IDA is its expensive computational cost compared to other available methods.

In this study, fragility curves were generated based on dynamic analysis to determine the probability of reaching or exceeding the Life Safety and Collapse Prevention performance levels at a given spectral acceleration. Fragility curves are important for estimating the potential damage from the expected earthquake. It can also be used for emergency response and disaster planning for overall loss estimation after the earthquake[3].

Retrofitting is expensive and thorough verification of the seismic analysis using a more advanced and a more detailed method like IDA might help in establishing the seismic performance of the NCAS building. Recommendation of the retrofitting procedure will follow if found to be necessary. Also, the result of this study can be used not only before the earthquake event but also after it. During the post-earthquake assessment, the MaxISDR determined in this study can help establish the structure's performance after the earthquake. This is beneficial because interstory drift is an easily measurable post-earthquake assessment parameter for standing buildings.

The main objective of this study is to assess the seismic performance of the UPLB NCAS building. This study specifically aims to:

1. Model the building using nonlinear column and beam elements using distributed plasticity approach;
2. Determine plastic chord rotations of beams and columns, and base shear as per ASCE 41-13 Life Safety Performance Level;
3. Determine the MaxISDR of the NCAS building as per FEMA 356 Life Safety Performance Level;
4. Generate IDA curves using a series of nonlinear time history analyses; and
5. Generate fragility curves based on Life Safety and Collapse Prevention performance levels.

Visual inspection was not conducted due to the COVID-19 restrictions at the time of the study. Moreover, the model was based mainly on the provided structural and architectural plans. Any discrepancies from the plan were not accounted for in structural modeling. Spectral acceleration was used as the intensity measure since it is more efficient to be used in conducting 3D nonlinear dynamic analysis as compared with the peak ground acceleration (PGA)[4]. Maximum interstory drift ratio (MaxISDR) was the damage measure since interstory drift ratio is easier to measure during the post-earthquake assessment. The MaxISDR is also a good damage measure in assessing global instability[5].

In this study, provisions on existing buildings were used rather than the provisions on new buildings. Based on ASCE 41-13 Section C2.2.1, the Basic Performance Objective for Existing Buildings (BPOE) allows a lower level of safety and a higher risk of collapse as compared to the Basic Performance Objective Equivalent to New Building Standards (BPON)[6]. This is in recognition that a new building has longer remaining life than an existing building. A new building requires a procedure that will obtain a more conservative design which not the case in the analysis of an existing building. It is also stated in the same section that achieving a higher level of safety based on the "new building equivalence" is often disproportionate to the incremental benefit. Unlike with the new construction, where there are more complete design flexibility and construction quality control, a higher level of safety is achieved at marginal additional cost.

The plastic rotations of beams and columns were assessed based on the Life Safety Performance Level.

Based on ASCE 41-13 Table 2-1, for the Tier 3 procedure, the structure under the Risk Category I (essential facilities) shall be evaluated based on the Life Safety and Collapse Prevention Performance Levels for BSE-1E (20% in 50 years) and BSE-2E (5% in 50 years) Seismic Hazard Levels, respectively. However, due to the time constraints, only the Life Safety Performance Level for BSE-1E was considered. Under the Life Safety, the building still has a safe margin before collapse. The BSE-1E seismic hazard level corresponds to an earthquake with 20% in 50-year probability of exceedance. This is equivalent to 225-year return period. Based on ASCE 41-13 Section 2.4.1.4, BSE-1N is the maximum of the BSE-1E Seismic Hazard Level. This was obtained by getting the two-thirds of the Maximum Considered Earthquake (MCE), equivalent to 2,475 year return period earthquake (2% in 50 years), from SAM-PH (DOST-PHIVOLCS, 2021) as per ASCE 7-05 (2005). The BSE-1N has a return period of 475 years (10% in 50 years) as per ASCE 41-13 Section C2.4.1.2.

For the fragility curves, Collapse Prevention limit state was also defined. This is to determine the structure's performance if it failed the Life Safety.

The IDA was conducted using the software SeismoStruct, and the rest of the mathematical calculations in MATLAB and MS Excel.

For the time history analysis, only three spectrally matched ground motion records were used due to time constraints. The original ground motion records were from the Pacific Earthquake Engineering Research Center (PEER).

Based on FEMA (2000), in performing nonlinear dynamic analysis, only the members that are part of the lateral-force-resisting system are required to be modeled. Thus, only the diaphragms, shear wall, and frame were considered in this study. The basement was not modeled since there is only one basement in the NCAS building and its effect on the local and global response can be neglected. The retaining wall of the basement was not modeled as it is not part of the lateral-force-resisting system. The cross-sections of the beams in the basement are relatively small so it is expected that the basement beams will not attract a significant lateral force. Thus, it can be neglected in this study. The frame members were modelled as nonlinear elements.

For the foundation, it is explicitly stated in the ASCE 7-16 that the use of a fixed base is permitted in conducting a seismic analysis. The flexibility of the foundations was neglected since the NCAS building is a mid-rise building which means that the structure is not highly flexible. It is also underlain by a stiff soil which means that the structure will be relatively more flexible than the soil. Thus, the soil flexibility impact is relatively small and can be neglected[7]. Additionally, FEMA P-2091 provided an equation for the rule of thumb test to determine whether the inertial soil-structure interaction (SSI) effects are likely to be significant or not [8].

Loadings were applied before proceeding with the analysis. The loads applied in the model were dead load, and live load. Load combination for the nonlinear procedure was used as per ASCE 41-13. Modal analysis was performed after the structural modeling. 20 modes were considered in the analysis and was subjected to verification whether the minimum modal participation factor of 90% was achieved. The Square Root of Sums of Square (SRSS) was used to determine the modal contributions. As per ASCE 41-13, the dynamic P-Δ effects can be incorporated in the analysis of NDP. The geometric nonlinearity such as the P-Δ effects was analyzed automatically in the software. This procedure captures the softening effect of compression and the stiffening effect of tension.

The resulting plastic rotation of each member was compared to the acceptance criteria based on Tables 10-7 and 10-8 of ASCE 41-13. Figure 3-4 shows the modeling parameters and numerical acceptance criteria for nonlinear procedures – reinforced concrete beams as lifted from Table 10-7 of ASCE.

The IM values used were based on the methodology of Vamvastikos and Cornell (2002) using the hunt and fill algorithm[4]. The appropriate IM values ensure that the entire range of structural response are covered. This structural response ranges from elasticity to yielding, and finally to global dynamic instability.

The hunt and fill algorithm is not available on the software used in this study. However, it can still be applied by manually computing the values and selecting the user-defined option for the inputs needed in scaling factors. The first run used a value of 0.005g which was meant to cover for the elastic region. The next run used was 0.1g that corresponds to the start of the hunting. The following runs used a value that is based on Equation 1.

$$IM_i = IM_{i-1} + 0.1 + 0.05(i-2) \qquad \text{(Equation 1)}$$

where: IM_i is the intensity measure at the i-th run starting from the 3rd run.

Equation 1 was used until the appearance of the first non-convergence which entails the structure's global collapse. In the IDA curve, the non-convergence refers to the flatline which means that the spectral acceleration where it occurs has a huge MaxISDR and can be interpreted as total collapse. After the appearance of the first non-convergence, additional two runs were performed to close the gap of the IM values to ensure that no collapse has been missed. The series of runs produced discrete points. To complete the IDA curve, these points were connected through spline interpolation. The spline interpolation was used rather than the basic piecewise interpolation since it has been proven to represent the IDA curve accurately[4]. The IDA results were used to generate fragility curves for the Life Safety and

Collapse Prevention limit states.

Equation 2 shows the formula of generating fragility curve that is given by a lognormal cumulative distribution function (CDF):

$$P=\emptyset(\ln(x\theta)/\beta) \quad \text{(Equation 2)}$$

where:
P is the probability of reaching or exceeding the specified limit state
$\emptyset$ is the standard normal CDF
θ is the mean
β is the standard deviation
x is the spectral acceleration

The pairs of spectral acceleration and MaxISDR from the IDA were used in generating the fragility curves. Using these values, the spectral acceleration at which the limit state will be reached was predicted using the forecast function in MS Excel. This was done on the selected earthquake records. Then, the mean (θ) and standard deviation (β) of the predicted spectral accelerations were computed. These values were then used in predicting the probability (P) of reaching or exceeding the specified limit state at a specified spectral acceleration (x). This was done by using the normal cumulative distribution function in excel where the ϕ parameter was automatically computed along with it.

The structural modeling of the NCAS building was performed in SeismoStruct as shown in Fig. 3. Only columns and beams were modelled with nonlinearity. Intermediate beams were not modelled since they are not part of the lateral force resisting system. The foundations were modelled as fixed base as permitted by ASCE 7-16 and was confirmed using the structure-to-soil stiffness ratio. The structure-to-soil stiffness ratio computed was less than 0.1 which means that SSI effects are not significant.

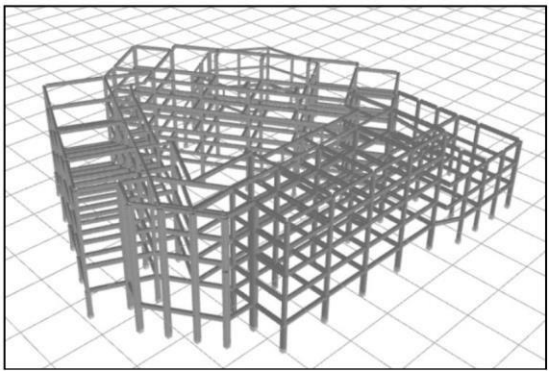

Fig. 3. Structural model of the NCAS Building in SeismoStruct

The model was then subjected to modal analysis to check the soundness as shown in Table 1. Table 1 shows that the fundamental period of the NCAS building is 0.751 s. Due to the irregularity of the NCAS building, 20 modes are needed to produce a participation factor of at least 90% as required by the code. This also serves as sanity check that assures that the result of this study is reasonable.

Table 1. Period and modal participation factors.

MODE	PERIOD (S)	SUM UX (%)	SUM UY (%)	SUM RZ (%)
1	0.751	15.30	52.16	3.25
2	0.733	70.59	75.43	10.43
3	0.665	83.25	78.68	65.64
.	.	.	.	.
.	.	.	.	.
.	.	.	.	.
20	0.305	89.36	90.41	86.94

Table 2 shows the maximum interstory drift ratio of the NCAS building to determine the building's performance against the Life Safety Performance Level in terms of the MaxISDR.

Table 2. MaxISDR along x- and y- directions.

EARTHQUAKE NAME	MaxISDR (%)
EQ 1 (Kobe)	0.751
EQ 2 (Darfield)	0.733
EQ 3 (Kocaeli)	0.665

Table 2 shows that the NCAS building obtained a MaxISDR of less than 2.5% when subjected to EQ 1 and EQ 3 earthquakes. On the other hand, the NCAS building obtained a MaxISDR of 2.523% when subjected to EQ 2 earthquake. FEMA 356[9] limits the MaxISDR to 2.5% for Life Safety Performance Level of reinforced concrete buildings. This means that the NCAS building passed the Life Safety Performance Level when subjected to earthquakes similar to Kobe and Kocaeli. However, the NCAS building failed the Life Safety Performance Level when subjected to earthquakes similar to Darfield. The difference of the evaluation can be attributed to the difference in earthquake duration, acceleration, and cycles. This can be improved by using ground motion records greater than three.

IDA curves were generated as shown in Fig. 4. The IDA curves generated from Darfield and Kocaeli are similar in that global collapse is observed at a spectral acceleration of around 1.75g. On the other hand, Kobe reached collapse at around 2.75g. The IDAs are known to be sensitive to ground motion records. Thus, encountering global collapse at different values of spectral acceleration is expected. The scattering can be addressed by using additional ground motion records, preferably more than three. Vamvastikos and Cornell (2004) suggested to use ten to twenty ground motion records. However, due to time constraints, performing IDA using ten earthquake records in this study is not feasible.

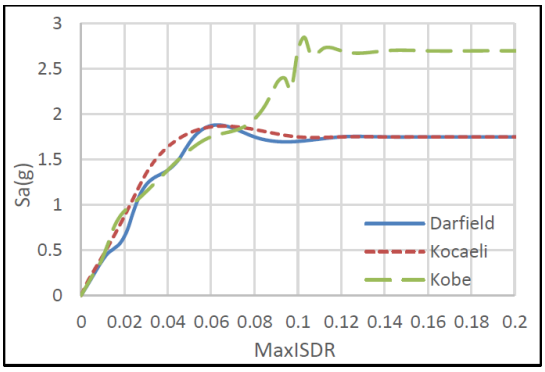

Fig. 4. Generated IDA curves

Using the IDA results, fragility curves were generated as shown in Fig. 5.

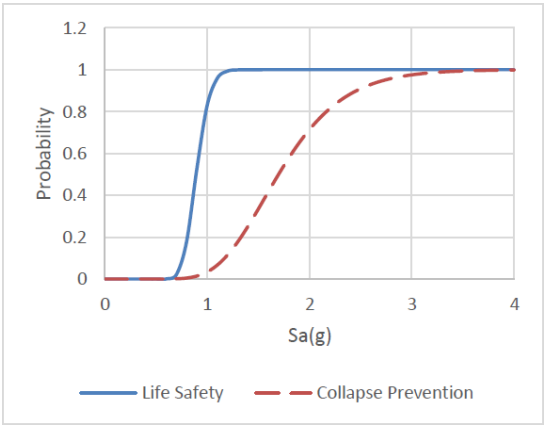

Fig. 4. Life safety and collapse prevention fragility curves

The fragility curves show that NCAS has 85% and 5% probabilities of reaching or exceeding the Life Safety and Collapse Prevention Performance Level, respectively, at a BSE-1E earthquake level.

It is recommended to use 10 to 20 ground motion records in the dynamic analysis to reduce the scattering of results.

It is also recommended to consider the Collapse Prevention Performance Level at BSE-2E Seismic Hazard Level for a full-building assessment in accordance to ASCE 41-13 Table 2-1. Since the seismic hazard level is higher, the building is expected to incur more damages.

Additionally, it would be better to use response spectrum generated from a PSHA study for better consistency with ASCE 41-13. This would ensure that the response spectral acceleration to be generated is accurate.

Also, other damage measures are recommended to be explored to assess the building performance such as residual interstory drift ratio (ResISDR) and peak story acceleration. The use of ResISDR will be significant in post-earthquake assessment as it is easier to be measured than the MaxISDR. Additionally, the use of peak story acceleration as damage measure is also recommended as it will be significant in assessing the content's damage and non-structural element's damage.

Considering the retrofitting cost, global retrofitting need not be considered. This is under the assumption that the material strengths and the structural condition did not degrade significantly. Otherwise, if cost is not a limitation and if the building is intended to be used beyond its design life retrofitting of columns in recommended considering that the probability of reaching the Life Safety performance level is 85%.

References:

[1] N.H. Cantos, [unpublished undergraduate thesis] (2015).

[2] Association of Structural Engineers of the Philippines, National Structural Code of the Philippines 2015, (2016).

[3] M. Remki, and F. Kehila, *International Congress and Exhibition "Sustainable Civil Infrastructures: Innovative Infrastructure Geotechnology,"* 42-54 (2008).

[4] D. Vamvastikos, and C.A. Cornell, *Earthquake Engineering & Structural Dynamics, 1-29* (2002)

[5] D. Vamvastikos, and M. Fragiadakis, *Engineering and Structural Dynamics, **39**, 141-163* (2009)

[6] R. Pekelnicky et al., ASCE 41-13: Seismic evaluation and retrofit rehabilitation of existing buildings, *Proceedings of the SEAOC*, (2012)

[7] Applied Technology Council, FEMA P-2091 A Practical Guide to Soil-Structure Interaction, (2020)

[8] Applied Technology Council, FEMA 356 Prestandard and Commentary for the Seismic Rehabilitation of Buildings, (2000)

Development of Seismic Vulnerability Curves of Reinforced Concrete Buildings of the University of the Philippines Los Baños using Computational Methods

Gabriel Antonio I. Pimentel, Richelle G. Zafra*, Carmina B. Borja and Bien Dave B. Papasin

Department of Civil Engineering, University of the Philippines Los Baños, Philippines
E-mail: gipimentel@up.edu.ph, rgzafra@up.edu.ph, cbborja1@up.edu.ph, bbpapasin@up.edu.ph

Abstract

Vulnerability curves are functions that aid in disaster risk assessment. With the University of the Philippines Los Baños (UPLB) located about 20 kilometers from the West Valley Fault Segment of the Valley Fault System which can potentially produce a magnitude 7.2 earthquake, there is a necessity to evaluate the built environment as an effort for earthquake preparedness. The study developed fragility and vulnerability curves for low and mid-rise reinforced concrete moment resisting frame structures within the campus. Based on seismic risk ranking conducted in a past study and the availability of structural models, the College of Engineering and Agro-industrial Technology B Building (CEAT B) and New College of Arts and Sciences (NCAS) Building were selected to represent low and mid-rise structures, respectively. Fragility curves per discrete damage state were developed from the capacity curves produced from a pushover analysis. The vulnerability curves were produced from mean damage indices taken from the fragility curves and then expressed in the Modified Mercalli Intensity scale (MMI). Results show that the qualitative descriptions of the MMI scale and the damage states for the obtained curves of reinforced concrete based on HAZUS MH compliments one another.

I. Introduction

The Philippines is highly susceptible to strong natural hazards due to its geographic location. Located along the Pacific Ring of Fire, the entire country is seismically active. Active earthquake sources include the Philippine Trench, the Manila Trench, the Philippine Fault Zone (PFZ), and the Valley Fault System (VFS).

The University of the Philippines Los Baños (UPLB) is located about 20 kilometers from the West Valley Fault Segment of the VFS [1]. Most of the structures within the campus are considered essential facilities based on the National Structural Code of the Philippines (NSCP) [2] and the functionality of these buildings must hold when subjected to an earthquake of devastating capability.

Due to the unpredictable nature of earthquakes, disaster risk mitigation plans should be adapted to reduce the impact of such events on people and structures. As part of disaster preparedness, building seismic vulnerability curves are useful in determining a building type's vulnerability to a given level of peak-ground motion.

Fragility curves are functions that describe the probability of being in or exceeding discrete damage states against a specific potential earth science hazard. Damage states are range of damage that qualitatively describes the conditions of a structure. Discrete damage is divided into slight, moderate, extensive, and complete [3].

Vulnerability curves are tools for earthquake preparedness that are developed to describe a specific building type's response, in terms of damage states, to a specific ground motion intensity. Tingatinga et al.[4] constructed vulnerability curves for multiple building classifications present in the Philippines. Various methodologies were applied in producing the vulnerability curves, namely heuristic, computational, and empirical approaches. They found that the computational approach is best suited for reinforced concrete (RC) structures.

This study produced fragility and vulnerability curves for a low-rise and mid-rise RC building in UPLB based on a modified version of the computational method described by [4] to address the earthquake intensity conversion for the vulnerability curves and the computation of the threshold values for the fragility curves.

II. Methodology

2.1 Building Selection

Only one building per class was considered based on HAZUS MH structural building classification [3]. The building selected for low-rise (C1-L), and mid-rise (C1-M) RC moment-resisting frames was the College of Engineering and Agro-industrial Technology (CEAT) B Building and New College of Arts and Sciences (NCAS) Building, respectively. These were also the buildings, among several buildings, considered by [5] and [6] in their study of building damage and seismic risk assessment of buildings in UPLB, respectively.

CEAT B Building, shown in Fig. 1, was built in 1968 and recently reached its 50-year serviceable design life. It stands at about 9.8m with two stories. The building features an out-of-plane discontinuity along its stairway.

The NCAS Building, shown in Fig. 2, was built in 1997 and stands at about 20.8 meters with four stories. The building features non-orthogonal irregularity as seen on its plan view and vertical geometric irregularity.

(a) Left side view

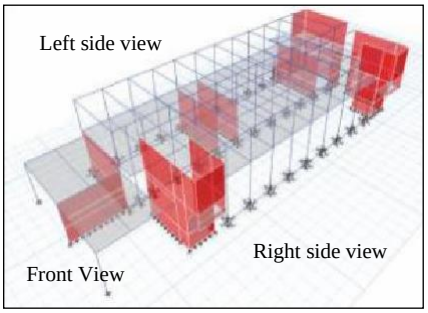

(b) Structural model

Fig. 1. CEAT B Building

(a) Front view

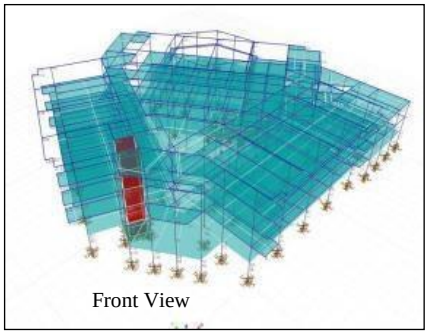

(b) Structural model

Fig. 2. NCAS Building

2.2 Response Spectrum Analysis

A site-specific response spectrum was made to determine the response of the buildings to seismic hazard. Values for spectral acceleration (SA) at 0.2 and 1.0 seconds were based from SA maps of [7] that consider the Maximum Considered Earthquake (MCE) with a 2475-year mean recurrence interval (MRI) on rock site with 5% damping. The design response spectrum was constructed following ASCE 7-16 [8] provisions with site coefficients for stiff soil (soil type D). Based on available soil investigation reports, soil Type D prevails in the UPLB campus.

2.3 Push-over Analysis

A nonlinear static pushover analysis was conducted to produce the fragility curves. The analysis considers taking a control point in the roof level of the model then a lateral load is applied monotonically until the ultimate capacity is reached. From the analysis, the capacity curve described by the base shear and control point displacement is plotted. The pushover analysis followed the provisions set in ASCE 41-17 [9]. Two procedures used the FEMA 440 Equivalent Linearization [10] and the ASCE 41-17 Nonlinear Static Procedure (NSP) [9].

FEMA 440 EL was used to apply the capacity spectrum method (CSM). The capacity curve was converted in terms of spectral parameters SA and SD. CSM works by converting the plots into an equivalent acceleration-displacement response spectra (ADRS) and then superimposing the capacity curve and the single demand curve from the response spectrum to obtain the performance point. The performance point describes the SA, SD, base shear, and displacement based on specific demand.

ASCE 41-17 [9] NSP was used for the equivalent linearization of the capacity curve via bilinear approximation of the displacement coefficient method (DCM). DCM is conducted by applying multiple computed modification factors to the peak elastic displacement to obtain base shear and roof displacement even beyond the elastic limit. The ultimate and yield capacities were obtained from the bilinear approximation of the capacity curve.

The pushover analysis was applied to the positive and negative x and y directions of the models to account for the asymmetrical layout of the buildings.

2.4 Fragility and Vulnerability Curves

Fragility and vulnerability curves are both described by a lognormal cumulative distribution function. The curves are governed by their median parameter and their logarithmic standard deviation. Eq'n. (1) shows the standard equation for the curves:

$$P(ds|X) = \emptyset\left[\frac{ln\left(\frac{X}{\bar{X}}\right)}{\beta ds}\right] \quad (1)$$

where: $\bar{X}$is the median value of parameter X for damage state ds ; β is the logarithmic standard deviation or uncertainty; and ϕ is the standard normal cumulative distribution function.

The fragility curves were constructed by taking the yield and ultimate SD of the resulting capacity curves from the converted bilinear approximation in ADRS format. The damage state thresholds for the median values of the curves were computed using the methods described by [11] as shown in the capacity

curve of Fig. 3.

Damage state	$\overline{Sd}_{dsi}$ values	Graphical representation of the damage thresholds in the bilinear capacity spectrum
Slight	$0.7\bar{d}y$	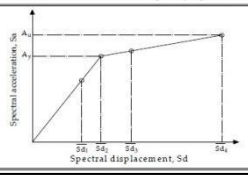
Moderate	$\bar{d}y$	
Severe	$\bar{d}y + 0.25(\bar{d}u - \bar{d}y)$	
Collapse	$\bar{d}u$	

Fig. 3. Damage state thresholds in the bilinear ADRS capacity spectrum [11].

Peak ground acceleration (PGA) fragility curves are needed to produce the vulnerability curves [4]. The resulting SD median values from the ultimate and yield capacity points were converted to their equivalent PGA values by matching the demand curves of the CSM to the median SDs as shown in Fig. 4. The demand curves were matched by applying a scale factor to the reference demand spectrum.

With the median PGA for each damage state determined, the fragility curves were generated by using Eq'n. (1) replacing X with PGA values, and setting β to 0.64 similar to [3]. A constant β for PGA curves was used based on the combination of individual variabilities [3].

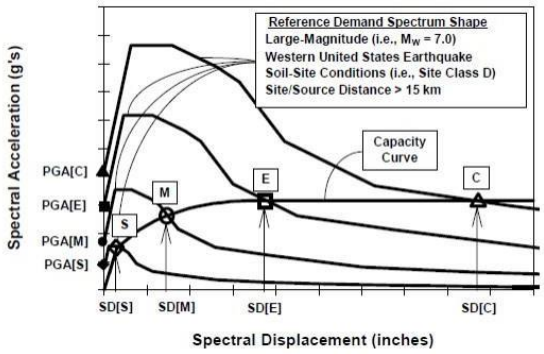

Fig. 4. Development of PGA fragility curves from median SD values [3].

The vulnerability curves were computed using the mean damage index from the PGA fragility curves and by converting the PGA values to its equivalent modified Mercalli intensity scale (MMI). The PGA-MMI conversion was done using the equations developed by [12] shown in Eq'ns. (2) and (3):

$$MMI = 2.20 \log(PGA) + 1.00 \ \ (MMI < V) \quad (2)$$

$$MMI = 3.66 \log(PGA) + 1.66 \ (V \leq MMI \leq VIII) \quad (3)$$

where: MMI is the modified Mercalli intensity scale and PGA is the peak ground acceleration, cm/s^2.

The mean damage index is the combination of the probabilities of the individual damage states of the fragility curve in a certain value of PGA and is computed using Eq'n. (4) as

$$DI = {}^{1}\sum_{n}^{n}{}_{ds=n} xdsPds \quad (4)$$

where: DI is the mean damage index, xds is the damage state number (1-Slight, 2-Moderate, 3-Extensive, and 4-Complete), and Pds is the probability of damage from fragility curves.

To obtain the median and β of the vulnerability curves, one thousand (1000) random points within the range of Eq'ns. (2) and (3) per fragility curve was generated. By combining the equivalent MMI values and their respective mean damage indices, a scatter plot was obtained. The plot was curve-fitted to a lognormal cumulative distribution curve through Matrix Laboratory's (MATLAB) distribution fitter application. The curve fitting was done to acquire the parameters of the best-fit curves.

III. Results and Discussion

3.1 Response Spectrum

The site-specific response spectrum considered in the study is shown in Fig. 5. The unfactored PGA value for the function was computed to be 0.347 g.

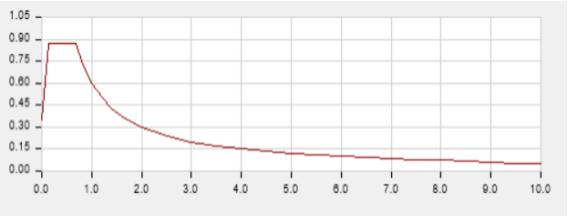

Fig. 5. Site-specific response spectra.

From the response spectrum analysis, the maximum story drifts and displacements for both structures were obtained. It was found that the drift values were within the limit of allowed values in [13]. For NCAS, the target roof displacements were found to be 233.52 mm and 182.96 mm for the global x and y-direction, respectively. As for CEAT B, the target roof displacements were 78.34 mm and 34.20 mm for the global x and y-direction, respectively.

From the modal analysis, it was found that twelve (12) modes were able to capture 90% mass participation in NCAS while eight (8) modes were sufficient in CEAT B. The fundamental period of NCAS was 0.84s with a translational mode in the y-direction. For CEAT B, it was 0.39s with a translational mode in the x-direction.

3.2 Push-over Analysis

From the pushover analyses, the capacity curves with bilinear approximation and the performance points with respect to the response spectrum were obtained. Tables 1 and 2 show the values obtained at the performance points. The yield and ultimate points from the idealized linearization of the capacity curves using bilinear approximation are shown in Tables 3 and 4 with the obtained global ductility. Both buildings have global ductility below that of ordinary RC moment-resisting frames having response modification factor R value of 3.5 [13].

Table 1. NCAS pushover summary of target displacement, SD, base shear, and SA

Direction	D_{ROOF} (mm)	SD (mm)	V_{BASE} (kN)	SA (g)
Positive x	155.40	98.26	28842.40	0.51
Negative x	132.90	92.98	29460.01	0.67
Positive y	139.83	93.25	28383.70	0.54
Negative y	141.64	90.73	31491.96	0.65

Table 2. CEAT-B pushover summary of target displacement, SD, base shear, and SA

Direction	D_{ROOF} (mm)	SD (mm)	V_{BASE} (kN)	SA (g)
Positive x	29.62	19.90	6234.49	0.94
Negative x	30.03	20.17	6318.24	0.96
Positive y	21.16	12.29	635.603	1.30
Negative y	24.59	14.28	7352.35	1.52

Table 3. NCAS bilinear approximation points

Direction	SD, $\bar{S}_{dy}$ (mm)	$\bar{S}_{du}$ (mm)	GLOBAL DUCTILITY, µg
Positive x	44.72	98.03	2.17
Negative x	35.65	97.95	2.59
Positive y	46.37	117.82	2.43
Negative y	48.55	110.44	1.99

Table 4. CEAT-B bilinear approximation points

Direction	SD, $\bar{S}_{dy}$ (mm)	SD, $\bar{S}_{du}$ (mm)	GLOBAL DUCTILITY, µg
Positive x	52.56	82.69	1.46
Negative x	53.08	91.03	1.60
Positive y	45.52	85.36	2.07
Negative y	42.25	84.58	2.12

3.3 Fragility Curves

The fragility curves were generated from the computed damage state thresholds based on the bilinear approximation points and Fig. 3. The median SD per damage state matched the factored response spectra allowing their equivalent median PGAs to be determined. The computed median PGAs are summarized in Tables 5 and 6.

Table 5. NCAS median PGA per damage state

DAMAGE STATE	+ X (g)	- X (g)	+ Y (g)	- Y (g)
Slight	0.11	0.10	0.12	0.13
Moderate	0.16	0.13	0.17	0.19
Extensive	0.21	0.19	0.24	0.24
Complete	0.35	0.37	0.44	0.42

Table 6. CEAT-B median PGA per damage state

DAMAGE STATE	+ X (g)	- X (g)	+ Y (g)	- Y (g)
Slight	0.64	0.64	0.90	0.72
Moderate	0.92	0.91	1.28	1.02
Extensive	1.05	1.08	1.57	1.28
Complete	1.44	1.56	2.41	2.05

The fragility curves produced using the computed threshold values based on Olteanu et al. [11] differ significantly from HAZUS MH [3] median PGAs due to their difference in determining the threshold values for the median. It can also be observed that the CEAT B mean PGA for all directions are significantly higher than NCAS. This was due to the low computed target displacements relative to their respective capacity curves. This means that the original unfactored response spectrum requires to be scaled with larger factors to match the computed SD damage state thresholds.

3.4 Vulnerability Curves

The resulting vulnerability curve from the curve fitting using MATLAB is shown in Fig. 6 and 7 for NCAS and CEAT B, respectively.

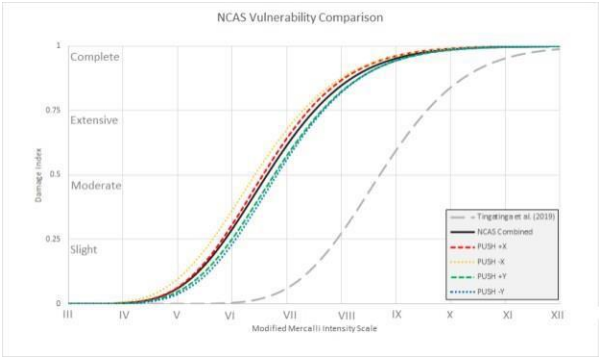

Fig. 6. NCAS Bldg. vulnerability curves for C1-M.

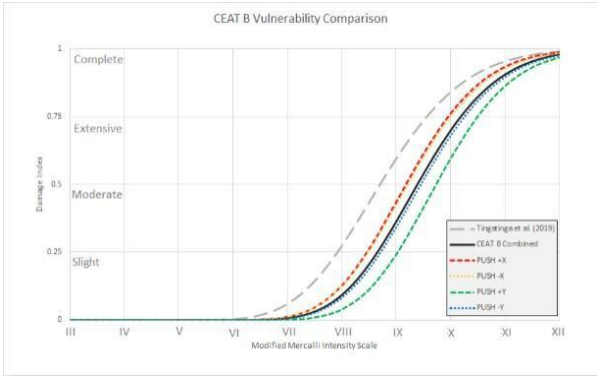

Fig. 7. CEAT-B Bldg. vulnerability curves for C1-L.

Tables 7 and 8 show the median and β values for the resulting vulnerability curves of NCAS and CEAT B building. Based on the results, the values between the generated vulnerability curves for NCAS lag at about 2 units of intensity to the curve for C1-M by [4] and lead to about 1 unit of intensity to the curve for C1-L by [4] for CEAT B. Although the vulnerability curves differ from [4], the results show that the qualitative descriptions of the MMI scale and the damage states for the C1 Class in HAZUS MH [3] compliments one another.

Table 7. NCAS vulnerability curve parameter summary.

Vulnerability Curve	MEDIAN (MMI)	BETA
Positive x	6.66	0.18
Negative x	6.53	0.19
Positive y	6.88	0.18
Negative y	6.92	0.17
Combined	6.75	0.18
C1-M [3]	8.70	0.14

Table 8. CEAT-B vulnerability curve parameter summary.

Vulnerability Curve	MEDIAN (MMI)	BETA
Positive x	9.24	0.12
Negative x	9.28	0.12
Positive y	9.79	0.11
Negative y	9.52	0.12
Combined	9.46	0.12
C1-M [3]	8.3	0.17

IV. Conclusion

The study developed fragility and vulnerability curves for low and mid-rise reinforced concrete moment resisting frame structures within the UPLB campus. Two buildings, representative of low-rise (CEAT B) and mid-rise buildings (NCAS) were selected. Although the vulnerability curves differ from the results of a previously conducted study, the results show that the qualitative descriptions of the MMI scale and the damage states for the obtained curves of reinforced concrete based on HAZUS MH compliments one another.

References:

[1] Philippine Institute of Volcanology and Seismology (PHIVOLCS). The PHIVOLCS Faultfinder. Retrieved October 19, 2022 from http://faultfinder.phivolcs.dost.gov.ph/

[2] Association of Structural Engineers of the Philippines. National Structural Code of the Philippines 7th ed., Vol. 1. Quezon City: Association of Structural Engineers of the Philippines (2015).

[3] Federal Emergency Management Agency (FEMA). (2010). Multi-hazard loss estimation methodology, Advanced Earthquake Model HAZUS-MH MR5. Washington, D.C., USA: Department of Homeland Security Emergency Preparedness and Response Directorate, FEMA (2010).

[4] EA. Tingatinga, BM. Pacheco, JY. Hernandez, MC. Pascua, LRE. Tan, RM. Suiza, and FJ. Germar, Development of seismic vulnerability curves of key building types in the Philippines. 2019 Pacific Conference on Earthquake Engineering and Annual NZSEE Conference (2019).

[5] SC. Garibay, Development of Structural and Non-structural Damage Functions for University of the Philippines Los Baños (UPLB) Buildings. Unpublished undergraduate thesis – Civil Engineering. University of the Philippines Los Baños (2016).

[6] NHC. Cantos, Seismic risk assessment of UPLB buildings. Unpublished undergraduate thesis – Civil Engineering. University of the Philippines Los Baños (2015).

[7] PHIVOLCS. Spectral Acceleration Maps of the Philippines. Quezon City, NCR, Philippines: PHIVOLCS (2021).

[8] American Society of Civil Engineers (ASCE). ASCE 7-16: Minimum Design Loads for Buildings and Other Structures. Reston, Virginia: American Society of Civil Engineers (2017).

[9] American Society of Civil Engineers. (2017). ASCE 41-17: Seismic Evaluation and Retrofit of Existing Buildings. Reston, Virginia: American Society of Civil Engineers (2017).

[10] Federal Emergency Management Agency. FEMA 440 Improvement of Nonlinear Static Seismic Analysis. Washington, D.C., USA: Department of Homeland Security Emergency Preparedness and Response Directorate, FEMA (2005).

[11] I. Olteanu, YF. Vargas, HR. Barbat, M. Budescu, & LG. Pujades. Vulnerability and Risk Evaluation for a Reinforced Concrete Frame. Buletinul Institutului Politehnic Din Iaşi, Vol. LIV. Retrieved March 17, 2022, from https://www.academia.edu/30512332/Vulnerability_and_Risk_Evaluation_for_a_Reinforced_Concrete_Frame (2011).

[12] DJ. Wald, V. Quitoriano,TH. Heaton, & H. Kanamori, H. Relationship between Peak Ground Acceleration, Peak Ground Velocity, and Modified Mercalli Intensity in California. *Earthquake Spectra*. Vol. 15 (1999).

[13] Association of Structural Engineers of the Philippines (ASEP). National Structural Code of the Philippines. 7th Ed. Quezon City, Philippines: Association of Structural Engineers of the Philippines, Inc. (2015).

Comparative Analysis on the Use of Low-Impact Development (LID) Practices and Flood Rerouting for Flood Mitigation using EPA-SWMM in San Isidro, Batangas City, Batangas, Philippines

Celwyn Joseph A. de Roxas*, Kale Ashley P. Carurucan, Perlie P. Velasco, Ma. Hazel T. Castillo

Department of Civil Engineering, College of Engineering and Agro-industrial Technology, University of the Philippines Los Baños, Philippines
E-mail: caderoxas@up.edu.ph

Abstract

In this paper, flood mitigating measures are implemented, compared and contrasted with each other in order to assess the individual flood reduction efficiency of these methods. LID controls of continuous permeable pavement, rooftop disconnection and rain barrels, and flood rerouting are tested against each other to examine the method that can be implemented in San Isidro, Batangas City, Batangas. Simulation of 24-hour rainfall time series of 2-, 5-, 10-, 20-, 25-, and 100-year return periods on the location of the study, with separate simulations for each flood mitigation method, was done through EPA-SWMM. The current condition of drainage shows 16.73 % to 18.87 % of conduits surcharged, and 10.50 % to 12.82 % of nodes flooded. The selection of LIDs to be implemented depends on the setting of the location and its existing structures. Whereas alternative paths for flood routes are established through the evaluation of the conduit links reaching capacity under the current drainage conditions. Of the four methods, rooftop disconnection expressed the most favorable results in the area in terms of the percentage of flood volume reduction, the number of highest volume reduction efficiency per node, and the least number of nodes with the lowest reduction efficiency. Alone, the said method simulates a maximum flood volume reduction efficiency of 98.95 %, 25.27 %, 16.23 %, 11.18 %, 8.22 %, and 6.17 % for their respective return periods of 2-, 5-, 10-, 20-, 25-, and 100-years.

1. INTRODUCTION

Annually, there are more than 20 typhoons that pass through the Philippines. Five of these typhoons are destructive and cause a rift in various infrastructures, livelihood, and human life. Tropical cyclones with high rainfall amounts and greater intensity have increased in recent times due to the adverse effects of climate change. In September of 2021, the Philippines was hit by a series of typhoons that left a massive toll on most Filipinos. The areas of Central Luzon, CALABARZON, MIMAROPA, Bicol, and Eastern and Western Visayas were severely affected by Typhoon Jolina (International Name: Conson), leaving 81,048 families affected, 24 people injured, seven people missing, Php 57.2 million of infrastructure damage, and Php 628 million of agricultural damage (Reyes, 2021).

San Isidro is described as a continuously urbanizing barangay in the city of Batangas this can be seen as the location is near the city proper of Batangas City, as well as near the refinery of the Pilipinas Shell Petroleum Corporation. Batangas City the capital of Batangas province is a first-class city in the country and is a strategic place for international trade and commerce due to its geographical location. In addition, the city harbors numerous domestic and international seaports. The city plays a significant role in the economic development of itself, its citizens, and the southern part of Luzon. Therefore, natural disasters and their effects like floods would take a big toll on the overall progress of the economic development of the city and its citizens. Given the geographic location and topography of San Isidro, several parts of the barangay are susceptible to flood, landslide, chemical hazards (brought by the nearby refinery), and strong winds because of typhoons. Furthermore, the Bugsukan River surrounds parts of the barangay in the northern part, and the Sabang River in the southern part. As San Isidro is susceptible to flooding and its adverse effect, and it is important to determine flood mitigation methods that can be applied to the location.

The study will help the barangay in establishing the initial steps to start a roadmap for the flood mitigation plan of the chosen location of the study. San Isidro has an existing contingency plan for the worst-case scenario of a signal no. 5 typhoon involving a warning system and an evacuation and rehabilitation plan. Although there is also a plan for the construction of flood-mitigating structures, there is no study conducted yet on these possible structures. Furthermore, the study may aid the BDRRMC, CDRRMC, and the City Engineering Office as the study will provide an overview of the capacity of the existing drainage system and give an insight into the possible revisions in the contingency plan for San Isidro and neighboring barangay.

The study's main objective is to create a comparison between chosen low-impact development practices and flood rerouting as flood

mitigation methods by comparing its effects and volume reduction efficiency in San Isidro, Batangas City.

Specific objectives of the study are to:

1. Develop a hydraulic model for San Isidro, Batangas City to simulate 2 year-, 5 year-, 10 year-, 20 year-, 25 year-, and 100 year-return periods of rainfall events.
2. Assess the condition of the current drainage system of San Isidro, Batangas City under the six different return periods.
3. Determine the LID practices that can be implemented in the flooded areas and their flood reduction efficiencies.
4. Identify alternative paths for flood rerouting and the respective reduction efficiency.
5. Compare the reduction efficiency of the different flood mitigating methods.

This study aims to determine the method to yield the highest flood reduction efficiency under different rainfall events. The LID controls that are to be used in the location of the study are based on their applicability to the location, surroundings where LID is to be implemented, and existing LID structures in San Isidro, Batangas City.

The study employs EPA-SWMM for the simulation and only focuses on the quantitative effects of the LID controls and flood rerouting on stormwater runoff. Specifications of LID methods were taken from studies of Pulgarinas (2019) and Mercado (2019). Flood rerouting is done by determining and establishing alternative paths for the stormwater runoff to flow through and is based on the available roads and passages that can be connected to the existing drainage system. The extent of the study covers comparing and contrasting the effects of each given flood mitigating method. Furthermore, this study focused on the flood reduction efficiency of the different methods based on the total volume of the flood that has entered the openings of the drainage system and does not consider the economic costs of these methods, and the comparison of the combination of the different flood mitigating methods. The openings that were considered depended on congested residential areas and passageways to these residential areas.

2. MATERIALS AND METHODS

Methodological Framework

The study uses EPA-SWMM 5.2 for the analysis of input parameters, the implementation of the different LID practices, the rerouting plan, and the current drainage system of the location.

The study employs the use of different LID practices, and the use of a flood routing plan and has differences in the structure between the two methods. Although these methods have differences, they are both compared to the existing drainage system of the location. Methods in determining the best LID practices are adapted from the studies of Pulgarinas (2019) on the existing drainage system along the North Luzon Expressway Malinta Exit, and Mercado (2019) in the municipality of Santa Cruz, Laguna. Methods in determining the adequacy of the proposed alternative flood routing are adapted from Cruz (2009) using HEC-RAS for the 1D-2D model of the floodwater passing through the drainage system of a subdivision in Metro Manila. The current study employs the use of the EPA-SWMM software for the hydraulic modeling and simulation of the proposed alternative flood routing of the drainage system in San Isidro, Batangas City. Input parameters that were used in EPA-SWMM are the amount of rainfall, the properties of the subcatchments, and the dimension and location of nodes and conduits.

The methods are summarized in Fig. 1 and 2.

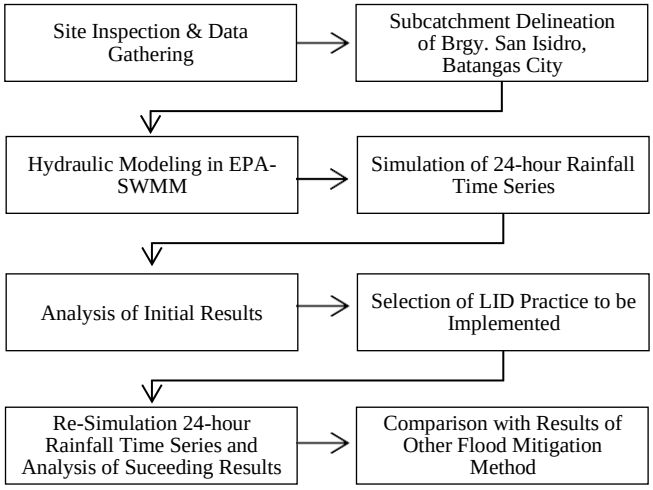

Figure 1. Methodological framework for flood mitigation using LIDs.

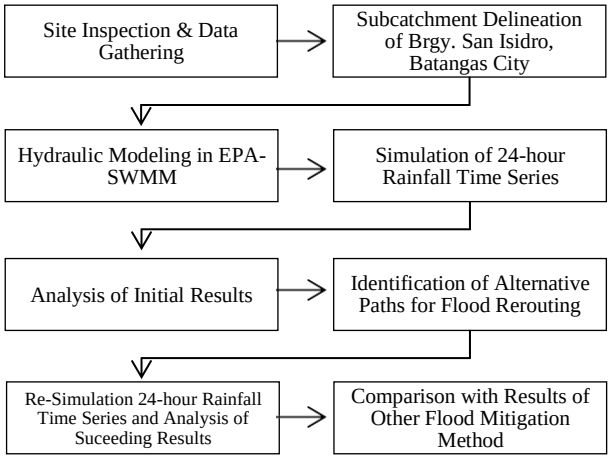

Fig 2. Methodological framework for flood mitigation using rerouting.

Analysis and Design Procedure

The location was divided into different subcatchments using the SAGA tool in the QGIS software. Flood map of the barangay and road map of the barangay from Google Earth Pro was used in providing the boundaries for the whole catchment area. The subcatchments that were processed from the DEM of Tayabas Bay through QGIS.

The nodes and conduits were mapped in EPA-SWMM prior to data simulation. The nodes represent inlets, conduit connectors, outlets and dividers, while the conduit represents the drainage canals. A base map was placed first as a backdrop in the software and is scaled based on real-life scale measurements. The nodes are placed based on the location identified from the site inspection, the Google Earth Street view, and the base map used for the location. The invert elevation of nodes was computed based on the identified elevation from Google Earth Pro minus the height of the drainage which ranges from 0.3 m to 0.5 m for rectangular shapes, and 0.4572 m to 0.6096 m for circular-shaped pipes, minus as well the thickness of the circular pipes (if applicable), and minus the distance of the surface from the top of the drainage or pipe which is 0.3 m. The distance between the surface and top of the drainage was based on the National Plumbing Code Chapter 3, Section 314.4. The depth of the nodes was based on whether they are open or not; For open nodes, the maximum depth was the highest depth of the connected conduits plus the surface distance of 0.3m; While for closed nodes, the maximum depth was only the highest depth of the connected conduits. The length of the conduits is measured using Google Earth Pro, and the Auto-length feature of EPA-SWMM. The latter was executed with relatively high precision as the map of the software was scaled based on real-life scale measurements.

The subcatchments were delineated from the DEM provided by the USGS Earth Explorer. Whereas the area and length were determined using Google Earth Pro. Important parameters that are needed for the subcatchments are the width of overland flow, the percentage of impervious areas, and the Manning's roughness coefficient of impervious and pervious areas.

The delineated subcatchments using Google Earth Pro can be seen in Fig. 4. The subcatchments were assigned different colors to contrast with other subcatchments.

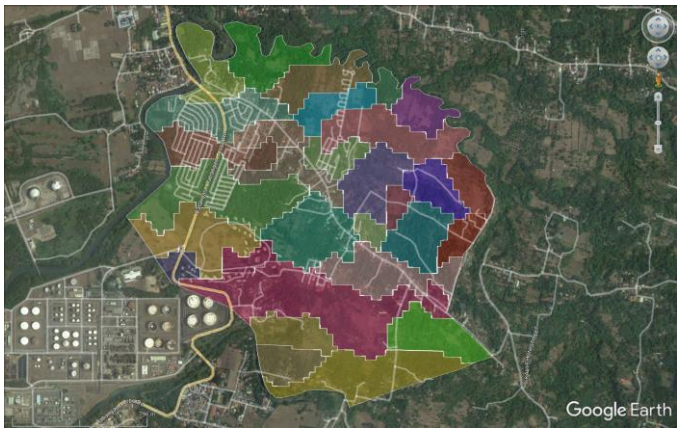

Fig. 4. Delineated subcatchments of the study location.
Source: Google Earth, 2022

The rainfall data used as input parameter are the 24-hour time series of 2 year-, 5 year-, 10 year-, 20 year-, 25 year-, and 100 year-return period rainfall events, with1-hour interval. The rainfall intensity per hour was evaluated from the power equation of each return period event. The rainfall time series were then placed into the rain gage of the software to produce the rainfall in the location.

Simulation has commenced after all the main parameters of the nodes, conduits, and subcatchments have been input into the software. Simulation options, that were used, are analyzed to account for external factors that were not produced from the data gathering. The infiltration model that was used for the simulation is the Modified Green-Ampt model as this accounts for the runoff on slopes of the area and in comparison, with the Horton model, the Modified Green-Ampt accounts that infiltration rate decreases over time (Ochsner, 2019). And the routing model that was used is the dynamic wave model as this accounts for possible backflows in the nodes and conduits.

After simulating the six rainfall events, the LID practices that were implemented in the location are determined based on the preference of the LGU of the barangay, the state of the structures and vegetation, and the allowed conditions for use of the LID Practice. Furthermore, analysis of the drainage system showed that flood rerouting was implemented in locations where link capacities of the drainages reached the maximum. The mapping of alternative flood routes was based on the location of additional canal entrances, new flood routes, and outlets using Google Earth. After plotting the nodes, and conduits in the map of the location, the research

proponent then identified roads without existing drainage. After identifying these roads, the proponent generated a hydraulic map with the additional nodes and conduits. The shapes and dimensions of the new drainages are based on the closest existing drainages and were only limited to circular and closed rectangular cross-sections.

The methods underwent simulation again under the six rainfall events and their results were then compared and were based on the maximum flood reduction efficiency, the number of nodes with reduced flood volume, and the number of nodes with completely reduced flood volume.

3. RESULTS AND DISCUSSION

Hydraulic Model of San Isidro

The area of San Isidro, Batangas City has a land area of 3,175,207 square meters. In the current setting, the study area has 476 junction nodes, 514 conduit links, and 19 outfall nodes, which are reflected in the generated hydraulic model, which can be seen in Fig. 5.

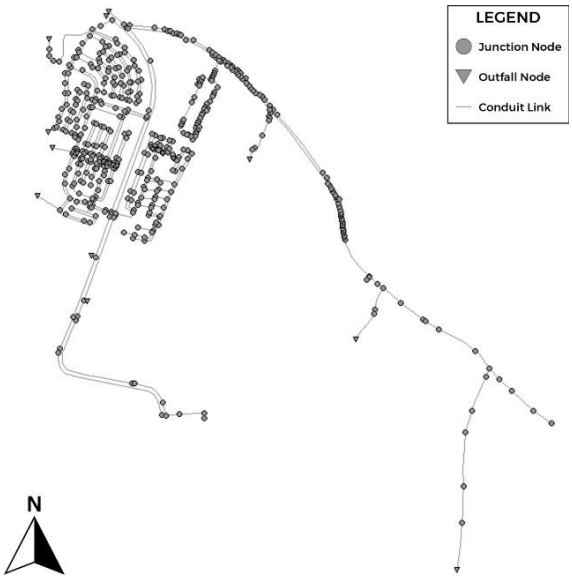

Fig. 6. Generated hydraulic map of San Isidro, Batangas City.

Condition of Current Drainage System

After the hydraulic map is generated, the simulation of the six return period rainfall events took place to determine the adequacy of the current drainage system of Brgy. San Isidro. These rainfall events are simulated for a 24-hour duration. One parameter to check the condition are the conduits surcharged which ranges between 16.73 % to 18.87 % and nodes flooded which ranges between 10.50 % to 12.81 %. These are summarized in Table 1.

Table 1. Summary of Conduits Surcharged and Nodes Flooded for the current drainage system

	RETURN PERIODS					
	2-Year	5-Year	10-Year	20-Year	25-Year	100-Year
Conduits Surcharged (% out of 514)	86 (16.73 %)	91 (17.70 %)	93 (18.09 %)	94 (18.29 %)	94 (18.29 %)	97 (18.87 %)
Nodes Flooded (% out of 476)	50 (10.50 %)	58 (12.18 %)	60 (12.61 %)	60 (12.61 %)	60 (12.61 %)	61 (12.82 %)

Another parameter used to examine the condition of the current drainage system is the total flood volume (in m^3) passing through the drainage system. Eleven nodes were considered for inspecting the total flood volume. The nodes are chosen based they are near residential areas in the location and in passageways to these residential areas. The location of these nodes is depicted in Fig. 6.

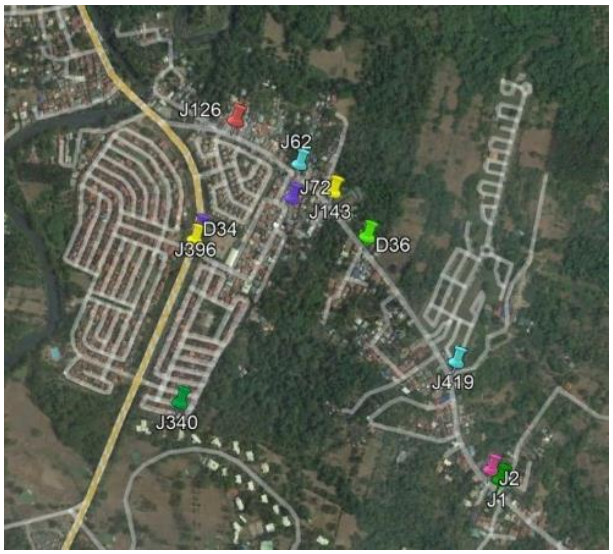

Fig. 6. Location of Nodes considered. Source: Google Earth Pro, 2022

Flooding in residential areas has been expected to be reduced as flooding affects the environment, the existing structures, and the people living in these areas. The total flood volume for the nodes under the six return periods of rainfall events is summarized in Table 2.

Table 2. Total flood volume in the nodes under the current drainage system.

SUBCATCHMENT	NODES	RETURN PERIODS					
		2-Year	5-Year	10-Year	20-Year	25-Year	100-Year
		total flood volume (m^3)	total flood volume (m^3)	total flood volume (m^3)	total flood volume (m^3)	total flood volume (m^3)	total flood volume (m^3)
KANLURAN 2	D34	285	4025	8442	14033	17089	31081
KANLURAN 3	D36	13057	28914	39409	49541	55291	72493
SILANGAN I 3	J1	48507	126821	180094	229958	258058	338483
SILANGAN I 3	J2	131790	164429	184480	203778	214558	247411
KANLURAN 1	J62	17021	21980	23111	23826	24332	25299
KANLURAN 3	J72	8463	19016	25836	32379	36111	47176
GITNA 1	J126	23672	40152	48209	54551	58664	64706
KANLURAN 3	J143	43200	75558	97027	117794	129294	164935
KANLURAN 4	J340	38572	83554	113389	142233	158274	207661
KANLURAN 1	J396	11910	33467	53468	76548	90482	127541
SILANGAN I 1	J419	114426	192095	243618	293428	321227	406464

Selection of LID Practices

For the study location, the number of houses, roads, vegetation, and distance from the roads are considered for the selection of LID Practices. Rain barrels and continuous permeable pavement are chosen from these criteria. However, upon site inspection, several houses are employing a variety of rooftop disconnection where the downspout is connected to drainage canal, instead of vegetative storage units. Thus, rooftop disconnection was also chosen. For the number of LIDs used, one rooftop disconnection was used per household, two rain barrels were used per household, and total impervious area were used for permeable pavements.

Determination of Alternative Route for Flood Rerouting

The basis of the addition of flood routes is from conduits that reached 100% link capacity on the map at any time during the 24-hour rainfall simulated for a 100-year return period.

It is identified that 39 conduits reached 100% capacity during the rainfall. The flood rerouting is manually generated in EPA-SWMM 5.2. The new drainage map contains 28 additional conduits, 10 additional junction nodes, and 4 additional outfall nodes. The generated drainage map is displayed in Fig. 7.

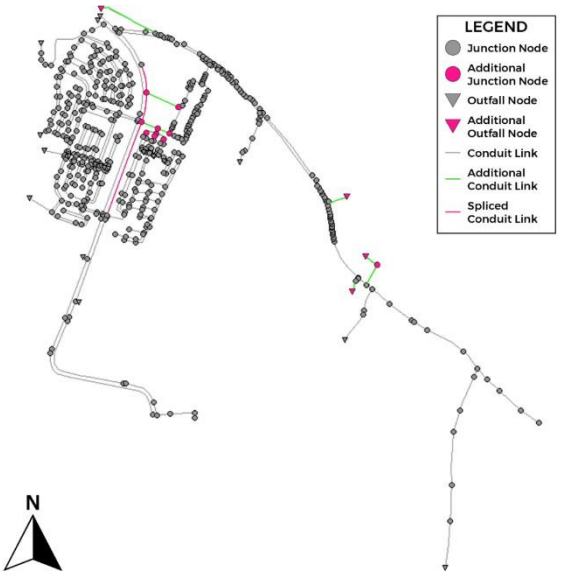

Fig. 7. Generated hydraulic map for flood rerouting in Brgy. San Isidro, Batangas City.

Comparison of Flood Mitigating Methods

For the comparison, results from the 100-year return period of rainfall are used to align with the contingency plan of the barangay for worst-case scenario of signal no. 5 Typhoon. The analysis of the comparison consists of maximum flood reduction efficiency, number of nodes whose volumes were reduced, and number of nodes completely reduced. The maximum flood volume reduction efficiency for permeable pavement is 8.19 %, rooftop disconnection is 6.17 %, rain barrel is 0.36 %, and flood rerouting is 46.54 %.

Flood rerouting showed the highest percentage of volume reduction, but it could not reduce the flood volume in 6 of the 11 nodes, thus it was not considered as the best option. Moreover, rain barrels cannot be considered, as this option showed the lowest flood reduction efficiency in most of the nodes. Therefore, the methods left to consider are permeable pavement and rooftop disconnection. Both methods reduced the flood volume in 10 of the 11 nodes considered. Between the remaining two methods, rooftop disconnection has seven nodes with the higher volume reduction efficiency, while continuous permeable pavement has three. Thus, the best option between the two is rooftop disconnection. The summary of the flood reduction efficiency of each flood mitigation method under a 100-year return period of rainfall is displayed in Table 3.

Table 3. Summary of flood reduction efficiency of flood mitigating methods under a 100-year return period of rainfall.

NODES	FLOOD VOLUME REDUCTION EFFICIENCY (%)			
	Flood Mitigating Methods			
	permeable pavement	rooftop disconnection	rain barrels	flood rerouting
D34	8.19	6.17	0.36	0.99
D36	0.76	2.10	0.17	0.00
J1	0.19	0.24	0.01	46.54
J2	0.33	0.55	0.06	2.41
J62	0.30	0.44	0.08	0.00
J72	1.34	3.58	0.26	0.00
J126	0.83	1.04	0.06	0.00
J143	0.00	0.00	0.00	0.00
J340	1.90	1.18	0.11	0.00
J396	3.79	3.53	0.30	0.23
J419	0.10	0.13	0.00	1.14

5. RECOMMENDATION

Recommendations for future studies are to implement a combination of implementation of LID practices and of the establishment of alternative flood routes to maximize flood reduction efficiency. It is also recommended to determine the economic costs. Furthermore, it is also recommended to use a Street shape for the cross-sectional parameter of conduit links, especially in roads and passageways with no existing drainage system.

6. REFERENCES

Cruz, E.C. (2009). Hydraulic computations for flood routing of a modular urban stormwater drainage system. Philippine Engineering Journal, 28(2), 45-58

Department of Public Works And Highways (1990). Feasibility study on the rural road network development project, (Volume 3). Japan: Japan International Cooperation Agency.

4. SUMMARY AND CONCLUSION

Among the four flood mitigation methods, rooftop disconnection proved to be the most effective in flood volume reduction as this method shows the greatest number of nodes with the highest maximum flood reduction efficiency, where all nodes have reduced flood volume. Under 2-, 5-, 10-, 20-, 25-, and 100-year return period of rainfall event, the rooftop disconnection exhibits maximum reduction efficiencies of 98.95 %, 25.27 %, 16.23 %, 11.18 %, 8.22 %, and 6.17 %, respectively.

Mercado, D.B. (2019). Hydraulic modelling of flood-mitigating Low-Impact Development (LID) projects in the municipality of Santa Cruz, Laguna, Philippines using EPA Stormwater Management Model. Unpublished undergraduate thesis – Civil Engineering. University of the Philippines Los Baños, College, Laguna

Ochsner, T. E. (2019). Rain or shine. Oklahoma City: Oklahoma State University Libraries.

Pulgarinas, N.A. (2019). Flood mitigation using Low-Impact Development practices of the existing drainage system along North Luzon Expressway (NLEX) Malinta exit, Valenzuela City, Philippines. Unpublished undergraduate thesis – Civil Engineering. University of the Philippines Los Baños, College, Laguna

REYES, D. (2021) Typhoon Jolina leaves 17 dead. Retrieved November 8, 2021, from https://www.manilatimes.net/2021/09/13/news/regions/typhoon-jolina-leaves-17-dead/1814511

Geostatistical Modeling Of Standard Penetration Test Data To Determine The Minimum Required Number Of Boreholes For Geotechnical Investigations

Roel Nikko T. Magno, Andre C. Cruz, Jedidiah Joel C. Aguirre, Ron Gabriel O. Navarro

Department of Civil Engineering, College of Engineering and Agro-Industrial Technology, University of the Philippines – Los Baños, Philippines
E-mail: roelnikkomagno@gmail.com

Abstract
The standard of determining the minimum required number of boreholes is currently governed by professional judgement and not scientifically justified in the current code. In this study, prior Standard Penetration Test (SPT) reports around the University of the Philippines – Los Baños Science and Technology Park Complex were used to perform geostatistical modeling using the simple kriging interpolation of the ArcGIS Pro software to predict the SPT-N values, uncertainties, and corresponding soil type in 22.5 x 22.5 m grid sizes, or blocks, within the study area having a soil depth of up to 10 meters. Statistical measures such as mean error, mean average error, root mean square error (RMSE), average standard error, and coefficient of determination were used to cross validate the accuracy of the models. A superimposed raster map of the maximum SPT-N standard errors of all layers was created, and the blocks with at most ±5 N-values as their 95% confidence interval were identified as 0-blocks, which suggests that no borehole exploration will be necessary. Guidelines to determine the minimum required number of boreholes of a specific area using this interpretation were then developed and a database program was created to access the data generated. Finally, this study established a method which requires less boreholes compared to the current code and produced a total of 401 0-blocks that may save up to 20.30 hectares of land that needs borehole exploration.

1.0 INTRODUCTION

1.1 Background of the Study

Geotechnical investigation is a necessary step for every construction to provide geotechnical reports that can be used in designing appropriate footing for the structures. The most common and widely used test for the geotechnical investigations is the Standard Penetration Test [9]. The number of boreholes necessary to have a sensible judgement for the soil bearing capacity to be used in designing the foundations is determined by the footprint area of the structure [1], geostructure to be used in building [2], or the spacing per type of structure [4] [9]. These values are rough estimates only and has no experimental or theoretical data basis by the authors and can only be considered as products of professional judgment.

Geostatistics on the other hand is a division of statistics that focuses on geographically referenced data through analysis and interpretation [7]. It is used to interpolate values for locations where samples are not taken yet. Geostatistical tools also provide measures of uncertainty for the computed values that is important for informed decision making [5]. Introducing the geostatistical modeling to the concept of determining the minimum required of boreholes in a geotechnical inspection can offer new method or can strengthen the decision making that will be backed by data and statistics.

Moreover, the University of the Philippines – Los Baños Science and Technology Park Complex buildings and nearby institutions have available borehole reports from their previous investigations using Standard Penetration Tests (SPT) which can be used for geostatistical mapping. The study site has considerable vacant areas for building new structures which may find benefit from this study.

Hence, the study will use the geostatistical modeling of ArcGIS Pro to determine the number of boreholes required in a study area using SPT data from previous geotechnical investigations around and within the site.

1.2 Significance of the Study

This study will provide a new method in determining the minimum required number of boreholes for geotechnical investigation, specifically for the shallow foundations. It will set a baseline backed by statistics in determining the number of required boreholes. This method may propose more reasonable and economical approach than the standard method used in the current codes which is governed by experience only [2]. It will also map the summary of predicted values in the location of the study area.

1.3 Objective of the Study

This study aims to determine through geostatistical mapping the minimum required number of boreholes for geotechnical investigations of low-rise buildings within the University of the Philippines – Los Baños Science and Technology

Park Complex land area. Specifically, this study aims to:

1. produce a geostatistical model of the SPT-N and soil type per layer of the data set and generate the raster map in the study area;
2. evaluate the standard error maps of SPT-N models to produce a map of recommended number of boreholes in the study area; and,
3. develop a database to summarize and access the collected results.

1.4 Scope and Limitations of the Study

This study will only use SPT data from official borehole logs, specifically, location of boreholes, soil type (clay or sand classification only), and SPT-N values, with corresponding depth from 1-10 meters with one meter interval and the 1.5-meter depth, as the parameter in the geostatistical mapping. This will only focus on determining the minimum required number of boreholes for shallow foundations. Furthermore, the study will only use ArcGIS Pro 2.9.3 as the software to use in the geostatistical mapping. Lastly, Visual Studio 2022 and Google Earth Pro 7.3 will be used to develop a result database and reference respectively to make the results more accessible.

One of the limits of the study is the assumption that the study area is homogenous in the interpolation of the software and have no erratic subsurface conditions such as sinkholes or unusual soil profiles relative to immediate areas, as assumed in geostatistical projects. Otherwise, future projects should conduct an additional geotechnical investigation for those kinds of area once determined in the site visit.

2.0 REVIEW OF RELATED LITERATURE

2.1 Determining Number of Boreholes

In the Philippines, the National Structural Code of the Philippines 2015 is followed for building requirements. The boreholes should be inside the footprint of the structure and is only required to be uniformly distributed throughout the footprint. The depth to be considered in this study will be down to 10 meters below the surface. The Table 1 below shows the minimum required number of boreholes per structure.

Table 1. Minimum required number of boreholes

Footprint Area of Structure (m^2)	Minimum Required Number of Boreholes
$A \leq 50$	1
$50 < A \leq 500$	2
$A > 500$	2+ (A/1000) (rounded up to nearest integer)

2.2 Standard Penetration Test

The Standard Penetration Test (SPT) is the most popular and widely used in situ test for geotechnical investigations [9]. It is developed around 1927 and is currently standardized as ASTM D1586/ D1586M. The number of blows to drive the sampler up to the last two 150mm distances of the boring is counted to obtain the N number, which is commonly known as the blow count. Corrections have been made for correlating soil properties as shown in Equation 1.

$$N_{60} = \frac{N\eta_H\eta_B\eta_S\eta_R}{60} \qquad (1)$$

where:

N_{60} is the SPT-N corrected for field conditions
N is the measured penetration number
η_H is the hammer efficiency (%)
η_B is the correlation of borehole diameter
η_S is the sampler correction
η_R is the correction for rod length

2.3 Geostatistical Modeling

Geostatistical interpolation started in the 1950s from the mining industry in search for ore reserves. They used the concept to estimate the probability of ore quantity in a certain area. This idea propagated to other fields after French mathematician G. Matheron derived the formulas that have founded the linear geostatistics [3]. According to the Practical Guide of Geostatistical Mapping [8], the most used in interpolation is the kriging and its standard version is called ordinary kriging (OK). The ArcGIS Pro mapping software extends a variation of kriging, known as simple kriging, that has normal score transformation for not normally distributed data.

3.0 METHODS AND MATERIALS

3.1 Data Gathering and Data Preparation

This study used the borehole reports, specifically the location of boreholes, N-values and the soil type obtained in previous Standard Penetration Tests conducted inside the Science and Technology Park Complex, UPLB and nearby areas. The N-values and the soil type, classified as (1) clay or (2) sand, were recorded from 1m-10m.

The raw data was corrected using Equation [1]. There are a total of 42 boreholes that were included in the geostatistical mapping.

3.2 Producing the Geostatistical Model

The outmost northing, easting, westing, and southing of the data set were determined to be the boundary of the geostatistical. A map area that covers the University of the Philippines – Los Baños

Science and Technology Park Complex was then created to streamline the boundaries of the study area. *Figure 1* presents the locations of each borehole of the dataset, and the study area.

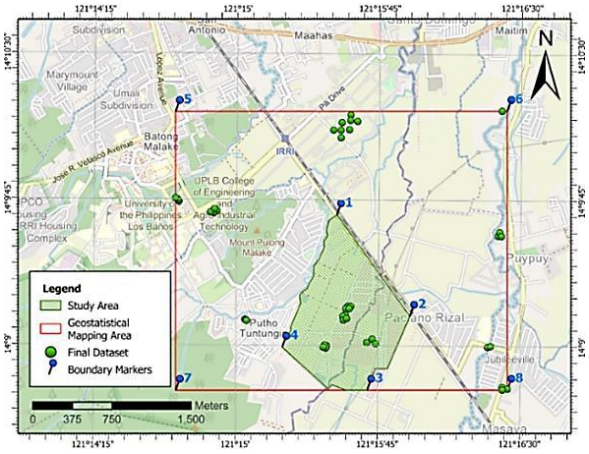

Figure 1. Mapping areas with the final data set.

The geostatistical mapping area has 8.312 km^2 while the study area has 1.1393 km^2 of land and a perimeter of 4.4765 km.

The next step was building the geostatistical models for each layer. The following algorithm in *Figure 2* retrieved from the ArcGIS Pro Manual was the basis of building the geostatistical models.

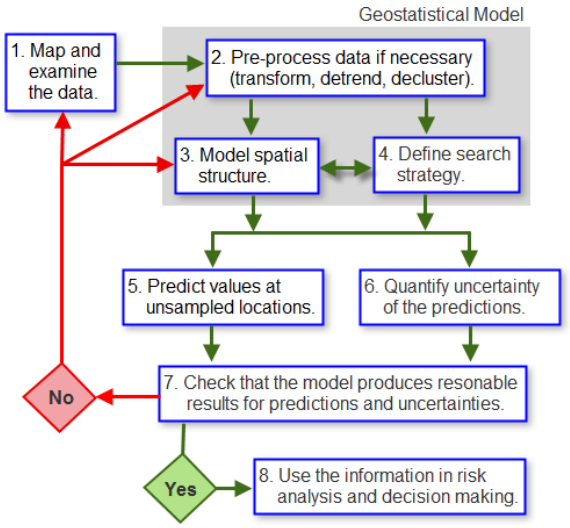

Figure 2. Workflow for the geostatistical model [5].

The dataset was run in three (3) candidate models; two simple kriging run, and one ordinary kriging run. The statistics of the three candidate models were computed and the best fit model was selected as paralleled from a study conducted in assessing the accuracy of interpolation method [10], specifically, the root mean square error (RMSE) and the average standard error. Model no. 1 of the simple kriging was used for the SPT-N values due to its advantage of having normal score transformation for not normally distributed data. The best fit model was examined using its Mean Error (ME), Mean Absolute Error (MAE), RMSE, and coefficient of determination, R^2.

On the other hand, since the soil type is a categorical data, the geostatistical mapping tool used was Empirical Bayesian Kriging (EBK) with inputs that mimics the nearest neighbor interpolation [1].

3.3 Cross Validation

The Geostatistical Wizard tool of the ArcGIS Pro has a built-in cross validation section at the end of the modeling. The idea is to remove one measured data at a time and predict its value using the rest of the measured data and compute the statistics. This study considered the R2 $\geq$ 0.85 criteria to have satisfactory accurate maps to be used in the decision making [8].

Raster maps were then produced with a 22.5mx22.5m cell size or blocks. The produced standard error (SE) maps were then superimposed for the maximum values to produce a reference map for decision making.

3.4 Correlating the Standard Errors of SPT-N to the Minimum Required Number of Boreholes

This study considered 95% confidence interval (95% CI) with ± 5 N-value or lower to be satisfactory enough to not conduct a borehole exploration at the grid area, and to assume the predicted values mapped in this study. It has 95% assurance that the true value in the site lies within this interval considering all the limitations of the procedure. The desired range have points of at most 2.551 for their standard error as computed in the formula of 95% CI in *Equation 2.*

$$95\%\ CI\ = x \pm 1.96SE \qquad (2)$$

The areas having a value of at most 2.551 standard error were called the 0-blocks since these areas were recommended adopting the values mapped in this study and save the necessary borehole explorations. Meanwhile, higher standard error areas were called 2-blocks since it was the standard in the code for area of 500m^2 [1].

3.5 Finalizing the Reference Maps and Guidelines

The flow of the process developed to determine the minimum required number of boreholes using this study was summarized in a flowchart in the Figure 3. The value acquired from these conditions will be the recommended number of boreholes for the geotechnical investigation on the site.

At the site during the investigation, additional boreholes may be conducted upon the judgement of the geotechnical engineer depending on the site

conditions and the degree of fit of the predicted values to the actual measured values.

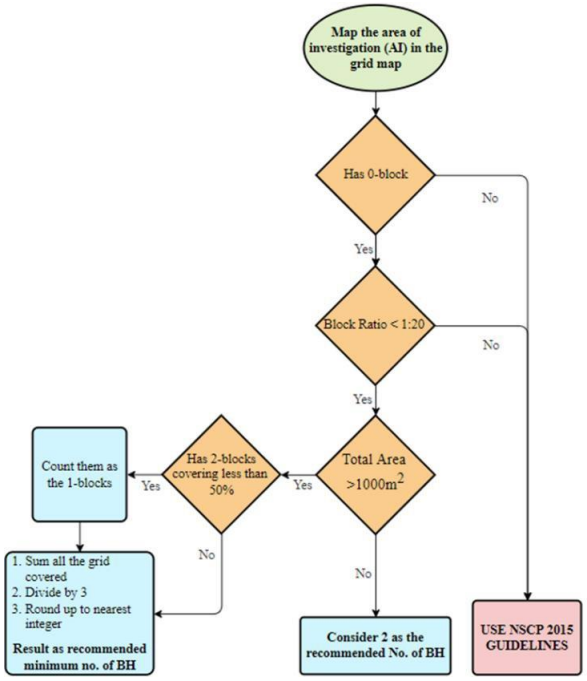

Figure 3. Process for determining the number of borehole explorations.

To simplify the use of the finalized reference maps, automation through a simple database program was made and sample building layouts were assessed to verify the objective of the study.

4.0 RESULTS AND DISCUSSION

4.1 Examining the Statistical Measures

The model used was examined using its Mean Error (ME), Mean Absolute Error (MAE), RMSE, and coefficient of determination (R^2). The summary was shown at *Figure 4*.

The ME have mostly negative values 7 out of 11 models which signifies that the model was mostly underpredicting which is better since lower values would mean more conservative predictions.

Next, the MAE showed that the magnitudes of the absolute errors range only from 0.942 of layer 1m up to 2.071 from layer 7m. It is considered relatively small which signifies the model produced a very good fit for the study area.

Meanwhile, the RMSE has extremes of 1.382 at layer 1m and 3.354 at layer 10m, respectively. It showed that the frequency distribution of error magnitudes of the models is relatively low and therefore, a good indication of its good accuracy.

Finally, all the R^2 values are above the standard set value of 0.85. Since 10 out of 11 layers have higher than 0.90 value, the model produced from the data set is highly accurate. It indicates that as much as around 90% of variance of the predicted value can be explained by the data set provided.

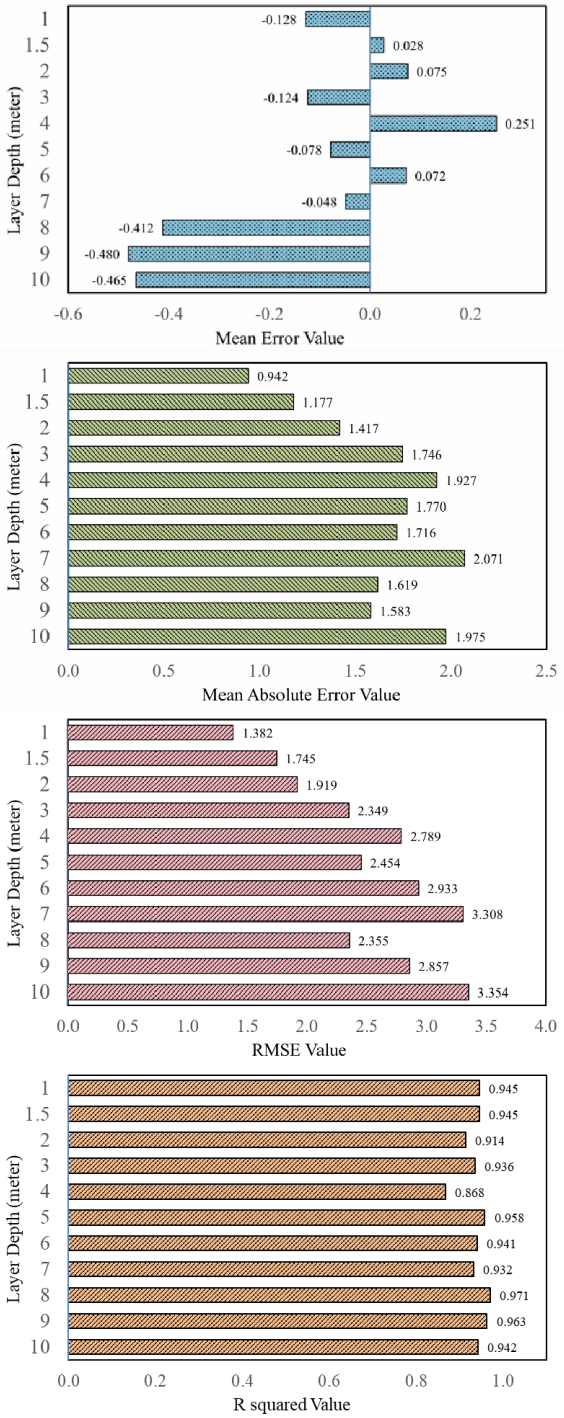

Figure 4. ME, MAE, RMSE and R^2 of the models.

4.2 Prediction value maps

The prediction value (PV) and standard error maps of SPT-N data and the PV map of the soil type for each layer were collected as shown in *Figure 5*.

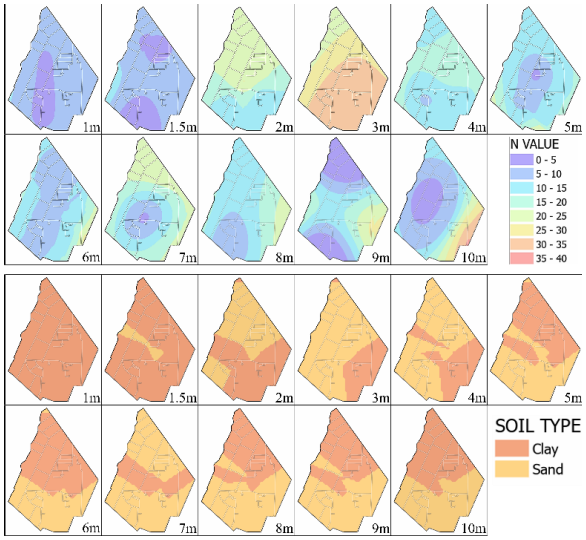

Figure 5. Raster maps of SPT-N and soil types.

It can be observed that in all layers or depth except layer 3m, the N values were mostly below 25. This indicates that the soil in the study is medium to very loose for its relative densities. In the deeper layers, it can be observed that the higher SPT-N values were skewed in the right side of the study area.

The predicted value maps show that for the first two meters of the soil, clay leads the study area in composition. Meanwhile, for the 3-4 m layer, sand started to govern, and clay was left mostly on the lower right side. For the 5-10 m except for the 7 m, clay occupies most of the top part of the study area while sand dominates the bottom part.

4.3 Reference Map in Determining the Minimum Required Number of Boreholes

The standard error maps of the SPT-N values were superimposed and the maximum value for each block and the blocks with at most ±5 N-values as their 95% confidence interval were identified as 0-blocks, which suggests that no borehole exploration will be necessary. These blocks are shown in Figure 6 with blue shades.

It created 401 blocks that can be considered as 0-blocks, where 347 blocks have between ±3 to ±5 interval and 54 blocks had less than ±3 interval of 95% confidence. The blue regions consisted of 17% of the total study area as seen in most of the distribution was covered by blocks with intervals between ±15 to ±20.

Also, 0-blocks cover near known borehole points in about 150 to 200 meters away. Conducting borehole explorations within the area with at least 200-meter distances from each other, and then including them in the dataset for remapping will efficiently increase the 0-blocks significantly.

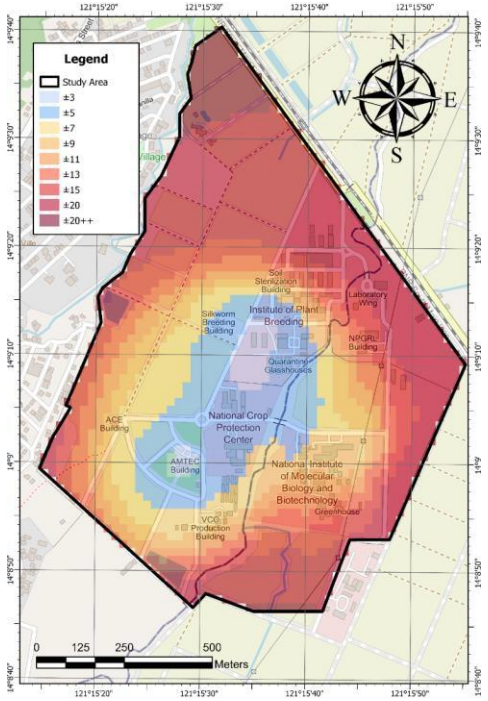

Figure 6. Superimposed raster map for maximum standard errors of all layers.

4.4 Discussion on the Assessment of the Results

As an assessment, three arbitrary building layouts were placed, and the minimum required number of boreholes were computed based on the steps in Figure 2 and by using the NSCP 2015 code. Table 2 shows the comparison of results for these two methods while the site layout and the corresponding SE map are shown in *Figure 7.*

Table 2. Comparison of computed minimum required number of boreholes.

Bldg.	Area (m^2)	NSCP code	Rec. no. of BH	Assumed known BH
1	2278	5	1	7
2	3037	6	2	6
3	5062	8	6	4

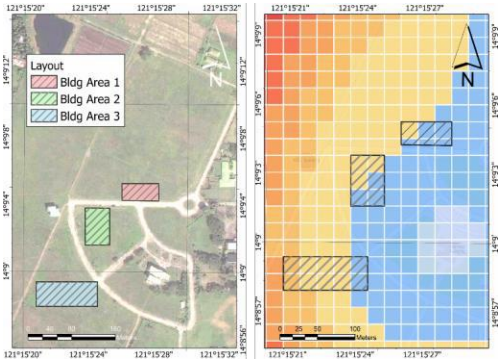

Figure 7. Site layout and the corresponding SE map of the arbitrary building layouts.

For the building layout 1, most of the area were covered with 0-blocks. Based on the geometry of the layout, it is proposed to conduct the borehole exploration at the top left most of the area. Additional borehole exploration can also be done to verify the accuracy of the 0-blocks or include another borehole on the 2-block to validate the SPT with two samples in that area.

For the building layout 2, there are equal number of 0-blocks and 2-blocks. It is proposed to conduct the borehole exploration at the middle top area with equal distance. An addition of extra borehole would layout the borehole points to be well-spaced in the 2-blocks.

For building layout 3, only a fifth of the area covers 0-block It is recommended to place the six borehole explorations equally spaced leaning to the right of the blocks of the 2-block areas.

Finally, it can be observed that for all the building layouts, the recommended number of boreholes obtained from this study is lower than the NSCP 2015 Code.

5.0 SUMMARY AND CONCLUSION

Standard Penetration Test (SPT) data were collected in the University of the Philippines – Los Baños Science and Technology Park Complex buildings and its nearby area. Geostatistical modeling of three candidates were then performed for 11 layers for the SPT-N value. The models for each layer with the lowest average standard error and root mean square error (RMSE) were selected as the best fit model and were evaluated.

The maps were analyzed statistically; by using their mean, absolute mean, RMSE and R^2, which had a conclusion that they are satisfactory models that can be used for decision makings. Visually, the layers had generally low SPT-N values aside from the layers 2m, 3m, and 4m. Meanwhile, the standard errors of all layers were superimposed to produce a single maximum standard error map that will be the basis to which areas can be values.

After the procedure, there are a total of 401 blocks that can be considered as known points with at most ±5 range of values, where 347 blocks have between ±3 to ±5 interval and 54 blocks have less than ±3 interval. This study resulted to save as much as 203,006.25 m^2 or 20.30 hectares of land area for borehole explorations in the future in the study area. Guidelines were developed for determining the minimum required boreholes using the reference maps.

Finally, this study shows that minimum required boreholes for geotechnical investigations in an area can be determined by geostatistically mapping the SPT data and will result to lower number than the code. This will highly benefit locations with abundant and nearby borehole data recorded from prior geotechnical investigations, such as cities, industrial parks, and business centers.

6.0 RECOMMENDATIONS

This study recommends modeling the area considering high-rise buildings. Also, since only three candidate models were compared, it is recommended to conduct more candidate models to improve the current models used. Deeper study in the kriging interpolation and its parameters to optimize the models may also be considered for further studies.

The study is highly recommended to be done in other locations and study areas to verify and utilize the concept.

7.0 REFERENCES

[1] ASEP. (2015). *National Structural Code of the Philippines.* In NSCP C101-15 (7th ed.).

[2] BUDHU, M. (2015). *Soil Mechanics Fundamentals.* John Wiley & Sons, Ltd Registered.

[3] CRESSIE, N. A. C. (1990). *The origins of kriging. Mathematical Geology*, 22(3), 239–252.

[4] DAS, B. M., & SOBHAN, K. (2018). *Principles of Geotechnical Engineering* -9th Edition.

[5] ESRI. (2020). *The geostatistical workflow.* http://pro.arcgis.com/en/pro-app/latest/help/analysis/geostatistical-analyst/the-geostatistical-workflow.ht

[6] ESRI CANADA. (2021). *Turn your borehole data into a complete exploratory 3D model in three easy steps.* https://www.youtube.com/watch?v=MMq0eAhGuIY&t=129s

[7] GOOVAERTS, P. (1997). *Geostatistics for Natural Resources Evaluation (Applied Geostatistics).* Oxford University Press.

[8] HENGL, T. (2009). *A Practical Guide to Geostatistical Mapping in Government Publications Review* (Vol. 13, Issue 6). https://doi.org/10.1016/0277-9390(86)90082-8

[9] LOOK, B. G. (2007). *Handbook of Geotechnical Investigation and Design Tables. In Handbook of Geotechnical Investigation and Design Tables.* https://doi.org/10.1201/9780203946602

[10] ZIRAKBASH, T., ADMIRAAL, R., BORONINA, A., ANDA, M., & BAHRI, P. A. (2020). *Assessing Interpolation Methods for Accuracy of Design Groundwater Levels for Civil Projects.* Journal of Hydrologic Engineering, 25(9), 04020042. https://doi.org/10.1061/(asce)he.1943-5584.0001982

Breakout Room #2
Architectural and Civil Engineering
Chairperson: Dr. Nguyen Van Quang, DUT

Electrical Resistivity of Concrete Containing Ceramic Tile Waste as Partial Replacement for Fine Aggregate

John Ezekiel D. Mateo[1,2], Marish S. Madlangbayan[2*], Marloe B. Sundo[2], Richelle G. Zafra[2] and Maricel A. Eneria[2]

[1]Rio Tuba Total Water Solutions Corp., Philippines
[2]Department of Civil Engineering, College of Engineering and Agro-Industrial Technology, University of the Philippines Los Baños, Philippines
*Corresponding author's e-mail: msmadlangbayan@up.edu.ph

Abstract

Concrete, one of the most widely used construction materials, consists of cement, water, and aggregates. However, river sand, the conventional fine aggregate used in concrete has become one of the most consumed natural resources and excessive consumption will lead to environmental damage. Ceramic tile wastes from production and demolition, however, are plentiful and are not reusable. This study will focus on the use of finely crushed ceramic tile waste from demolition and its effect on electrical resistivity, a key parameter in assessing the durability of concrete. Six design mixes with constant water to cement ratios were prepared incorporating fine crushed ceramic tiles as partial substitute for fine aggregate with replacement levels of 10%, 20%, 30%, 40%, and 50%. A slump test was used to investigate the effect of the ceramic tiles on the workability of fresh concrete and electrical resistivity was measured using a DC circuit. Compressive strength was also measured to verify that ceramic tile waste from demolition will not negatively impact strength as previous studies used ceramic from different sources. Statistical analysis showed that the electrical resistivity of concrete with finely crushed ceramic tile waste has no significant difference compared to control concrete.

Introduction

Construction and demolition have generated a significant amount of solid waste. According to the European Commission of 2016, construction and demolition wastes (CDW) account for 25-30% of the total waste[1]. Most of these waste materials are not reused and are being sent to landfills. A significant part of this waste material is composed of ceramic material such as bricks and tiles.

In the Philippines, the ceramic tile industry has a production capacity of 30 million square meters per year according to the Department of Trade and Industry and according to Binici (2007), an estimated 30% of daily production in the ceramic industry goes to waste[2, 3]. This equates to 9 million square meters of ceramic tile waste per year.

A great deal of research into the properties of concrete with ceramic waste introduced into the mix as a partial or total replacement for aggregate has already been done. Currently, there is a lack of information on the durability of concrete with partial replacement of fine aggregate with ceramic tile waste, particularly in terms of its electrical resistivity.

Research done by Koyuncu et al. (2004), Topcu and Guncan (1995), De Brito et al. (2005), and Bakri et al. (2006) confirmed the possibility of using general ceramic waste as natural aggregate replacement in non-structural concrete[4-7]. They also obtained results that showed increased tensile strength and resistance to abrasion. However, Gomes and De Brito (2009) found that total replacement of coarse aggregates by ceramic waste aggregates had negative effects such as reduced workability due to the high water absorption of the ceramic[8].

Higashiyama et al. (2012) conducted research on the use of ceramic waste from electrical insulators as fine aggregates and its effect on the compressive strength and chloride penetration resistance of mortar[9]. Their study found that there was an increase in both compressive strength and chloride penetration resistance compared to mortar made with ordinary river sand. The study also discovered smaller pore volume and pore diameters in the specimens that incorporated ceramic waste compared to conventional concrete. Higashiyama et al. also tested the possibility of using very fine ceramic powder as partial replacement for cement up to 20% by weight is effective in terms of compressive strength and chloride penetration resistance.

In 2014, Arive used ceramic tile waste from production as partial substitute for sand in concrete and investigated its effect on the workability, wet bulk density, and compressive strength[10]. In this study ceramic was used replace sand by 5%, 10%, 15%, and 20% of the mass. It was found that the use of ceramic tile waste as partial replacement for sand decreased the workability of the concrete. However, as the amount of ceramic was increased, compressive strength also increased.

Urbano (2015) also used ceramic tile waste from production as replacement of sand by up to 20% by mass and investigated the effect of the use of ceramic on the chloride penetration resistance of concrete. It was found that as the amount of ceramic tile waste used in concrete increased, the chloride penetration resistance also increased[11].

In 2016, Ruedas used ceramic tile waste from production as 25%, 50%, 75%, and 100%

replacement of sand by volume and investigated the effect of using greater amounts of ceramic tile waste as fine aggregate on the compressive strength of concrete[12]. It was found that compressive strength increased but only up to 50% replacement by volume. The study therefore concluded that the optimum replacement amount of ceramic tile waste is only up to 50% by volume of fine aggregate.

This study will contribute information to the current knowledgebase of the field of material technology with respect to the use of ceramics in concrete. This study will also contribute baseline resistivity values of concrete with no fine aggregate replacement. The results of this study would give an inclination to the durability of concrete with ceramic waste as partial replacement for fine aggregate and be helpful in the development of a standard practice that will serve as a guide in the use of ceramic waste in concrete production where cost efficiency, durability, and ecological impact is a major concern.

The general aim of this study is to determine the durability of concrete with varying amounts of ceramic tile waste as partial replacement for fine aggregate by evaluating its electrical conductivity using a DC uniaxial electrical resistivity test.

Methodology

The concrete mix constituents were: Type I Portland cement with a specific gravity of 3.15, river sand, fine ceramic aggregate (FCA), and gravel with a maximum size of 20mm specific gravity of 2.52 and dry-rodded unit weight of 1554.77 kg/m^3.

This study is designed to investigate the effect of varying percentages of ceramic tile waste replacement for fine aggregate on the electrical resistivity of concrete. In this study, five varying levels of replacement of FCA (10%, 20%, 30%, 40%, and 50% of total fine aggregate) and a control with no FCA was considered. The electrical resistivity of the concrete was measured using a uniaxial electrical resistivity test with DC current. In this test, current measurements were done at two different voltages on 100 x 50 mm cylindrical concrete specimens. Test results were then analyzed with the aim of establishing a relationship between percent replacement of ceramic tile waste and electrical resistivity. A total of 42 100 x 200 mm parent specimen were cast (7 for each design mix) and was cured for 28 days. Three (3) parent specimen for each design mix were cut to produce 6 test specimen for electrical resistivity testing and 4 parent specimen for each design mix for compressive strength testing.

The ceramic tile waste was collected from renovation projects inside the campus, specifically, from the Institute of Animal Sciences. The ceramic tile wastes were crushed using a hammer mill and only those that passed through sieve No. 4 were used. Fig. 1 shows the ceramic tile waste after being mechanically crushed.

Fig. 1. Crushed ceramic tile waste

Standard ASTM methods were used to determine the properties of the crushed ceramic tile along with sand and gravel such as particle size distribution, fineness modulus, specific gravity, and dry-rodded unit weight. These properties of the fine aggregates are shown Table 1.

Table 1. Properties of varying amounts of FCA mixed with sand.

Fine Aggregate	Fineness Modulus	Specific Gravity
Sand	2.46	2.47
10% FCA	2.53	2.45
20% FCA	2.65	2.43
30% FCA	2.58	2.41
40% FCA	2.65	2.39
50% FCA	2.88	2.37

Fig. 2 below illustrates the particle size distributions of the fine aggregates used.

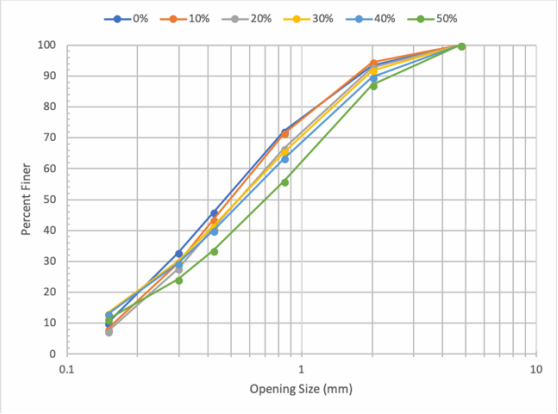

Fig. 2. Particle size distributions of the varying amounts of FCA with sand.

Using the ACI method 211, the measured properties of the cement and the aggregates, and a desired slump of 80 – 100 mm and a fixed w/c ratio of 0.5, the following mix designs shown in Table 2 were constructed.

Table 2. Concrete mix proportioning (kg/m^3 of concrete)

Mix ID	Cement	Water	CA	FA	Ceramic Tile
Control	400	200	1018	608	0
FCA10	400	200	1006	552	61
FCA20	400	200	988	501	125
FCA30	400	200	999	428	183
FCA40	400	200	989	370	246
FCA50	400	200	952	323	323

After mixing, slump tests were performed for all mix designs according to ASTM C143. The concrete was then cast into 100 x 200 mm cylindrical molds and set aside for 24 hours to harden. Hardened specimens were then cured in a distilled water tank for 28 days. After curing, the hardened cylindrical specimens were patted dry and cut into disc samples having a height of 50 mm using a concrete cutting blade. Fig. 3 below shows the schematic diagram of a parent specimen and the cutting planes.

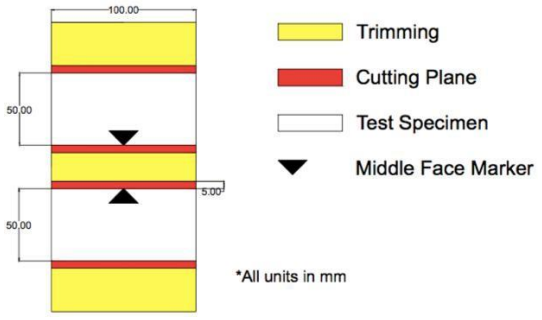

Fig. 3. Schematic diagram of test specimen cutting planes.

According to Monfore (1968), when using direct current, there is polarization in the concrete due to it conducting electricity as an electrolyte[13]. The polarization causes a drop in the actual voltage causing current by a certain amount. Monfore assumed that this effect is constant at different voltages and can be taken into account by using different voltages to take measurements and used the following equation to determine the DC resistance value.

$$R=(E_{a2}-E_{a1})/(I_2-I_1) \qquad (1)$$

Where:
E_{a1}, E_{a2} are the applied voltages
I_1, I_2 are the respective currents

For a cylindrical specimen, resistivity (ρ) is given by the following formula (McCarter et al., 2009)[14].

$$\rho = R\frac{A}{\ell} \qquad (2)$$

Where:
R is the electrical resistance
A is the cross-sectional area
ℓ is the length of the material or the distance between the two electrodes

The computed DC resistance value from equation 1 is then plugged into equation 2 to obtain the resistivity. Fig. 4 below shows the set-up of the electrical resistivity test.

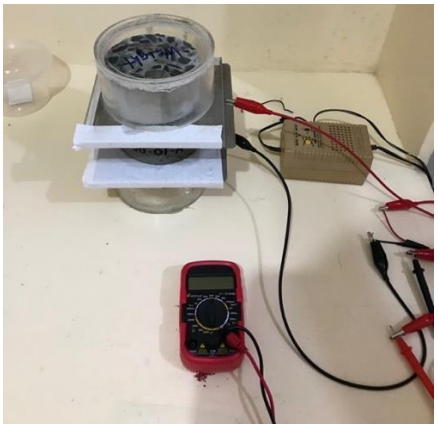

Fig. 4. DC uniaxial electrical resistivity test set-up.

To perform the DC electrical resistivity test, conductive gel was placed at both ends of the 100 x 50 mm specimen and the specimen was then placed in between two steel plate electrodes covered in tissue. The multimeter was first set to read DC voltage to measure the voltage supplied by the power supply. The multimeter was then set to read current to determine the current passing through the concrete test specimen. This was done at two different voltages to eliminate the effect of polarization and the resistance of the test specimen was then computed using equation 2 and using the resistance computed, resistivity was computed using equation 1.

A compressive strength test was also conducted according to ASTM C39 to verify that the mix design and the ceramic tile waste from demolition was of comparable strength to that of ordinary concrete.

Any outlier data points from the electrical resistivity test and the compressive strength test were determined by using the Inter Quartile Range (IQR) method and removed from the statistical analysis.

One-way Analysis of Variance (ANOVA) was then performed to determine the significance of the varying results for the DC uniaxial electrical resistivity test and the compressive strength. The one-way ANOVA that was performed on both the electrical resistivity results and compressive strength

results had a level of significance of 0.05 and a level of confidence of 95%.

Results and Discussion

Effect of FCA on workability

The slumps of the fresh concrete mixtures are shown in Table 3. The control mixture had a slump of 99 mm. Results for the concrete mixes with FCA were slightly lower, ranging from 81 to 97 mm.

Table 3. Slumps of freshly mixed concrete with ceramic tile waste

Mix ID	Slump (mm)
Control	99
FCA10	97
FCA20	94
FCA30	91
FCA40	86
FCA50	81

From the observed values in the Table 3, the slump of concrete with ceramic tile waste was found to decrease as the amount of crushed ceramic tile used increased. This could be due to the brittle nature of ceramic that when mechanically crushed, produces irregular, rough, and more angular shapes which may make it more difficult for the particles to slide over one another.

Effect of FCA on Electrical Resistivity

Results of the DC uniaxial electrical resistivity test are summarized in Fig. 5. It should be noted that electrical resistivity values were computed from voltage and current measurements done on test specimens whose cross-sectional areas and lengths were known.

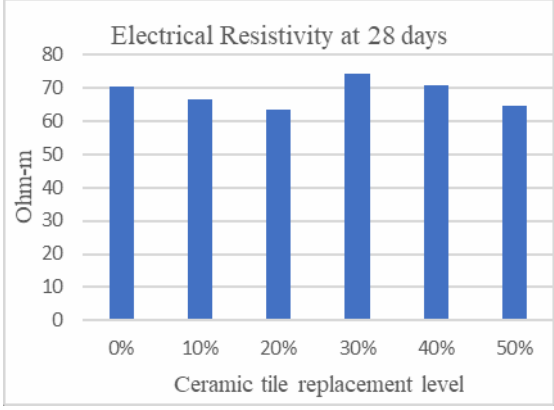

Fig. 5. Average electrical resistivity values at 28 days.

As shown in the Fig. 5, the lowest electrical resistivity value of was given by the FCA20 group (63.26 Ohm-m) which was a 10% decrease from the control. The peak electrical resistivity value was given by the FCA30 group (74.02 Ohm-m) which showed a 5.3% increase from the control.

The one-way ANOVA performed on the results yielded a P-value of 0.129221 which is greater than the level of significance, 0.05, indicating that there is no significant difference between the means of the different groups and that no further statistical analysis was required. This result could be due to the similarity in properties of the FCA and sand as shown in Table 2-1 and Fig. 2.

Effect of FCA on compressive strength

The compressive strength of the specimens was determined using the ASTM C39 test procedure. The results are summarized in Fig 6.

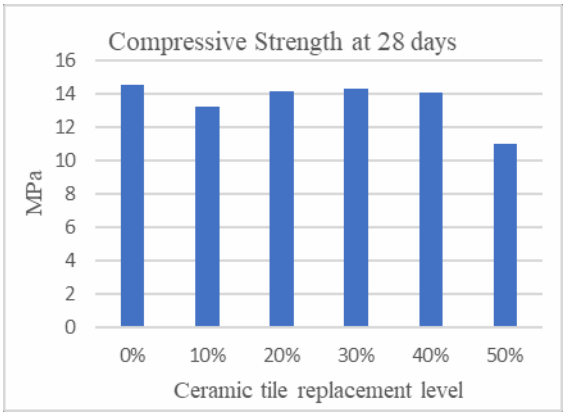

Fig. 6. Compressive strength of test specimens.

As shown in Fig. 6, all groups yielded similar values of compressive strength. The peak mean strength value for mix designs with ceramic tile waste was 14.29 MPa, given by the FCA30 group, which is a 1.65% decrease from the control value and the lowest mean strength produced (11.03 MPa), given by the FCA50 group, was 24% weaker than the control specimens.

The one way ANOVA performed on the results yielded a P-value of 0.308 which is again greater than the level of significance, 0.05, indicating that there is no significant difference between the means of the different groups and that no further statistical analysis was required.

Summary and Conclusion

Crushed ceramic tile waste generally decreases workability however, the electrical resistivity and compressive strength were not found to increase or decrease significantly with respect to ordinary concrete at any of the replacement levels used. The decrease in workability could be attributed to the more angular aggregates being unable to glide over each other as easily as the rounder sand particles. However, the more angular shape did not significantly affect the electrical resistivity and

compressive strength due to the similarities in physical properties such as gradation and fineness modulus. The 100 by 50 mm cylindrical test specimens also had smooth cut surfaces that indicate sufficient bonding was achieved by the crushed ceramic particles. This supports the findings of previous studies that the optimum level of replacement of crushed ceramic tile for fine aggregate in terms of compressive strength is around 20%-50%.

It can be concluded that within the limited scope of experiments carried out in this study, the use of crushed ceramic tile waste as a partial replacement for sand in concrete at 10% to 50% by mass is not majorly detrimental to the electrical resistivity of concrete meaning that durability is not sacrificed at the expense of using recycled ceramic. Slump, however, is decreased and should be noted when attempting to use a mixture of crushed ceramic tile waste and sand fine aggregate for applications requiring higher workability.

References:

[1] European Commission. Construction and Demolition Waste (2016).

[2] Department of Trade and Industry. Ceramic Tiles. Retrieved from http://industry.gov.ph/industry/ceramic-tiles/

[3] H. Binici, Effect of Crushed Ceramic and Basaltic Pumice as Fine Aggregates on Concrete Mortars Properties. *Construction and Building Materials*,*21*(6), 1191-1197 (2007).

[4] H. Koyuncu, Y. Guney, G. Yilmaz, S. Koyuncu, & R. Bakis, "Utilization of ceramic Wastes in the Construction Sector," Euro Ceramics viii, Part 1-3, 264-268,(2004)

[5] I. Topcu, & N. Guncan, "Using Waste Concrete as Aggregate," *Cement and Concrete Research*, 25, 1995, pp. 1385-1390 (1995).

[6] J. De Brito., A. Pereira & J. Correia (2005). "Mechanical Behaviour of Non-Structural Concrete Made with Recycled Ceramic Aggregates," *Cement & Concrete Composites*, 27, 2005, pp. 429-433 (2005).

[7] M. Bakri, K. Hussin, C. Mohd, S. Baharin, R. Ramly, R.,& Khairiatun, N. "Concrete Ceramic Waste Slab (CCWS)", *Journal of Engineering Research & Education*, 3, pp. 139-145 (2006).

[8] M. Gomes, & J. De Brito, "Structural Concrete with Incorporation of Coarse Recycled Concrete and Ceramic Aggregates: Durability Performance," *Materials and Structures*, 42, 2009, pp. 663-675 (2009).

[9] H. Higashiyama, F. Yagishita, M. Sanoand, & O. Takahashi, "Compressive Strength and Resistance to Chloride Penetration of Mortars Using Ceramic Waste as Fine Aggregate," *Construction and Building Materials*, 26, pp. 96-101 (2012).

[10] K. Arive, Investigation on the Compressive Strength of Concrete with Ceramic Tile Wastes as Partial Replacement of Fine Sand Aggregates. Undergraduate Thesis – Civil Engineering. University of the Philippines Los Baños, College, Laguna (2014).

[11] T. Urbano, Investigation of Chloride Penetration in Concrete with Ceramic Tile Waste as Partial Replacement to Fine Sand Aggregates Using Colorimetric Method. Undergraduate Thesis – Civil Engineering. University of the Philippines Los Baños, College, Laguna (2015).

[12] P. Ruedas, Investigation on the Compressive Strength of Concrete with High Percentage Replacement of Ceramic Tile Waste as Fine Aggregate. Undergraduate Thesis – Civil Engineering. University of the Philippines Los Baños, College, Laguna (2016).

[13] G. Monfore, "The Electrical Resistivity of Concrete", *Journal of the PCA Research and Development Laboratories*, pp. 35-48 (1968).

[14] W. McCarter, G. Starrs, S. Kandasami, M. Jones, M. Chrisp, "Electrode Configurations for Resistivity Measurements on Concrete", *ACI Matls. J*., 106(3), 258-264 (2009).

Feasibility Study of Rooftop Rainwater Harvesting System for Flushing Demand in Different Philippine Climate Types

Ricahlee R. Sabilla*, Kale Ashley P. Carurucan, Richelle G. Zafra, and Perlie P. Velasco

Department of Civil Engineering, College of Engineering and Agro-industrial Technology, University of the Philippines Los Baños, Philippines
E-mail: rrsabilla1@up.edu.ph

Abstract

The Rainwater Harvesting Act mandates the establishment of rainwater harvesting systems. It requires Metro Manila and other major Philippine cities such as Pasig, San Fernando, Legazpi, Cebu, and General Santos City, to construct a rainwater harvesting system (RHS) for commercial buildings with a total property area of at least 1500 m². In accordance with the act, this study sought to assess the feasibility of rooftop RHS of commercial buildings in the mentioned cities characterized by different Philippine climate types, by determining the tank size using a supply and demand approach, designing a layout, and providing an economic analysis. The capacities of the storage tank varied in the different areas, with the tank in San Fernando City, La Union having the highest storage capacity, while General Santos City with the lowest. Through the tank sizing method, the differences can be mainly attributed to the nature of the rainfall data. Climate type with extremely varying rainfall rates affects the storage tank size as it has to store more rainwater for the dry period. In this regard, the obtained tank sizes can accommodate the toilet flushing demand for the whole year. Moreover, the Benefit-Cost Ratio (BCR) for areas with moderately varying rainfall rates results to a value greater than one and positive Net Present Value (NPV) with a payback period of as early as 18 years. In contrast, areas with extremely varying rainfall rates resulted to a BCR value less than 1 and negative NPV. Thus, installing RHS is feasible only for certain climate types. For non-feasible to be beneficial, optimized tank sizing is recommended.

1. INTRODUCTION

1.1. Background of the Study

In a tropical country such as the Philippines, abundant rainfall is considered a water resource for development. The annual rainfall rate of this country varies from 965 to 4065 millimeters (PAGASA, n.d.), one of the world's highest rainfall rates. Nevertheless, it is not fully used due to the seasonality of its occurrence. The dry season results in water supply crisis or supply and demand problems, while the wet season results in flooding due to a lack of stormwater management. More than three million people rely on unsafe and unsustainable water sources, and seven million lack access to improved sanitation (Conteras et al., n.d.). Despite its growing economy, the Philippines faces significant water and sanitation access challenges. Numerous studies refer to alternative measures to address this problem (Lee et al., 2016). Regarding water consumption, those alternatives include water-efficient fixtures and appliances, gray water recycling systems, and rainwater harvesting systems implementation.

Rainwater harvesting (RWH) generally collects rainwater through a collection system. It diverts the rainwater from the gutters to the storage tank for specific applications such as toilet flushing, horticulture, bathing, dishwashing, cooking, and drinking. A rainwater harvesting system usually consists of three main components: collection, transportation, and storage tank. Designing a reservoir tank is vital as it is considered the most expensive part of the rainwater harvesting system. Thus, determining storage tank size applicable for a given set of conditions such as demand, supply, and roof area is required (Ward, 2010).

Rainwater harvesting systems (RWHS) have been implemented significantly in countries such as Australia, Brazil, and Japan resulting in non-potable water savings (Eroksuz & Rahman, 2010). In the Philippines, government action occurs through the Republic Act 6716, the Rainwater Collector and Springs Development Act of 1989, and the Rainwater Harvesting Act of 2019. The Rainwater Collector and Springs Development Act of 1989 mandates the construction of water wells, rainwater collectors, spring development, and rehabilitation of existing water wells in all barangays throughout the Philippines to secure a continuous supply of safe drinking water and prevent flooding during dry seasons. Moreover, the Rainwater Harvesting Facility Act requires new commercial, institutional, and residential infrastructure projects in Metro Manila and other major cities in the Philippines to install rainwater harvesting or retention facilities, providing penalties for violations and other purposes.

Despite having an act regarding RWHS, rainwater reuse is rarely performed in the Philippines. Many factors and obstacles arise. One is the assumption that installing the RWH system is expensive and not significantly provides benefits from the financial side. Stakeholders are still reluctant to apply the concept, and utilizing groundwater or tap water is still the best preference. Due to the lack of comprehensive studies on the use of rainwater and the absence of proof, many people still hesitate to implement RWHS. People are not aware of the benefits that can be obtained with the use of rainwater. Thus, this study aims to analyze the benefits of implementing RWH systems for a commercial building or domestic water use, especially in terms of financial overview. Lastly, this study may serve as a basis for the Rainwater Harvesting Act's feasibility and applicability for Metro Manila and other major cities in the Philippines, considering different climate types in the country.

1.2. Significance of the Study

This study will provide feasible plan to reuse rainwater for domestic use. Also, this study may help to conserve water and lower the expected water bill. Since most of the structures in Metro Manila and other major cities in the country are being serviced by commercial water providers, the water bill is expected to decrease due to the reduction of water usage. Moreover, this study may serve as a reference to a large-scale rainwater harvesting system that can contribute to the community. This study will also provide an economic analysis to assess the financial benefits and payback period of rainwater harvesting installation.

The result of this study can be used as a reference or basis for the feasibility of rooftop rainwater harvesting systems in the country, considering different climate types. Also, it may serve as evidence for the applicability of an act mandating the establishment and maintenance management of Rainwater Harvesting Systems in the Philippines. In the case that one of the representative areas is not feasible, this study would further help the revision of such an act to limit the areas to places with sufficient rainfall rates, which is another area for research.

1.3. Objectives of the Study

The study generally aims to assess the feasibility of rooftop rainwater harvesting systems for a commercial building in the Philippines with different climate types. In relation to the main objective, this study was conducted according to the provisions of the Rainwater Harvesting Act of 2019. Specifically, the objectives of the study are:

1. Determine the tank size for the representative areas of each climate type using supply and demand approach;
2. Create the design and layout of the rooftop rainwater harvesting system; and
3. Provide economic analysis using Benefit-Cost Ratio and Net Present Value.

2. REVIEW OF LITERATURE

2.1. Rainwater Harvesting System in the Philippines

Climate

The climate of the Philippines is tropical and monsoonal. It is characterized by uniformity of temperature with an average annual temperature of 27℃, high relative humidity (above 70% throughout the year), high solar radiation, diversity of rainfall, and high frequency of tropical cyclones, contributing 38% of the annual rainfall. Furthermore, with an average annual rainfall of 2,400 mm, the mean runoff is estimated at 257 km^3 with a 90% probability of occurrence (Fujihara et al., 2014).

The climate type is a factor that influences the rainfall rate of an area. For instance, General Santos City under Type IV has more or less even distribution of rainfall throughout the year resulting in a low rainfall rate. On the other hand, Legazpi City under Type II has no dry period throughout the year, resulting in a high rainfall rate, with a pronounced wet season from November to February.

Rainwater Harvesting Act

Republic Act No. 6716 of 1989, also known as the Rainwater Collector and Springs Development Law, gives the Department of Public Work and Highways a mandate to construct water wells and rainwater collectors, develop springs, and rehabilitate existing water wells in barangays nationwide.

Along with the RA 6716, Senator Emmanuel D. Pacquiao introduced an act mandating the country's establishment, maintenance, and management of rainwater harvesting systems. An explanatory note of this act indicates that the harvested and stored rainwater can be used for irrigation and other agricultural purposes, groundwater recharge, firefighting, and non-drinking water sources such as watering plants, flushing toilets, and washing cars and gardens. The collected rainwater is expected to address the problems of water shortages due to population growth, rapid urbanization, and inadequate waste management.

According to Article II, Section 4 of the Rainwater Harvesting Act, an owner or developer of a new commercial, institutional, or residential development project in major cities in the Philippines with an area of at least 1500 m^2 is required to reserve, develop, and maintain at least 3% of the total property area, as a rainwater harvesting facility.

2.2. Rainwater Harvesting

Rainwater harvesting collects runoff from a structure or other impervious surface to store it for later use (Maxwell-Gaines, 2020). Traditionally, rainwater is collected from a roof. The rain collects in gutters that lead the water into downspouts and a storage tank. Rainwater harvesting systems can be as simple as collecting rain in a rain barrel or as elaborate as collecting rainwater in large cisterns to meet household demand.

The harvested rainwater can provide an alternative source of water for households. Alternative waters are sustainable water sources that are not fed by surface or groundwater but meet the demand for freshwater (Ogale, 2019). Typical uses of rainwater are garden irrigation, washing applications, filling ponds and ornamental fountains, freshwater for cooling towers, and flushing toilets and urinals. With additional filtration and disinfection, the collected rainwater can also be made potable to supplement the municipal potable water supply.

2.3. Related Studies

A study conducted by Palla et al. published in 2012, entitled Performance analysis of domestic rainwater harvesting systems under various European climate zones, investigated the impact of climate conditions on the performance of rainwater harvesting systems in Europe. The results were produced in terms of the water quantity and quality performance. From these, cold and humid temperature zones exhibit highest quantitative performance, as characterized by the frequency of rainfall events. Consequently, for reduced frequency of rainfall events, there would be a decrease in water saving efficiency. In the operational conditions, it was also found that the influence of the rainfall event characteristics (including rainfall depth, intensity and duration) may be reduced by increasing the storage capacity. This is possible with the (large) volume potentially sufficing the water demand for constant dry weather periods. While the work in the discussed paper was conducted in the European setting, its similarity with this study is the consideration of different climate types for the installation of a RWH system. Its conclusions regarding the effect of climate can be used as basis or supplementary evidence to back up the results of this study. These include the generalization of the performance of the RWH system at cold climates, the effect of having large storage capacities, and the frequency of rainfall events.

3. MATERIALS AND METHODS

This study used quantitative data. The quantitative data are the annual rainfall data, population of the location, per capita water demand, rooftop area and cost for initiating rainwater harvesting system. Generally, this study contributes to the continuous research on green building techniques, specifically developing economically efficient structures.

3.1. Water Demand

One method of determining rainwater harvesting tank is to calculate the storage requirement based on the consumption rates and occupancy of the building. Data for flush demand was generated from the estimated average daily use of toilet flush of a person which is based from the Guidelines for Residential Rainwater Harvesting Handbook and the number of toilet fixtures in a commercial building.

3.2. Rainfall Data

Rainfall data of Pasig City, San Fernando City, Legazpi City, Cebu City, and General Santos City was obtained from PAGASA. The data was similar to the sample taken from the study of Anchan (2021). The mean annual precipitation is determined using Microsoft excel and was used to design the tank.

3.3. Catchment Area

One of the significant parameters in designing a rainwater harvesting tank and determining the estimated rainwater being collected is the catchment area. Roof area was derived from the commercial building plan acquired from Laguna Technopark Incorporated.

3.4. Estimating Water Tank Capacity

Estimating water tank capacity was based on the cumulative monthly demand and cumulative monthly rainwater harvested. It takes into consideration the accumulated inflow and outflow from the tank and the capacity of the tank is calculated as the greatest excess of water over and above consumption. All this water will have to be stored to cover the shortfall during the dry period.

3.5. Costing

Costing is any system for assigning costs to an element of a business. Costing is typically used to develop costs for materials. Type of material,

size/length of material, cost per item/length/size are the key parameters in obtaining the cost for rainwater harvesting system.

3.6. Economic Analysis

Financial analysis is performed to calculate the economic feasibility of the rainwater harvesting system. There are various economic methods that can be used to calculate the investment feasibility. The benefit–cost ratio method was used to calculate the financial benefits of RWH system implementation. Benefit–cost ratio (BCR) is a method that often used in the early stages of investment plan evaluation or as an additional analysis with the aim to validate the results of the evaluation that has done previously. BCR method gives an emphasis to the aspect ratio between the value of benefits that would be obtained with the aspect of cost and losses incurred by these investments. BCR values can be calculated from the year that the system would return on investment. The cost component is the capital cost, maintenance, and operational costs. Annual cost is all cost spent along the age of the system

4. RESULTS AND DISCUSSION

4.1. Storage Tank Design

The obtained tank capacity of Pasig City under Type I is 1089.10 m^3, 1674.72 m^3 for San Fernando City under Type I, 1062.43 m^3 for Legazpi City under Type II, 206.69 m^3 for Cebu City under Type III, and 75.77 m^3 for General Santos City under Type IV. From the acquired data, it can be seen that Pasig City, San Fernando City, and Legazpi City obtained large tank capacity as these areas receive a massive amount of rainfall that greatly exceeds their monthly demand. However, storing a huge amount of rainwater is unnecessary for areas with constant high rainfall rates since these areas can already provide for its monthly demand. For instance, Legazpi City under Type II has no dry season, with a very pronounced maximum rain period from December to February. In contrast, Pasig City and San Fernando City under Type I have two pronounced seasons, dry from November to April and wet during the rest of the year. Legazpi City can cover its monthly demand using its monthly rainfall harvested. On the other hand, Pasig City and San Fernando City having extremely high and low rainfall rates, had to store a large amount of rainwater to cover the demand during the dry period.

Cebu City under Type III and General Santos City under Type IV used the initial computed tank capacity as their monthly available water did not exceed the computed demand. Thus, overflow is not considered. Moreover, due to the low rainfall rate of Cebu City and General Santos City, low capacity of storage tanks was obtained compared to other selected cities. Table 4-1 shows the final storage tank capacity of the selected areas.

Table 4-1. Final storage tank capacity for selected cities.

Representative Areas	Computed Storage Tank Capacity (m^3)	Final Storage Tank Capacity (m^3)
Pasig City	631.00	650
San Fernando City	732.00	750
Legazpi City	111.00	150
Cebu City	206.69	250
General Santos City	75.77	100

Since exact sizes of computed storage tank capacity are not readily available on markets, the final storage tank capacities, rounded up to the nearest multiple of fifty, were obtained. Final storage tank capacity must not be lower than the computed storage capacity as it will result to insufficient supply for the monthly demand of the selected cities. Furthermore, storage tank dimensions for computed storage tank capacity and final storage tank capacity were computed, as shown in Table 4-2.

Table 4-2. Storage tank dimensions for selected cities.

Representative Areas	Dimensions for Computed Storage Tank Capacity		Dimensions for Final Storage Tank Capacity	
	Radius (m)	Height (m)	Radius (m)	Height (m)
Pasig City	5.36	7.00	5.44	7.00
San Fernando City	5.77	7.00	5.84	7.00
Legazpi City	2.43	6.00	4.81	2.06
Cebu City	3.07	7.00	4.81	3.44
General Santos City	2.00	6.00	4.81	1.38

Having the volume of the storage tank, Article II, Section 4 of Rainwater Harvesting Act requires that the base area of the storage tank must be at least three percent of the commercial building's total area, 72.44 m^2. In compliance, the radius of the storage tank was adjusted to meet the minimum floor area requirement. Moreover, the height of the storage tank must not exceed the height of the downspout to let the water move from roof to storage tank without using a pump. In this study, reinforced concrete tank

design was used, as it is economical for large size tanks compared to steel tank design.

4.2. Economic Analysis

Financial analysis was performed to calculate the economic feasibility of the rainwater harvesting system. In this study benefit-cost ratio was used to calculate the financial benefits of RWH system implementation. BCR method emphasizes the aspect ratio between the value of benefits that would be obtained with the aspect of cost and losses incurred by the investments. The cost component is the capital cost and maintenance. Moreover, benefits were calculated based on rainwater volume used to replace the water use. The calculated BCR, payback period, and net present value of the representative areas are shown in Table 4-3.

Table 4-3. The calculated BCR, payback period, and net present value for selected cities.

Representative Area	BCR	Payback Period (years)	Net Present Value (PhP)
Pasig City	0.56	More than 30	-2,300,177.09
San Fernando City	0.98	More than 30	-117,838.50
Legazpi City	2.06	18	1,855,780.14
Cebu City	0.85	More than 30	-429,858.25
General Santos City	1.21	27	272,277.47

In the study of Tam et al. (2010) the variation in result in payback periods was due to the variation in water rates, monthly rainfall harvested, roof area, and storage tank capacity. The higher value of BCR corresponds to the earlier payback period. Legazpi City under Type II obtained the earliest payback period, 18 years, as it only has a storage tank capacity of 150.00 m^3 while supplying its 160.00 m^3 monthly demand. The storage tank size significantly affects the payback period as having a larger storage tank results in a higher construction cost (labor, material and land cost). On the other hand, Pasig City and San Fernando City under Type I, and Cebu City under Type III, obtained a payback period of more than 30 years as they have large storage capacities and high land cost.

Considering a discount rate of 2% and a water cost inflation rate of 4.5% (Philippine Statistics Authority, 2022), the BCR for Legazpi City under Type II, and even for General Santos City under Type IV, the area with the lowest rainfall rate in the Philippines, results in a value greater than 1. Moreover, in 30 years, the net present value obtained for the said representative areas are positive, ranging from PhP272,277.47 to PhP1,855,780.14.

On the other hand, Pasig City and San Fernando City under Type I, and Cebu City under Type III, obtained a BCR value less than 1, which means that in a span of 30 years, the financial benefits for rainwater harvesting system in these cities is lower than the cost for maintenance and constructing of a rainwater harvesting system. This is mainly due to the large size of storage tanks and high construction cost. For the case of Cebu City under Type II, despite of having a storage tank capacity of 250 m^3, the obtained BCR is less than 1, primarily caused by high land cost in the area, PhP25,000.00 per square meter.

With all of these, installing a rainwater harvesting system in commercial buildings for the representative areas considering different climate types is beneficial for cities with moderately varying rainfall rates (Type II and Type IV), with the possibility of obtaining a payback period of as early as 18 years. In contrast, for cities with extremely varying rainfall rates (Type I and III), installing a rainwater harvesting system is not financially beneficial. This is primarily due to the large sizes of storage tanks obtained from supply and demand approach. Large sizes of tanks are obtained as the assumption in this study was to supply whole year flushing demand.

5. CONCLUSION

This study sought to assess the feasibility of rooftop rainwater harvesting systems for commercial buildings in different Philippine Climate Types in accordance with the provisions of the Rainwater Harvesting Act. Rainwater Harvesting act is an act mandating the establishment and maintenance management of Rainwater Harvesting Systems for commercial buildings within a certain area, in the country. The harvested rainwater is to be used for toilet flushing for the whole year. This was determined by a series of linear steps of determining the tank size, designing a layout, then finally providing an economic analysis.

Considering different climate types, it was necessary to choose five representative areas where a Rainwater Harvesting System is to be built, along with the commercial building. From the rainfall data, Legazpi City in the province of Albay has the highest rainfall rate, while General Santos City in South Cotabato receives the lowest rainfall rate. These rainfall data was utilized, including the computed water demand of the commercial building, for the supply and demand approach to tank sizing.

Despite high total direct costs, the results imply that installing this system for commercial

buildings in areas with moderately varying rainfall rates (Type II and Type IV) is beneficial. However, for areas with extremely varying rainfall rates (Type I and Type IV), installing a rainwater harvesting system is not feasible as the supply and demand approach for tank sizing results in non-economical tank sizes to supply the whole year flushing demand. These large tank sizes are necessary for months with extreme low rainfall rates (dry period). For this to become beneficial, optimized tank sizing is recommended.

6. REFERENCES

B. EROKSUZ, A., RAHMAN (2010, September). *Optimisation of rainwater tank design from large roofs: A case study in Melbourne Australia*. Research Gate. Retrieved May 26, 2022, from https://www.researchgate.net/publication/251605769_Optimisation_of_rainwater_tank

CONTRERAS, S., TEJADA, S., & SANDOVAL, T. (2013, December). *Rainwater harvesting, its prospects and challenges in the uplands of Talugtog, Nueva Ecija, Philippines*. Researchgate. Retrieved May 23, 2022, from https://www.researchgate.net/publication/275219219_Rainwater_Harvesting_its_Prospects_and_Challenges_in_the_Uplands_of_Talugtog_Nueva_Ecija_Philippines

FUJIHARA, M., MOHAWESH, O., SHARIFI, E., TAKEUCHI, J., & UNAMI, K. (2014, May 6). *Stochastic modelling and control of rainwater harvesting systems for irrigation during dry spells*. Science Direct. Retrieved May 24, 2022, from https://www.sciencedirect.com/science/article/abs/pii/S0959652614004119

GUIDELINES FOR RESIDENTIAL RAINWATER HARVESTING SYSTEMS HANDBOOK (2012, September). *Guidelines for residential rainwater harvesting systems handbook* Retrieved May 26, 2022, from https://www.crd.bc.ca/docs/default

LEE, J., CHAUDHRY, A. M., MULETA, M. K., & DALLMAN, S. (2017, September 2). *The value of rain: Benefit-cost analysis of rainwater harvesting systems - water resources management*. SpringerLink. Retrieved May 23, 2022, from https://link.springer.com/article/10.1007/s11269-016-1429-0

MATOS, C., BENTES, I., SANTOS, C., IMTEAZ, M., & PEREIRA, S. (2015). *Economic Analysis of a Rainwater Harvesting System in a Commercial Building* (thesis). Springer Science Business Media Dordrecht .

MAXWELL-GAINES, C. (2020, July 27). Rainwater harvesting 101: Your how-to collect rainwater guide. Innovative Water Solutions LLC. Retrieved October 21, 2021, from https://www.watercache.com/education/rainwater-harvesting-101.

OGALE, S. (2019, February 15). Rainwater harvesting system. Encyclopedia Britannica. Retrieved October 21, 2021, from https://www.britannica.com/technology/rainwater-harvesting-system.

PAGASA. (n.d.). Retrieved April 29, 2022, from https://www.pagasa.dost.gov.ph/information/climate-philippines#:~:text=The%20Climate%20of%20the%20Philippines,high%20humidity%20and%20abundant%20rainfall.

TAM, V., ZENG, S., & TAM, L. (2010, January). *Cost effectiveness and tradeoff on the use of rainwater tank: An empirical study in Australian Residential Decision- Making*. Retrieved May 26, 2022, from https://www.researchgate.net/publication/229216187_Cost_Effectiveness_and_Tradeoff_on_the_Use_of_Rainwater_Tank_An_Empirical_Study_in_Australian_Residential_Decision-Making

WARD, S., BUTTER, D., & MEMON, F. A. (2010, April). *Harvested rainwater quality: The importance of appropriate design*. Retrieved May 23, 2022, from https://www.researchgate.net/publication/43050217_Harvested_Rainwater_Quality_The_Importance_of_Appropriate_Design

Sorptivity of Concrete with Ceramic Tile Waste as Partial Replacement for Fine Aggregate

Yusaine R. Maon[1,2], Marish S. Madlangbayan[2*], Marloe B. Sundo[2], Richelle G. Zafra[2] and Maricel A. Eneria[2]

[1]Yokogawa Techno Philippines Inc., Philippines
[2]Department of Civil Engineering, College of Engineering and Agro-Industrial Technology, University of the Philippines Los Baños, Philippines
*Corresponding author's e-mail: msmadlangbayan@up.edu.ph

Abstract

Large production of ceramic tiles in the world generates wastes from the forming of the tiles, their transportation, and their use in construction. Therefore, ceramic tile waste has been sought as a viable replacement in concrete as both coarse and fine aggregates. However, studies on the durability of concrete that uses ceramic tiles are scarce. This study focused on investigating the use of ceramic tiles that come from construction wastes. Ceramic tiles were crushed to the size of fine aggregates that passed through sieve #4 (4.76mm sieve) and then used for the concrete mixes. Fine aggregate replacement levels of 10, 20, 30, 40, and 50% were used to design six (6) concrete mixes. Disk specimens, 50 mm in thickness, were cut from parent cylindrical concrete specimens having a diameter of 100 mm. These concrete disk specimens were then subjected to the sorptivity test following ASTM C 1585 -13. Test results showed no significant difference in the initial sorptivity of concrete with 10, 20, 30, and 40% ceramic tile waste as fine aggregate compared to control specimens. However, a significant difference was observed for concrete with 50% ceramic tile waste as fine aggregate. In addition, concrete with ceramic tile waste as fine aggregate showed no significant difference in secondary sorptivity compared to control specimens across all replacement levels. Test results show that using crushed ceramic tiles as a partial replacement of 10, 20, 30, and 40% of the total fine aggregate mix is acceptable.

Introduction

Concrete which is second to water as the most consumed material is found almost everywhere in our modern age society[1]. In the data gathered by the ERMCO (2017), Europe produced 216 million cubic meters, while United States- 230 million cubic meters and Russia- 40 million cubic meters[2].

Sand serves as a fine aggregate which is a major component of concrete. Every year, in between 47-58 billion tons are mined each year according to UNEP (2014) and making sand as the most consumed raw material next to water[3].

Excess excavation of this material may lead to detrimental damages to the environment. To reduce the consumption for sand, alternative materials have been sought. One of these materials is ceramic tiles.

Around 13 billion sq. meters of ceramic tiles were produced globally in the year 2016. In the Philippines, around 30 million sq. meters are produced per year[4]. Around 30% of the production from this industry goes to waste. This makes around 9 million sq. meters of the ceramic tiles in the Philippines wastes during the forming of the tiles, its transportation, and used in construction.

This is evident in the construction side of a developing country such as the Philippines. Construction and demolition wastes (C&D wastes) are produced in so many numbers in hopes of promoting the economic growth of the country. C&D wastes can be classified as bricks, tiles, masonry, cement, timber, metals, plastics and cardboard[5]. In the Philippines, ceramic tiles make up a small fraction of the household waste but over 90% is disposed-off [6].

The possibility of using ceramic tile wastes as a substitute component in concrete has been studied over the years. Example of this would be the study of Tanquerido & Certeza (2015) ceramic tiles was used as a partial replacement to the fine aggregates of the concrete. In the conducted study, it was proven that the use of ceramic tiles showed better results as compared to the traditional concrete mix after substitution of 25 and 50%. The remaining tests with a substitution of 75 and 100% failed to reach the target compressive strength of 15MPa[7].

Ruedas (2016) also investigated the effects of using ceramic tiles waste on compressive strength. In his study, he used ceramic tiles from production and used it as a high replacement of sand from 0% up to 100% in 25% increments by volume. The study, therefore, concluded that the optimum replacement amount of ceramic tile waste is only up to 50% by volume of fine aggregate[8].

In the study of Awoyera et al. (2016), used ceramic tiles obtained from construction and demolition[9]. It was used as a partial replacement to fine and coarse aggregates. They determined that there is a direct relationship between the curing period and the compressive strength, split tensile strength and flexural strength of the concrete. The results gathered showed a better increase as compared to the regular concrete mix that does not use ceramics.

Most studies that use ceramic tiles have mostly been strength tests both in the Philippines and in other countries. There has been a lack of tests in terms of its performance on durability.

In considering durability, we can consider one of the most abundant raw materials in nature, water. It comes in several forms. As a small molecule, it can penetrate porous materials with ease affecting its overall durability. To measure this transport of water into an unsaturated sample, the Sorptivity test can be used. Through this test, concrete structures exposed to these water-related conditions can be observed.

This study aims to evaluate the effect of Fine Ceramic Tile Aggregate (FCTA) on the durability of concrete, focusing on the influence of FCTA on the Sorptivity of concrete when sand is partially replaced with FCTA. Specifically, this study aims to determine the effect of FCTA in varying percent of replacements from 0% to 50% in 10% increments. Also, this study aims to evaluate the Initial and Secondary Sorptivity of FCTA.

The study used FCTA derived from brown ceramic tiles from a renovation project University of the Philippines Los Baños, specifically, from the Valente M. Villegas Hall, Institute of Animal Sciences in the Institute of Animal Sciences, University of the Philippines – Los Baños. The results will supplement existing data on the ability of FCTA as a sand replacement, particularly in terms of its effect on the Sorptivity of concrete.

Methodology

This study is designed to investigate the Sorptivity of type I ordinary Portland cement concrete with FCTA as partial replacement for sand. Five varying levels of replacement of FCTA, namely, 10%, 20%, 30%, 40%, and 50% of the total fine aggregate by mass and a control with no FCTA were considered. A total of 42 parent specimens of size 100 x 200 mm were cast (7 for each design mix) and was cured for 28 days. 3 parent specimens for each design mix being cut to produce 6 disk specimens of size 100 x 50 mm for Sorptivity testing and 4 parent specimens for each design mix for compressive strength testing. The Initial and Secondary Sorptivity of the concrete were determined through Sorptivity Test (ASTM C1585-13). Test results were then analyzed to determine the relationship between the percent replacement of ceramic tile waste and their Initial and Secondary Sorptivity.

The concrete mix constituents were: type I Portland cement with a specific gravity of 3.15, gravel with a maximum size of 20 mm specific gravity of 2.52 and dry-rodded unit weight of 1554.77 kg/m^3, and river sand, fine ceramic tile aggregate (FCTA).

The ceramic tile waste was collected from renovation projects inside the campus. The ceramic tile wastes were crushed using a customized hammer mill from the Agricultural Mechanization Development Program (AMDP) part of the College of Engineering and Agro-Industrial Technology in the campus. Only those that pass through sieve No. 4 was used. Fig. 1 below shows the ceramic tile waste after being mechanically crushed.

Fig. 1. Crushed ceramic tile waste.

Standard ASTM methods were used to determine the properties of the crushed ceramic tile along with sand and gravel such as particle size distribution, fineness modulus, specific gravity, and dry-rodded unit weight. These properties of the fine aggregates are shown Table 1.

Table 1. Properties of varying amounts of FCTA mixed with sand.

Fine Aggregate	Fineness Modulus	Specific Gravity
0% FCTA + 100% Sand	2.46	2.47
10% FCTA + 90% Sand	2.53	2.45
20% FCTA + 80% Sand	2.65	2.43
30% FCTA + 70% Sand	2.58	2.41
40% FCTA + 60% Sand	2.65	2.39
50% FCTA + 50% Sand	2.88	2.37

Sieve analysis performed on the fine aggregate mixtures followed ASTM C136. US Standard Sieve Nos. 4, 10, 20, 40, 50, and 100 (4.75 to 0.150 mm) were used to determine the particle size distribution of the different fine aggregate mixtures and is shown in Fig. 2.

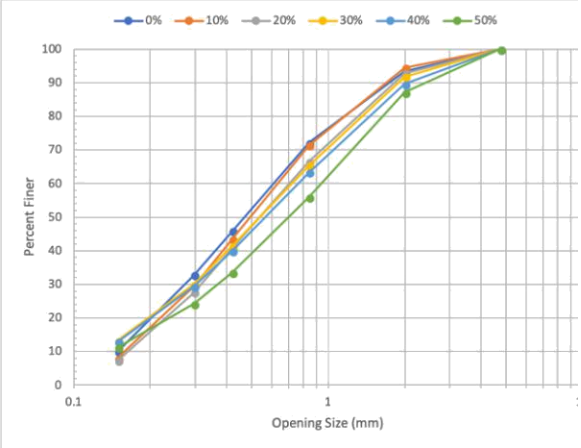

Fig 2. Particle size distributions of the varying amounts of FCTA with sand.

Using the ACI method 211, the measured properties of the cement and the aggregates, a desired slump of 80 – 100 mm, and a fixed w/c ratio of 0.5, the following mix designs shown in Table were constructed.

Table 2. Concrete mix proportioning (kg).

Mix ID	Cement	Water	Gravel	Sand	Ceramic
Control	400	200	1018	608	0
FCTA10	400	200	1006	553	61
FCTA20	400	200	988	501	125
FCTA30	400	200	998	428	183
FCTA40	400	200	988	370	247
FCTA50	400	200	952	323	323

The specimens were removed from the water tanks and blotted dry after the set curing period. A template was used to mark the base of the specimen as cutting planes (See Fig. 3).

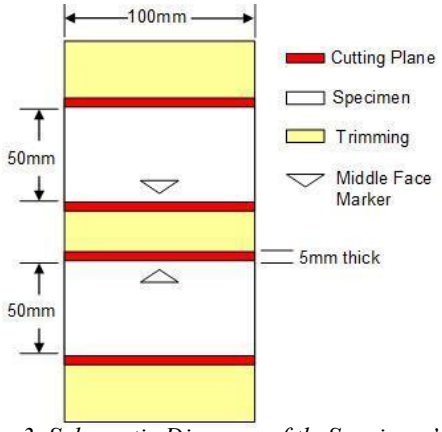

Fig. 3. Schematic Diagram of theSpecimen's cutting planes.

Specimens were labeled and the middle face (inner face) of the specimen will be noted. The hardened cylindrical specimens were then cut into disc samples having a height of 50 ±3 mm using a concrete cutter (Powercraft PCCM 400, China) (See Fig. 4).The disk samples obtained should have a diameter of 100 ± 6 mm and be cut to a thickness of 50 ±3 mm. The cut specimens will be checked for correct dimensions using the caliper and brushed clean.

Fig. 4. Specimen placed in concrete cutter before cutting.

Disk specimens were then placed in an oven at 50±2°C for 3 days. After three days the specimens were placed in plastic containers and sealed. Caution as to the specimen be not in contact with the walls of the container to allow circulation of air inside the container will be observed. The specimens were then allowed to cool and reach equilibrium moisture content inside the sealed container prior to testing (See Fig. 5).

The sorptivity experiment was performed in accordance with ASTM C1585-04. The specimens were removed from the sealed containers after conditioning. The specimen diameter and thickness were measured 4 times to the nearest 0.1mm and the average taken and recorded. The initial mass of the specimen were taken and recorded to the nearest 0.01g. The sides of the specimen were sealed with duct tape and the top with a plastic cover. The sealed mass of the specimen were recorded.

Fig. 5. Sealed disk specimens.

The specimen was placed inside the test set-up and the interior face was allowed to be in contact with 1mm to 3mm of water as shown in Fig. 6 & Fig. **7.** It should be noted that the water does not seep in from the sides of the specimens as this may affect the data obtained. The water was only allowed to enter the exposed bottom of the specimen to exhibit the capillary action of the water.

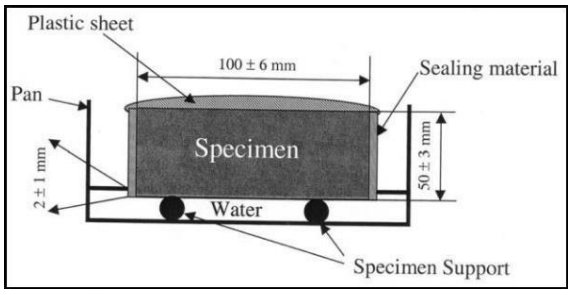

Fig. 6. Schematic Diagram of the Procedure. Source: ASTM C1585 (2004)

Fig. 7. Actual test set-up for sorptivity

Once the set-up is complete, the change in mass should be continuously observed. The increase in mass due to the capillary intake of water will be measured to 0.01g at regular time intervals as shown in Table 3, taken from ASTM C1585. Before each sample is weighed, the excess water from the exposed surface should be wiped off.

Table 3. Time intervals and Tolerances.

TIME	TOLERANCE
60s	± 2s
5min	± 10s
10min	± 2min
20min	± 2min
30min	± 2min
60min	± 2min
Hour 2	± 5min
Hour 3	± 5min
Hour 4	± 5min
Hour 5	± 5min
Hour 6	± 5min
Hour 24	± 2hrs
Hour 48	± 2hrs
Hour 72	± 2hrs
Day 4	± 2hrs
Day 5	± 2hrs
Day 6	± 2hrs
Day 7	± 2hrs

The absorption (I) of each specimen was computed at each time interval. Temperature was neglected for the purposes of the testing. Using equation 1, the absorption I in (mm) was computed, where △m is the weight gain of the specimen in (g), A is the area of the exposed surface in (mm2) and is the density of water (0.001 g/mm^3).

$$I = \frac{\Delta m}{(A)(\rho)} \qquad (1)$$

Using least squares linear regression analysis, the rate of absorption or Sorptivity was computed for, as the slope of the best fit line to the absorption (I) plotted against the square root of time (sec$^{0.5}$). Initial Sorptivity was the first slope observed with a coefficient of correlation of at least 0.98. This usually occurs from time zero to hour 6. The Secondary Sorptivity occured at the start of a change in slope with a coefficient of correlation of at least 0.98. This is usually measured from hour 24 to day 7. The average Initial and Secondary Sorptivity per mix design was determined. Any outlier data points from the Sorptivity test were determined by using the Inter Quartile Range (IQR) method and removed from the

statistical analysis. One-way Analysis of Variance (ANOVA) was then performed to determine the significance of the varying results for the Initial and Secondary Sorptivity. The one-way ANOVA that was performed on Sorptivity Test had a level of significance of 0.05 and a level of confidence of 95%.

Results

The results of the Sorptivity test are summarized in Table 4 & Table 5. It should be noted that the Initial and Secondary values were computed by determining the best fit line of the slopes from plotting the absorption (*I*) against the square root of the time in seconds ($\sqrt{s}$) whose cross-sectional areas and lengths were known.

Table 4. Average Initial Sorptivity at varying percent replacement.

Mix ID	Initial Sorptivity ($1x10^{-4}$ mm/sec$^{0.5}$)
Control	82.18
FCTA10	95.63
FCTA20	85.63
FCTA30	81.56
FCTA40	88.83
FCTA50	102.86

Table 5. Average Secondary Sorptivity at varying percent replacement.

Mix ID	Secondary Sorptivity ($1x10^{-4}$ mm/sec$^{0.5}$)
Control	23.59
FCTA10	25.34
FCTA20	24.99
FCTA30	22.56
FCTA40	25.03
FCTA50	23.15

As shown both tables, given the same order of magnitude the values do not drastically change. In the Table 4, the highest Initial Sorptivty value was given by the FCTA50 group (102.68 x 10^{-4} mm/sec$^{0.5}$) which was a 25.1% increase from the control. The lowest Initial Sorptivity value was given by the FCTA30 group (81.56 x 10^{-4} mm/sec$^{0.5}$) which showed a 0.75% decrease from the control. In Table 5, the highest Secondary Sorptivity was given by FCTA10 group (25.34 x 10^{-4} mm/sec$^{0.5}$) which was a 7.4% increase from the control. The lowest Secondary Sorptivity value was given by the FCTA30 group (22.56 x 10-4 mm/sec0.5) which was a 4.4% decrease from the control.

The One-way ANOVA performed on the Initial Sorptivity results yielded a P-value of 0.0131 which is less than the level of significance, 0.05, indicating that there is a significant difference between the means of the different groups. Through Post Hoc analysis, Tukey HSD Test was performed to determine the group with a significant difference. The group found to have a significant difference from the control was the FCTA 50 group.

The One-way ANOVA performed on the Secondary Sorptivity results yielded a P-value of 0.0802 which is greater than the level of significance, 0.05, indicating that there is no significant difference between the means of the different groups.

Therefore, the Initial Sorptivity performance of concrete with FCTA and the Secondary Sorptivity at any of the replacement levels considered is comparable to that of the control concrete. This result could be due to the similarity in properties of the FCTA and sand as shown in Table 1 and Fig. 2.

Conclusions

Concrete with a water-to-cement ratio of 0.5 and was cured at 28 days with FCTA (up to 40% replacement of sand by mass) performed similarly with the control concrete specimens in terms of Initial Sorptivity. While FCTA (up to 50% replacement of sand by mass) performed similarly with the control concrete specimen in terms of Secondary Sorptivity. This similar performance in terms of Sorptivity could be due to the similarity in the physical properties of sand and FCTA.

References:

[1] Cement Sustainability Initiative (CSI). Recycling Concrete (2009)

[2] European Ready Mixed Concrete Organization (ERMCO). Ready-Mixed Concrete Industry Statistics year (2016).

[3] United Nations Environment Programme (UNEP). Sand, Rarer Than One Thinks (2014).

[4] Department of Trade and Industry (DTI)/Board of Investments (BOI). Ceramic Tiles (2017).

[5] P. Zou, R. Hardy & R. Yang, (2014). Building and construction waste materials: REDUCE , REUSE AND RECYCLE - Opportunities and strategies for the Capital region. Canberra Business Chamber, 01(December), 88 (2014)

[6] M. Bennagen, G. NEPOMUCENO, & R. COVAR. Solid Waste Segregation and Recycling in metro Manila: Household Attitudes and Behavior (2002).

[7] N. Tanquerido & L Certeza, Ceramic Tile Wastes as Partial Substitution to Aggregates in Concrete Mix. De La Salle University Manila (2015).
[8] P. Ruedas, Investigation on the Compressive Strength of Concrete with High Percentage Replacement of Ceramic Tile Waste as Fine Aggregate. Undergraduate Thesis – Civil Engineering. University of the Philippines Los Baños, College, Laguna (2016).
[9] P. Awoyera, J. Ndambuki, J. Akinmusuru, & D. Omole, Characterization of ceramic waste aggregate concrete. HBRC Journal (2016).

Breakout Room #3
Advanced Functional Materials
Chairperson: Dr. Ho Viet Thang, DUT

Presentation No.	Title	Author	Page
AFM1.	Twin-Free α-Ga2O3 Films Grown by Mist CVD On (0001) - Al2O3 Substrates	R. Yamada, A. Kobayashi, K. Ueno, A. Sekiguchi, T. Onuma, T. Honda, H. Fujioka, T. Yamaguchi	65
AFM2.	Physicochemical Properties of Chitosan-Acrylic Acid Hydrogel Prepared Using Atmospheric Pressure Plasma	Kathrina Lois Taaca, Eloise Prieto, Magdaleno Vasquez Jr.	66
AFM3.	Investigation of Fracture Behavior of Self-Healing Ceramics Using Acoustic Emission	Toyoki Agata, Koji Hasegawa, Masaki Hiratsuka, Tetsuro Yanaseko	68
AFM4.	Label-Free Electrochemical Immunosensor for Detection of Mycobacterium Tuberculosis Culture Filtrate Antigen	Resmond L. Reaño, Glenson R. Panghulan, Clydee Anne T. Hernandez, Joseph P. Ortenero, Jeffrey P. Tamayo	69

Twin-free α-Ga_2O_3 films grown by mist CVD on (0001) α-Al_2O_3 substrates

R. Yamada[1*], A. Kobayashi[2], K. Ueno[2], A. Sekiguchi[3]
T. Onuma[1], T. Honda[1], H. Fujioka[2], and T. Yamaguchi[1]**
[1]*Department of Electronic Engineering and Electronics, Graduate School of Engineering, Kogakuin University, Tokyo, Japan*
[2]*Institute of Industrial Science, The University of Tokyo, Tokyo, Japan*
[3]*Education Support Functions, Kogakuin University, Tokyo, Japan*
[*]E-mail: cm21057@ns.kogakuin.ac.jp, [**]E-mail: t-yamaguchi@cc.kogakuin.ac.jp

Abstract

Corundum structure gallium oxide (α-Ga_2O_3) has been attracted attention as a widegap semiconductor material for electrical and optical devices. The growth of α-Ga_2O_3 film is possible by mist chemical vapor deposition (mist CVD). In this study, suppression of twin formation by growth using N_2 gas that increased surface migration in the mist CVD growth of α-Ga_2O_3 was investigated.

Recently, corundum-structured gallium oxide (α-Ga_2O_3) has been attracting attention as a next primary material suitable for power electronics, etc. [1]. α-Ga_2O_3 films have been obtained by mist chemical vapor deposition (mist CVD) growth method [2]. However, a twin structure with 180° rotational domains is sometimes observed on (0001) α-Al_2O_3 substrate by mist CVD [3]. In contrast, twin-free growth of α-Ga_2O_3 was reported by HVPE [4]. In this study, we report on twin-free α-Ga_2O_3 films grown by mist CVD on (0001) α-Al_2O_3 substrates.

Ga_2O_3 thin films were grown for 1h by mist CVD on (0001) α-Al_2O_3 substrates. $Ga(C_5H_7O_2)_3$ was used as a source precursor. The precursor was first dissolved in deionized water to prepare a solution with precursor concentration of 0.05 mol/L, and 36% HCl was then added with a HCl concentration of 0.28 mol/L. The growth temperature was 500°C. The precursor solution was atomized by an ultrasonic transducer with a frequency of 2.4 MHz, and the aerosol was transferred to the substrate using either O_2 or N_2 as both carrier and dilution gases. X-ray diffraction (XRD) ϕ scan measurement was used to evaluate the crystal structure. Surface morphology was evaluated using scanning electron microscopy (SEM).

Figure 1 shows the results of the ϕ scan measurements for the 10-14 reflections of α-Ga_2O_3 in the sample grown using O_2 or N_2 gas. The results of ϕ scan measurements for those of α-Al_2O_3 substrate are also shown in this figure. It was found from this result that a twin-free α-Ga_2O_3 film was obtained when N_2 was used as carrier and dilution gases. Figure 2 shows surface SEM images of α-Ga_2O_3 grown using O_2 or N_2 gas. A larger grain size of α-Ga_2O_3 was obtained when N_2 gas was used. This result suggests that surface atom migration is enhanced when N_2 gas is used. The twin structure formation is expected to be correspondingly suppressed, because of the enhancement of surface atom migration.

References:

[1] X. Zhao *et al*., Semicond. Sci. Technol. **31**, 065010 (2016).
[2] D. Shinohara and S. Fujita, Jpn. J. Appl. Phys. **47**, 9 (2008).
[3] T. Ma *et al*., J. Semicond. **40**, 012804 (2019).
[4] Y. Oshima, *et al*., Appl. Phys. Express **8**, 055501 (2015).

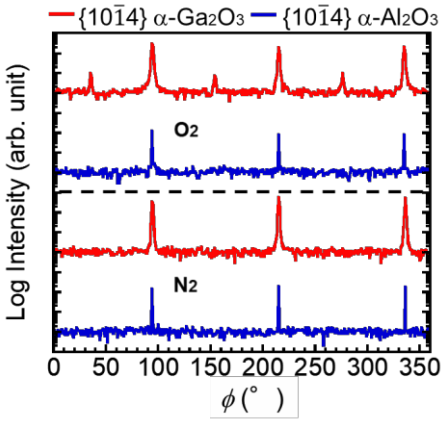

Fig. 1 XRD ϕ scan patterns for 10-14 diffraction for α-Ga_2O_3 grown using O_2 and N_2 gases. The patterns for α-Al_2O_3 is also shown.

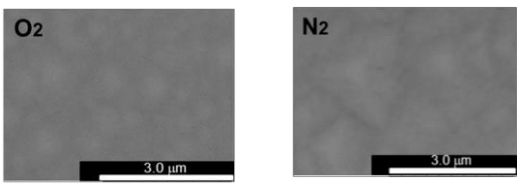

Fig. 2 Surface SEM images of α-Ga_2O_3 grown with either O_2 or N_2 gas.

Physicochemical properties of chitosan-acrylic acid hydrogel prepared using atmospheric pressure plasma

Kathrina Lois Taaca[1,2,] *, Eloise Prieto[3] and Magdaleno Vasquez Jr.[1]

[1] Department of Mining, Metallurgical and Materials Engineering, University of the Philippines-Diliman, Philippines
[2] Materials Science and Engineering Program, University of the Philippines-Diliman, Philippines
[3]National Institute of Molecular Biology and Biotechnology, University of the Philippines-Diliman Philippines
E-mail: kmtaaca@up.edu.ph

Abstract

In this work, chitosan-acrylic acid (Cs-AA) blends were formed into hydrogels wherein an atmospheric pressure plasma jet facilitated the process. Plasma-treated Cs-AA blends were created with air as the working gas and a 6 lpm as a fixed flow rate. The treatment time in this study was 2 min and 5 min. The physicochemical properties of the Cs-AA hydrogels were investigated in this study. Results showed lower yield was obtained for plasma-treated hydrogels due to the evaporation of water at longer treatment time. Moreover, increasing treatment time increases the temperature. This leads to forming a humid atmosphere that is conducive for RONS to occur. At longer treatment time, pH of the Cs-AA hydrogel blend decreases but the electrical conductivity increases. The evaporation and changes in the RONS concentration influenced the porosity as well as the swelling behavior of the plasma-treated Cs-AA hydrogel samples.

Introduction

Chitosan (Cs) and acrylic-acid (AA) blends have been routinely prepared as hydrogel products for biomedical applications. Most of the studies on Cs-AA hydrogels utilized chemical crosslinking techniques with glutaraldehyde, methylene bisacrylamide (MBA), and ethylene glycol dimethacrylate (EGDMA) as crosslinkers. This route creates a more stable and permanent hydrogel. However, one concern for this approach is the toxicity that may be present to the chemical crosslinkers. Radiation crosslinking can be an alternative method but the use of gamma or electron beam sources can be expensive and more hazardous where the high energy can result to homopolymerization or degradation of polymers. In this study, the use of an atmospheric pressure plasma (APP) jet to facilitate the synthesis of Cs-AA hydrogel was investigated.

Methodology

The Cs-AA hydrogel was synthesized by mixing Cs and AA in 2% acetic acid (HAc) solution. Cs solution was first prepared by completely dissolving 2.5 wt% Cs powder in the solvent. The monomer AA, with wt% coming from the 4:1 AA:Cs ratio was added to the Cs solution, followed by the addition of the ammonium persulfate (APS) initiator. After 2 hrs of mixing, the blend was sonicated for 5 min to remove excess bubbles. The Cs-AA mixture was then exposed to APP treatment with air as working gas for 2 min and 5 min. Fig. 1 shows the schematic diagram of the plasma-treatment of the Cs-AA blends. Post-treatment was done to remove excess monomer and dry the samples prior to characterizations.

The swelling behavior of the pristine and plasma-treated was measured using the tea-bag method. Initial weights of the Cs-AA hydrogels as well as the weight of the empty teabag was measured. The weight at each time interval was recorded. The temperature, pH, and electrical conductivity (EC) were also investigated in this study.

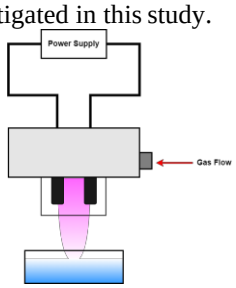

Fig. 1. The experimental schematic of the atmospheric pressure plasma treatment of Cs-AA mixtures.

Results and Discussion

The yield for each Cs-AA hydrogel was measured using the gel weight and the weight after the post-treatment. As shown in Fig. 2, there is a decrease in the yield when plasma treatment was included in the hydrogel synthesis. This may be due to the use of a closer gap distance when treating the samples.

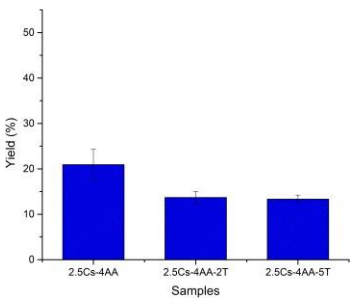

Fig. 2. Yield after the Hydrogel Process.

Physicochemical features like temperature, pH and EC were also evaluated. Fig. 3a shows that the use of longer treatment times increases the solution temperature. This, in turn, creates a more humid atmosphere that influences the concentration of reactive oxygen and nitrogen species (RONS). The possible change in the RONS concentration is manifested in the change in pH (Fig. 3a) and EC (Fig. 3b) where the decrease in pH may imply an increase in the H^+ concentration as well as other charged particles in the solution.

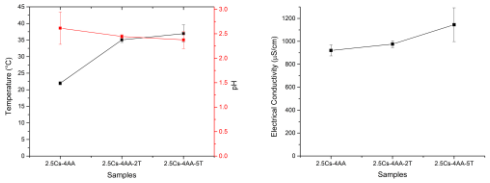

Fig. 3. Physicochemical features of Cs-AA hydrogels. (a) pH and temperature, and (b) electrical conductivity.

Given that pristine 2.5Cs-4AA hydrogels have a higher yield compared to the plasma-treated hydrogels, the weight measured in the pristine hydrogel may be attributed to the water weight. The excess water present in the pristine 2.5Cs-4AA samples could lead to the decreased presence of bubbles or air traps. This then results to lower porosity as illustrated in Fig. 4.

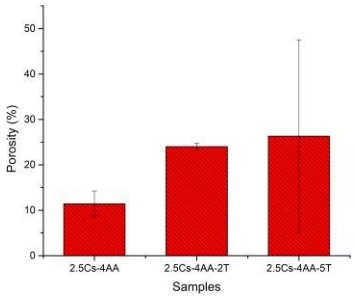

Fig. 4. Porosity of pristine and plasma-treated 2.5Cs-4AA hydrogel samples.

The swelling behavior of the pristine and plasma-treated 2.5Cs-4AA hydrogels is then influenced by the changes induced in their physicochemical features. As depicted in Fig. 5, 2.5Cs-4AA hydrogel treated for 5 min (2.5Cs-4AA-5T) showed the highest swelling capacity after 1 week of soaking in the PBS medium.

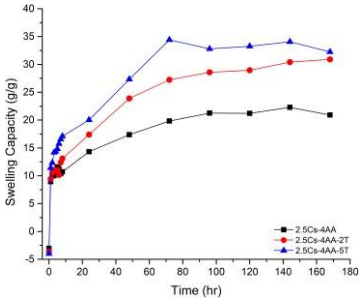

Fig. 5. Swelling behavior of pristine and plasma-treated 2.5Cs-4AA hydrogel samples in PBS medium.

Conclusion

This study showed that Cs-AA hydrogels can be synthesized using atmospheric pressure plasma treatment. Results revealed that the physicochemical properties of the hydrogel can be tailored depending on the operating parameters.

References:

[1] L. Yin, L. Fei, F. Cui, C. Tang, & C. Yin, *Biomaterials*, ***28***(6), 1258–1266.

[2] J. S. Oh, E. J. Szili, K. Ogawa, R. D. Short, M. Ito, H. Furuta, & A. Hatta, *Jpn J Appl Phys*, **57**(1).

Investigation of Fracture Behavior of Self-Healing Ceramics Using Acoustic Emission

Toyoki Agata[*1], Koji Hasegawa[*2], Masaki Hiratsuka[*2], Tetsuro Yanaseko[*2]

[*1] Graduate School of Engineering, Kogakuin University, Japan
[*2] Department of Mechanical Engineering, Kogakuin University, Japan
E-mail: am22002@ns.kogakuin.ac.jp

Abstract

Self-healing ceramics are heat-resistant materials with self-healing capabilities and are candidates for next-generation materials for jet engine turbine blades. Previous studies have shown that these ceramics are capable of complete strength recovery with sufficient healing time, but a detailed strength evaluation of the healed area has not been conducted. In this study, we investigated how the fracture behavior changes between incomplete and complete healing using a three-point bending test and the acoustic emission method.

Self-healing ceramics are self-healing materials in which the self-healing agents are encapsulated in the ceramics, when the ceramics are cracked, the agents are exposed to the atmosphere and initiate an oxidation reaction to fill the crack with the generated oxide, thereby achieving complete strength recovery [1]. Because of this property, applications such as jet engine turbine components have been proposed, however, since oxidation reactions are used, self-healing agents must be selected that are suitable for the operating ambient temperatures in each application. The selection of a self-healing agent depends on the volume expansion rate of the oxide to fill the crack, the healing time to complete self-healing, and the bonding strength between the oxidation product and the matrix phase. While some previous studies have been conducted on the volume expansion rate and healing time, the bonding strength of the oxidation products has not been fully evaluated.

In this study, the bonding strength between oxidation products and matrix by using acoustic emissions (AE) generated in strength evaluation tests of completely and incompletely healed SiC/Al_2O_3 composites, which are typical self-healing ceramics were evaluated. $SiC30Vol.\%/Al_2O_3$ composites, which showed complete strength recovery in the previous studies, were prepared. The fabricated composites were cut and polished to fabricate "smoothed" specimens. Next, “damaged” specimens with semi-elliptical cracks (crack length $2c$ = approx. 200 μm) were fabricated by pressing an indenter into the smooth specimen with a load of 2 kgf using a Vickers hardness tester. And the damaged specimens were heat-treated at 1100°C in air for 5 and 120 hours to fabricate incompletely healed (healed-5h) and completely healed (healed-120 h) specimens. These specimens were subjected to a three-point bending test, and a short-time Fourier transform was performed on the AE signals obtained during the bending test to perform a time-frequency analysis. Figure 1 shows the spectrum of the AE signal obtained during the three-point bending test of each specimen. The spectrum of the smooth specimen is broad up to around 400 kHz, whereas the spectrum of the damaged and the healed-5 h specimens move to the lower frequency side. This suggests that the energy required for crack propagation is reduced by the damage, resulting in a shift toward lower frequencies with lower energy. In contrast, spectrum of complete healing (healed-120 h) specimen again moves toward the high-frequency side, however, some peaks at a specific frequency compared to the smooth specimen. In the other specimens, the cracks propagate through the matrix, whereas in the fully healed specimen, the cracks propagate healed section, which have created specific peaks. These results suggest that the AE method can be used to evaluate the details of fracture behavior of healed sections.

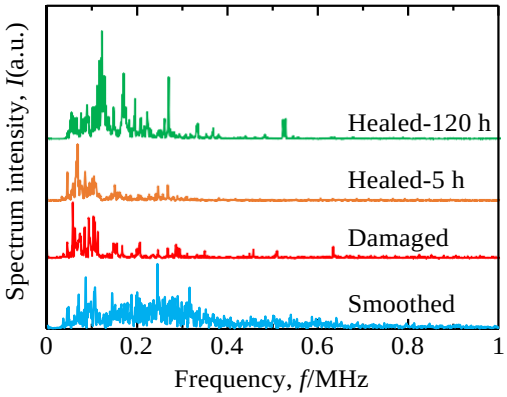

Fig. 1 Spectra of AE signal obtained during 3-point bending test of each specimen.

References:

[1] K. Ando, K. Takahashi, N. Murase, S. Sato, *Journal of High Pressure Institute of Japan*, Vol.41, No.6 (2003), pp.316-326 (In Japanese).
[2] T. Osada, T. Hara, M. Mitome, S. Ozaki, T. Abe, K. Kamoda, T. Ohmura, *Sci. Tech. Adv. Mat.*, Vol. 21, Issue 1 (2020), pp. 593-608.
[3] S. Yoshioka, W. Nakao, *J. Intell. Mat. Syst. Struct.*, Vol. 26, Issue 11 (2014).

Label-free electrochemical immunosensor for detection of *Mycobacterium tuberculosis* culture filtrate antigen

Resmond L. Reaño[1]*, Glenson R. Panghulan[1], Clydee Anne T. Hernandez[1], Joseph P. Ortenero[2], Jeffrey P. Tamayo[3]

[1]Department of Engineering Science, College of Engineering and Agro-Industrial Technology, University of the Philippines Los Baños, Laguna, Philippines
[2]Department of Chemical Engineering, Gokongwei College of Engineering, De La Salle University, Manila, Philippines
[3]National Institute of Molecular Biology and Biotechnology, University of the Philippines Los Baños, Laguna, Philippines
*E-mail: rlreano@up.edu.ph

Abstract

Label-free immunosensor using culture filtrate antigen (Ag) as a *Myctobacterium tuberculosis* biomarker has a strong potential for development of rapid detection and monitoring of tuberculosis. Sensitivity and specificity of monoclonal antibody (mAb) against TB culture filtrate antigen is validated using Enzyme-linked immunosorbent assay (ELISA). The mAb is immobilized passively on the surface of screen-printed carbon electrode (SPCE). The SPCE/mAb assembly is then tested using cyclic voltammetry (CV) and electrochemical impedance spectroscopy (EIS). Electrochemical responses at various Ag dilutions were also measured using CV and EIS. EIS offers a more sensitive technique than CV, showing a wider gap between measurements. Iron oxide nanoparticles (IONP) were added to the SPCE matrix, which resulted in an increase in CV measurements.

Mycobacterium tuberculosis (*M.Tb*.) is an ancient pathogen that has been persistent due to its complex survival strategies in the living host and the environment. It has developed a repertoire of culture filtrate antigens that change as the disease progresses[1,2]. These antigens are recognized by specific antibodies. Among these antigens include the LpqH, a 19 kDa *M.Tb.* lipoprotein.

There are several biosensing techniques available based on the strong affinity between an antibody and its target antigen, known as immunoassay and immunosensor.

An Immunosensor is a biosensor that uses antibody as a capture element, wherein such antibody forms a stable immunocomplex with the antigen, which results in generation of a measurable signal given by the transducer. In contrast, in an immunoassay the signal recognition from the Ag-Ab interaction takes place elsewhere[3].

Electrochemical biosensors offer advantages such as rapid, easy (sample processing and implementation), cost-effective, and sensitive (reces) detection method[4]. These biosensors can be applied in a wide range of fields such as medicine, food-industry, agriculture, and environmental monitoring[5].

Most electrochemical detection requires labels or probes to produce electrochemical signals. However, the use of solution-phase probes may result in lower detection efficiency due to the diffusion limit. It may also cause contamination especially for repetitive detections[6]. In a label-free approach, the attachment of the biomarker on the electrode's surface hinders electron transfer and results in a decrease in signal intensity. However, this method is more direct forward, easy to implement, quick and more desirable due to its simplicity[7].

Nanomaterials have been developed and incorporated in biosensors to improve the sensitivity and specificity of target detection[4]. Appropriate nanomaterials are key to improve the performance of an electrochemical biosensor. Most research focuses on the modification of the electrode's surface with nanomaterials to promote electron transfer, signal amplification, and decrease the limit of detection (LOD)[8]. Functionalized nanoparticles such as iron oxide (Fe_3O_4 or IONP) have been used in biosensing systems due to their biocompatibility, signal amplification, and ability to form covalent bond with Ab vis its functional group[7]. Electrochemical probes are modified with nanomaterials to increase the surface area and create a more favorable environment leading to excellent biocompatibility, higher conductivity and stability[4].

Cyclic voltammetry, differential pulse voltammetry, square wave voltammetry, chronoamperometry, and electrochemical impedance spectroscopy are typical electrochemical detection techniques. The main benefits of these techniques are their high sensitivity and specificity, rapid response, compactness, and portability. Nonetheless, they are affected by the working electrode and are temperature and environment sensitive[9].

Voltammetry is well-suited for rapid biosensors due to the ease with which printed electrodes and printed electronics can be integrated. Voltammetry is performed by applying a voltage to the working electrode. Current is then measured. Depending on the way the electric potential changes, various types of voltammetry exist[10].

Cyclic voltammetry (CV) is the most frequently reported electrochemical technique. The CV permits the characterization of reduction and oxidation

processes, such as intermediate steps or reaction reversibility[10]. The time-varying electric potential applied to the electrode increases linearly, then decreases. Since a molecule's electrochemical reaction is governed by the Nernst equation, temperature and concentration influence the outcome. Additionally, the scan rate is an essential variable. Increasing scan rates increases the measured current.

Electrochemical impedance spectroscopy (EIS), in contrast to voltammetry, is not based on varying the voltage, but rather on the frequency of the applied voltage[10]. The primary advantage of EIS biosensor is that antibodies do not need to be conjugated with an enzyme to provide the electrochemical signal.

In this study, monoclonal antibody (mAb) against *M.Tb.* culture filtrate antigen (Ag) – LpqH is immobilized on the surface of SPCE via direct spotting and passive adsorption.

Electrochemical impedance spectroscopy (EIS) and cyclic voltammetry (CV) are used to characterize and test the immunosensor.

Figure 1 shows the cyclic voltammogram at increasing voltage scan rate, performed on the bare electrode (SPCE).

The CV (Figure 2A) and EIS (Figure 2B) measurements show the decrease in current (or increase in resistance) upon immobilization of mAb on the surface of SPCE. The mAb-Ag interaction is also shown in Figure 2A using CV and Figure 2B using EIS. Figure 3 shows the increase in current measured after incorporating IONP on the SPCE/mAb matrix.

The electrical resistance of SPCE is expected to increase as the antibodies are adsorbed on its surface. Addition of metal nanoparticles such as IONP increases the electronic capacity of the assembly, resulting in an increase of measured current. Binding of antigen to the antibody passively adsorbed on the electrode's surface results in an increase in measured current, as shown in both CV and EIS. Possible explanations include the antigen providing electrons to the assembly, or its interaction with the antibody releases it from the SPCE's surface.

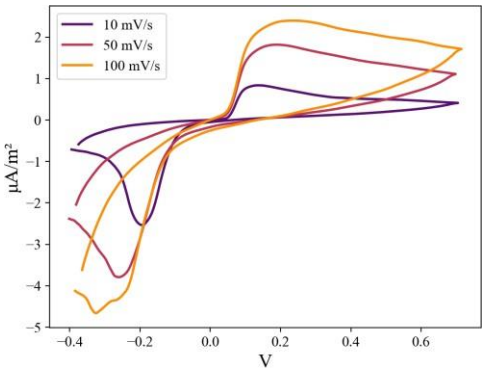

Fig. 1. Cyclic voltammogram of bare SPCE at various scan rates (10, 50, 100 mV/s)

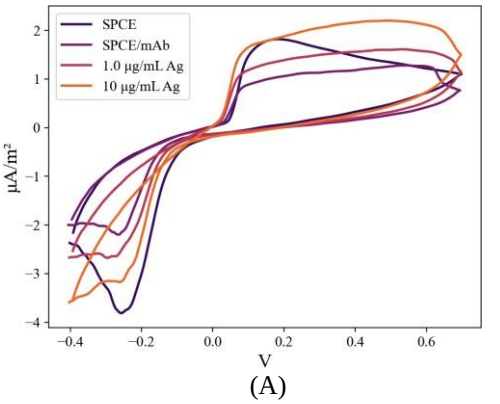

(A)

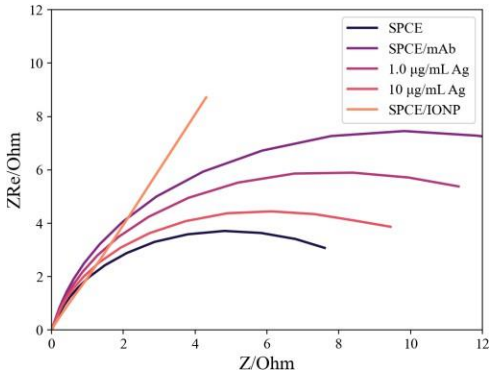

(B)

Fig. 2. Cyclic voltammogram (A) and Nyquist plot (B) of bare SPCE, SPCE/mAb, and SPCE/mAb-Ag of various dilutions (scan rate = 50 mV/s)

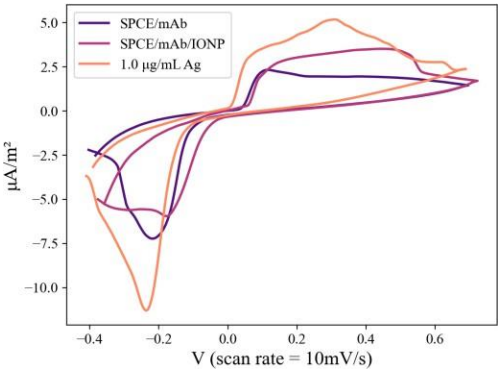

Fig. 3. Cyclic voltammogram showing the increase in measured current after incorporation of IONP on the SPCE/mAb assembly (scan rate = 10 mV/s)

Future directions include further improvement in the electrochemical immunosensor assembly. Covalent linking will produce more stable SPCE/mAb platform[11]. Use of more sensitive electrochemical techniques such as differential pulse voltammetry (DPV) can also be used. The use of hybrid organic and inorganic molecules to amplify the electrochemical signal can also be explored.

References:

[1] K M Samanich, M A Keen, V D Vissa, J S Spencer, J T Belisle, S Zolla-Pazner, S Laal, Clin. Diagn. Lab. Immunol., 7(4), 662-668 (2000).

[2] P Tucci, M Portela, C Rivas Chetto, G Gonzalez-Sapienza, M Marin, journal.pone.0221837 (2020).

[3] Mollarasouli, Kurbanoglu, Ozkan. Biosensors, 9(3), 86 (2019).

[4] B Wei, K Mao, N Liu, M Zhang, Z Yang, Biosens. Bioelectron., 121, 41–46 (2018).

[5] M Jafari, M Hasanzadeh, E Solhi, E, S Hassanpour, N Shadjou, A Mokhtarzadeh, A Jouyban, S Mahboob, Int. J. Biol. Macromol., 126, 1255–1265 (2019).

[6] H Zhong, C Zhao, J Chen, M Chen, T Luo, W Tang, J Liu, RSC Adv., 10(38), 22291-22296 (2020).

[7] M Emami, M Shamsipur, R Saber, R Irajirad, Analyst, 139(11), 2858-2866 (2014).

[8] M. Freitas, H Nouws, C Delerue-Matos, Electroanalysis, 31(1), 121-128 (2019).

[9] B Lou, Y Liu, M Shi, J Chen, K Li, Y Tan, L Chen, Y Wu, T Wang, X Liu, T Jiang, D Peng, Z Liu, TrAC Trends in Anal. Chem., 157, 116738 (2022).

[10] S Monteil, A Casson, S Jones, journal.pone.0258002 (2021).

[11] M Sharafeldin, K McCaffrey, J F Rusling, Analyst, 144(17), 5108-5116 (2019).

Breakout Room #4
Mechanical Engineering
Chairperson: Dr. Pham Anh Duc, DUT

Fabricating CuCr1Zr Parts by Using Laser Powder Bed Fusion Process – Simulation and Experimental Approach

Vi-Long Vo[1], Hong-Chuong Tran[1]*

[1]Department of Mechanical Engineering, Southern Taiwan University of Science and Technology, Tainan, Taiwan

* Email: tranhongchuong@stust.edu.tw

Abstract

Due to its excellent thermal and electric conductivity with considerable mechanical strength, CuCr1Zr copper alloy has strong potential in several high-end industry applications such as: induction coils, heat exchanger, electrical components. Additionally, these applications also require part with complex geometry which is hard for traditional manufacturing process to fabricate. Thus, using Laser Powder Bed Fusion (L-PBF) process to fabricate the complex CuCr1Zr part is consider as one of the most promising ways to apply CuCr1Zr material for high-end industrial application. However, processing CuCr1Zr by using L-PBF process is extremely difficult due to its high reflectivity at a common laser wavelength of 1064nm and its high thermal conduction. Accordingly, finding the optimal L-PBF processing conditions for producing fully dense copper alloys using experimental trial and error approaches is expensive and time consuming. In an effort to address this challenge, in this work, we construct a multi-physics simulation to investigate the effect of processing conditions on the stability of single scan track. The processing conditions of laser power, scanning speed, hatching space and layer thickness that lead to the smooth single scan track and surface scanning will be utilized for producing 3D parts. Accordingly, the density and mechanical property of fabricated parts is measured to verify the prediction from experiment. By using the predicted parameters to fabricate the 3D parts, the maximum density of fabricated parts is 99.98%, Yield Strength is 185.2 MPa, Ultimate Tensile Strength is 235.6 MPa and Elongation is 60.45%.

Keywords: Copper alloys, Laser Powder Bed Fusion Process, Computational Fluid Dynamic (CFD).

Fundamental study on nondestructive estimation of three-dimensional creep strain using surface displacement

Satoshi Fujii[1], Ryota Iwasawa[1], and Masaru Ogawa[1]

[1]Mechanical Engineering Program in the Graduate School of Engineering, Kogakuin University
1-24-2, Nishishinjuku, Shinjuku-ku, Tokyo 163-8677, Japan
E-mail: am22054@ns.kogakuin.ac.jp

Abstract

This study proposes an inverse problem method for the non-destructive evaluation of larger creep strains in turbine rotor blades before crack initiation, and validates the principle by numerical analysis using a simple model. Numerical analysis was performed to evaluate the estimation accuracy of the proposed method. Consequently, the estimates converged to an exact value. This demonstrated the validity of the principles of the method.

Recently, turbine rotor blades for power generation have been able to withstand harsh environments of high temperature, pressure, and cycle rates in order to improve power generation efficiency. However, the risk of failure is relatively high, making it important to predict the remaining service life of blades.

A non-destructive evaluation method for creep strains using contour changes of a turbine blade before and after deformation has been proposed[1][2]. The effectiveness of the proposed method was demonstrated through numerical analysis using a relatively simple turbine blade model. However, this method assumes a linear relationship between creep strain and displacement differences. Therefore, relatively large creep strains could not be accurately estimated using this method.

This study proposes an inverse problem method that can be used to estimate large deformation problems with relatively large values of creep strain, and aims to demonstrate its effectiveness by numerical analysis using a simplified model.

In this method, the solution is not obtained in a single estimation but through iterative calculations. First, a large deformation analysis was performed where the estimated creep strain was input to the turbine model before deformation, and the difference between the resulting displacement difference and the actual displacement difference of the blade was determined. Next, the creep strains expressing the differences were estimated using inverse analysis. The estimated creep strains were then updated. The solution was obtained by repeating this procedure until convergence was achieved.

To validate the principle of the method, a simple FEM model was used to evaluate its accuracy. The model was an unconstrained flat plate 700 mm long, 200 mm wide and 10 mm thick, with a Young's modulus of 207 GPa and Poisson's ratio of 0.3, with 99 nodes and 40 elements. The creep strains of 0.04 in the y direction in element numbers 1 and 6 of the model were considered as exact. The displacement differences were assumed to be measured at the two nodes at x = 10 mm, y = 700 mm, z = 0 mm, and z = 200 mm. It was assumed that u_x and u_y were measured at each node.

Figure 1 shows the estimated creep strain obtained from the iterative calculations. The figure shows that as the number of iterations increase, the correct value is approached and eventually converges.

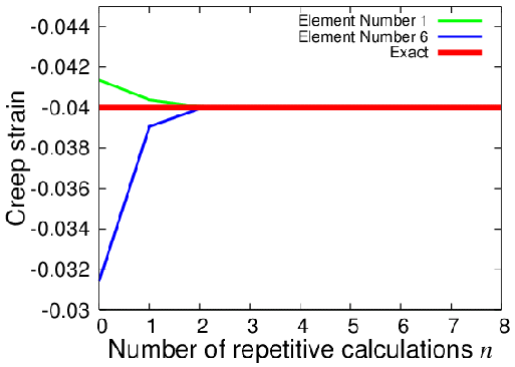

Fig. 1. Exact and estimated creep strains

In conclusion, an inverse problem method was investigated to estimate the three-dimensional creep strain distribution from the displacement difference before and after deformation for large deformation problems. Numerical analyses were performed to evaluate the accuracy of this method. The result confirmed that the method converged to the correct solution, thereby demonstrating the validity of the principle of this method.

References:

[1] M. Ogawa, T. Inohara, K. Hatano, and H. Nakamura, Proposal of a non-destructive evaluation method of inelastic strain based on the eigen-strain theory for turbine blades, *Proceedings of the Annual Meeting of Kanto Branch, JSME*, (2018), OS0715.

[2] F. Fukushima, M. Ogawa, T. Inohara, K. Hatano, and H. Nakamura, Proposal of Inelastic Strain Estimation Method for Turbine Driving Blade Using Displacement Information, *Proceedings of JSME M&M2019 Conference on Mechanics of Materials*, (2019), PS21.

A Numerical Study on the Motion of a Moored Semisubmersible in Irregular Waves

Thua T. Nguyen, Long T. Phan*, and Thai Q. Pham

Department of TRANSPORTATION MECHANICAL ENGINEERING, The University of Danang - University of Science and Technology, Vietnam
E-mail: ntthua@dut.udn.vn

Abstract

This research aims to evaluate the motion characteristics of a semisubmersible that is moored in both regular waves and irregular waves. The 6-DOF motion responses and tensions of mooring cables have been investigated using the 3D panel method in Ansys Aqwa software. Pierson-Moskowitz wave spectrum has opted for the environmental load acting on the vehicle. The results of numerical simulation are verified with those of experiment data in both frequency domain and time domain in regular waves. The motion responses of the semisubmersible and the cable tensions in irregular waves of sea state 5 and sea state 6 are then evaluated.

INTRODUCTION

Floating structures have been widely used to exploit oil resources in sea areas because of their mobility and well-drilling capacity. A number of studies have been done for investigating the behaviors of the semisubmersible with mooring lines. Günther et.al. investigated the heave, pitch, and roll motions as well as air gap of the semisubmersible in extreme seas by numerical method and experiment study [1]. The maximum responses of the platform in the frequency domain were also predicted. In addition, the influence of the mooring line pattern on the surge and sway motion of a semisubmersible was analyzed by Hadi et. al. [2]. The motion responses had been exposed to wave directions of 0, 45, and 90 degrees for various types of mooring systems using numerical analysis. Regarding the failure of the mooring line, Chenglin et. al performed the time-domain analysis of the semisubmersible wind turbine under both aerodynamics and mooring nonlinear dynamics model [3]. The results showed that the cable failure has less effect on the heave and roll motion of the platform, but it has a significant effect on the surge motion. Furthermore, the wave-induced motions and steady wave drift forces acting on the ship in oblique waves were conducted numerically in the time domain by the Rankine panel method [4]. The motion responses of the oil tanker at zero speed and the container ship at a forward speed were verified with the published experimental data. The favorable agreement proved that the panel method gave a reasonable accuracy in the seakeeping assessment. Yu-Hsien and Cheng-Hao implemented the hydrodynamic analysis of the semisubmersible floating platform based on the potential flow theory [5]. The hydrodynamic and diffraction analysis of the structure in the frequency domain was first performed. The obtained results were then transformed to the time domain by the Cummins equation. It was proved that the hydrodynamics acting on the semisubmersible are in good agreement with the ones by the WAMIT. In the view of experimental study, Sheng et. al performed model tests to obtain the dynamics of the moored semisubmersible irregular waves [6]. The effects of the side-mooring lines on the platform and mooring tensions were evaluated in beam and quartering seas. The experimental data goes along with the numerical results obtained from the 3D panel method. Also, Constantine et. al. carried out the model experiment of the semisubmersible of combined wind/wave energy [7]. Experimental data of the structure motion and cable tensions in both regular waves and irregular waves were similar to numerical results obtained from the panel method in Simo/Riflex software. The hydrodynamic characteristics of a three-column semisubmersible platform were investigated by a series of model tests in irregular waves [8]. Numerical simulation in the frequency domain was implemented as well. The experiment results showed that the low-frequency pitch motions were relatively small but high-frequency components in the airgap response much stronger responses for the extreme wave run-up appear at the higher frequency range.

In this paper, the responses of the moored semisubmersible in both regular waves and irregular waves are analyzed for assessing the motion characteristics and cable tensions in harsh weather conditions. The structure motion in regular waves is first calculated and compared with the experimental results. Dynamical behaviors of the semisubmersible and mooring line systems in irregular waves are then investigated through the integration of the body responses in the frequency domain by time.

THEORY BACKGROUND

A right-handed orthogonal coordinate system $Ox_by_bz_b$ is used to describe to the mean position of the vehicle. The origin is located in the horizontal plane of the undisturbed free surface with the z-axis pointing upward through the center of gravity of the ship and the x-axis pointing toward the bow. Fig. 1 shows the employed coordinate system in which the translational displacements in the x, y, and z directions are surge, sway, heave and the angular displacements of rotational motion about the x, y, and z axes are roll, pitch, yaw, respectively. The displacements of the vehicle are defined as follows,

$$\vec{X} = \begin{bmatrix} x & y & z & \phi & \theta & \psi \end{bmatrix}^T \quad (1)$$

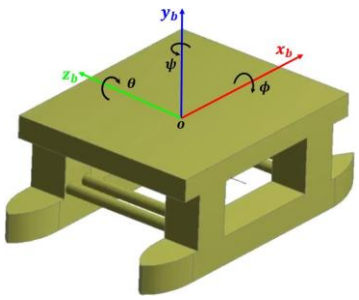

Fig.1 Coordinate systems and symbols

Considering oscillation of a platform due to wave impact loads and mooring line forces, the motion equations of the structure are expressed by [9],

$$(M + A_w)\ddot{X}(t) + B\dot{X}(t) + CX(t) = F_w(t) + F_{moored}(t) \quad (2)$$

where M, A_w, B, and C are the inertial mass matrix of the platform, added mass, total damping, and stiffness matrices, respectively. F_w and F_{moored} are total wave forces and mooring load vectors acting on the platform. ω is the frequency of incident waves.

The potential flow method is opted for simulating the seakeeping performance of the floating structure because of its efficiency in time and accuracy. Governing equations and boundary conditions of the method are described as follows:

+ Laplace equation in the fluid domain Ω:

$$\frac{\partial^2\varphi}{\partial x^2} + \frac{\partial^2\varphi}{\partial y^2} + \frac{\partial^2\varphi}{\partial z^2} = 0 \quad (2)$$

+ Boundary conditions on free water surface z=0:

$$-\omega^2\varphi + g\frac{\partial\varphi}{\partial z} = 0 \quad (3)$$

+ Body surface conditions:

$$\frac{\partial\varphi_r}{\partial n} = -i\omega\dot{h}\ ;\ \frac{\partial\varphi_d}{\partial n} = -\frac{\partial\varphi_I}{\partial n} \quad (4)$$

+ On the bottom of water area:

$$\frac{\partial\varphi}{\partial z} = 0 \quad (5)$$

+ Potential velocity is zero at the farfield area.

Considering fluid flow around the hull, potential velocity consists of three components due to incident wave φ_I, diffracted wave φ_D, and radiation wave φ_{rj}, such as:

$$\Phi(\vec{X}, t) = A\varphi\left(\vec{X}\right)e^{-i\omega t} \quad (6)$$
$$\varphi\left(\vec{X}\right)e^{-i\omega t} = \left(\varphi_I + \varphi_d\right) + \sum_{j=1}^{6}\varphi_{rj}\dot{x}_j e^{-i\omega t}$$

The potential velocities of diffraction and radiation waves can be determined from the Green function. The first-order hydrodynamic pressure, *p*, is then

$$p = i\omega\rho\varphi(x)e^{-i\omega t} \quad (7)$$

$$F_{Ij} = -\rho\int_{S_0} i\omega\varphi_I(x)n_j dS \quad (8)$$

$$F_{dj} = -i\omega\rho\int_{S_0}\varphi_d(x)\,n_j dS \quad (9)$$

$$F_{rjk} = -i\omega\rho\int_{S_0}\varphi_{rk}(x)\,n_j dS \quad (10)$$

where S_0 is the mean wetted surface of the ship.

Finally, the ship response in the frequency domain can be achieved by solving the following equation,

$$\left[x_{jm}\right] = H\left[F_j\right] \quad (11)$$
$$H = \left\{-\omega^2\left(M_{jk} + A_{jk}\right) - i\omega B_{jk} + C_{jk}\right\}^{-1} \quad (12)$$

A time history of the RAO-based position and acceleration can be constructed by combining RAOs at a series of frequencies with the wave spectrum as follows:

$$X_{RAO}(t) = \sum_{m=1}^{N_w}\sum_{j=1}^{N_d}\mathrm{Re}\left\{a_{jm}x\left(\omega_{jm},\beta_m\right)e^{\,j\left(k_{jm}X_G\cos\chi + k_{jm}Y_G\sin\chi - \omega_{jm}t + \alpha_m\right)}\right\} \quad (13)$$

$$\ddot{X}_{RAO}(t) = \sum_{m=1}^{N_w}\sum_{j=1}^{N_d}\mathrm{Re}\left\{-a_{jm}\omega_{jm}^2 x\left(\omega_{jm},\beta_m\right)e^{\,j\left(k_{jm}X_G\cos\chi + k_{jm}Y_G\sin\chi - \omega_{jm}t + \alpha_m\right)}\right\} \quad (14)$$

where $x(\omega_{jm},\beta_m)$ is the motion RAO at frequency ω_{jm} and relative wave direction $\beta_m = \chi_m - \theta_3(t)$.

For a semisubmersible working in stable condition, mooring line systems are used to connect with a fixed point in the seafloor. In this case, the structure is moored by four nonlinear catenary mooring lines as described in Fig. 5. Each mooring line is divided into a number of finite elements and the mass of each element is distributed on the corresponding node. S_j stands for the unstretched line length between the anchor and the j_{th} node, and D_e indicates the local segment diameter of one mooring cable. The properties of mooring lines are depicted in Table 2.

Each mooring line is modeled as a chain of Morison-type elements subjected to various external forces. The equation of motion for an arbitrary cable element is represented by (Newman, 2018) [10],

$$\frac{\partial T}{\partial S_e} + \frac{\partial V}{\partial S_e} + W + F_h = m\frac{\partial^2 R}{\partial t^2} \quad (15)$$

$$\frac{\partial M}{\partial S_e} + \frac{\partial R}{\partial S_e}\times V = -q$$

where *M* is the bending moment vector of the first element node, and *q* denotes the distributed moment load per unit length, *T* and *V* indicate the tension force and shear force vectors of the first element node, respectively, *R* is the position vector of the first node of the line element, ΔS_e and D_e are the length and diameter of a unstretched element, *W* and F_h denote the element weight and hydrodynamic load vectors

per unit element length respectively, *m* denotes the mass per unit length.

The bending moment and tension force are described as functions of bending stiffness *EI*, axial stiffness *EA* of the cable material, the strain of the line ε, and the position vector, such as:

$$M = EI\frac{\partial R}{\partial S}_e \times \frac{\partial^2 R}{\partial S^2}_e \qquad (16)$$
$$T = EA\chi\varepsilon$$

For ensuring a unique solution to the equation of cable motion, the pinned connection boundaries are set at the top and bottom ends:

$$R(0) = P_{bot}, R(L) = P_{top}$$
$$\frac{\partial^2 R(0)}{\partial S^2}_e = 0, \frac{\partial^2 R(L)}{\partial S_e^2} = 0 \qquad (17)$$

where P_{bot} and P_{top} are the locations of the attachment points, and L is the total unstretched length of the cable.

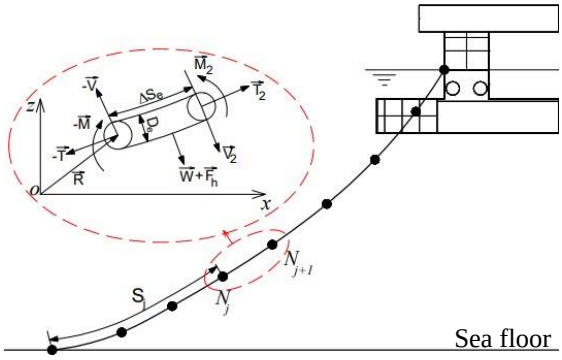

Fig. 5 Dynamic model of mooring lines

NUMERICAL SIMULATION

A semi-submersible model with mooring lines in irregular waves is analyzed to obtain the dynamic behaviors in random waves. Fig. 2 illustrates the geometry of the structure, and the main parameters of the structure are summarized in Table 1. The definition of wave directions in the coordinate system fixed to the platform is shown in Fig. 3. In order to investigate the motion response of the semi-submersible under irregular waves, Pierson-Moskowitz wave spectrum in sea state 5 and sea state 6 are chosen as shown in Fig. 4. Based on the relative position between the wave and structure, the wave direction μ is defined. Wave frequency is selected from the wave spectrum where the wave energy has a significant value and is suitable for the operating conditions of the platform. In this case, the wave frequency in the range from 0.2 to 2.5 rad/s are chosen.

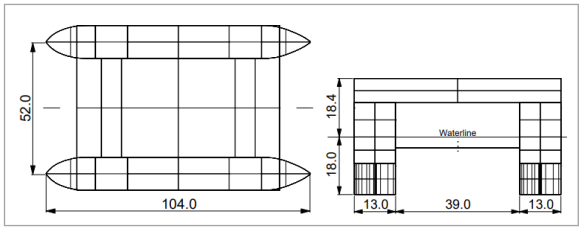

Fig. 2 Geometry diagram of semisubmersible

Item	Value	Unit
Length overall, L_{OA}	104.0	m
Beam overall, B	65.0	m
Draft, T	18.0	m
Separation distance, S	52.0	m
Displacement, Δ	31636	T
Center of gravity, (x_G,y_G, z_G)	(-0.64, 0.0, -3.8)	m
Radius of gyration, (k_{xx}, k_{yy}, k_{zz})	(27.3, 31.2, 31.2)	m
Metacentric height, GM_T	7.45	m
Water depth, d	108.0	m

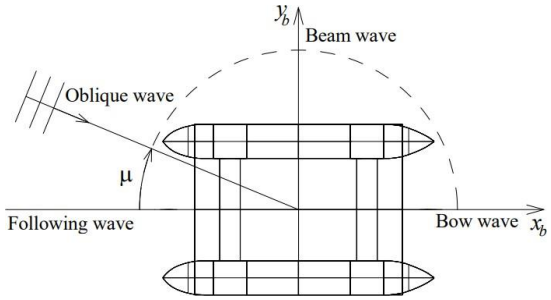

Fig. 3 Definition of wave direction

For nonlinear catenary mooring line, the dynamics of the cable are involved the influence of cable mass, drag forces, inline elastic tension, and bending moment. The cable properties for modeling this kind of mooring line are shown in Table 2.

Table 2. Catenary properties

Item	Value	Unit
Line length	453.6	m
Mass/Unit length	128	kg/m
Stiffness, EA	7.0E+08	N
Maximum tension	2.5E+06	N
Diameter	0.08	m

The motion characteristics of the moored platform in irregular waves is numerically studied using Ansys AQWA 19.2 software. The computational model is divided into 19221 elements in which there are 9007 diffracted elements, as shown in Fig. 3. The ship responses in the frequency domain are simulated through the hydrodynamic diffraction approach. The obtained results are then applied for simulating the ship motion in irregular waves in time domain.

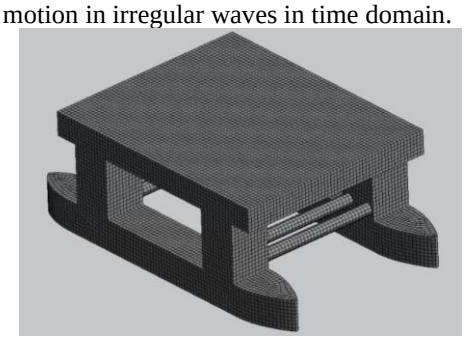

Fig. 5 Generated meshing on the semisubmersible

RESULTS AND DISCUSSION

To verify the accuracy of the simulation method, a comparison of semisubmersible motion between the current study and experimental results by Hong, et. al. was conducted in both frequency domain and time domain of regular waves. Figs. 5 and 6 show the comparison of RAO (Response Amplitude Operators) values of the structure in cases of the head sea and beam sea, respectively. It can be observed that the present simulation is matched well with those of experiment results in sway, heave, and pitch motion. A slight difference in surge and roll motion may be caused by ignorance of water viscosity. In addition, the surge, heave, and pitch motion at a frequency of 0,525 rad/s in the time domain are also compared with the experimental data by Sa et.al [11], Fig. 7. It is seen that the heave and pitch responses are in good agreement with the experiment results but there is a difference at peak values in surge motion and roll motion between the current simulation and the experimental results. These demonstrate that the current numerical method is suitable for predicting the seakeeping performance of the semisubmersible.

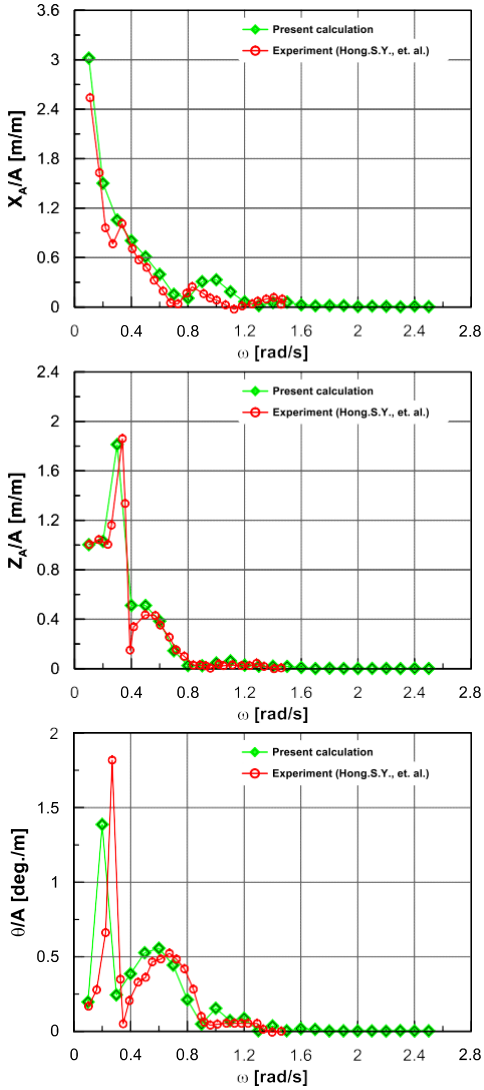

Fig. 5 Comparison of the surge, heave, and pitch motion, μ=180°, ω=0.525 rad/s

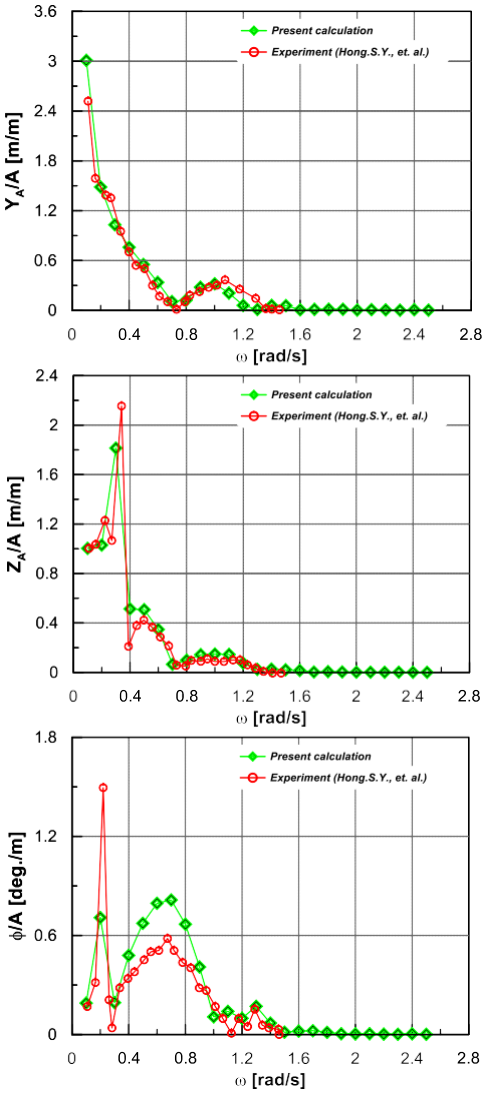

Fig. 6 Comparison of sway, heave, roll motion of semisubmersible in beam sea conditions with the experimental results

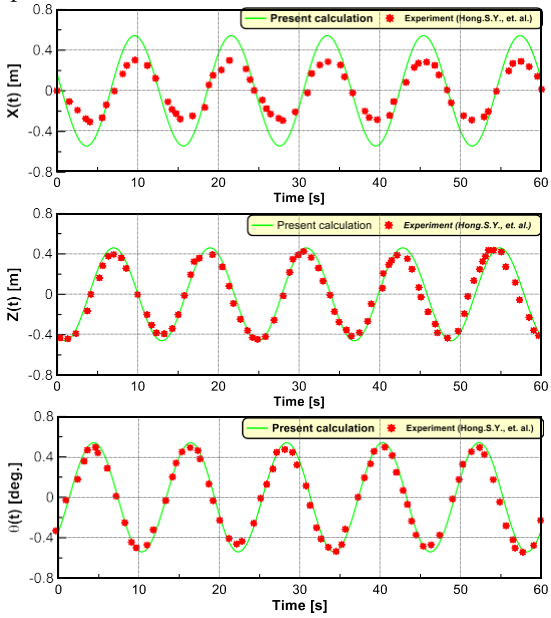

Fig. 7 Comparison of the surge, heave, and pitch motion, μ=180°, ω=0.525 rad/s.

In this part, the motion responses of the platform in the head sea and beam sea conditions are investigated in the two load cases, as shown in Fig. 8. The time responses in irregular waves are calculated from the corresponding RAO values of the structure at various frequencies. It is clearly found that the angular displacements occupy small values in both load cases. However, surge, sway, and heave motions are significantly enlarged when the platform is moored in sea state 6. For the structure acceleration, it can be seen that irregular waves result in significant accelerations of the surge, sway and heave but the angular accelerations are well controlled.

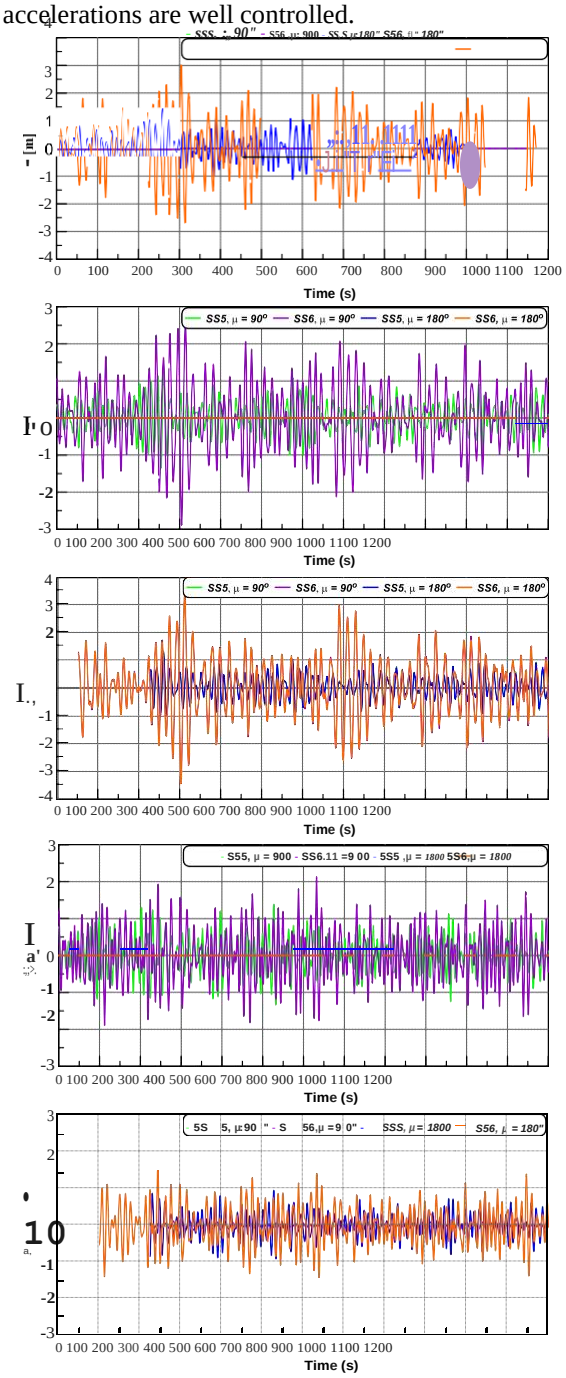

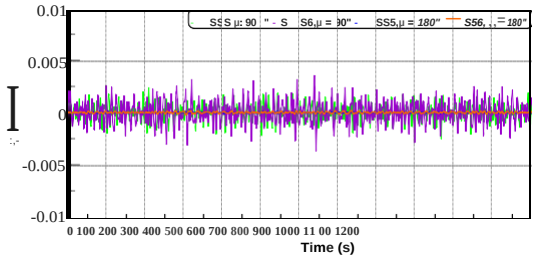

Fig. 8 Motion of the semisubmersible in irregular waves at sea state 5 and sea state 6

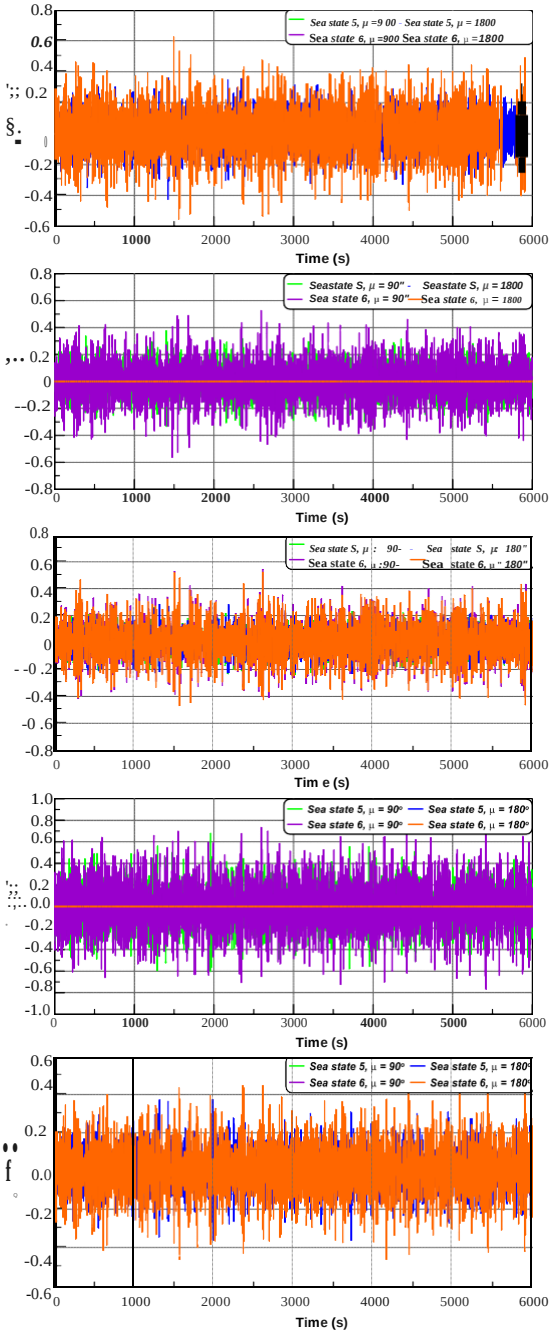

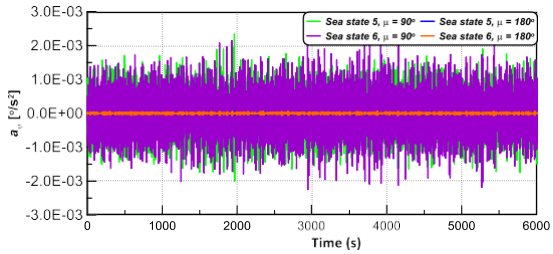

Fig. 9 Semisubmersible accelerations in irregular waves

Time histories of mooring tension at each cable are drawn in Fig. 10 to evaluate the cable extreme in harsh weather conditions. There is only a minor discrepancy for the tensions on the cables located on the same side of the structure. The tension force becomes extremely large in the case of sea state 6. A large-amplitude motion with time is observed in this case. However, the tension forces gain gradually as the irregular waves are in sea state 5.

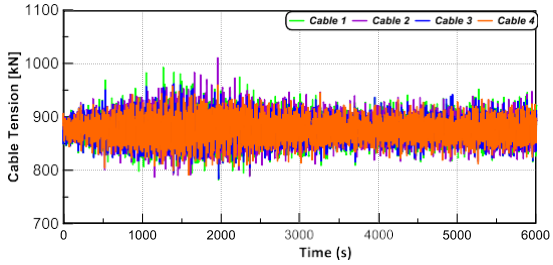

a. Sea state 5, μ =90°

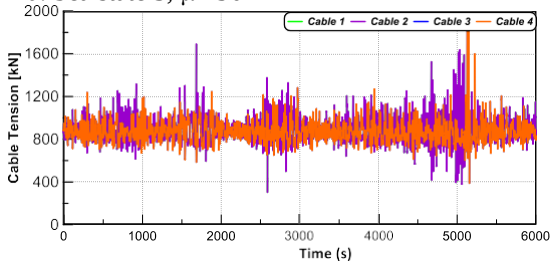

b. Sea state 6, μ =90°

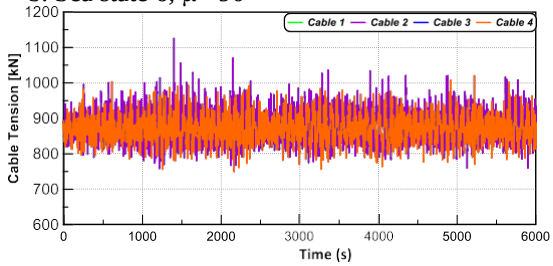

c. Sea state 5, μ =180°

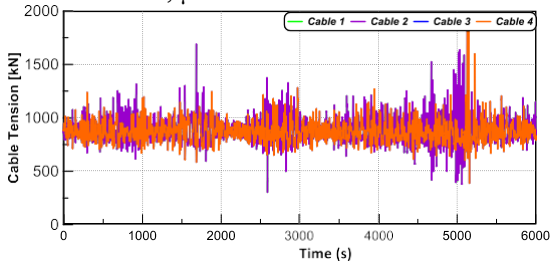

c. Sea state 6, μ =180°

Fig. 10 Cable tensions at sea state 5 and sea state 6

CONCLUSIONS

The responses of moored semisubmersible in regular waves are in good agreement with the experimental results. The discrepancies in peak values of surge and roll motions are found.

The irregular waves might result in significant translational responses of the moored semisubmersible in the head sea and beam sea conditions. However, the wave impacts on the rotational motions of the vehicle are relatively minor. Similar issues can be observed in the body accelerations.

Funding Statement

Fund funds this research for Science and Technology Development of the University of Danang under project number: [B2020-DN02-85].

References:

[1] F.C. Günther, S. Christian, S. Katja, "Time-domain investigation of a semisubmersible in rogue waves", OMAE'02, (2002) 1-8.

[2] S. Hadi, G. Hassan, A. Farhood, K. Saeid, "Effect of mooring lines pattern in a semi-submersible platform at surge and sway movements", Ocean Research, **2**(1) (2014) 17-22.

[3] Z. Chenglin, W. Shiming, X. Shuang, H. Jiao, G. Jian, T. Changfeng, "Effects of mooring line failure on the dynamic responses of a semisubmersible floating offshore wind turbine including gearbox dynamics analysis", Ocean Engineering, **245** (2022) 1-15

[4] Z. Wei, M. Ould, E.S. Thomas, "Numerical study on wave-induced motions and steady wave drift forces for ships in oblique waves", Ocean Engineering, **196** (2020) 1-13.

[5] L. Yu-Hsien, Y. Cheng-Hao, "Hydrodynamic simulation of the semi-submersible wind float by investigating mooring systems in irregular waves", Applied Sciences, **10** (2020) 1-26.

[6] X. Sheng, J. Chun-yan, C.G. Soares, "Experimental study on effect of side-mooring lines on dynamics of a catenary moored semi-submersible system", Engineering for Maritime Environment, **234** (1) (2020) 127-142.

[7] M. Constantine, G. Zhen, M. Torgeir, "Experimental study of the functionality of a semisubmersible wind turbine combined with flap-type Wave Energy Converters", Renewable Energy, **93** (2016) 675-690.

[8] L. Wenyue, Z. Xiantao, T. Xinliang, G. Xiaoxian, "Experimental study on the wave run-up and air-gap response of a three-column semi-submersible platform". Ocean Engineering, 203 (2020)

[9] Ansys, AQWA Reference Manual Release 2019 R2. Ansys Inc., Canonsburg, USA, 2019.

[10] J.N. Newman, "Marine hydrodynamics. MIT Press, 2018.

[11] H.Y. Sa, L.M. Pan, K.C. Yong, H.C. Do, "An experimental analysis on the motion response of a moored semi-submersible platform in regular waves", Ocean Engineering and Technology, **2** (1) (1988) 59-70.

Breakout Room #5

Mechanical Engineering

Chairperson: Dr. Vo Nhu Thanh, DUT

Aerodynamic performance of footballs with different complex panel surface geometries

Kaito Tada[1], Kazuya Seo[2] , Shinichiro Ito[2], and Masaki Hiratsuka[2]

[1]Department of Mechanical Engineering, Graduate School of Kogakuin University, Tokyo, Japan
E-mail: am21039@ns.kogakuin.ac.jp
[2] Department of Mechanical Engineering, Kogakuin University, Tokyo, Japan
E-mail: ito@cc.kogakuin.ac.jp

Abstract

The design of soccer balls continues to change at every World Cup. The difference in panel shape has a great effect on the aerodynamic characteristics that affect the trajectory of the ball. In this study, the fluid force of 14 soccer balls with different panel patterns was measured by wind tunnel tests. The drag crises with different Reynolds numbers were confirmed depending on the panel shape. To understand this, the shapes of panel grooves were measured and the relationship between them was investigated. The flow separation point was also visualized by the oil film method and the particle image velocimetry (PIV) analysis.. The flow separation points were found to be almost the same position in the subcritical and supercritical state and to be partly different around the Reynolds number of drag crisis.

1 Introducton

The difference in panel shape will have a major influence on the aerodynamic characteristics that affect ball trajectory. The patterns of recent soccer balls are greatly different from that of the conventional soccer ball, with several changes being made to the shape and design of the surface of the ball. Various aerodynamic studies on soccer balls have been reported. Goff et al.[1] reported the aerodynamic difference of non-spinning several soccer balls by the different panel shapes. Hong et al. [2] showed that the separation point changed depending on the number of seams by a 2D-particle image velocimetry (PIV) method. In this study, the different aerodynamic characteristics of the different panels of soccer balls was investigated, and the relationship between the groove shape and drag crisis phenomenon was confirmed. The 2D-PIV analysis was also conducted on the different orientations of balls, and the reason for the different aspects of the drag crisis by the different panels was investigated.

2 Method

In this study, experiments were conducted using 14 different types of soccer balls. Table1 shows all the footballs. It can be seen that the number of panels and the shape of the balls differ significantly. The diameter of all balls tested was 0.22 [m] and the air pressure was all set to 90 [kPa].

Table1 Balls used in the experiment and the experiment items

Name	Merlin	Telstar18	Krasava	Ordem	Finale	Vantaggio (Pimple)	NikeFlight
Design							
Fluid force	○	○	○	○	○	○	○
Groove measurement	○	○	○	○	○	○	○
2D-PIV	×	×	×	×	×	○	○
Name	Evopower	Delta	Jabulani	Tango12	Teamgeist	Vantaggio (Smooth)	Vantaggio (Dimple)
Design							
Fluid force	○	○	○	○	○	○	○
Groove measurement	○	○	○	○	○	○	○
2D-PIV	○	×	○	×	○	○	○

2.1 Fluid force experiment

Drag measurements were performed on 12 kinds of different soccer balls with a wind tunnel and a three-components load cell whose maximum load was 50.0 N on each component. The samplings were conducted at 1000 Hz for 9.0 seconds from a wind speed of 3 to 29 m/s in every 1 m/s under computer control, and the experimental values were averaged.

2.2 Groove shape measurement

The cross-sectional area and the dimensions of the groove were taken with a one-shot 3D-shape instrument by VR-3000, KEYENCE. The groove length in the panel joint of each ball was measured by putting strings in all grooves. The total groove volume was calculated by multiplying and summing the groove length and the same cross-sectional area.

2.3 2D-PIV measurement

The 2D-PIV measurement in the section of flow circumferential direction was performed to visualize the separation point on a subcritical, critical, and supercritical *Re* number on the four types of balls.

3 Result and Discussion

3.1 Fluid force experiment

Fig.1 shows the C_D diagram for each ball. Drag crisis is a phenomenon in which the drag coefficient drops off suddenly as the Reynolds number increases. The drag coefficients of balls changed rapidly from about 0.5 to 0.2 at a Reynolds number in the range of 1.0×10^5 and 2.4×10^5, as shown here. This corresponds to the flow aspect change around the ball from the laminar separation to the turbulent separation. In order to explain these phenomena, the drag crisis was defined as the Starting and the Ending Reynolds number. The Starting Reynolds number and the Ending one was lowest at 1.0×10^5 and 1.2×10^5, respectively, on the Evopower, and they were highest at 1.8×10^5 and 2.4×10^5, respectively, on the Jabulani. It was found that the flow around the Evopower turned into a turbulent flow on about 5 m/s. however, the flow around the Jabulani turned into a turbulent flow on about 12 m/s. We considered that the cause of these phenomena was the difference in the panel shape of the ball.

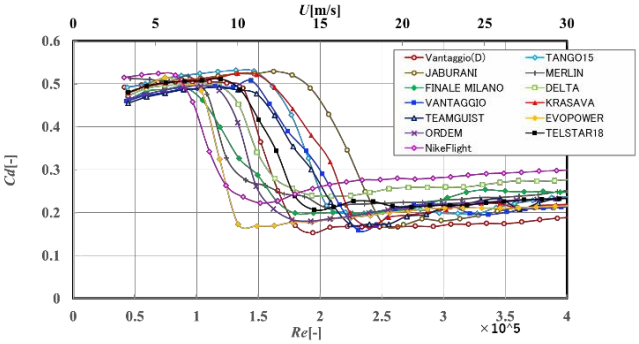

Fig.1 The C_D diagram of each ball

3.2 Groove shape measurement

The measurement results are shown in Fig.2. Balls with larger groove volumes, such as EvoPower and Nikeflight, have lower end Reynolds numbers than balls with smaller volumes, such as Jabulani. It has a tendency that the larger the groove volume is, the smaller the end-Reynolds number becomes. The correlation between the total volume and the End-Reynolds number was strongly correlated with -0.83.

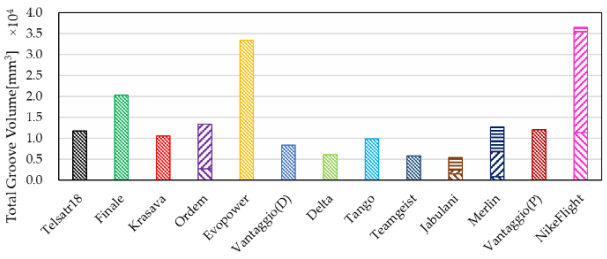

~~Fig.2 Total groove volume~~

3.3 2D-PIV measurement

Table2 shows the results of 2D-PIV measurements of the Evopower. The wind flows from left to right and the green line is the laser irradiation position. The separation point and wake direction are illustrated in each diagram. From left to right subcritical, critical and supercritical regions, where the separation point and wake are shown in each diagram. In the subcritical region, when the left part of the ball is defined as 0º from the ball centre, the separation occurred around 90º, the CD of the Reynolds number below 1.8×105 in Fig.1 is about 0.5, and the separation around 90º resulted in a larger wake flow width. In the supercritical region, on the other hand, a separation point was observed above 90º, and the CD was reduced to about 0.2 for Reynolds numbers above 2.9×105 in Fig.1. This is because the Reynolds number increased and the ball grooves stimulated the boundary layer, resulting in turbulent flow near the boundary layer. The separation point of the flow moved backwards and the turbulent width of the wake became narrower.

In the circumferential flow during the drag crisis, the position of the separation point and the flow direction of the wake depended on the orientation of the ball panel. It was found that during the drag crisis, laminar and turbulent detachments were mixed depending on the panel, and the flow around the ball was partially different.

Table2 The 2D-PIV Results of the Evopower

Panel Orientation & Laser position	Subcritical (5m/s) $Re=7.3\times10^4$	Critical (8m/s) $Re=1.2\times10^5$	Supercritical (15m/s) $Re=2.2\times10^5$
flow	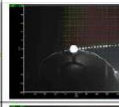	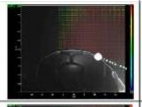	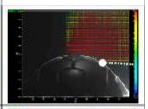
flow	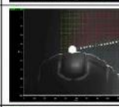	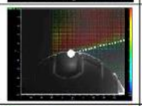	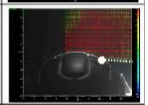
flow	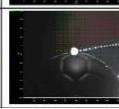	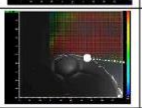	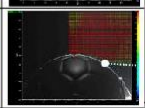

4 Conclusion

1. The total volume of the groove affects the Reynolds number at which the drag crisis occurs.
2. The panel groove affects the shape of the drag crisis.
3. The position of the flow separation point did not change in the subcritical and supercritical regions by the ball orientation. On the other hand, The aspect change of the drag crisis in panel difference causes the panel groove mixed with laminar and turbulent regions.

References

[1] Goff, J., Asai, T., Hong, S., J. Sports Eng. Technol, 228, 188–194 (2014).
[2] Hong, S., Asai, T., Seo, K., Procedia Eng.,112, 391–394 (2015).

Directional Control of Jets near a Boundary using Coander Secondary Flow

Hiroki Tezuka*, Minoru Nakagawa, Qiang Zhang, and Kotaro Sato

Mechanical Engineering Program in the Graduate School of Engineering, Kogakuin University, 2665-1 Nakano-cho, Hachioji, Tokyo 192-0046, Japan
E-mail: am22042@ns.kogakuin.ac.jp

Abstract

Focusing on the coanda effect of the jet, a fundamental study on the jet direction control near the wall surface is conducted experimentally. The continous jets, continuous suction flow, and synthetic jets is used as a secondary flow while the continous jets is used as a primary jet to discuss the effect of the secondary jet on the primary jet near a flat wall surface. The main result shows that the primary jet near a flat wall surface is attracted toward the wall surface due to the coanda effect when there is no secondary flow, but the direction of the jets in the presence of a secondary flow depends on the momentum ratio and vibration characteristics. Furthermore, under certain conditions, the primary jets is deflected toward the anti-wall surface.

For efficient thermal management, it is essential to elucidate the flow characteristics of the jet near the wall surface. Many discussions have been conducted and a certain amount of knowledge has already been obtained [1]-[4]. However, the effect of fluidic thrust vectoring near a plane wall is still unclear. In this study, we attempt to control the direction of the primary jets near a plane wall by using a secondary flow with a coanda surface. The steady continuous jet, steady continuous suction flow, and synthetic jet are used as a secondary flow.

In this experiment, the steady continuous jet was set as a primary jet. The primary jet was generated by a blower and fed through a plenum tank to the primary slot of the experimental machine. The secondary flow was generated by a blower and a speaker. The details of the experimental method and coordinate system refer to the references [1],[5].

Figure 1 shows the velocity distribution in a typical flow field for various secondary flows. Experimental conditions are $x_W/h_1 = 18.5$, $y_W/h_1 = 0$ and $M_2/M_1 = 0.08$. The results of velocity distribution measurement experiments obtained under the condition that the momentum ratio of the primary jet to the secondary flow $M_2 / M_1 = 0.08$, show that the continuous jets as a secondary flow does not affect the deflection of the primary jet when the momentum ratio $M_2 / M_1 = 0.08$. On the other hand, when the continuous suction flow and synthetic jets were used as a secondary flow, it was found that the length of the wall surface affected the deflection characteristics of the primary jet. In the case of the synthetic jet, the velocity distribution measurement results show that the jet splits in two directions. This suggests that the primary jet adheres to the wall surface during the injection process, and the jet is detached from the wall surface during the suction process.

These results show that the deflection characteristics of the primary jet using secondary flow with a coanda surface depend on the length of the flat plate and the characteristics of the secondary flow.

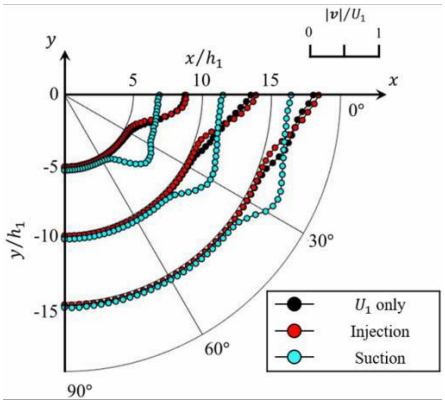

Fig. 1. Dimensionless time-averaged velocity distributions under the condition of $x_W/h_1 = 18.5$, $y_W/h_1 = 0$ and $M_2/M_1 = 0.08$ ($h_1 = 1.0 \times 10^{-2}$ m, $h_2 = 2.0 \times 10^{-3}$ m, $U_1 = 8$ m/s , $U_2 = 5.06$ m/s , $Re = 5.3 \times 10^3$)

References:

[1] Kobayashi, R., Watanabe, Y., Tamanoi, Y., Nishibe, K., Kang, D., and Sato, K., "Jet vectoring using secondary Coanda synthetic jets", Bulletin of the JSME, Mechanical Engineering Journal, Vol. 7, No. 5 (2020),

[2] Hunter C. A. and Deere K. A., "Computational Investigation of Fluidic Counterflow Thrust Vectoring", AIAA, 99–2669, (1999).

[3] Mason, M. S. and Crowther, W. J., "Fluidic thrust vectoring of low observable aircraft," CEAS Aerospace Aerodynamic Research Conference, Cambridge UK, (2002).

[4] Al-Asady, A., and Abdullah, A.M., "Fluidics thrust vectoring using co-flow method". Al-Nahrain Journal for Engineering Sciences, Vol. 20, No. 1 (2017), pp. 5-18.

[5] Tezuka, H., Nakagawa, M., Tamanoi, Y., Sato, K., "Direction control of primary jets using secondary flow near boundaries", Proceedings of the 28th Annual Meeting of the Kanto Branch of the Japan Society of Mechanical Engineers, 2022, (in Japanese).

Effect of the frequency of jet excitation on the symmetric flow field

Takumi Ito*[1], Kotaro Sato[1]

[1]Mechanical Engineering Program in the Graduate School of Engineering, Kogakuin University
1-24-2 Nishi-shinjuku, Shinjuku-ku, Tokyo 163-8677, Japan
E-mail: am21005@ns.kogakuin.ac.jp

Abstract

Research on fluid thrust vectoring, which adjusts the fluid force without changing the outlet geometry, has attracted considerable attention in academia. In this study, an excitation jet (pulsating jet) was generated by superimposing a continuous jet and synthetic jet using asymmetric slots. Subsequently, the jet direction was controlled based on its oscillatory characteristics. Typical flows of a two-dimensional planar excited jet in an asymmetric slot were presented, and the effects of dimensionless amplitude and frequency on the deflection characteristics of the excited jet were discussed.

Recently, a method for controlling the direction of a single jet leveraging the oscillation characteristics of a synthetic jet has been proposed [1][2]. However, the difficulty in achieving high flow rates with a stand-alone synthetic jet means that the flow rate may be insufficient for flow control in fluid machinery and other applications. In this study, we aim to control the direction of jets with relatively large flow rates by creating an excitation jet (pulsating jet) by superimposing a continuous jet with a synthetic jet.

In this experiment, the slot width was set to $b_0 = 5.0 \times 10^{-3}$ [m]. To achieve the best possible two-dimensional flow, the upper and lower test sections of the channel were sandwiched between two acrylic plates. For a detailed description of the experimental setup, please refer to Reference [3]. The velocity of the continuous jet was assumed to be constant at $U_{c0} = 2.0$ [m/s] with a Reynolds number of $R_e = 666$. The ratio of the continuous jet velocity U_{c0} to the excitation jet velocity amplitude U_{pa} is defined here as the dimensionless amplitude U_{pa}/U_{c0}, which is the main parameter characterizing the experiment. In the experiment, velocity amplitude U_{pa} was adjusted using an amplifier. A dimensionless step length $C = c/b_0$ was applied as the geometric shape parameter, where c is the x-axis step length and b_0 is the slot width.

Figure 1 shows the relationship between the dimensionless amplitude U_{pa}/U_{c0} of the experimentally excited jet and jet deflection degree θ_m. The velocity distribution was measured on the arc at $r/b_0 = 30$, and the maximum velocity angle was set to θ_m. The dimensionless projection length $C = 8$ was kept constant, while the controlled parameter was the frequency f. When the dimensionless projection length remained constant at $C = 8$, the jet tended to go straight, regardless of the dimensionless amplitude for low frequency $f = 10$ [H_z] and high frequency $f = 60$ [H_z]. However, at an intermediate frequency of $f = 30$ [H_z], the jet deflected as the dimensionless amplitude increased. This result suggests that the deflection characteristics depend not only on the dimensionless amplitude but also on the frequency.

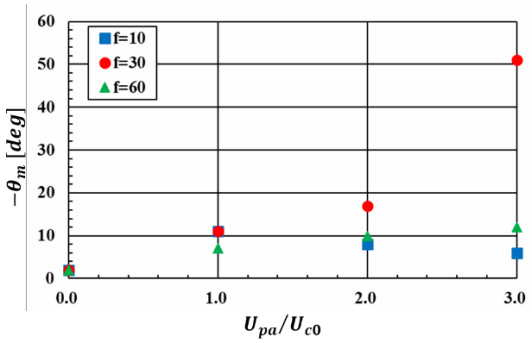

Fig. 1. Jet deflection for an excitation jet experimentally created by an asymmetric step shape slot. The horizontal axis is the dimensionless amplitude and vertical axis is the deflection angle. The measurement radius is $r/b_0 = 30$.

References:

[1] Nishibe, K., Fujita, Y., Sato, K., Yokota, K., and Koso, T., 2011, "Experimental and Numerical Study on the Flow Characteristics of Synthetic Jets," J. Fluid. Sci. Tech., 6(4), pp. 425-436

[2] Kobayashi, R., Nishibe, K., Watabe, Y., Sato, K., and Yokota, K., 2018, "Vector Control of Synthetic Jets Using an Asymmetric Slot," ASME J. Fluid Eng., 140(11), p. 051102

[3] Ito, T., Nishibe, K., Kang, D., and Sato, K., 2022, "Flow deflection of excited jets produced by asymmetric slot," Proc. Of the Interdisciplinary Conference on Mechanics, Computers and Electrics (ICMECE2022).

Breakout Room #6

Electric Engineering and Electronic Engineering and Information and Communications Technology (ICT)

Chairperson: Dr. Huynh Nhat To, DUT

Automatic Font Generation System Reflecting Emotions in Voice Based on Adversarial Generative Network

Keita Tsuchiya, Takuto Nonaka, and Qiu Chen

Graduate School of Engineering, Kogakuin University, Japan
E-mail: {cm22033, cm20041}@g.kogakuin.jp, chen@cc.kogakuin.ac.jp

Abstract

In TV shows and video distribution services, various texts are designed and used in subtitles to express the emotions the media wants to convey. However, in order to generate such emotional text, it is necessary to determine the complex information such as the font and color of the texts, thus requiring a high degree of professionalism. Therefore, in this research, to support font design that requires special expertise, we utilize an adversarial generative network (GAN) to learn the relationship between fonts and emotions contained in voice, and construct an automatic font generation system that reflects the emotions in voice.

1 Introduction

In recent years, it has become a matter of course that a variety of characters are used in TV program and video distribution services, which have become widely popular, decorated with creative fonts and designs to express the emotions that the media wish to convey. However, it is very difficult for ordinary users who do not have knowledge of design to create fonts to express such emotions, because it is necessary to determine.

In this study, we focus on the generation of fonts, which requires expertise, and have conducted a previous study [1] that supports expression by changing the shape of characters according to the emotional components of facial images. Based on the method of [1], this study aims to construct an automatic font generation system that quantitatively analyzes the emotions contained in voice input in real time and reflects them.

2 Methods

21 Web Empath API

Web Empath API of Empath Inc. was used as a method for detecting emotions from speech. Web Empath API uses a unique algorithm to determine the emotion information from the physical features (volume, pitch, speed, and intonation) of the speech, and calculates four emotions of “anger”, “joy”, “calm”, and “sad” with a certainty of 0 to 50 for each.

22 Zi2zi

Zi2zi (Master Chinese Calligraphy with Conditional Adversarial Networks) [2] is a model proposed by Tian that adapts the pix2pix model based on GAN to handle Chinese characters. Pix2pix is a model that learns the relationship between images from two pairs of images, and completes a single image by considering the relationship and generates a pair of images.

23 Proposed system

Fig. 1 shows an overview of the proposed automatic font generation system that can reflect voice sentiment. The entire system is divided into a learning phase and a generation phase. The learning phase uses zi2zi to learn to generate fonts corresponding to emotional information. In the generator section, speech is input and converted into text using speech recognition, and emotional information is analyzed using the Web Empath API. The generator generates fonts by changing the font formulation based on the emotional features of the voice by feeding the emotion features and text data.

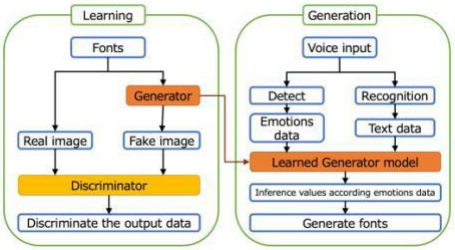

Fig. 1. Overview of the proposed automatic font generation system.

3 Experimental Results

Figure 2 shows an example of a font generated in real-time by the proposed method. The input of the utterance “font generation” in Japanese automatically generates fonts that reflect the two highest-scoring emotions.

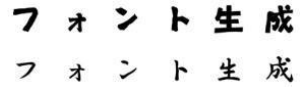

Fig. 2. Examples of a font generated

References:

[1] A. Nakamura, S. Takizawa, T. Hoshi, H. Tsunashima, and Q. Chen, “Automatic font generation algorithm based on image kansei,” *Trans. Japan Soc. Kansei Eng*., **17**(5), 523-529 (2018).

[2] Y. Tian, “zi2zi: Learning Chinese character style with conditional GAN”, (2017)

A Study On Skin Modeling Based On Monte Carlo Simulation For Skin Health Diagnosis

Duc D. D. Luu[1], Khanh D. Phan[1], Phuong T. Kieu[1], Nhan T. Nguyen[1], Thien T. Nguyen[2], Minh T. Nguyen[2], Tuan P. Van[1, 2], Thu T. A. Nguyen[1, 2]*

[1] Faculty of Advanced Science and Technology, University of Science and Technology - The University of Danang

[2] The L.Y.D.I.N.C Co., Ltd

Email: ducluu2201@gmail.com, phandinhkhanh14@gmail.com, nkkieuphuong232@gmail.com, thenhan144@gmail.com, thiennguyenthanh257@gmail.com, minh151197@gmail.com, pvtuan@dut.udn.vn, ntathu@dut.udn.vn.

Abstract – Due to environmental conditions, there is currently a significant increase in demand for skin treatment and diagnostic services. Some principal methods to diagnose skin conditions include transepidermal water loss and Wood's lamp evaluation technique. Another potential approach is multi-spectral imaging, which is a non-invasive method. Furthermore, this type of diagnosis can be performed in a quicker and more precise way thanks to the development of computer technology with simulation tools. This study built a three-layer European skin model and then simulated how light would interact with it by using the Monte Carlo method. The simulation results were compared to a real-world European data source obtained from the US National Institute of Standards and Technology (NIST). This study also built a three-layer Asian skin model and compared its simulation results to measured Asian reflectance data obtained from a DLP NIRscan spectrophotometer. This study's results show the precision of the three-layer mathematical model as well as the reliability of the Monte Carlo simulation approach. This result represents the prerequisite for the big data simulation of skin light reflectance in combination with artificial intelligence. From there, it is possible to complete a diagnosis of skin health parameters to develop an application on a smartphone.

Keywords - Skin Health Diagnosis, Multi-Spectral Imaging, Monte Carlo Simulation, Diffuse Reflectance, Non-Invasive Diagnosis.

1. Introduction

The skin plays an important role in human organs. It functions as a protective layer and contains tactile receptors to receive information from the outside. This indispensable beauty organ, the skin, has become an integral part of our lives.

However, it is also well-known that problems caused by environmental pollution, sun exposure, bad nutrition habits, etc., have made dermatology a community concern. A survey commissioned by the Binh Thuan Provincial Dermatology Hospital, which collected data from 2,400 people, showed that 41% of people suffered from atopic dermatitis and 20.6% from fungal and parasitic diseases [1]. A significant factor in this problem is the heat coming from a tropical climate, especially in combination with worrying levels of air pollution in urban and industrial areas. Considering the current state of the environment, there is an increase in the need for both skin treatment and diagnostic services. In 2016, the American Academy of Dermatology embarked on a study of 84.5 million Americans, one in four of whom was affected by skin disease and presented a cost to the healthcare system of up to $75 billion [2]. Moreover, according to recent statistics, cosmetics imports to Vietnam have risen from $500 million in 2011 to almost $2 billion in 2016 [3].

On the other hand, most people are too busy with work and other life responsibilities, making it too difficult to see a dermatologist. That is why it takes a long time for many to notice their skin problems. Therefore, the need for a quick and convenient way to diagnose skin health is more urgent than ever.

For this reason, there have been many studies and approaches to this problem, such as the Wood lampshade technique [4], the transepidermal water loss measurement technique [20], or the technique of measuring the water content of the skin through its electrical properties, particularly capacitance and conductivity [21]. These methods have produced several products on the market as the Nova DPM® 9003 (Nova Technology Corp., Gloucester, MA), the CM820 Corneometer® (Courage et Khazaka, Koln, Germany), and the Skicon® 200 (I.B.S. Co., Ltd., Shizuoka-ken, Japan) [21]. However, these methods either take a lot of time or cost a lot of money and manpower to implement [5]. To bypass these limitations, this study will examine a non-invasive diagnostic technique that diagnoses the skin condition by allowing light to pass through the skin and collecting diffuse reflections for quantitative analysis of its layer condition.

This paper begins with the skin model method used and the Monte Carlo application for implementation. It will then go on to the simulation, the analysis, and evaluation of the results, and finally, the conclusion.

2. Methodology

2.1. Skin Model

Human skin is composed of many different layers with a complex structure, **divided into 3 main layers: the epidermis, the dermis, and the subcutaneous layer.** These three main layers can be divided into 9 sublayers, in order: stratum corneum, stratum granulosum, stratum basale, papillary dermis, sub-papillary dermis, upper blood net dermis, reticular dermis, deep blood net dermis, and subcutis [6]. This 9-layer skin model has a complex structure with more impact parameters. In this study, we used a skin model with 3 main layers (Fig. 1) but still ensured the structure and main information of the skin.

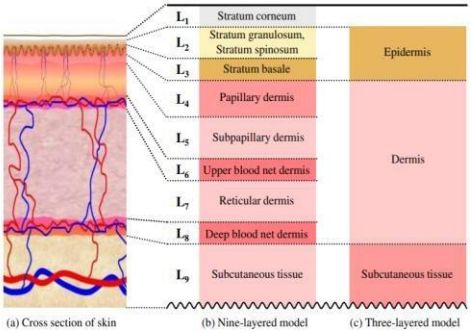

Figure 1: *Diagram of skin's structure [8]*

The outermost layer of human skin is known as the epidermis, which has no capillaries or veins. The average

thickness of this layer is about 0.027 to 0.150 mm [7]. The light that passes through the epidermis is mainly absorbed by melanin. This protein creates skin pigment cells and helps protect against UV rays from the sun.

The dermis is approximately 0.6 - 3 mm thick [7]. The layer structure consists of connective fibers, water, hemoglobin, and collagen. Hemoglobin is known to be of two types: oxyhemoglobin and deoxyhemoglobin. The amount of collagen in this layer represents 90% of all the collagen in the human body. Present within the collagen layer are the lymphatic vessels, the blood vessels, the nerve fibers, and the muscle cells.

Lastly, the subcutaneous layer has a thickness of 1 to 5 mm [8]. It is made up of connective tissue called sponges, interspersing with fat cells containing energy. These fat cells are retained and grouped by collagen fibers. Blood vessels dot the subcutaneous layer, ensuring a rapid supply of essential nutrients to the body.

Skin health can be measured by the optical attributes of each layer, namely **thickness, absorption coefficient, scattering coefficient,** etc. The proportions and properties of substances in the skin affect the absorption factor of photons in each layer.

Assume μ_{a_i} is the absorption coefficient of the i-th pigment of volume C_i. For each layer of skin modeled, the absorption capacity is the sum of the main skin components' absorption capacities. As Jacques discovered in 1996, there was a part of the skin that absorbs spectra but contains no pigment [9].

So, we have the formula to represent **the absorption coefficient of a layer** in linear form, where n is the total amount of pigment present in the layer:

$$\mu_{a_{layer}} = \sum_{i=1}^{n} \mu_{a_i} C_i + (1 - \sum_{i=1}^{n} C_i)\, \mu_{a_{base}} \quad (1) \quad [8]$$

with $\sum_{i=1}^{n} C_i < 100\%$

However, if n is too large and $\sum^{n} C_i$ exceeds 100%, the condition will no longer be satisfied. To avoid the above situation, the formula is adjusted to the excess volume:

$$\mu_{a_{layer}} = \sum_{i=1}^{n} \prod_{j=1}^{i-1} [(1 - C_j)] C_i \mu_{a_i} + \prod_{i=1}^{n} (1 - C_i) \mu_{a_{base}} \quad (2)$$

Then, the absorption coefficient in the epidermis is expressed as follows:

$$\mu_{a_{epi}} = C_m * (\mu_{a_{pheo}} * \beta + \mu_{a_{eu}} * (1 - \beta)) + C_{w_{epi}} * \mu_{a_w} + (1 - C_m - C_{w_{epi}}) * \mu_{a\_base}$$

C_m and $C_{w_{epi}}$ represent the volume proportion of two different types of melanin and water in the epidermis: eumelanin with brown or black pigment and pheomelanin with red or yellow pigment; β is the ratio between pheomelanin and eumelanin; $\mu_{a_{pheo}}$, $\mu_{a_{eu}}$ and μ_{a_w} are respectively the absorption coefficients of pheomelanin, eumelanin, and water.

Also, most of the absorption in the dermis is due to blood hemoglobin, including oxyhemoglobin and deoxyhemoglobin, which have varying absorption coefficients. The remaining amount is due to water and the non-pigmented part. The final layer, the subcutaneous layer, is made up of blood, fat, water, and unpigmented skin. So, we have the absorption spectrum of the dermis and the subcutaneous layer, respectively:

$$\mu_{a\_der} = C_{bl\_der} * (\mu_{a_{oxy}} * S + \mu_{a_{deoxy}} * (1 - S)) + (1 - C_{bl_{der}}) * C_{w_{der}} * \mu_{a_w} + (1 - C_{bl_{der}}) * (1 - C_{w_{der}}) * \mu_{a\_base}$$

$$\mu_{a\_sub} = C_{bl\_sub} * (\mu_{a_{oxy}} * S + \mu_{a_{deoxy}} * (1 - S)) + (1 - C_{bl_{sub}}) * C_{fat} * \mu_{a_{fat}} + (1 - C_{bl_{sub}}) * (1 - C_{fat}) * C_{w_{sub}} * \mu_{a_w} + (1 - C_{bl_{sub}}) * (1 - C_{fat}) * (1 - C_{w_{sub}}) * \mu_{a\_base}$$

The coefficients and symbols are described in the table below:

Table 1: *Descriptions, symbols, and parameter ranges in the skin model*

Symbol	Description	Range
C_m	volume fraction of melanin	1.3-43% [9]
$C_{w_{epi}}$	volume fraction of water in the epidermis	10-20% [8]
$C_{bl_{der}}$	volume fraction of blood in the dermis	0.2-7% [10]
$C_{w_{der}}$	volume fraction of water in the dermis	40-90% [8]
$C_{bl_{sub}}$	volume fraction of blood in the subcutis	5-20% [8]
$C_{w_{sub}}$	volume fraction of water in the subcutis	40-90% [8]
C_{fat}	volume fraction of fat	40-70% [8]
μ_{a_m}	absoprtion coefficient of melanin	1.70×10^{-12} $nm^{-3.48}$ cm^{-1}
μ_{a_w}	absoprtion coefficient of water	10^{-4} - 9.9×10^{-5} cm^{-1}
$\mu_{a_{oxy}}$	absoprtion coefficient of oxyhemoglobin	0.5 - 1.26cm^{-1}
$\mu_{a_{deoxy}}$	absoprtion coefficient of deoxyhemoglobin	0.1 - 3.7cm^{-1}
$\mu_{a_{fat}}$	absoprtion coefficient of fat	0.3 - 13.1m^{-1}
S	oxygen saturation	50-95% [12]

In addition to the absorption, the skin has a continuous scattering capacity. Rayleigh and Mie scattering can be used to determine this mechanism in the skin.

Rayleigh scattering is the scattering of light by particles with a radius of about one-tenth the wavelength of the radiation. The light from this scattering has almost the same wavelength as the incident light [13].

Mie scattering is the scattering of light by particles with a diameter equal to or larger than the wavelength of the incident light. Some typical elements are collagen, nucleus, and mitochondria [14].

The scattering coefficient was calculated by this formula:

$$\mu_s = \mu_{s_{500(nm)}} * f_{ray} * \left(\frac{\lambda}{500(nm)}\right)^{-4} + (1 - f_{ray}) * \left(\frac{\lambda}{500(nm)}\right)^{-b_{mie}}$$

Where:

$\mu_{s_{500(nm)}}$: the scattering coefficient measured at 500 nm

f_{ray} : Rayleigh scattering

$1 - f_{ray}$: Mie scattering

b_{mie} : the scattered power obtained by the data measured [9].

Based on the formulations for skin modeling with the above optical properties, we simulated how light is spread in the skin and reflected on the skin surface through the Monte Carlo algorithm [8].

2.2. Monte Carlo simulation

With a clearly defined skin pattern, the Monte Carlo (MC) method can be applied to build a model that can reconstruct the diffuse reflectivity of the skin. The Monte Carlo simulation process follows the steps shown in the diagram in Fig. 2 below:

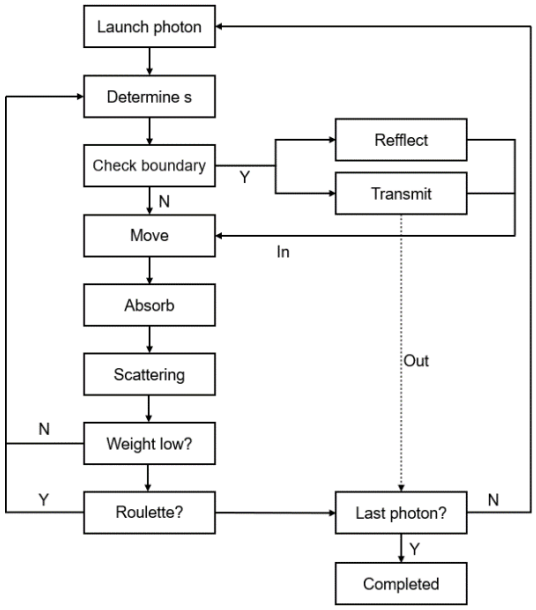

Figure 2: *Monte Carlo flowchart [8]*

This process simulates the process of projecting perpendicular photons into the skin. The skin layers in this simulation are assumed to be infinitely wide. We describe each layer using indicators such as thickness, refractive index, absorption coefficient μ_a, scattering coefficient μ_s, and variation coefficient g. Of these, the refractive index is the fraction of photons that are absorbed in a unit distance, and the scattering coefficient is the rate at which photons are scattered over a unit distance. As a result, it leads to the conclusion that the interaction coefficient μ_t is equal to the sum of the absorption and scattering coefficients. The anisotropy factor g is a mean cosine of the deviation angle (Fig. 3).

During this process, photons are allowed to propagate in a 3-dimensional space and the number of photons absorbed is recorded. This simulation uses variable random sampling from probability distributions. To simulate propagation, we randomly iterate on a variable based on the pseudo-random number generator ξ. [17]

First of all, the program determines the current position of the photon using the Cartesian coordinate system (x, y, z). At this point, the photons will begin to eject. Before launching, each photon is assigned a weight W. Using stochastic data, the step size through probability distribution sampling for the photon's free path is calculated.

In each step, photons can potentially collide with the boundary wall of the skin or continue to propagate. If the photon hits the boundary wall, we will check whether the photon will be reflected or exited. This test is based on a set of pseudo-random numbers ξ and a total reflection coefficient $R(\alpha_i)$.

Next, the photon began to move inside the tissue with a constantly updated weight. After each step, the simulation process began to calculate the attenuation of the photon due to absorption in the tissue. The photon continues to be scattered and its direction will be changed. This change depends on the 2 angles, the deflection $\theta \in [0, \pi)$ angle and the azimuth $\psi \in [0,2\pi)$, which are decided based on a random value.

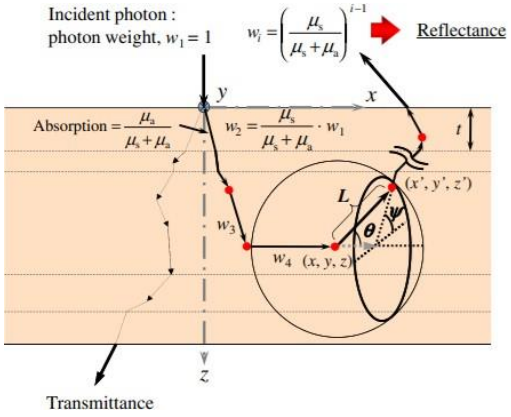

Figure 3: *How photons move in Monte Carlo [7]*

This constant change in weight means that some photons lose too much weight during travel, resulting in them not being able to yield enough information. The Roulette technique is used to end the movement of these photons, which ensures the conservation of energy and does not distort the distribution of photon deposition.

This method allows the photon to continue moving with weight mW. If the photon weight falls below the specified threshold, the weight is reduced to zero and the process of this photon ends.

$$\mathrm{W} \leftarrow \begin{cases} mW & if\ \xi \le 1/m \\ 0 & if\ \xi > 1/m \end{cases}$$

If it is the last photon, the simulation will stop. Otherwise, the simulation process will continue with a new photon.

3. Results and Evaluation

3.1. Compare simulation results with experimental data set NIST

Based on the value ranges of skin parameters collected in Tab. 1, this study performed simulations with Caucasian skin parameters as follows:

$$C_m = 5\%,\ C_{w\_epi} = 15\%,\ C_{bl\_der} = 4\%,\ \beta = 21\%,$$
$$\mu_{a\_oxy} = 0.88cm^{-1},\ \mu_{a\_deoxy} = 1.9cm^{-1}$$

The Monte Carlo simulation process was customized following these parameters and the skin texture proposed by Lihong Wang [22].

To evaluate this approach's effectiveness, this study makes use of the NIST's skin reflection database. This database was built by measuring the real reflected spectrum of 100 participants using a commercial spectrophotometer. It covers a range of wavelengths from 250 to 2500 nm with each step increasing by 3 nm. We reshaped the data using an interpolation algorithm and limited the range from 430 to 650 nm. From there, we reformatted the patterns in the Monte Carlo program and received a simulated reflection spectrum.

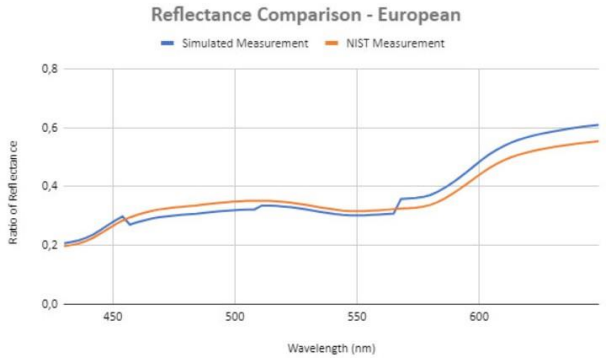

Figure 4: *Comparison of the reflection spectra*

It can be seen from the data in Fig. 4 that the reflected spectrum received from our simulation is close to the actual dataset published by the National Institute of Standards and Technology (NIST) [14]. The average Euclidean distance between the simulated index and the NIST real measurement obtained was 0.0292. In particular, the largest difference was 0.0554 at the 649 nm wavelength and the smallest difference was 0.0099 at the 430 nm wavelength.

The discrepancy between the simulation results and the real measurement results came from the adjustment of the parameters of the epidermis and dermis. Besides, the three-layer skin model used by us had a less complex structure than the nine-layer model and real skin. However, the reflection spectrum graph can still retain a relatively uniform and distinctive shape.

Experimental results showed that the reflected spectrum tended to increase on the wavelength domain of 430 - 650 nm. This may be due to a steady decrease in the absorption factor of melanin in this range. We must also consider the issue of the melanin content being too large, prevailing over the foreign substances in the mesoderm [8]. In addition, this value is inversely proportional to the blood absorption coefficient [8], as can be seen from Fig. 4 and Fig. 5. Both figures show that as the concentration of hemoglobin and oxygen-hemoglobin increases between 510 and 565 nm, the reflection coefficient decreases.

At a wavelength of 450 nm, the coefficient varies due to the influence when the wavelength passes through the layer separating the epidermis and mesoderm (Fig. 6).

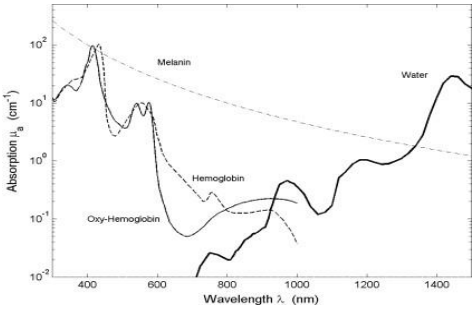

Figure 5: *Absorption coefficient spectrum of pigments in human skin [15]*

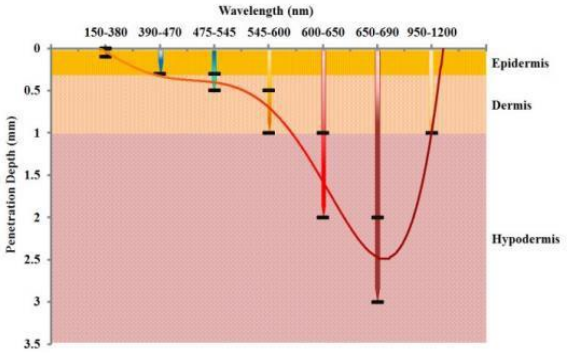

Figure 6: *Depth of light penetration into the skin [16]*

3.2. Comparison of simulation results with self-constructed empirical datasets

At the same time, we have also simulated a model of Asian human skin based on previous studies. This time, we put in a melanin content (C_m) of 12% [8]. The thickness of the epidermis is 0.0728 nm, and the thickness of the dermis is 1.0943 nm [18]. In addition, we also found a ratio between pheomelanin and eumelanin $\beta = 6.2125$ [19].

After we had built a model of Asian skin, we ran Monte Carlo in a wavelength range of 900-1700 nm to compare with the data we collected from the Texas Instruments DLP NIRscan Nano Evaluation Module (EVM). We measured three Vietnamese volunteers in the age range of 20 and 25 years. The result was put together, rebuilt using an interpolation algorithm, and plotted in the figure below.

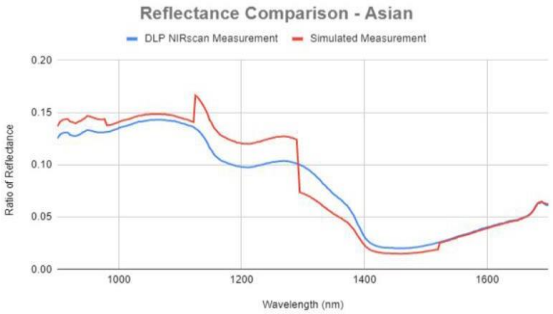

Figure 7: *Measured results and simulation results*

In Fig. 7, we see that the reflection spectrum received from the simulation results is roughly the same shape as the reflection spectrum obtained from the real measurement results. However, there is a sharp variation between 1100 and 1300 nm.

This difference can come from adjusting the parameters of the epidermis, dermis, and three-layer skin pattern. Besides, we can see that from a wavelength of 1000 nm there is no hemoglobin and deoxyhemoglobin but only water and melanin. At the same time, melanin is also in a sharp decline, which leads to interference with the program, and we also see a sharp increase in the absorption of water at 1100 nm. Therefore, the reflection spectrum of real skin and simulated skin both show signs of a sharp decrease. In this wavelength range water becomes the value of the concentration in the stratum, thus leading to that variation.

The average Euclidean distance between the simulated index and the measured index is 0.0105. In particular, the largest difference is 0.0316 at 1125 nm wavelength and the smallest difference is 0.0001 at 1689 nm wavelength.

We have also observed that while the discrepancies between the two lines in figures 4 and 7 may appear to be large, the actual difference is not that significant. The reason for such discrepancies lies in the difference in scale. When we take into consideration the difference between the Euclidean distances of both figures, we see that the average difference is 0.0292 for figure 4 and 0.0105 for figure 7. These small differences further prove that the skin models that we built, and the Monte Carlo simulation process are reliable.

4. Conclusion and Future Work

This project was undertaken to design a simulation of human skin structure with two sets of parameters suitable for European and Asian skin models proposed in previous studies with the Monte Carlo method and evaluate the data set simulated with experimental data published by the NIST Institute as well as measured data from volunteers.

By changing the parameters of human skin according to different health conditions of the skin, the data simulating the degree of skin reflection in the respective situations will be reproduced. This is the premise for simulation to diagnose human skin health.

In addition, because the Monte Carlo simulation takes a long time and requires a high-configuration computer, it reduces the feasibility of the diagnostic process. Therefore, in future research, Neural networks will be trained to create a big data model simulation as well as speed up the diagnosis.

Furthermore, in the next studies, we will proceed to build an integrated system on smartphones, using the phone camera to measure the reflectivity of human skin by integrating an artificial intelligence model on edge devices and performing diagnostic analysis on skin health conditions.

5. Acknowledgment

This work would not have been possible without the support of the L.Y.D.I.N.C Co. Ltd., which provides financial support, research equipment, and expert consultancy for the project. We are grateful to the International Institute of Technology, the University of Da Nang (DNIIT) for loaning us a NIRscan device, and we would like to thank University of Danang - University of Science and Technology for supporting part of the cost of this research.

6. References

[1] Nguyễn Thạnh, "Mỗi năm người dân chi tới 75 tỷ USD để điều trị bệnh về da," 2020.
[2] American Academy of Dermatology, "Burden of skin disease," 2016.
[3] Hà Mai, "Người Việt chi 2 tỷ cho mỹ phẩm nhập," 2018.
[4] Ev V., et al, "Experience with Wood Lamp Illumination and Digital Photography in the Documentation of Bruises on Human Skin," 2002.
[5] Ministry of Public Health, "Quy trình chụp và phân tích da bằng máy phân tích da," 2017.
[6] Maeda T., Arakawa N., Takahashi M. et al. "Monte Carlo simulation of spectral reflectance using a multilayered skin tissue model." *OPT REV 17*, 223–229, 2010.
[7] Baranoski G. V., Krishnaswamy A., "Light and skin interactions: simulations for computer graphics applications," 2010.
[8] Shiwei L., Mohsen A., Abdelmalek Z., "Quantitative Analysis of Skin using Diffuse Reflectance for Non-invasive Pigments Detection", 2021.
[9] Jacques, S. L, "Origins of tissue optical properties in the uva, visible, and NIR regions", 1996.
[10] Flewelling, R. "Noninvasive optical monitoring, in the biomedical engineering handbook", 2000.
[11] Parsad D., Wakamatsu K., Kanwar A. J., Kumar B., and Ito S., "Eumelanin and pheomelanin contents of depigmented and repigmented skin in vitiligo patients", 2003.
[12] Angelopoulos, E. "Understanding the color of human skin", 2001.
[13] David J. L., Encyclopedia of Color Science and Technology, pp. 1097-1107, 2016.
[14] Catherine C. Cooksey, David W. Allen, and Benjamin K. Tsai, "Reference Data Set of Human Skin Reflectance", 2017.
[15] Dam J. S., "Optical analysis of biological media: Continuous wave diffuse spectroscopy'', 2000.
[16] Yi-Han C., Kuo-Cheng H., Ching-Ching Y., Hsin-Yi T., "Evaluation of absorbed light dose in human skin tissue during Light Therapy by 630nm LED light,", 2015.
[17] Jacques S. L., "Optical properties of biological tissues: a review", 2013.
[18] Lee Y., Hwang K., "Skin thick of Korean adults", 2002.
[19] Alison H., Carol O., Brian D., Kazumasa W., Shosuke I. and Jonathan R., "Eumelanin and pheomelanin concentrations in human epidermis before and after UVB irradiation", 2005.
[20] Maxwell G., et al, "Transepidermal water loss (TEWL): Environment and pollution—A systematic review", 2022.
[21] Lee CM, Maibach HI," Bioengineering analysis of water hydration: an overview", 2002.
[22] Lihong Wang, Steven L. Jacques, Liqiong Zheng, "MCML—Monte Carlo modeling of light transport in multi-layered tissues", 1995.

Vision aid for drones with precise positioning of landing targets

Jia-Shing Shih [1*], Hsuan-Hsin Wu [1†], Chun-Chieh Tsai [1], Guan-Yu Lin [1] and Cheng-Dian Zhan [1]

[1] Department of Electrical Engineering, Southern Taiwan University of Science and Technology, Tainan, Taiwan
[*]Corresponding author's e-mail: jasonshih@stust.edu.tw

Abstract

Multi-rotor drones are moving towards automation, so the accuracy of drone landings is very important. Currently, most drones use the Global Positioning System (GPS) for positioning, but satellite signals are affected by interference factors such as atmospheric refraction. Causes an error of 5 meters to 30 meters, so we designed a precise landing solution based on visual aids with a low-cost concept.

Keywords: Precise landing, Visual recognition, Drone

I. Basic Theory

First, the aircraft uses the Global Positioning System (GPS) to move to the ArUco marker (binary square marker) that we pre-placed at the landing location. At this time, using the aruco library of OpenCV (Open Source Computer Vision Library), we can know that the ArUco Markers are relative to the coordinate vector based on the airborne camera, use the Proportional-Integral-Derivative (PID) algorithm, and use the rotation matrix (1) to convert the control vector into NED (North East Down) coordinates, and then pass for WGS (World Geodetic System) coordinates, you can get the GPS coordinates that the drone will move. The final execution result of the program will use the DroneKit library to send control commands to the flight controller, and finally the motor starts to move.

II. Visual Identification

The camera first grabs the ArUco marker, captures the marker through the program and identifies its ID, and then converts the coordinates through the rotation matrix to correct the error between the drone and the ArUco marker. When the error is small enough, reduce the height.

III. PID

We can adjust the stability, accuracy and rapidity of the aircraft through PID. The adjustment of P (Proportional) is proportional to the output and the input error signal, and the adjustment output of I (Integral) is proportional to the integral of the input error signal. , is to integrate the error time, which increases with the increase of time, which can further

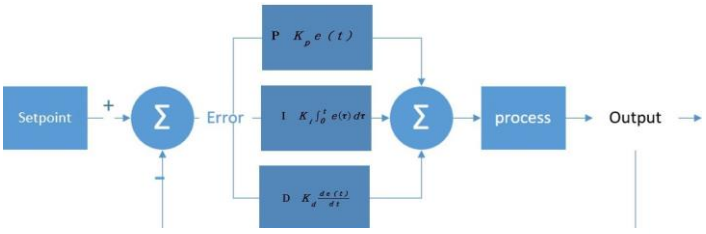

Fig 1. Block diagram of a PID controller

en

the output and the input error signal are in a differential relationship, the differential adjustment can be used to realize the advanced control of the system.

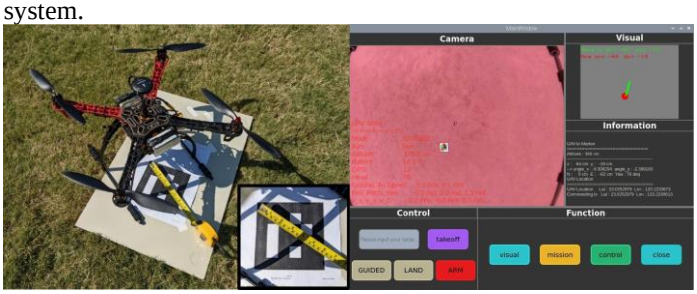

Fig 2. Drone lanGraphical User Interface

IV. Results

After the drone takes off automatically and completes the pre-planned flight path, it moves to the place where the ArUco marker is placed. At first, the drone slowly descended to 8 meters and began to use the ArUco marker as a basis for detection. If the ArUco marker is not detected, the drone is forced to land. When the camera recognizes a specific ArUco marker, it lands. At this time, during the descending process, the coordinate transformation is carried out through the ArUco marker, so that the drone is continuously corrected to the position of the ArUco marker, and accurate visual recognition is performed to assist the positioning. When the altitude is 50 cm, the aircraft will land on the spot.

References:

[1] Y. Ohko, T. Tatsuma, T. Fujii, K. Naoi, C. Niwa, Y. Kubota, A. Fujishima, Nature Materials, 2, 29–31 (2003).
[2] H. Nagai, S. Aoyama, H. Hara, C. Mochizuki, I. Takano, N. Baba, M, Sato, J. Mater. Sci., 44, 861–868 (2009).
[3] H. Nagai, C. Mochizuki, H. Hara, I. Takano and M. Sato, Sol. Energy Mater. Sol. Cells, 92, 1136-1144 (2008).

A genetic algorithm-based CNN approach for ceramic tile defects classification

Nhat-To Huynh

The University of Danang, University of Science and Technology, Danang, Vietnam
Email: hnto@dut.udn.vn

Abstract

Classifying and grading the product relied on human vision has caused the quality problem due to inception and fatigue. However, most of ceramic tile factories still have relied on human vision to deal with this problem. This study aims to propose a genetic algorithm based convolutional neural network which can automatically generate an optimal convolutional neural network (CNN) for classification based on genetic algorithm.

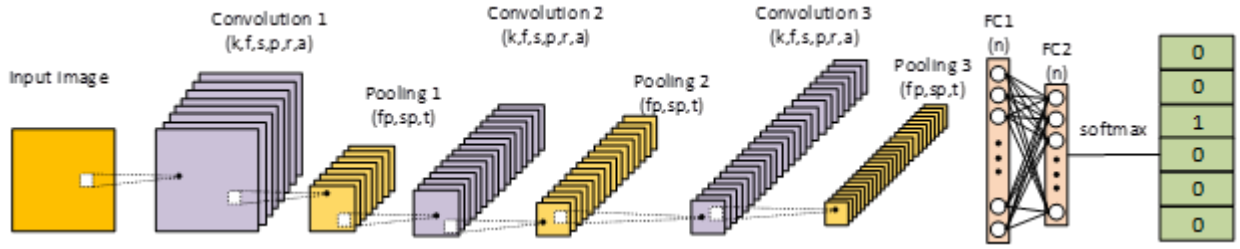

Figure 1: general structure of CNN mode

For ceramic tile defect classification problem, based on well-designed structure of some famous CNN and experts, the proposed GA-CNN consists of 3 convolutional layers, 3 pooling layers and 2 fully connection layers as Figure 1. The parameters of convolution layers include number of kernel (k), kernel size (f), stride (s), padding (p), learning rate (r), and activate function (a). For pooling layers, the parameters consist of kernel size (fp), stride (sp), and pooling type (t). Two fully connected layers, number of nodes of each one needs to be determined. These parameters of CNN structure are optimized by GA.

GA is used widely and efficiently for optimization problem. The algorithms are designed based on evolution to find the optimal solution. General procedure of GA-CNN is designed as follows.

Algorithm: GA-CNN

Output: Optimal CNN
Input: Dataset of images, GA parameters
Begin
t = 0
Generate initial population P0 by Encoding routine
Assign crossover rate (rc), mutation rate (rm), and elitist rate (re)
While (NOT termination condition) do
Create offspring by crossover routine
Create offspring by mutation routine
Temporary population = Pt + Offpring
For (each chromosome in the temporary population) do
Build a CNN model with structural parameters based on gen values
Train the CNN model on training dataset
Calculate accuracy of each model on test dataset by Equation (1)
End;
Select chromosomes for next generation by Selection routine
t = t+1
End
End.

To validate the proposed GA-CNN algorithm, firstly a database of ceramic tile images (CTD) was collected. These images were taken from a ceramic tile company including 6 common types of defects and non-defect product. The total number of taken images are 1000. For each type of defect, 100 images were taken. And non-defect images are 400. Only color and non-texture ceramic tiles were taken and collected for validating of the proposed algorithm. After taking and collecting, those images were preprocessed to adjust the same size.

In order to understand how the proposed GA-CNN constructs an optimal CNN, a convergency or evolution chart with population size as 50 are shown as in Figure 2. For each generation, a boxplot is used in term of classification accuracy of each chromosome. The figure shows that convergency of the proposed algorithm.

Although the proposed GA-CNN took long running time, its result performed well on both datasets. For Fashion_MNIST, the accuracy is a little bit small than ResNet with 91.18 percent. But on CTD dataset, the GA-CNN returns the highest accuracy with 96.56 percent as shown in Table 1.

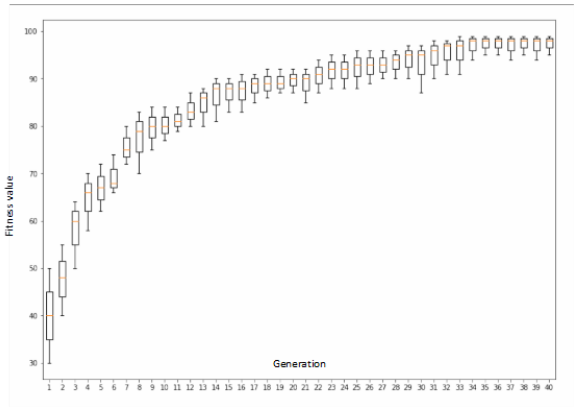

Figure 2: Convergence of the GA-CNN

Table 1: the accuracy of algorithms for different dataset

Algorithm	Fashion_MNIST (%)	CTD (%)
ResNet	92.03	92.20
VGG	90.12	92.18
CNN-GA	87.22	90.55
Genetic CNN	82.81	90.73
GA-CNN	91.18	96.56

Defect detection and classification automatically can enhance the quality control in ceramic tile production. Due to different defect types of ceramic tile products, it is lack of models can deal with this problem completely. Thus, the study proposed an efficient algorithm to automatically generate an optimal CNN model for ceramic tile product. In particular, a general structure of CNN is constructed. Then, based on evolution process, genetic algorithm is designed to find optimal parameter of CNN layers automatically.

Keywords:

Ceramic tile, defect detection and classification, genetic algorithm, convolutional neural network

Acknowledgement

This research is funded by Funds for Science and Technology Development of the University of Danang under project number B2019-DN02-64.

References

Huynh, N. T., & Chien, C. F. (2018). A hybrid multi-subpopulation genetic algorithm for textile batch dyeing scheduling and an empirical study. Computers & Industrial Engineering, 125, 615-627.

Huynh, N. T., Huang, Y. C., & Chien, C. F. (2018). A hybrid genetic algorithm with 2D encoding for the scheduling of rehabilitation patients. Computers & Industrial Engineering, 125, 221-231.

Jajal, B., & Dobariya, A. R. (2021). Leveraging Machine Vision for Automated Tiles Defect Detection in Ceramic Industries. In Emerging Technologies in Data Mining and Information Security, pp. 725-733.

Verification of Low voltage ride-through requirement for a Large-Scale Wind Farm

Cheng-Ting Hsu*

Department of Electrical Engineering, Southern Taiwan University of Science and Technology, Taiwan
E-mail: cthsu@stust.edu.tw

Abstract

Renewable energy generations (REG) grow rapidly and play a role in mitigating climate change problems in the world. The Taiwan government also aims to install 30.1GW of REG capacity by 2025. Among various types of REG, wind power generation (WPG) and photovoltaic power generation (PVPG) is the most developed potential with a total capacity of 6.9GW and 20GWp respectively. However, both the WPG and PVPG are highly intermittent and fluctuating. They will have a great adverse impact on the power system as increasing penetration. Therefore, REG can be allowed integrated into the power system if they can follow the interconnection grid code [1].

There are many issues with interconnection grid code like power flow analysis, contingency analysis, fault current, voltage variation, flicker, angle stability, power factor, low voltage ride-through (LVRT), high voltage ride-through (HVRT), harmonic, etc. This paper focuses on the analysis of LVRT [2]. Taiwan Power Company (Taipower) suggests an LVRT curve as shown in Fig. 1. Wind power plants should continue to operate if the voltage at the point of common coupling (PCC) is higher than the curve. And it should continue to operate for at least 0.15 seconds if the voltage drops to 0pu.

A large-scale WPG plant was selected for the study. Figure 2 shows the one-line diagram of the WPG plant. There are 14 wind turbines provided by the Enercon with a rating capacity of 4.2MW each. The power output of each annular generator is fed to a full converter. The converter generates a nominal voltage of 720V and then connects to a step-up transformer to boost voltage to the 22.8kV. After that, the electric power generated from the 14 WPG was collected to a step-up substation where the voltage is converted to 69kV via a transformer with a rating capacity of 100MVA. And a 4.8km electric cable is used for connecting to the PCC at the Taipower substation.

To follow the requirements of Taipower grid codes, the dynamic analysis of the LVRT scenarios is executed by applying for the PSS/E program [3]. Two scenarios are considered in the paper. One has an initial voltage of 0.95pu at the PCC while the other is 1.03pu. By the way, the dynamic model and parameters of the WPG are provided by the manufacturer. Figures 3 and 4 show the dynamic active and reactive power output of the WPG by applying the low voltage disturbance as described in Fig 1. It is observed that the active power of WPG (green curve) decreased almost to 0 and then recovered slowly as the voltage raised in both cases. However, the reactive power has greater variation while the initial voltage at 1.03pu. There are no WPG units that will be tripped due to the LVRT simulation test. It is concluded that the interconnection of the large-scale WPG plant can follow the LVRT limits of Taipower grid codes.

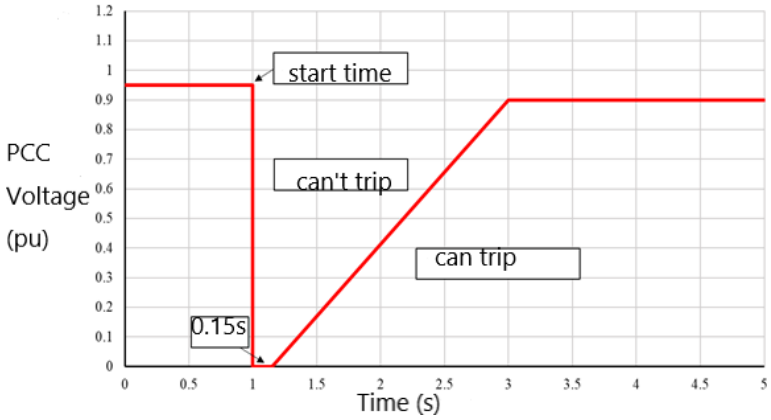

Fig. 1. The LVRT curve of Taipower.

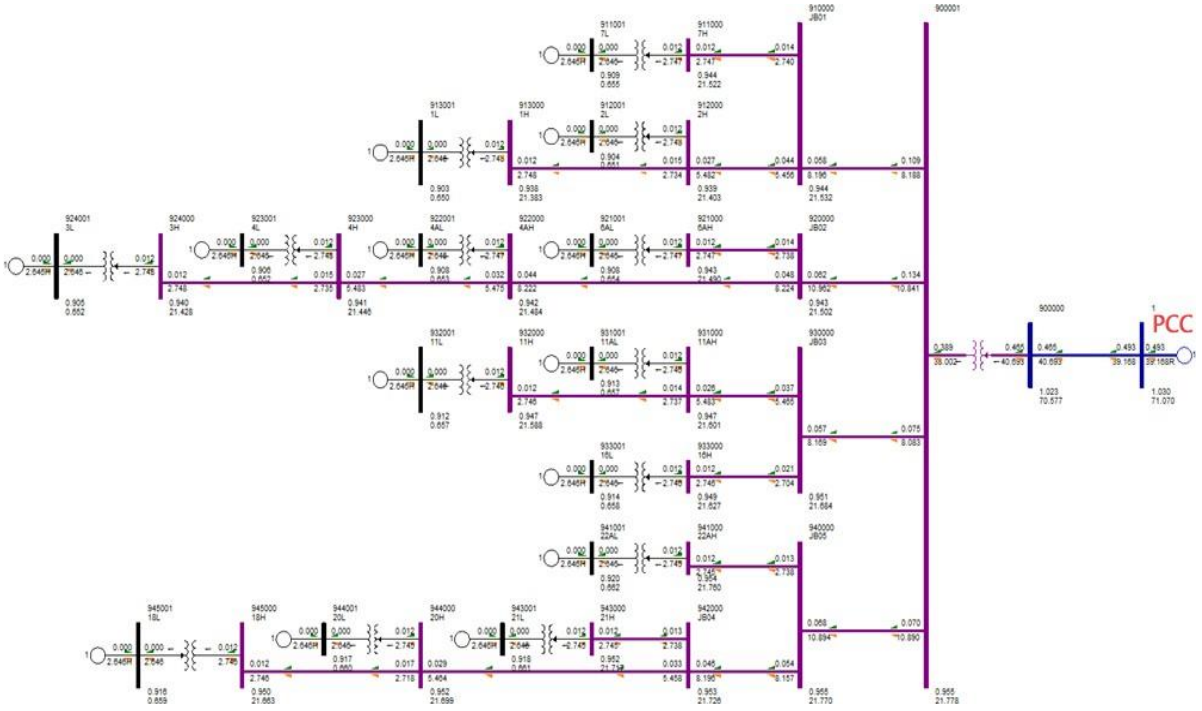

Fig. 2. One-line diagram of the study WPG plant.

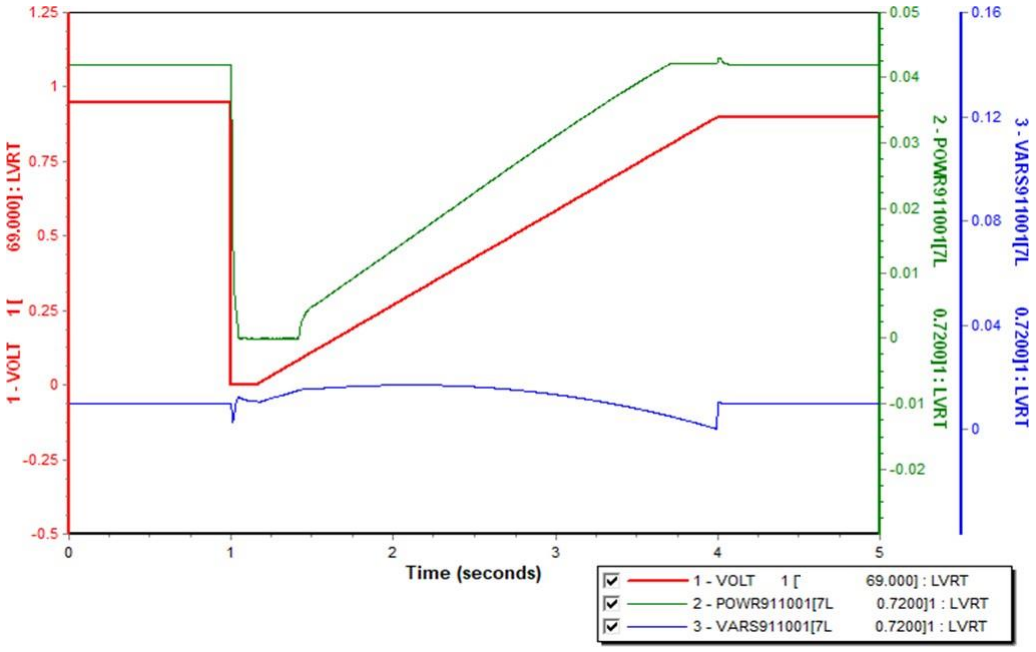

Fig. 3. The power output of a WPG unit for the LVRT disturbance with an initial voltage of 0.95 at PCC.

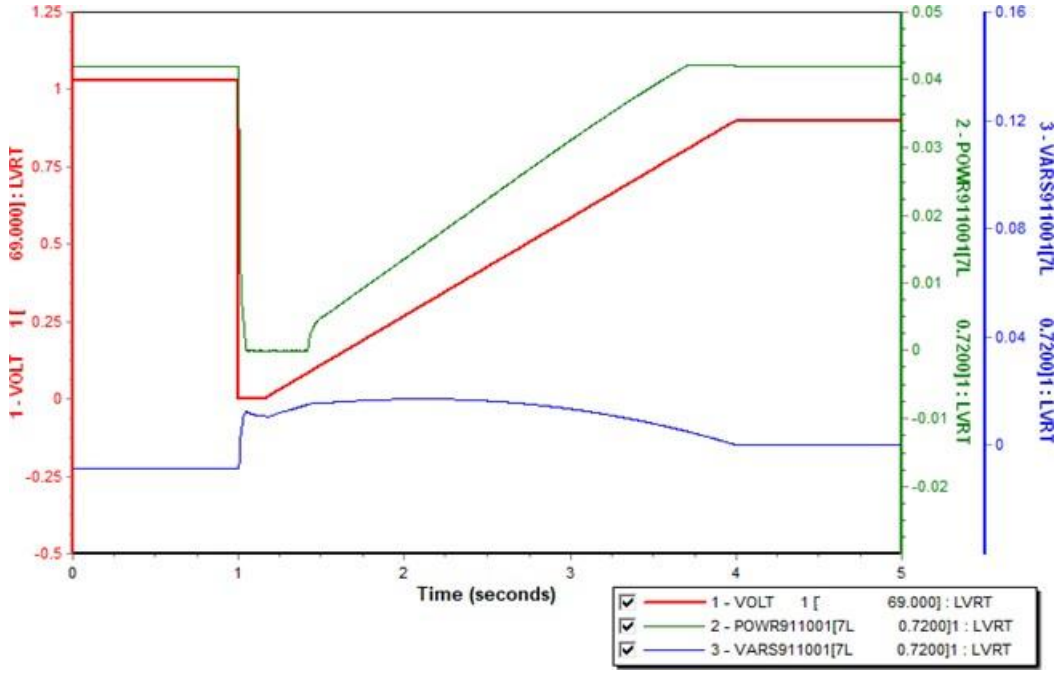

Fig. 4. The power output of a WPG unit for the LVRT disturbance with an initial voltage of 1.03 at PCC.

References:

[1] Renewable energy interconnection grid codes: https://www.taipower.com.tw/upload/228/2018120409203473289.pdf

[2] M. M. Kabsha, Z. H. Rather, *IEEE Transactions on Power Delivery*., 36-6, 3893–3902 (2021).

[3] PSS® E 32.05, Siemens Energy, Inc., Power Technologies International.

Lightning Talk Session (November 25th from 15:40 to 16:50 (JST))

Breakout Room #1

Environmental Chemistry and Chemical Engineering & Advanced Functional Materials

Chairperson: Dr. Nguyen Thanh Binh, DUT

Presentation No.	Title	Author	Page
ECCEL1.	Dependence Of The Cuo Layer On Photocatalytic Properties Of Tio2/Cuo Thin Films	Katsuyuki Takeda, Ichiro Takano	101
ECCEL2.	XPS Analysis Of The Binding States In Nitrogen-Doped Snox Thin-Films Deposited By RF Magnetron Sputtering In N2 Atmosphere	Takuma Kawaguchi, Kotaro Watanabe, Shinya Aikawa	102
ECCEL3.	Crystal Growth Of Cu3N By Mist CVD With Ethylenediamine	Shogo Yoshida, Hiroki Nagai, Tomohiro Yamaguchi, Takeyoshi Onuma, Tohru Honda	105
ECCEL4.	Deposition Of Nitrogen-Doped Titanium Dioxide Thin Films Via Rf Magnetron Sputtering	Melanie M. Martinez, Takeyoshi Onuma, Hiroki Nagai, Tohru Honda, Shinya Aikawa, Tomohiro Yamaguchi, Magdaleno R. Vasquez Jr	106
ECCEL5.	Growth Of Zno Thin Films Via Magnetron Sputtering Using A Custom-Made Sintered Target	Rozen Grace B. Madera, Hiroki Nagai, Takeyoshi Onuma, Tohru Honda, Tomohiro Yamaguchi, Magdaleno R. Vasquez Jr	108
ECCEL6.	Study For Composition Control In Mist CVD Growth Of α-GIO Alloys	Kai Yamada, Tomohiro Yamaguchi, Takeyoshi Onuma, Tohru Honda	110
ECCEL7.	Investigation on the Stability of Source Solution for the a-In2O3 Growth by Mist CVD	T. Yamamoto, A. Taguchi, R. Yamada, H. Nagai, T. Onuma, T. Honda, T. Yamaguchi	112
ECCEL8.	Roles Of In Doping In Rocksalt-Structured Mgzno Films Grown By Mist CVD Method	Masaki Matsuda, Kotaro Ogawa, Yuichi Ota, Tomohiro Yamaguchi, Kentaro Kaneko, Shizuo Fujita, Tohru Honda, Takeyoshi Onuma	113
ECCEL9.	Realization Of High Mobility In α-In_2O_3 Film Grown By Mist CVD With Different Concentration Of In_2O_3 Powder As Source Precursor	Akito Taguchi, Takeyoshi Onuma, Tohru Honda, Tomohiro Yamaguchi	115
ECCEL10.	Electrochemical Preparation Of Copper Complex Aqueous Solution For Complex Reduction Method	K. Kumagai, T. Suzuki, P. Hishimone, M. Sato, H. Nagai	116
ECCEL11.	Analysis Of Traditional Wood Roofing Materials And Surface Protection Agents By Color Value Analysis Estimation Of Deterioration Properties	Hideto Takeuchi, Masaki Tamura	118
ECCEL12.	Room-Temperature Deposited Flexible B-Doped In2O3 Transparent Conductive Film	Shun Mori, Kanta Kibishi, Shinri Yamadera, Ayumu Nodera, Kotaro Watanabe, Ichiro Takano, Shinya Aikawa	119

ECCEL13.	Partial Reduction Of Weakly-Bonded Oxygen In Snox Thin Films By Dissociated Nitrogen Atoms	Kotaro Watanabe, Takuma Kawaguchi, Shinya Aikawa	121

Dependence of the CuO layer on photocatalytic properties of TiO_2/CuO thin films

Katsuyuki Takeda*, Ichiro Takano**

*Graduate school of Engineering, Electrical Engineering and Electronics, Kogakuin University, Japan
E-mail: cm21035@ns.kogakuin.ac.jp
******Faculty of Engineering, Department of Electrical and Electronic Engineering, Kogakuin University, Japan
E-mail: ct97912@ns.kogakuin.ac.jp

Abstract

For TiO_2, whose light absorption band is limited to ultraviolet light of about 380 nm, CuO thin films were placed as a lower layer to absorb energy in the visible light region. Photocatalytic properties improved with inserting the CuO layer and showed the higher value with increasing thickness of the CuO layer.

In recent years, various reports on artificial photosynthesis using metal oxides have been published. The first of these was the Honda-Fujishima effect using titanium dioxide[1]. Although many oxides have been studied since then, titanium dioxide is still at the center of research. The future goal of photocatalytic materials is the generation of organic compounds production, such as CH_4 or CH_3OH.

The photocatalytic effect of TiO_2, which is a typical photocatalytic material, has the strong antifouling and antibacterial property, whereas the problem of TiO_2 is that the photoenergy absorption wavelength band is limited to the ultraviolet region below 380 nm. Therefore, the authors have payed attention to multilayer films with CuO or Cu_2O as a lower layer to expand the light absorption band. In this study, the photocatalytic effect of TiO_2/CuO thin films using CuO having 570 nm in an absorption wavelength band was investigated.

The multi-process coating apparatus with RF helicon-plasma sputtering cathodes was used for TiO_2 and CuO thin film deposition. The glass (Eagle-XG) of 15 mm × 9mm × 1 mm in a size was used as a sample substrate, which was ultrasonically cleaned with an alcohol solution for 10 min. The substrates were introduced into the vacuum chamber and cleaned for 5 min by Ar plasma. The CuO thin films were deposited by reactive magnetron sputtering with an Ar flow rate of 20 sccm and an RF input power of 100 W. The film thickness of CuO was varied from 100 nm to 300 nm. After the CuO layers were prepared, the TiO_2 layers of 200 nm in a film thickness were deposited, by the condition of an Ar flow rate of 20 sccm, O_2 flow rate of 1.5 sccm, and an RF input power of 100 W.

The surface chemical state of the samples was analyzed by X-ray photoelectron spectroscopy (JPS-9030, JEOL Co.). The crystal structure was measured using X-ray diffractometer (SmartLab, Rigaku Co.) at an X-ray incident angle of 0.4°. Optical properties (absorbance) were measured by using a UV-visible spectrophotometer (UV-2550, Shimadzu Co.). The methylene-blue immersion test was carried out using quartz cells filled with 3 ml of a 10 ppm methylene blue solution. The cells with the sample were irradiated at 200 W/m^2 for 5 hours using an artificial solar lamp and the transmittance of the methylene blue chromaticity (peak wavelength: 667 nm) was measured at one-hour intervals.

Figure 1 shows transmittance changes of a methylene blue solution of a glass substrate without a film, TiO_2, TiO_2/CuO (100~200nm). The highest photocatalytic efficiency was obtained at the sample of the TiO_2/CuO (300 nm) thin film showing 91.7 % (5 hours) in a methylene blue transmittance, because the absorbance of the TiO_2/CuO (300 nm) thin film showed a longer absorption wavelength band than the those of other samples. The initial slopes indicating the photocatalytic ability was 43 (300 nm), 30 (200 nm), 28 (100 nm) , respectively.

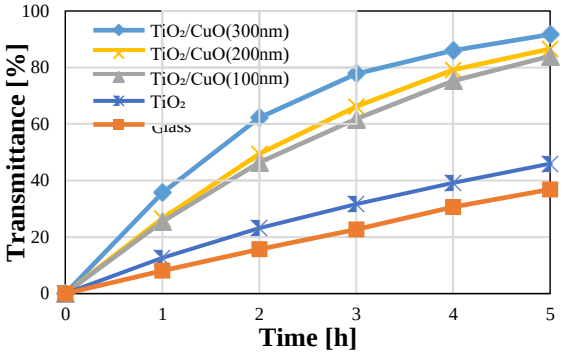

Fig. 1. Methylene blue chromaticity change (photocatalytic evaluation)

The absorption specta of the samples were measured using a UV-visible spectrophotometer, and it was found that the absorption edge expanded toward the longer wavelength side as the thickness of the TiO_2/CuO film increased, suggesting that the efficient absorption of visible light led to the improvement of the photocatalytic effect. This study confirms the effectiveness of CuO layers in TiO_2/CuO thin films.

References:

1)A. Fujishima and K. Honda, Nature, 238(5358), 37(1972).

2) Akihiro Joichi, Ichiro Takano: 2018 Japan Surface Vacuum Society Academic Lecture, 1P51S (2018.11.19).

XPS analysis of the binding states in nitrogen-doped SnO_x thin-films deposited by RF magnetron sputtering in N_2 atmosphere

Takuma Kawaguchi, Kotaro Watanabe and Shinya Aikawa

Department of Electrical and Electronic Engineering, Kogakuin University
E-mail: aikawa@cc.kogakuin.ac.jp

Abstract

In this study, we investigated the binding states of the nitrogen (N)-doped SnO_x thin-films deposited by RF magnetron sputtering in N_2 atmosphere. The fabricated N-doped SnO_x films deposited with the different N_2 concentrations were compared. The characterization was performed using X-ray diffractometer, X-ray photoelectron spectroscopy (XPS), and Hall effect measurement. The film deposited at 75% of N_2 concentration showed p-type behavior and carrier density was decreased compared to other conditions. The XPS analysis showed that amount of oxygen vacancy (V_O) decreased and the peak shift derived from adsorbed N species was observed in the higher binding energy, as the N_2 concentration increased. This indicates that N atoms substituted into O sites, and resulting that holes were generated. We believe that the adsorbed N atoms contribute to the reduction of carrier density causing charge trapping as NO^- components.

1. INTRODUCTION

Recently, all oxide CMOS and transparent solar cell applications composed of oxide semiconductors have been developed because they have unique advantages, for example low-temperature and large-area processability, high performance and optical transparency [1]. Typical p-type oxide semiconductors show less electrical properties compared to n-type, in particular mobility [1-3]. Thus, development of p-type oxide semiconductors similar to n-type are required. Generally, oxide semiconductors include large amount of oxygen vacancies (V_O). Because V_O generates electrons, sputtering conditions for obtaining p-type behavior is still challenging issue, thus far [4]. Various metal acceptor doping such as Al is attempted. Such cation doping causes unintentional charge compensation when acceptor ions are located next to V_O [5]. To solve the issue, we have focused on nitrogen (N) doping as a V_O passivation [6]. Since N^{3-} has almost same ionic radius and electronegativity as O^{2-}, it can be replaced into O-site in the SnO_2 matrix. N substitution leads to decrease the density of V_O; thus, improvement of hole mobility is expected [5-8]. In this study, we optimize sputtering conditions in N_2 ambient to fabricate p-type N-doped SnO_x (SnO_x:N) thin films and clarify their electrical properties, crystal structure and binding states.

2. EXPERIMENTS

SnO_x:N thin films was deposited on a Si/SiO_2 substrate using an RF magnetron sputtering in Ar/N_2 mixed gas atmosphere. The substrate temperature during deposition was set at 300 °C. A ceramic SnO_2 target (purity: 99.99 %) was used as the starting material. The RF power and the deposition pressure were fixed at 100 W and 0.12 Pa, respectively. The N_2 ratio was varied between 25 and 75 % for the deposition. The electrical properties of the thin films were measured at room temperature using a Hall-effect measurement system (Accent HL5500PC). The crystal structure was determined by an X-ray diffractometer (XRD, Rigaku SmartLab). The composition analysis and binding states of the thin film were characterized by X-ray photoelectron spectroscopy (XPS, JEOL JPS-9000MC).

3. RESULTS AND DISCUSSION

Figure 1 shows the relationship between N_2 concentration and the electrical properties (sheet resistance, carrier density, and mobility) of the fabricated SnO_x:N films deposited at N_2 ratio of 25 – 75 %. As the N_2 concentration increased, the sheet resistance increased and the carrier density decreased. In addition, the films deposited at 75 % showed p-type behavior.

Figure 2 shows the XPS O 1*s* spectra of the SnO_x:N films deposited at 25, 50 and 75 %, respectively. The O 1*s* spectrum can be deconvoluted into four peaks at 529.4−529.55, 530.35−530.37, 531.55−531.64, and 532.5 eV, which are components derived from SnO, SnO_2, V_O, and chemisorbed oxygen (O_{chem}), respectively [9,10]. The V_O concentration decreased from 17.52 to 15.14 % as the N_2 concentration increased. This is because N substitution to O site occurred, resulting that majority carriers were converted to holes. Furthermore, the SnO_2 component was decreased and SnO component was increased as the N_2 concentration increased. We suggest that this is because partial SnO bonds were generated as the N_2 concentration increased because of reduction by N plasma. As a result, valence band maxima become close to Fermi level by formation of hybridization orbitals of O and N.

Figure 3 also shows the XPS N 1*s* spectra of the SnO_x:N films deposited at 25, 50 and 75 %, respectively. The N 1*s* spectrum can be deconvoluted into three peaks at 396.98−397.05, 398.51−398.69 eV, and others, which are components derived from N-Sn bonding, Sn-O-N bonding, and chemisorbed

nitrogen (N_{chem}), respectively [11]. The adsorbed nitrogen can be decomposed into two peaks, 402.05 and 403.5 eV for molecular N_2 and NO^-, respectively [12,13]. The Sn-N bonding was dominant in all cases, which might be originated from N substitution to O site. Moreover, the Nchem component shifted to the higher energy, from 402.05 to 403.5 eV, as the N_2 concentration increased. This indicates that the chemisorbed species changed from N_2 to NO^- [9], and adsorbed species on the surface affect the carrier density. In other words, p-type conduction could be obtained in Ar/N_2 sputtering by optimization of both concentrations that V_O passivation of atomic N, and NO^- components.

4. SUMMARY

We investigated the optimum sputtering conditions for obtaining a p-type SnO_x:N thin-films using RF magnetron sputtering in an Ar/N_2 mixed gas atmosphere. The carrier density was decreased as the N_2 concentration increased, and resulting p-type conduction was obtained at N_2 concentration of 75 %. The XPS analysis indicated that V_O was decreased as the N_2 concentration increased. This suggest that the majority carriers in the SnO_x:N was converted to holes due to the N substitution to O site. Furthermore, since SnO component were increased as the N_2 concentration increased, N plasma was effectively reduced the film during deposition. The N 1*s* spectra revealed that chemisorbed specie was changed depend on the N_2 concentration and affects carrier density. We believe that the present result is useful for fabrication of p-type SnO_x-based films by reactive sputtering in N_2.

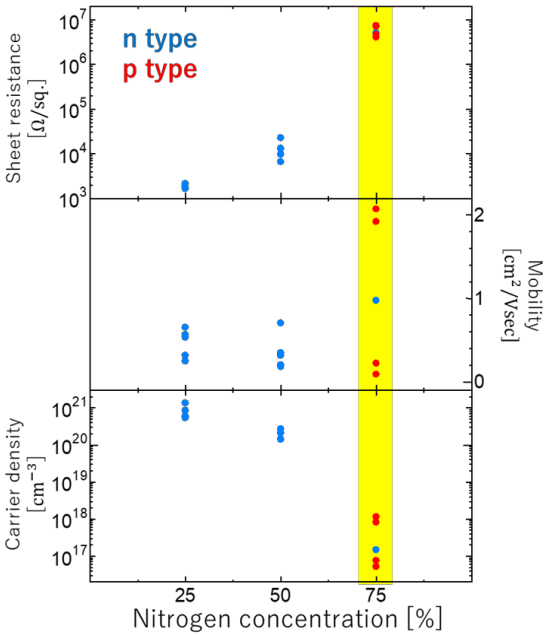

Fig. 1. Electrical properties of SnO_x:N thin films deposited at 25-75 % nitrogen partial pressure.

References:

[1] R. Barros, et al., Nanomaterials., **9**, 320 (2019).
[2] J. Um, et al., Mater. Sci. Semicond. Process., **16**, 1679 (2013).
[3] P.-C. Hsu, et al., ACS Appl. Mater. Interfaces, **6**, 13724 (2014).
[4] A. W. Lee, et al., ACS Appl. Electron. Mater., **2**, 1162 (2020).
[5] T. T. Nguyen, et al., Ceram. Int., **45**, 9147 (2019).
[6] K. Watanabe, et al., Submitted.
[7] Y. Kim, et al., Mater. Sci. Eng., B, **177**, 1470 (2012).
[8] Y. Kim, et al., Curr. Appl Phys., **11**, S139 (2011).
[9] M. Kwoka, et al., Thin Solid Films, 1,36-42 (2005).
[10] T. T. A. Tuan, et al., Opt. Mater., **111**, 110665 (2021).
[11] S. S. Pan, et al., Appl. Phys. A, **2**, 267 (2012).
[12] T. Maruyama, et al., J. Appl. Phys., **77**, 6641 (1995).
[13] J. Jiang, et al., Phys. Status Solidi B, **253**, 1087 (2016).

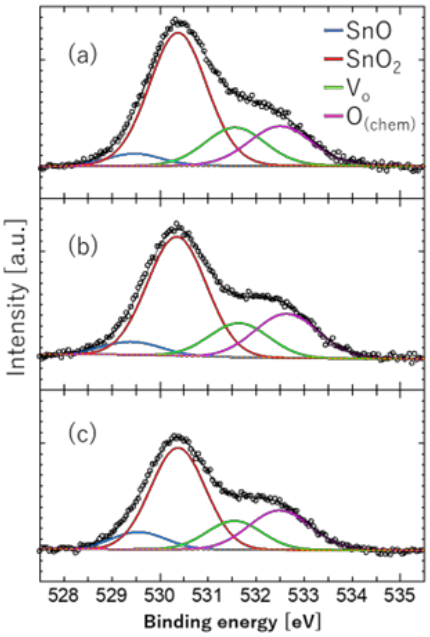

Fig. 2. XPS O 1s spectra of SnO_x:N film in various N_2 concentrations: (a) 25 %, (b) 50 %, and (c) 75 %.

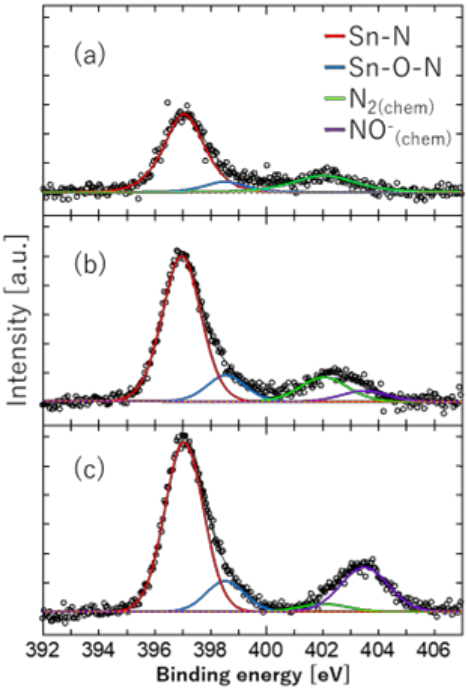

Fig. 3. XPS N 1s spectra of SnO_x:N film in various N_2 concentrations: (a) 25 %, (b) 50 %, and (c) 75 %.

Crystal Growth of Cu_3N by Mist CVD with Ethylenediamine

Shogo Yoshida, Hiroki Nagai, Tomohiro Yamaguchi, Takeyoshi Onuma, and Tohru Honda

Department of Electrical Engineering and Electronics, Graduate School of Engineering, Kogakuin University, Tokyo, Japan
E-mail: cm22047@ns.kogakuin.ac.jp

Abstract

In this study, Cu_3N films were grown on (0001) α-Al_2O_3 substrates by mist chemical vapor deposition. The source solution was prepared under different conditions and their crystalline properties were observed. In a solution of NH_3(aq.) mixed with ethylenediamine, Cu_3N was obtained thicker film than sample grown in solution with only NH_3(aq.). It was clarified that additional ethylenediamine affects the crystalline properties.

Introduction

Cu_3N is an indirect transition semiconductor that is composed by copper and nitrogen. These atoms are abundant on the earth. It has a band-gap of about 1.0 eV and high optical absorption coefficient in the 10^4 to 10^5 cm^{-1}. Therefore, Cu_3N is expected for solar cells application that doesn't include scarce resources [1]. It is reported that Cu_3N can be grown by mist CVD (chemical vapor deposition) [2]. Mist CVD is crystal growth method that uses atomized solution by the ultrasonic containing source material. The atomized solution is transferred to substrates by gas, then it grows on the heated substrates with thermal reaction. Since this method doesn't require vacuum, it has a simple system configuration and low cost. However, Cu_3N grown by mist CVD has some issues, it is hard to obtain sufficient film thickness. It is due to the aqueous ammonia (NH_3(aq.)) being highly volatile, it is speculated to be lost from solution during the crystal growth. Ethylenediamine (EDA) forms more stable complex with Cu than NH_3 [4].

In this study, we focused on ethylenediamine instead of NH_3(aq.) to increase Cu_3N film thickness.

Experiment

Cu_3N was grown on (0001) α-Al_2O_3 substrates by vertical type Mist CVD. Copper (II) acetylacetonate ($Cu(C_5H_7O_2)_2$) was used as a source material. Also 28% concentration of NH_3(aq.) was used. Table 1 shows the conditions for preparation of source solution. The solution was atomized by an ultrasonic transducer at 2.4 MHz, then the formed aerosols where it is transferred to a quartz furnace by nitrogen gas. The growth conditions are as follows, growth temperature: 300°C, growth time: 60 min., carrier gas and dilution gas are both nitrogen, and flow rates are 3.0 L/min., 0.3 L/min., respectively. Film thickness was measured by field emission scanning electron microscope (FE-SEM), crystal structure was evaluated by X-ray diffraction (XRD) measurement.

Table 1. Conditions of source solution.

	Concentration of $Cu(C_5H_7O_2)_2$ [mol/L]	Ratio in solution [%]		
		NH_3	EDA	H_2O
1	0.050	100	-	-
2	0.050	-	10	90
3	0.050	90	10	-

Results and Discussion

The cross-sectional SEM images are shown in Fig.1. The results show that film thickness of about 110, 750 and 350 nm were obtained for the solutions 1, 2, and 3, respectively. It is suggested that Cu forms a complex with NH_3 or EDA ligands. The complex of Cu and EDA is more stable than that of Cu and NH_3, which might supply the increased film thickness.

The XRD θ-2θ patterns are shown in Fig. 2. The peaks of 100 and 200 Cu_3N were observed for the samples grown with the solutions 1 and 3. On the other hand, the peaks were not clearly observed in the samples using the solution 2. The results indicate that NH_3 is a nitride source, and it has an important role in Cu_3N grown by mist CVD.

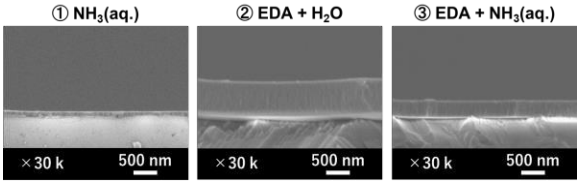

Fig 1. The cross-sectional SEM images for samples with different source solutions.

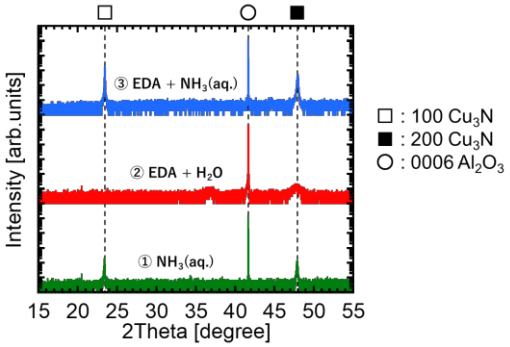

Fig 2. XRD θ-2θ patterns for samples with different source solutions.

References:

[1] K. Matsuzaki *et al.*, Adv. Mater. **30**, 1801968 (2018).
[2] T. Yamaguchi *et al.*, Appl. Phys. Express **13**, 075505 (2020).
[3] T. Kawaharamura, Jpn. J. Appl. Phys. **53**, 05FF08 (2014).
[4] F. Carrera *et al.*, Inorg. Chem. **43**, 6674-6683 (2004).

Deposition of nitrogen-doped titanium dioxide thin films via rf magnetron sputtering

Melanie M. Martinez[1], Takeyoshi Onuma[2], Hiroki Nagai[2], Tohru Honda[2], Shinya Aikawa[2], Tomohiro Yamaguchi[2] and Magdaleno R. Vasquez Jr. [1*]

[1]Department of Mining, Metallurgical and Materials Engineering, College of Engineering, University of the Philippines Diliman, Quezon City, Philippines
[2]Department of Electrical Engineering and Electronics, School of Advanced Engineering Kogakuin University Tokyo, Japan
E-mail: mrvasquez2@up.edu.ph

Abstract

Titanium dioxide (TiO_2) is commonly explored as an optoelectronic material because of its high stability. These applications include photocatalysis and photovoltaic (PV) devices. However, TiO_2 has poor visible light absorption, so its structure is modified to make it more active in the visible light region. TiO_2 can be modified in a variety of ways, such as adding a dopant, such as nitrogen (N). N-doped TiO_2 exhibits broad absorption in the visible light region, allowing the utilization of a large part of the solar spectrum when used as a photovoltaic device. In this study, thin films of undoped TiO_2 and N-doped TiO_2 are fabricated using an RF magnetron sputtering system that varies the gas ratio of oxygen and nitrogen gas.

Introduction

TiO_2 is active by UV light, so the efficiency of light utilization to the visible light region is very low. Therefore, it is necessary to extend the absorption wavelength range of TiO_2 to the visible light region by doping some elements to enhance the visible light sensitivity of TiO_2. Nitrogen doping showed good long-term stability, reduced recombination, and increased cell efficiency compared to undoped TiO_2. In this study, thin films of N-doped TiO_2 thin films will be fabricated using the rf magnetron sputtering system.

Experimental Method

Glass slides were cut into 1 x 1 cm^2 and ultrasonically cleaned in a series of acetone, ethanol, and deionized water baths for 10 min and air-dried using nitrogen gas. High-purity metallic titanium (Ti) target was used to grow the thin films. TiO_2 thin films were deposited via magnetron sputtering using the Ti target with varying nitrogen and oxygen gas concentrations. Deposition was made using different oxygen concentrations of 5%, 10 %, 15%, 20% and 25% oxygen. The sputtering power, deposition time, target-to-substrate distance, and working pressure were fixed at 150W, 30 minutes, 10 cm, and 1 Pa, respectively. The thin films were subjected to different characterizations.

Results and Discussion

X-ray diffractogram (Fig. 1) confirmed the presence of the anatase phase of TiO_2 at 2θ values at 25.30°, 37.87°, 48.03°, 54.16°, 55.34°, 62.76°, 69.17°, 70.43° and 75.39° with a tetragonal crystal structure.

UV-Vis (Fig. 2(a)) showed that the 5% O_2 has the highest transmittance in the visible region of around 75% while the pure TiO_2 is around 60% transmittance in the visible region. Thus, enhancing the transmittance of the thin film. The band gap was calculated using Tauc's plot method (Fig. 2(b)), and the deposited film thickness is around 120 nm.

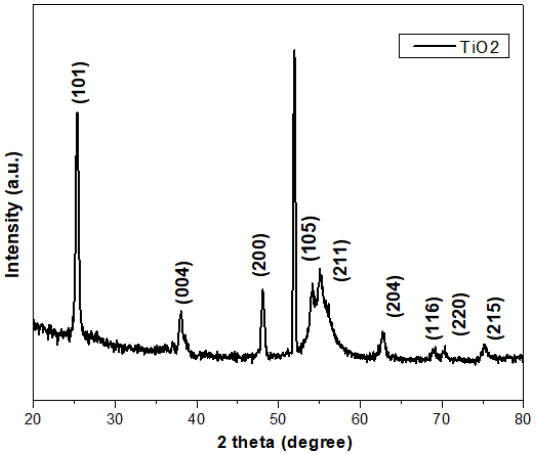

Fig 1. X-ray diffractogram of TiO_2 thin film

The optical band gap decreased upon the incorporation of nitrogen in the TiO_2 lattice. The lowest band gap is 3.40 eV which was obtained in 10% O_2 while the pure TiO_2 is around 3.78 eV.

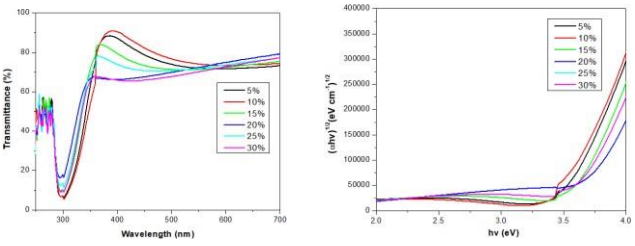

Fig 2. Transmittance of TiO_2 thin films

Table 1. Calculated Optical band gap

O_2 Concentration	Band gap (eV)
A-5%	**3.73**
B-10%	**3.40**
C-15%	**3.67**
D-20%	**3.85**
E-25%	**3.51**
F-30%	**3.78**

SEM images showed the morphological structure of the TiO_2 thin films with varying oxygen concentrations. SEM images showed uniformly distributed nanograins.

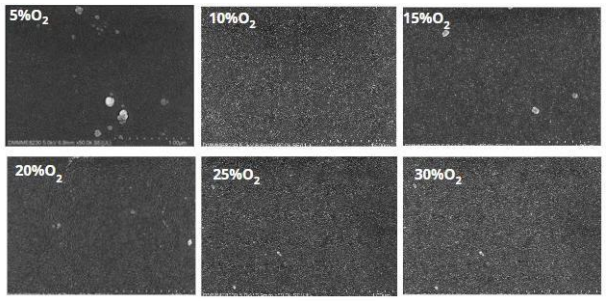

Fig 3. SEM images TiO_2 thin films.

The nitrogen doping in the TiO_2 lattice enhanced the optical band gap by shifting its wavelength towards the visible region and reducing its optical band gap. The presence of oxygen and titanium atoms were present in the samples**.** Further characterization will be done to confirm the presence of nitrogen on the TiO_2 thin film.

References:

[1] H. Fakhouri *et al*., Applied Catalysis B: Envi.l, 144, 12-21. (2014)

[2] D. Duarte et al., Materials Research, *20*, 549-554. (2017)

Growth of ZnO thin films via magnetron sputtering using a custom-made sintered target

Rozen Grace B. Madera[1], Hiroki Nagai[2], Takeyoshi Onuma[2], Tohru Honda[2], Tomohiro Yamaguchi[2] and Magdaleno R. Vasquez Jr. [1*]

[1]Department of Mining, Metallurgical and Materials Engineering, College of Engineering, University of the Philippines Diliman, Quezon City, Philippines
[2]Department of Applied Physics, School of Advanced Engineering, Kogakuin University, Tokyo, Japan
E-mail: mrvasquez2@up.edu.ph

Abstract

In this work, zinc oxide (ZnO) films were deposited on precleaned glass and silicon (Si) substrates via custom-built radio frequency (RF) magnetron sputtering using a sintered target. The substrates were deposited in an argon (Ar) environment with a base and working pressures of 5 and 9.5 Pa, respectively, at 50W incident RF power with varied deposition time. X-ray diffraction (XRD) of the films revealed a ZnO wurtzite structure with a dominant (002) crystallographic plane. Raman spectroscopy confirmed bands related to the wurtzite structure and a uniform thin film for a 4x4 um mapping mode. Scanning electron microscopy (SEM) images showed discernible grains with a size of 299 nm ± 20 for deposited film at 30 min which shows that grain growth has a proportional relation to the deposition time. UV-Vis spectra showed a thin film transparency in the range of 75-87% in the region of visible light. This study was able to demonstrate a method to prepare ZnO thin films via magnetron sputtering using an inexpensive target in sub atmospheric conditions.

Introduction

ZnO is an *n*-type semiconductor with a direct band gap of 3.37 eV that crystallizes into a hexagonal wurtzite structure under ambient conditions[1]. It is widely used in different industrial applications such as sensors, actuators, photodetectors, and so forth. Among the vacuum-based deposition techniques, RF magnetron sputtering is commonly used because of the ease of sputtering metal or oxide compounds, which is suitable for large-scale thin film deposition. However, commercial oxide targets are expensive and deposition systems require expensive turbomolecular pumps. In this work, ZnO films were deposited on glass and Si substrates via a custom-built RF magnetron sputtering system using a pressed powder target.

Methodology

A total of 8 g of ZnO powder (LR grade ≥ 99.99%) were grinded, loaded and pressed followed by calcination then sintering to make the target compact. The films were deposited in 1 cm x 2 cm pre-cleaned glass and Si substrates via custom-built RF magnetron sputtering system in an argon environment as shown in Fig 1.

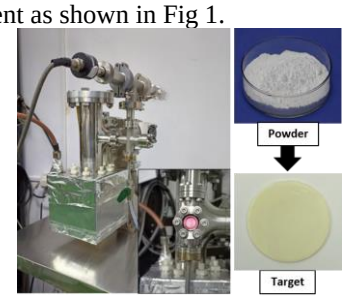

Fig. 1. The custom-built RF magnetron sputter system.

Table 1 shows the parameters used in this study. The deposited films were characterized include XRD and Raman spectroscopy for the structural properties, SEM for morphological analysis and UV-Vis spectroscopy for the optical band gap calculation.

Table 1. Summary of deposition parameters.

Parameters	Values
Base pressure (Pa)	5
Working pressure (Pa)	9.5
RF power (W)	50
Deposition time (min)	5-30

Results and Discussion

XRD of the powder target revealed a hexagonal wurtzite structure with major diffraction peaks at 31.75°, 34.41° and 36.23° which corresponds to (100), (002) and (101) planes respectively. In comparison with the powder target, XRD spectra of the ZnO film showed a dominant growth orientation at (002) plane while the other peak corresponds to the silicon substrate as shown in Fig. 2.

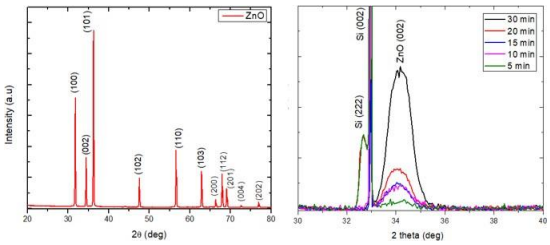

Fig. 2. XRD spectra of ZnO (a) powder target and (b) deposited thin film.

Raman analysis confirmed bands at 99, 437, and 574 cm^{-1} that corresponds to E2 (low), E2 (high) and A1 (LO) of the ZnO Raman vibrations while additional peak at 272 cm^{-1} which corresponds to additional vibrational modes related to defects as shown in Fig. 2[2]. Raman mapping mode was performed on the representative sample to check the uniformity for a 4x4 um size film as shown in Fig. 3.

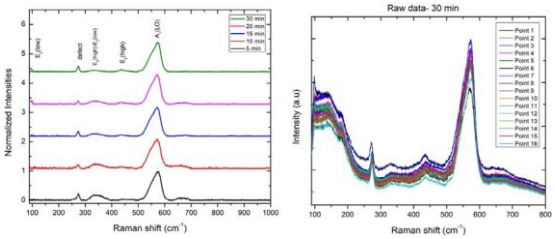

Fig. 3. Raman spectra of deposited ZnO thin film (a) point mode and (b) mapping mode.

SEM images of ZnO sputtered films revealed grains with larger size as deposition time is increased as shown in Fig. 4. The average grain size of the thin film deposited at 30 min is 299 nm ± 20 while grain sizes for 10-20 min are not discernable for 30kX magnification.

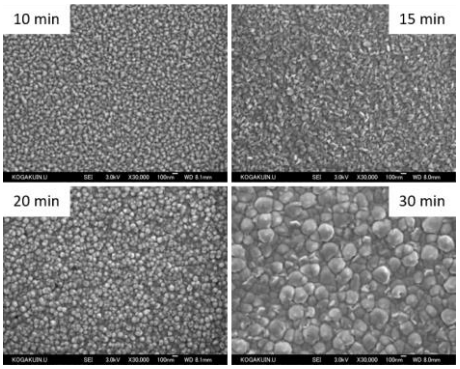

Fig. 4. SEM images of the deposited ZnO films.

UV-Vis transmittance spectra of the deposited ZnO thin films showed a transparency range of 75-87% at the visible light region as shown in Fig. 5. The optical band gap was calculated using Tauc's equation as shown in Table 2. The calculated band gap has a proportional trend with the deposition time which suggests that as thickness increases the optical band gap gets closer to the bulk value.

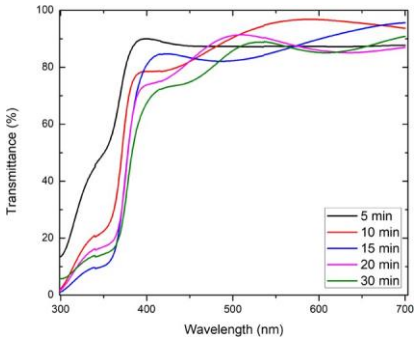

Fig. 5. UV-Vis transmittance spectra of the thin films.

Table 2. Optical band gap of the thin films.

5 min	3.25 eV
10 min	3.26 eV
15 min	3.25 eV
20 min	3.27 eV
30 min	3.31 eV

Conclusion

This study was able to demonstrate a method to prepare ZnO thin films via magnetron sputtering using an inexpensive target in sub atmospheric conditions.

References:

[1] A. Janotti and C.G. Van de Walle, *Rep. on Prog. Phys*, **72**, 126501.

[2] D. Montenegro, V. Hortelano, O. Martinez, V. Martinez, M.C Tomas, V. Sallet, V. Munoz-Sanjose and J. Jimenez, *Jour. Phys D: Appl. Phys*, **46**, 235302.

Study for Composition Control in Mist CVD Growth of α-GIO Alloys

Kai YAMADA[1], Tomohiro YAMAGUCHI[1,2], Takeyoshi ONUMA[1,2], and Tohru HONDA[1,2]

1. Department of Electrical Engineering and Electronics, Kogakuin University, Tokyo, Japan
2. Department of Applied Physics, School of Advanced Engineering, Kogakuin University, Tokyo, Japan

E-mail: cm22045@ns.kogakuin.ac.jp

Abstract

Gallium Indium Oxide (GIO) is an alloy semiconductor, which is composed of Ga_2O_3 and In_2O_3. The GIO alloys can be grown by Mist CVD, but it is difficult to control the composition of the alloys. Therefore, experiments were conducted by varying the In supply ratio. Cubic-GIO grew in the high In supply ratio region, and □- or □-(□-)GIO grew in the low In supply ratio region. This result suggests that □-GIO growth was reduction of premature reaction leads to □-GIO growth.

Introduction

Gallium Indium Oxide[$(Ga_{1-x}In_x)_2O_3$:GIO] is an alloy of Ga_2O_3 and In_2O_3, with each advantage of wide bandgap and excellent electrical conductivity, respectively. This can be applied to TFTs in displays[1]. In addition, the Mist chemical vapor deposition (Mist CVD) method has the potential to be used for the growth at a lower cost than conventional growth methods. Growth of high-quality Ga_2O_3 and In_2O_3 thin films has been reported by the Mist CVD, especially the metastable □ phase[2, 3]. □-GIO alloys growth of Mist CVD is also reported[4]. However, it is difficult to control the alloy composition. Composition control of □-GIO alloys is very important in term of mixing the source solutions at their respective supply ratios.

In this study, we aimed to grow □-GIO alloys on □-Al_2O_3 substrates. The In supply ratio was varied, and □-GIO was attempted to grow at each In supply ratio.

Experiment

GIO alloys thin films were grown on (0001)□-Al_2O_3 substrates by Mist CVD. Experimental conditions are shown in Table 1. X-ray diffraction (XRD) was used to evaluate the crystal structure, and scanning electron microscopy (SEM) was used to measure the cross-sectional morphology.

Table 1 Growth Condition.

Solutions	$Ga(C_5H_7O_2)_3$, $In(C_5H_7O_2)_3$
HCl concentration	1.2 mol/L
In supply ratio	0 ~ 100 mol%
Temperature	550ºC
Growth Time	60 min.

Result and Discussion

Figure 1 shows the results of XRD □-2□□measurements of GIO alloys thin films grown by changing the In supply ratio between 0 and 100 mol%, and Fig. 2 shows their cross-sectional SEM images. In the high In-supply ratio region, (100)-oriented cubic GIO films were grown three-dimensionally. On the other hand, at an In-supply ratio of 20 mol%, □- or □-(□-) GIO film was grown two-dimensionally.

This result suggests that □-GIO growth was inhibited by a premature reaction. It is known that even in other chemical vapor deposition methods such as MOCVD, the growth of crystals is inhibited by the change of precursors due to premature reactions. Especially in alloy systems, premature reactions occur during composition control, and studies have been conducted to suppress the progress of premature reactions[4]. In the Mist CVD , premature reactions are considered to occur at the stage of mixing the raw material solutions when they are prepared. Therefore, it is suggested that premature reactions affected the growth of □-GIO alloys by the Mist CVD.

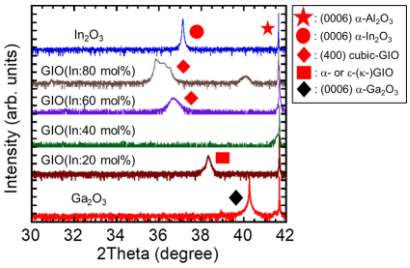

Fig. 1 XRD □-2□ measurements of GIO alloys grown at various In supply ratios.

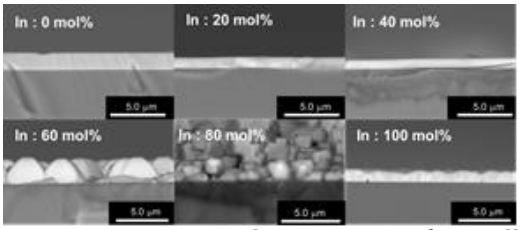

Fig. 2 Cross-sectional SEM images of GIO alloys grown at various In supply ratios.

References:

[1] Y. Terai, Sony Co., The journal of the Institute of Image Information and Television Engineer, 66, j339 (2012).
[2] D. Shinohara and S. Fujita, Jpn. J. Appl. Phys. 47, 9 (2008).
[3] N. Suzuki, K. Kaneko, and S. Fujita, J. Cryst. Growth 364, 30 (2013).
[4] N. Suzuki et al., Journal of Crystal Growth 401 670–672(2014).
[5] O. Makino et al, Appl. Surf. Sci. 159, 374 (2000).

Investigation on the Stability of Source Solution for the α-In_2O_3 Growth by Mist CVD

T. Yamamoto, A. Taguchi, R. Yamada, H. Nagai, T. Onuma, T. Honda, and T. Yamaguchi

Department of Electronic Engineering and Electronics, Kogakuin University, Japan
E-mail: cm22046@ns.kogakuin.ac.jp

Abstract

The variation in the incubation time of source solutions prepared for the α-In_2O_3 growth by mist chemical vapor deposition (mist CVD) was investigated. It was shown that the change in incubation time of the solutions affected the formation of acetylacetonate-derived organic substances, which in turn affected the growth of α-In_2O_3.

Mist chemical vapor deposition (mist CVD) is a solution-based growth method with a simple system configuration because of its ability to grow under atmospheric pressure. Single-crystalline group-III oxide semiconductor films, such as indium oxide (In_2O_3), have been realized by mist CVD [1]. Indium oxide (In_2O_3) has two types of crystal structures; body-centered cubic bixbyte-type (c-In_2O_3) and rhombohedral corundum-type (α-In_2O_3). Among these, we have successfully grown α-In_2O_3 films by mist CVD on α-Al_2O_3 substrates [2].

In the mist CVD growth of α-In_2O_3, the In-based powders, such as $In(acac)_3$ and In_2O_3 powders, is first dissolved by HCl. The source solution is prepared by adding the dissolved In-based powders to deionized water. However, the stability of the source solution has uncleared. In this study, the variation in the incubation time of source solutions prepared for the growth of α-In_2O_3 by mist CVD was investigated.

$In(acac)_3$ was mixed with HCl of 36% concentration to 0.05 mol/L as a starting material. Similarly, In_2O_3 powder was mixed with HCl at a concentration of 0.025 mol/L. The concentration of HCl was kept at 1.2 mol/L, and the incubation time of the dissolved In-based powders with HCl was varied from 0 to 25 days. Afterward, 100 mL of the source solution was adjusted by adding deionized water. Absorbance measurement was performed on these solutions. In_2O_3 thin films were grown on (0001)α-Al_2O_3 substrates by mist CVD in order to study the effect of solution change. The growth conditions were as follows: growth temperature was 550°C, carrier gas (O_2) flow rate was 5.0 L/min., dilution gas (O_2) flow rate was 0.5 L/min., and growth time was for 60 minutes. For the grown thin film, surface observation by scanning electron microscopy (SEM) was used for evaluation.

The absorbance spectra for each solution used in the growth are shown in Fig. 1. In the $In(acac)_3$ solution, the absorbance spectra shifted to longer wavelengths as the incubation time increased, and changes in the waveforms were observed. On the other hand, for the In_2O_3 powder solution, the spectral shift was not observed after 1 day of incubation. Figure 2 shows the surface SEM image of the grown In_2O_3 thin film. In the $In(acac)_3$ solution, the growth pattern of the In_2O_3 thin film changed with the time of incubation, and the longer the incubation time, the rougher the surface morphology was observed. In the case of In_2O_3 powder solution, no significant change in the surface condition was observed after 1 day of incubation time. It has been reported [3] that a peak appears at the long wavelength side when an organic compound having conjugated bonds is present in the solution, and the present results may be attributed to the formation of acetylacetonate-derived organic compound having a conjugated system. In addition, the change shown in Fig. 2 occurs in the $In(acac)_3$ solution, indicating that these organics affect the crystal growth.

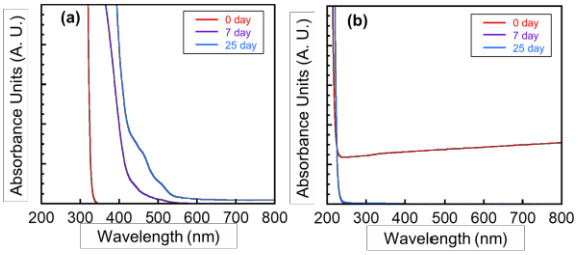

Fig. 1 Absorbance spectra of source solutions With different incubation times. (a) $In(acac)_3$, (b) In_2O_3 powder

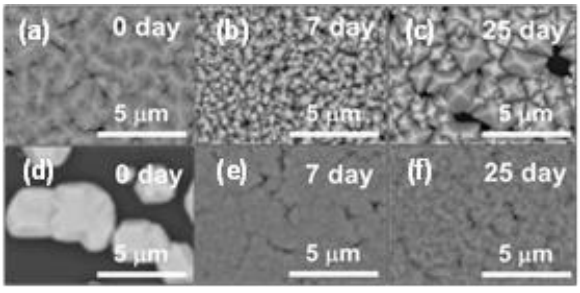

Fig. 2 Surface SEM images of In_2O_3 thin films grown by varying the solution incubation time. (a-c) $In(acac)_3$, (d-f) In_2O_3 powder

References:

[1] K. Kaneko *et al.*, Appl. Phys. Exp. **8**, 095503 (2015).
[2] T. Yamaguchi *et al.*, Appl. Phys. Exp. **13**, 075504 (2020).
[3] H. Sahabudeen *et al.*, Nature Communications. **7**, 13461 (2016).

Roles of In Doping in Rocksalt-structured MgZnO Films Grown by Mist CVD Method

Masaki Matsuda[1,*], Kotaro Ogawa[2,1], Yuichi Ota[3], Tomohiro Yamaguchi[1], Kentaro Kaneko[4], Shizuo Fujita[5], Tohru Honda[1], and Takeyoshi Onuma[1]

[1] Kogakuin University, Japan, [2] ORC Manufacturing Co., Ltd., Japan
[3] Tokyo Metropolitan Industrial Technology Research Institute, Japan
[4] Ritsumeikan University, Japan, [5] Kyoto University, Japan
**E-mail: cm21047@ns.kogakuin.ac.jp*

-Abstract-

Control of n-type conductivity is an important function to realize the RS-MgZnO based far UV emitter. In this study, we investigated the roles of In doping in RS-MgZnO films grown by mist CVD. The In concentration in MgO substrate stayed 0.4% even if the molar concentration in the solution increased. The electrical resistivity values of In doped MgZnO films could be reduced much lower than MgO substrate.

-Introduction-

Rocksalt-structured (RS) MgZnO is attracting attention as an emerging ultra-wide bandgap semiconductor for far UV light emitter [1]. We have reported growth of RS-MgZnO films by the mist CVD method and their emission properties [1-3]. Control of n-type conductivity is an important function to realize the RS-MgZnO based far UV emitter. In traditional wurtzite-structured MgZnO alloys, n-type conductivity has been realized by doping with group-III elements, i.e., Al or Ga [4,5]. In this study, we investigated the roles of In doping in RS-MgZnO films grown by mist CVD.

-Experiment-

$Mg(CH_3COO)_2{\cdot}4H_2O$ and $Zn(CH_3COO)_2{\cdot}2H_2O$ were dissolved in a mixed solution of deionized water and acetic acid (4 : 1 in volume) with different Mg content in the solution. The In doping was achieved by adding $In(CH_3COCHCOCH_3)_3$ to the precursor solution in the range from 0.2 to 3.0 mol%. Oxygen gas was used as a carrier and a dilution gas with flow rates of 4.0 and 0.5 L/min, respectively. The films were grown on MgO (100) substrates at 700°C. The films were evaluated by spectroscopic ellipsometry, X-ray diffraction (XRD), Rutherford backscattering spectrometry (RBS), and electrical resistivity measurements.

-Results and Discussion-

Figure 1 shows 204 XRD reciprocal space mapping (RSM) of the In doped MgO films (MgO:In). Grown layer was almost coherently grown on MgO substrate. The solidus concentration of In, which was determined by using the lattice constant from the XRD RSM and elastic stiffness constants [6], was 0.40% for both samples. The solidus concentration of In were also quantified by the RBS measurements to be 0.36%, 0.40% for the films with the molar concentration of In in the solution of 0.9 mol% and 1.8 mol%, respectively. XRD RSM results were in agreement with the RBS results. The result implies that the solidus concentration of In in MgO was no more than 0.4% even if the molar concentration in the solution increases. The electrical resistivities for the $Mg_{0.8}Zn_{0.2}O$:In films were 21.7 Ω·cm and 8.6 Ω·cm with In concentration in the solution of 1.0 mol% and 2.0 mol%, respectively. The values were much lower than the MgO substrate being 6.4 MΩ·cm.

-Summary-

In this study, we investigated the roles of In doping in RS-MgZnO films grown by mist CVD. The In concentration in MgO substrate stayed 0.4% even if the molar concentration in the solution increased. The electrical resistivity values could be reduced much lower than MgO substrate.

-Acknowledgement-

This work was supported in part by Grants-in-Aid for Scientific Research Nos. 20H00246 and 22K04952 from MEXT, Japan.

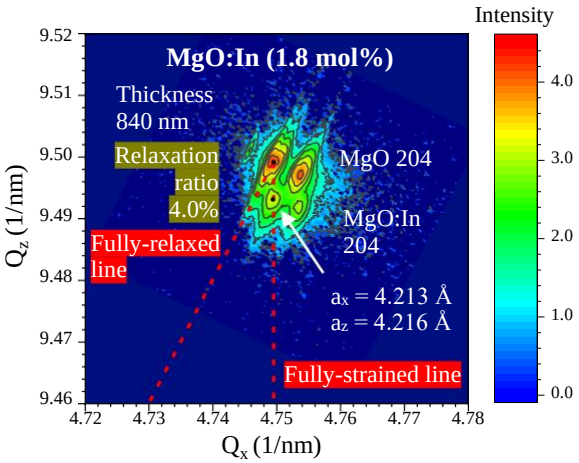

Figure 1. XRD RSM for MgO:In (1.8 mol%) near 204 diffraction spots.

-Reference-

[1] K. Kaneko *et al*., J. Soc. Mat. Sci., Japan **70**, 727 (2021).
[2] T. Onuma *et al*., Appl. Phys. Lett. **113**, 061903 (2018).
[3] K. Ishii *et al*., Appl. Phys. Express **12**, 052011 (2019).
[4] K. Matsubara *et al*., Appl. Phys. Lett. **85**, 1374 (2004).
[5] J. G. Lu *et al*., Appl. Phys. Lett. **89**, 262107 (2006).
[6] M. C. Wen *et al*., J. Cryst. Growth **477**, 169 (2017).

Realization of high mobility in α-In_2O_3 film grown by mist CVD with different concentration of In_2O_3 powder as source precursor

Akito Taguchi[1,*], Takeyoshi Onuma[1,2], Tohru Honda[1,2], and Tomohiro Yamaguchi[1,2]

1. Department of Electrical Engineering and Electronics, Graduate School of Engineering, Kogakuin University, Tokyo, Japan
2. Department of Applied Physics, School of Advanced Engineering, Kogakuin University, Tokyo, Japan

*E-mail: cm21033@ns.kogakuin.ac.jp

Abstract

The epitaxial growth of α-In_2O_3 films by Mist CVD method with different concentration of In_2O_3 powder as a source precursor was carried out. With increasing the concentration of In_2O_3 powder, improvement of the thickness, crystallinity, carrier concentration and Hall mobility were observed. The lowest carrier concentration of 3.0×10^{17} cm^{-3} and the highest Hall mobility of 265 $cm^2 V^{-1} s^{-1}$ was obtained in the film grown with the powder concentration of 0.15 mol L^{-1}. Temperature-dependent Hall measurements of the film indicated that the mobility is dominated by optical phonon scattering at room temperature.

1. Introduction

Amorphous and polycrystalline In_2O_3 films doped with Sn are widely used as transparent conductive oxides for flat panel displays and solar cells [1,2]. Alternatively, research interest has been directed towards single crystalline In_2O_3 due to its potential for active element in the electronic devices. In_2O_3 has two types of crystal structures: one is a cubic bixbyite structure (c-In_2O_3) as the most stable phase, and another is a rhombohedral corundum structure (α-In_2O_3) as a metastable phase. The pure α-In_2O_3 films can be grown by mist chemical vapor deposition (mist CVD) method on α-Al_2O_3 substrates [3]. The mist CVD method has been attracting attention as a new generation epitaxial growth method because it can be performed under atmospheric pressure, and it is a solution-based growth method using a simple system configuration.

In the mist CVD growth of α-In_2O_3, a small amount of hydrochloric acid (HCl) has usually been added to an aqueous solvent to dissolve the source precursor. We have found that adding HCl to the source solution affected not only the dissolution of source precursor but also the growth kinetics itself [4,5]. The growth-rate enhancement and film-quality improvement were clealy obserevd with increasing HCl concentration [5], suggesting that high growth rate (or thick film growth) improves the crystal qualty of α-In_2O_3. In this study, α-In_2O_3 films were grown by mist CVD with different concentrations of In_2O_3 powder as a source precursor.

2. Experiment

In_2O_3 films were grown by mist CVD. In_2O_3 powder was used as the source precursor. The In_2O_3 powder concentration was varied between 0.025 and 0.25 mol L^{-1}, in which the HCl concentration was fixed to be at 2.3 mol L^{-1}. The In_2O_3 films were grown at 550°C for 1 h on (0001) α-Al_2O_3 substrates.

3. Results and Discussion

X-ray diffraction (XRD) 2θ-ω profiles of In_2O_3 films grown with different concentration of In_2O_3 powder was shown in Fig. 1. 0.025-0.15 mol L^{-1} of In_2O_3 powder showed only α-phase peaks, though the peak from cubic phase was slightly observed for the films grown with over 0.20 mol L^{-1}. Figure 2 (A) shows the growth rate of α-In_2O_3 films. The growth rate increased with increasing In_2O_3 powder concentration, and the highest growth rate of 4.6 μm h^{-1} was obtained at the powder concentration of 0.15 mol L^{-1}. Further increase of the powder concentration caused the decrease of growth rate. Figure 2 (B) shows the full width at half maximum (FWHM) values of the X-Ray rocking curve (XRC) profile of 0006 and 10-14 α-In_2O_3 diffraction. With increasing powder concentration up to 0.15 mol L^{-1}, the improvement of crystal quality, especially on the twist distribution, was observed. Figure 2 (C) shows the carrier concentration and Hall mobility of α-In_2O_3 films. With increasing the powder concentrations up to 0.15 mol L^{-1}, the improvement of electrical properties (decrease of carrier concentration and increase of Hall mobility) was also observed. The Hall mobility of 265 $cm^2 V^{-1} s^{-1}$ and the carrier concentration of 3.0×10^{17} cm^{-3} was obtained in the film grown with the powder concentration of 0.15 mol L^{-1}. Thus, it can be concluded that high growth rate (or thick film growth) was realized by increasing the concentrations of HCl as well as In_2O_3 powder, and this resulted in the improvement of the crystal quality. Figure 3 shows the temperature dependence of carrier concentration and Hall mobility in the α-In_2O_3 film grown with powder concentration of 0.15 mol L^{-1}. Pronounced carrier

freeze-out was observed in a temperature range of 300-100 K, suggesting that the α-In_2O_3 film would be in a near-non-degenerate conductivity. A saturation of the carrier freeze-out was observed in low temperature. The result would be explained by the existence of SEAL as has been reported for the cubic-In_2O_3 films [6,7]. The Hall mobility increased by following $\mu \propto T^{-1.5}$ as temperature decreased. The highest Hall mobility of 686 $cm^2\ V^{-1}\ s^{-1}$ was observed at 100 K. The result indicated that, the mobility is dominated by optical phonon scattering at room temperature.

Acknowledgement

The authors would like thank Prof. S. Fujita of Kyoto University, and Prof. K. Kaneko of Ritsumeikan University, and Profs. M. Sato, H. Nagai and A. Sekiguchi of Kogakuin University for their fruitful discussion.

References:

[1] B. G. Lewis and D. C. Paine, *MRS Bulletin* **25**, 22 (2000).

[2] T. Koida, *Phys. Status Solidi A* **214**, 1600464 (2017).

[3] N. Suzuki, K. Kaneko, S. Fujita, *J. Cryst. Growth* **364**, 30 (2013).

[4] T. Yamaguchi, S. Takahashi, T. Kiguchi, A.Sekiguchi, K. Kaneko, S. Fujita, H. Nagai, M. Sato, T. Onuma, and T. Honda, *Appl. Phys. Express* **13**, 075504 (2020).

[5] A. Taguchi, S. Takahashi, A. Sekiguchi, K. Kaneko, S. Fujita, T. Onuma, T. Honda, and T. Yamaguchi, *Phys. Status Solidi B* **259**, 2100414 (2021).

[6] O. Bierwagen, and James S. Speck, *Appl. Phys. Lett.* **97**, 072103 (2010).

[7] K. Goto A. Mori, H. Nakahata, R. Togashi, and Y. Kumagai, *Jpn. J. Appl. Phys.* **60**, 125506 (2021).

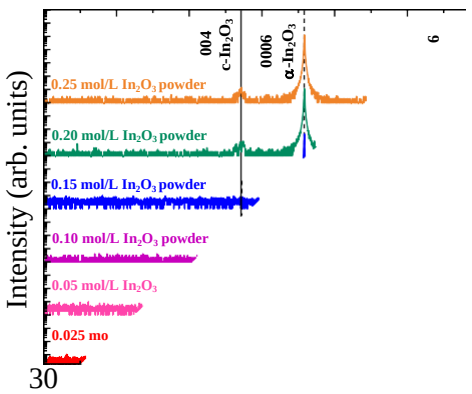

Fig. 1. 2θ-ω profiles of In_2O_3 films grown with different concentrations of In_2O_3 powder as a source precursor.

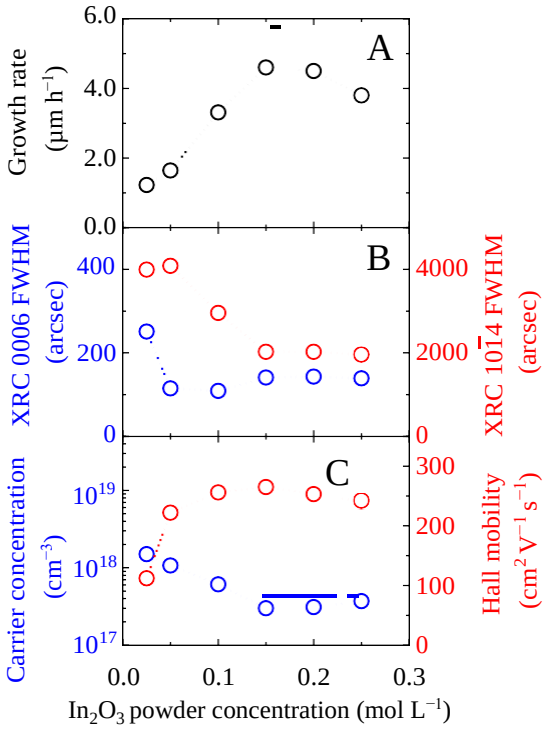

Fig. 2. Growth rate (or thickness), XRC profile of 0006 and 10-14 α-In_2O_3 diffraction, carrier concentration and Hall mobility of a-In_2O_3 films as a function of In_2O_3 powder concentration.

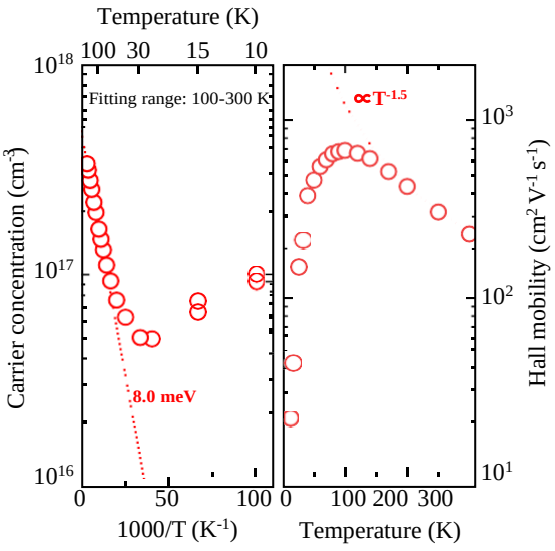

Fig. 3. Temperature dependence of carrier concentration and Hall mobility in the α-In_2O_3 film grown with powder concentration of 0.15 mol L^{-1}.

Electrochemical Preparation of Copper Complex Aqueous Solution for Complex Reduction Method

K. Kumagai[1)], T. Suzuki[2)], P. Hishimone[3)], M. Sato[2)], and H. Nagai[1), *]

1) Electrical Engineering and Electronics Program, Graduate School of Engineering, Kogakuin University, Japan
2) Kogakuin University, Japan
3) Faculty of Agriculture, Engineering & Natural Sciences, University of Namibia, Namibia
E-mail: nagai@cc.kogakuin.ac.jp

Abstract

The copper complex aqueous solution as a source of copper film via the complex reduction method was prepared by an electrochemical procedure from copper plates. Electrolysis for solution preparation was performed at a constant current of 1.7 A and ambient temperature for 160 min, and the copper concentration of 0.38 mg/L was determined by using flame atomic absorption spectrometry.

Introduction; Many researchers attempted to prepare copper films for use in various applications due to their thermal and electrical conductivity. Various deposition technologies including PVD, CVD, and plating for good quality copper film were reported. Very recently, we reported that the anti-SARS-CoV-2 (COVID-19) copper film can be produced on a Na-free glass surface by simply immersing it in a mixed copper complex aqueous solution which involves copper formate, ammonia, and ascorbic acid [1]. A well-adhered copper film was formed on the glass substrate without surface treatment such as catalyst addition.

The direct preparation of copper complex aqueous solutions, which will be the source of copper films, from metallic copper indicates the recyclability of the obtained copper films. In this study, the copper complex aqueous solution was directly prepared from a copper plate via electrochemical method, and the copper film on a quartz glass substrate using the complex reduction method was then fabricated.

Experimental; The aqueous solution of 25% NH_3 (24.9 g) and $HCOONH_4$ (11.5 g) was added to 269 g of deionized water. The mixed solution was mechanically stirred for 1 h at room temperature and used as the electrolytic solution. The electrochemical preparation of the copper complex aqueous solution was performed in a 300 mL glass container at ambient temperature. Two Cu plates (300 × 37 × 0.3 mm^3) as electrodes were immersed into the electrolytic solution. The constant current of 1.7 A was applied to the Cu electrodes, from a constant-current direct current power supply (AD-8723D, A&D Co., Ltd). Electrolysis was performed for 160 min at ambient temperature with mechanical stirring on a magnetic stirrer to obtain the precursor solutions (**S_{Elect}**).

An aqueous solution containing the copper (II) complex of ammonia (**$S_{complex}$**) was prepared as a reference. The solution was prepared by mixing the 13.7 g of copper (II) formate tetrahydrate and 24.3 g of 25% ammonia solution in 160 g of deionized water. The mixed blue solution was stirred for 1 h at approximately 23°C. The concentration of Cu^{2+} ions was 0.3 mmol g^{-1}.

The absorbance of **S_{Elect}** and **$S_{complex}$** were measured by a UV-Vis spectrophotometer (UV-1900i) in the double beam mode with the wavelength range of 200–1100 nm. A quartz glass cell of a 1 mm light path was used for measurement, and the air was used as a reference. The concentration of Cu ions of **S_{Elect}** and **$S_{complex}$** was determined using flame atomic absorption spectrometry (FAAS) (AA-7000). These solutions were 5×10^4 times diluted for the FAAS measurement. The pH of the solutions was measured using a pH meter (PH-201).

Results & Discussion; The absorption spectra of **S_{Elect}** and **$S_{complex}$** are shown in Figure 1. The maximum absorption position of a characteristic band in the visible region was observed at 610 nm for both solutions. Based on Lambert-Beer's law, the absorption spectra suggest that the Cu concentration of **$S_{complex}$** is 1.7 times higher than that of **S_{Elect}**. However, the Cu concentration of **S_{Elect}** and **$S_{complex}$** measured by using FAAS was 0.38 and 0.30 mg/L, respectively. The pH values of **S_{Elect}** and **$S_{complex}$** were at 11.2 and 10.8, respectively. These results suggest that the electrochemically prepared solution is different from that of typical ammine complex of Cu(II). The copper film fabrication using the **S_{Elect}** will be also presented.

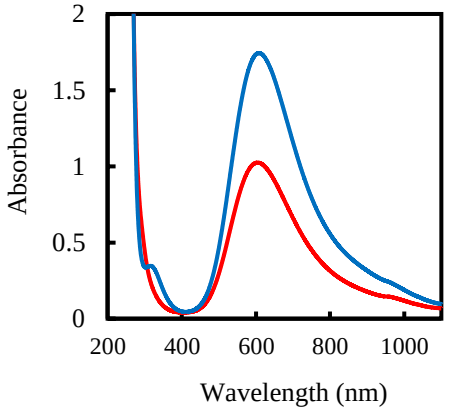

*Figure 1. Absorption spectra of **S_{Elect}** (Red) and **$S_{complex}$** (Blue).*

References:

[1] H.J. Wu, H. Nagai, T. Douura, M. Ishii, H. Kawakami, E. Nakayama, T. Shioda, M. Sato, *Funct. Mater. Lett.*, **15**, 1−8 (2022).

Analysis of Traditional Wood Roofing Materials and Surface Protection Agents by Color Value Analysis Estimation of Deterioration Properties

Hideto Takeuchi*,[a],Masaki Tamura**

*1st-Master Course student, School of Architecture, Kogakuin University, Tokyo, Japan
**Professor, School of Architecture, Kogakuin University, Tokyo, Japan
E-mail: [a]dm22041@g.kogakuin.jp

Abstract

Traditional roofing is the subject of this study. The purpose of this study is to examine the extension of the roof replacement period and the establishment of an index for judging deterioration. We divided the deterioration of wood into four stages, and conducted experiments related to each stage. Each result was subjected to multiple regression analysis, and a calculation formula for estimating the result of each test was created. In this outline, only the examination of the color value is described. The results are as follows. It was found that the necessary period of maintenance can be estimated by grasping the period during which the brightness increases due to the elution of lignin. By creating a calculation formula, it became possible to estimate from the measurement results of non-destructive tests even in tests involving destruction.

1. Introduction:

In recent years, while environmental problems such as global warming have attracted attention, the realization of a low-carbon society has been advocated. Wood has the effect of storing carbon and reducing carbon dioxide emissions, and contributes to low carbonization. More and more use of wood is expected.

However, the physical lifespan of wooden roofing materials is about 25 to 30 years, and there are issues such as a decrease in the number of craftsmen with traditional skills and long-term economic viability. Therefore, it is necessary to consider the application of modern technology such as surface protection[3]. Therefore, we will investigate the state of deterioration of the modified wooden roof materials, verify the difference in the state of deterioration depending on the modification process, and aim to prolong the period of reroofing. This synopsis is an in-depth analysis based on previous research[4), 5)].

2. Test Items and Materials Used:

Table 1 shows the types of specimens used in this study. Categorized according to tree species and locality and so on. Table 2 shows the modification treatment conditions applied to the specimens. The test specimen was constructed in Enzan, Koshu City, Yamanashi Prefecture in 2009 and has been exposed to the outdoors until now[1)2)]. Test items are shown in Table 3.

3. Overview of Deterioration Property Investigation Test:

From the items in Table 3, the deterioration of the test specimens in which each wood was subjected to the modification treatment was evaluated. Based on the survey of past research, the degradation properties of wood were divided into levels. Conduct the tests associated with each degradation. Fig. 2 shows a conceptual diagram of deterioration.

Table 1 Characteristics of materials used for shingle roofing material specimens[1)]

sign	tree species	production area	age of a tree (years)
Aas45	Cedar(s)	Akita(A)	46
Aas90			88
Ans170			170
Mas35		Miyazaki(M)	35
Mas80			80
Ank50	chestnut tree(k)	Akita(A)	50
Casa40	Chamaecyparis pisifera	Chichibu(C)	40

Table 2 Modification treatment conditions

No.	Type	colour
①	Highly water-repellent silicone	Clear
②	Highly durable acrylic silicone	White
③	stain paint	Black
④	stain paint	White
⑤	Persimmon astringent liquid	Brown
⑥	Pyroligneous acid	Brown
⑦	None(Draining copper plate)	-
⑧	None	-

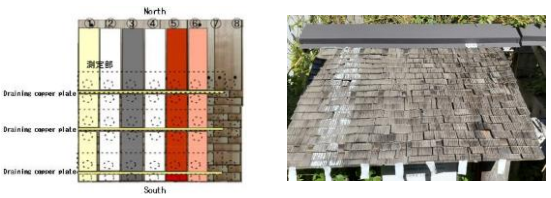

a) Test object image diagram　　b) Photo of the specimen(2021)

Fig 1 Schematic diagram of the specimen

Table 3 Deterioration level of wood and test details

Assumed degradation level	Degradation type	Test items	Contents of the test
L1	surface fading	surface color measurement	Measure the L*a*b* of the specimen
L2	material elution	Elution part measurement	Volume measurement of the elution part of the specimen exposed to the outdoors
L3	Increase of void space	Water content test	Measure water absorption (%) and drying speed (g/min)
L4	Decrease in strength and increase in defect	Surface penetration strength test	Measuring surface penetration strength with a digital force gauge
		Measurement of roof area reduction rate	Measure the amount of falling off and elution of the material by the reduction rate (%) of the area of the specimen

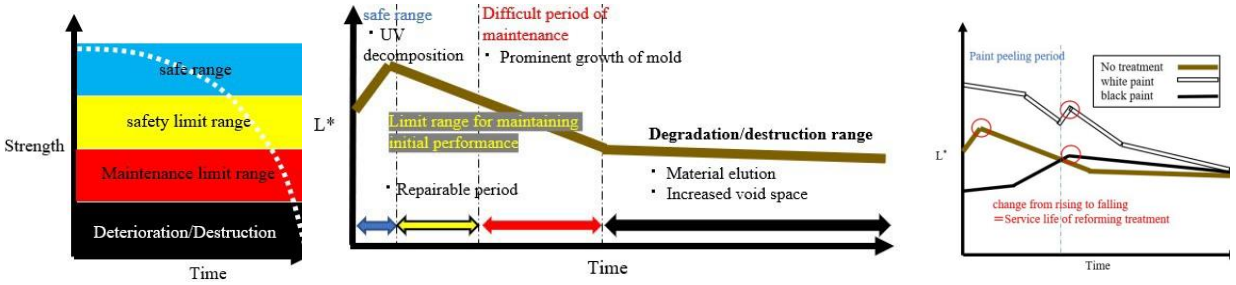

a) Degradation curve

b) Relationship diagram between degradation curve and color value

c) Criteria for service life of the specimen

Fig 2 Conceptual diagram of the concept of deterioration

4. Overview of Deterioration Property Investigation Test:

4.1 Measurement of Surface Color of Wood Roofing Material Specimen (L1)

The L*a*b* values of specimens exposed for a long period of time were measured. Measure 48 times in total, twice each at the top, middle, and bottom for the 8 types of modification treatment. The color values over time are shown graphically.

FIG. 3 shows the measurement results of Aas45. The horizontal axis represents time, and the vertical axis represents L* values. The L* value of the test piece (⑧) without modification treatment increased once in about half a year after construction. It can be assumed that this is due to the elution of lignin. After that, the lightness is reduced by dirt and black mold.

This tendency was also seen with highly water-repellent silicone paint (①), persimmon astringent liquid (⑤), pyroligneous acid (⑥), and none (Draining copper plate) (⑦). The white stain-based paint (④) showed the same tendency after the brightness decreased due to peeling of the paint. The black stain-based paint (③) increased in brightness due to the peeling of the paint, and after that, the change was similar to that of the other specimens. From these, the required period of maintenance can be estimated. Results of other specimens are shown in Fig4. The result is similar to Aas45.

4.2 Estimation of Service Life of Reforming Treatment (L1)

Surface colorimetric measurements were found to be predictive of paint service life. The service life of the paint is defined as the point at which the brightness changes from an increase in brightness due to lignin elution to a decrease in brightness due to dirt, etc. [Fig. 2(b) and Fig. 5]. Fig. 7 shows the average service life of each specimen. The highly durable acrylic silicone paint (②) is excluded because the aforementioned tendency cannot be found from Fig. 3. Pyroligneous acid (⑥), none(Draining copper plate) (⑦), and no treatment (⑧) are less than 5 months old. The untreated specimen showed earlier increase in brightness due to the elution of lignin than any specimen. It can be said that even traditional treatments are effective in preventing this deterioration. Highly water-repellent silicone paint (①) and persimmon astringent liquid (⑤) lasted more than 6 months. In these two cases, the traditional protective paint had a higher protective ability than the modern paint. Black stain paint (③) and white stain paint (④) have a service life of 2 years or more. Relatively long duration of protection. Maintenance before this number of years leads to longlife.

5. Conclusion

This study clarified the following.

1) The useful life of each modification treatment can be estimated by the period of lightening caused by the elution of lignin.
2) We were able to quantitatively evaluate the degree of deterioration of wooden roofs at each deterioration level of wood.
3) Penetration strength, which is an item of L4, can now be estimated non-destructively by a calculation formula.

References:

[1] Minako Kiyonaga: Evaluation of long-term durability properties of traditional shingled roofs with modified materials and development of sustainable conservation techniques, Part 1. Outdoor exposure test of various shingled roofs (roofing materials, material construction), Japan Society of Finishing Engineers, Conference Proceedings of academic lectures, 2010-7H. Nagai, S. Aoyama, H. Hara, C. Mochizuki, I. Takano, N. Baba, M, Sato, J. Mater. Sci., 44, 861–868 (2009).

[2] Minako Kiyonaga: A study on maintenance and preservation methods for high-grade wood used in traditional wooden buildings, Result of one-year outdoor exposure test of six woods, The Japan Society of Finishing Engineers, Proceedings of Annual Conference, 2011

[3]–Architectural Institute of Japan: Concept of Soundness Survey and Diagnosis of Existing Wooden Buildings (Draft) (Wooden Members, Joints, etc.), 2022-03, pp205-235

[4]–Hideto Takeuchi: Study on how to maintain and preserve the high quality of cedar wood used in traditional wooden buildings, Part 7 Results of outdoor exposure tests for more than 10 years, Japan Society of Finishing Engineers, Proceedings of Annual Conference, 2022

[5] Hideto Takeuchi：Quantitative evaluation of the deterioration state of the modified wood shingle exposed outdoors and construction of an index to judge the deterioration, The 20th International Symposium on Advanced Technology, November 23-24, 2021

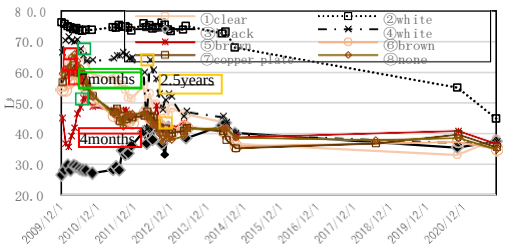

a) Aas45

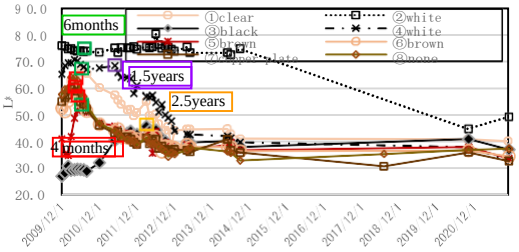

b) Ans170

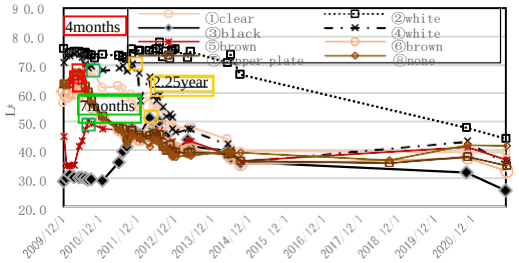

c)Mas35

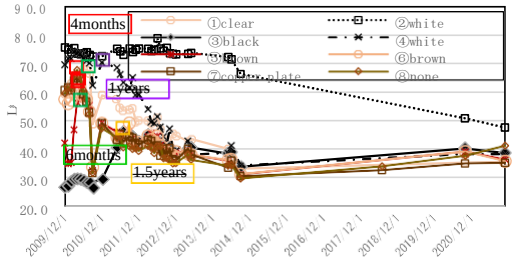

d) Mas80

Fig 3 Change in L* value over time(L1)

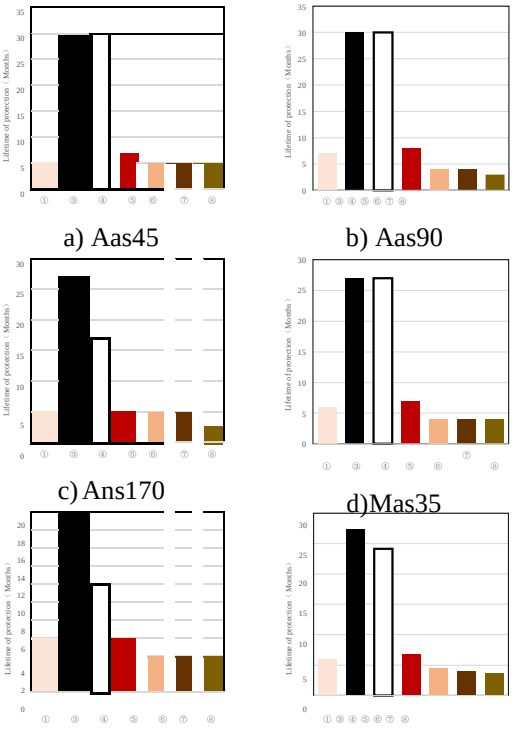

a) Aas45 b) Aas90

c) Ans170 d)Mas35

e) Mas80 d)-Average value

Fig 4 Service life of modification treatment =Duration of safe range(Months)(L1)

Room-temperature deposited flexible B-doped In_2O_3 transparent conductive film

Shun Mori, Kanta Kibishi, Shinri Yamadera, Ayumu Nodera, Kotaro Watanabe, Ichiro Takano and Shinya Aikawa

Department of Engineering, Graduate School of Engineering, Kogakuin University, Tokyo, Japan
E-mail: aikawa@cc.kogakuin.ac.jp

Abstract

Recently, amorphous transparent conductive oxides having high electrical conductivity are strongly demanded for realization of next-generation flexible devices. In this study, we fabricated highly amorphous B-doped In_2O_3 (IBO) with comparable electrical properties of a commercial ITO, even at room-temperature deposition. We also demonstrated the bending test to compare mechanical flexibility. The result showed that the IBO forms large domains with polygonal shape. We believe that the domain shape is important to improve mechanical flexibility of brittle oxide thin films.

1. INTRODUCTION

Room-temperature processable highly transparent and flexible conductive films are demanded for next-generation energy and information devices. However, a conventional ITO requires annealing treatment after deposition, which is the limit of room-temperature processes. In addition, ITO deposited on a flexible substrate has some problems such as occurring cracks at the grain boundaries when it is deformed [1]. Thus, completely amorphous and room-temperature processable transparent conductive oxides have been strongly required. Indium oxide-based materials reduce the electron scattering probability and improve their carrier mobility by decreasing the ionic radius of the dopant [2]. Trivalent B ion with VI coordination has very small ionic radius of 0.027 nm. We found that the mobility of IBO was improved than that of non-doped In_2O_3 even deposited at room-temperature [3]. To utilize these features of IBO, we developed the IBO as flexible transparent electrode on a plastic substrate. However, the optimum B concentration and necessity of annealing treatment is still under investigation. Here, we investigate B concentration dependence of electrical properties of IBO, and also clarify thermal treatment requirements. Furthermore, we compare the electrical and mechanical properties by I-V characteristics during bending and by using a nanoindentation equipment. An improvement of mechanical flexibility of brittle oxides will be discussed.

2. EXPERIMENTS

IBO thin films with a different B concentration were deposited on a substrate at room-temperature using an RF magnetron sputtering. The RF power and the total pressure during deposition were fixed at 100 W and 0.24 Pa, respectively. Only Ar was used as a sputtering gas. Incorporation of B was carried out by co-sputtering method using B grains. The annealing conditions were for 30 min in the range between 150 and 300 ℃ in O_2, Ar/H_2, and N_2 atmosphere. ITO thin films were also prepared using an ITO target deposited by same sputtering equipment. The sheet resistance was measured using a four-probe method. The carrier mobility and electron density were estimated using Hall-effect measurement system (ACCENT HL5500PC) at room-temperature. The optical transmittance was measured using UV-vis-NIR spectrophotometer (Shimadzu UV-3600). The film thickness was measured using a surface profiler (Dektak XT-E). The crystal structure was analyzed using XRD (SmartLab.). The chemical bonding states were characterized by XPS (JEOL JPS-9000MC). The film composition was also determined by EDX which is mounted on a scanning electron microscope (JEOL JSM6380LA) at an acceleration voltage of 10 kV. The mechanical properties of the films were characterized using nanoindentation equipment (Shimadzu DUH-W201). To examine the resistance during bending, both films deposited on a PET was characterized using a lab-made bending tester.

3. RESULTS & DISCUSSION

Figure 1 shows the change in the resistivity of IBO as a function of annealing temperature. Here, we focused on two parameters of annealing temperature and atmospheres. Although the minimum value was obtained at 150 ℃ in reducing Ar/H_2 atmosphere, almost same resistivity in the as-deposited and annealed at 300 ℃ was achieved. The reason for such practical resistivity was realized even in the as-deposited film is due to the reducing sputtering atmosphere. In this study, we fabricated IBO only use Ar, no introducing O_2. This means many oxygen vacancies (V_O) are generated in the film, thus, electron density originated from V_O is intrinsically high. In case of ITO deposited on such a reducing environment, a transmittance would be deteriorated. However, B has a strong oxygen bond-dissociation energy, leading to make moderate oxygen incorporation into the film.

Figure 2 shows a relationship between bending cycles and the relative resistance of ITO and IBO deposited on PET substrate. After 10000 bending

cycles, the resistance of the ITO was finally 2.3 times higher than that of IBO. ITO has a relatively low amorphous/polycrystalline transition temperature and crystal grains are easily formed in the film even at room-temperature deposition [4]. In contrast, the IBO is completely amorphous material, thus the bond lengths and angles are expected to be random. We believe those structural distortions are effective for stress relaxation during bending. For this reason, the surface morphology after bending test was obviously different. As shown in Figure 3, some clacks in ITO seem to be longitudinal direction, and polygonal shaped domains were observed for IBO. We speculate that the polygonal large domains are important factor to improve mechanical flexibility in brittle oxides.

4.SUMMARY

We investigated optimum B concentration in IBO. The resistivity, electron density, mobility and average transmittance in the visible region for 3.1×10^{-4} Ωcm, 4.0×10^{21} cm^{-3}, 9.1 cm^2/V_S, and 87.3 % were obtained at the 2.5 at.% of B, respectively. These values are comparable to a commercial ITO, even at room-temperature fabrication. We found that any annealing treatment is not necessary because IBO has intrinsically high electron density caused by high density of V_O. The IBO on PET exhibited better mechanical flexibility than ITO. We believe that this is originated from high amorphization of IBO.

References:

[1] S. Jung, et al., *Thin Solid Films*, 550, p.435 (2014).
[2] N. Mitoma, et al., *Appl. Phys. Lett.*, 106,p.042106 (2015).
[3] S. Aikawa, et al., *Proc. of IEEE-NANO*, p.202 (2020).
[4] K-H Choi, et al., *Sol. Energy Mater. Sol. Cells*, 93, p.1248 (2009).

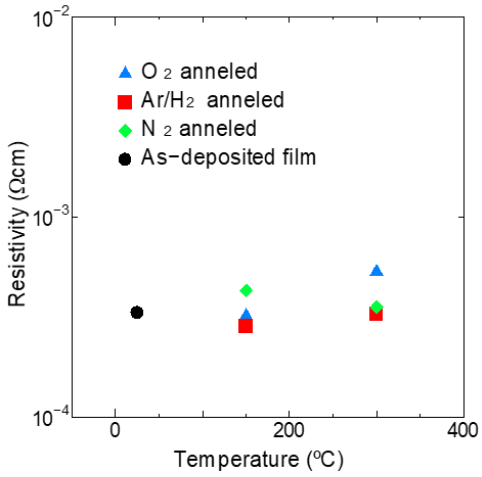

Fig.1 Resistivities of IBO films as a function of annealing temperature.

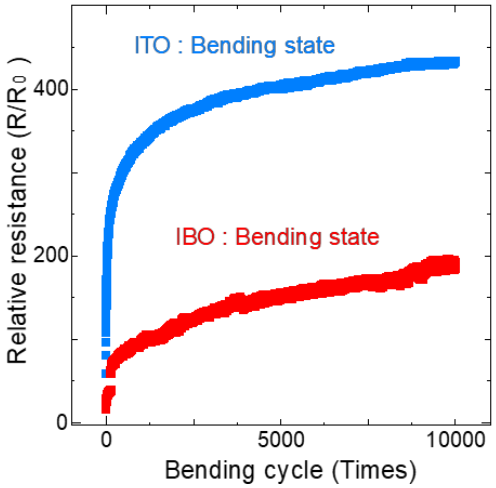

Fig.2 Comparison of relative resistance during bending for ITO and IBO deposited on PET substrate.

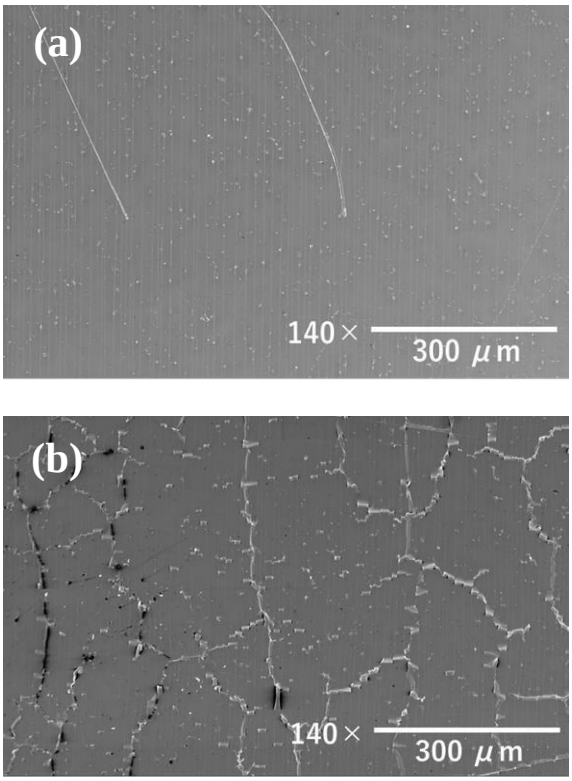

Fig.3 SEM images of (a) ITO and (b) IBO after 10000 bending cycles.

Partial reduction of weakly-bonded oxygen in SnO_x thin films by dissociated nitrogen atoms

Kotaro Watanabe, Takuma Kawaguchi and Shinya Aikawa

Department of Electrical and Electronic Engineering, Kogakuin University
2665-1 Nakano-machi, Hachioji, Tokyo 192-0015, Japan.
E-mail: aikawa@cc.kogakuin.ac.jp

Abstract

For realization of p-type oxide-based semiconductors, nitrogen (N)-doping is one of the promising candidates. However, there still have unclear mechanism how hole is generated and where N atom is incorporated. In our previous study, we demonstrated n- to p-type conversion of SnO_x film only by N_2 annealing. Here, we show the role of N in n-type SnO_x based on the detailed analysis of chemical binding states. The results suggest that N contributes important role in both V_O passivation and hole generation in the SnO_x film.

1. INTRODUCTION

Recently, all oxide CMOS circuit has been developed because it has unique advantages, for example low-temperature processability, low-power consumption and optical transparency [1]. Typical p-type oxide TFT shows less electrical properties compared to n-type TFT, such as field effect mobility and on/off current ratio [2]. Thus, development of superior p-type TFTs similar to n-type TFTs is required. Among p-type oxide semiconductors, SnO-based materials are attractive attention because of ambipolar conduction, earth-abundant element and high mobility but the deposition condition in p-type SnO is very narrow compared to n-type SnO_2. To convert n-type SnO_x to p-type, nitrogen (N) doping is effective method because N incorporation into O-site is expected to act as an accepter without unintentional charge compensation [3]. Although nitridation is usually performed using plasma treatment, this technique induces surface damages. On the other hand, it is known that N_2 dissociation is difficult by post-deposition annealing (PDA) due to the high binding energy of ~10 eV. Lee *et al.* discussed that N_2 can be dissociated at 600 °C annealing when N_2 incorporated in the bulk. This is understood by the elongation of N_2 bond length trapped inside bulk [4]. Refer to their results, we have focused on the N doping by PDA to fabricate p-type SnO_x thin films [5]. We have investigated the origin of hole generation in N-doped SnO_x based on the bonding states by XPS analysis. As a result, partial reduction of SnO_x film by N_2 annealing was observed. In this study, we report the correlation between change in carrier density by N_2 annealing and the bonding states in the film based on the detailed analysis of XPS spectra, and also discuss the role of N atom during annealing.

2. EXPERIMENTS

SnO_x thin films (thickness: 100 nm) were deposited on a Si substrate with a 200 nm of thermal SiO_2 using RF magnetron sputtering at room temperature. A ceramic SnO_2 target (purity: 99.99%) was used as the starting material. Ar and O_2 gas flow was precisely controlled using mass flow controller and RF power was fixed at 100 W during deposition. The oxygen ratio (O_{pp}) was estimated in the ratio of the Ar and O_2 flow rate and varied between 2% and 10%. The total pressure was fixed at 0.12 Pa. After the deposition, the films were annealed for 30 min under pure N_2 atmosphere in the range between 150 and 600 °C using a rapid thermal annealer (ULVAC MILA- 3000). The electrical properties of the film (sheet resistance, Hall mobility, and carrier density) were measured at room temperature using Hall-effect measurement system (Accent HL5500PC). The composition analysis and binding states of the film were characterized by XPS (JEOL JPS-9000MC, MgKα excitation). The optical transmittance was measured using UV-vis-NIR spectrophotometer (Shimadzu UV-3600). The SnO_x films on a fused quartz were also prepared for the transmittance measurement.

3. RESULTS & DISCUSSION

Figure 1 shows a histogram of the peak area ratio of O 1*s* (SnO/SnO_2) of the SnO_x thin-film before and after N_2 PDA. The result showed that the SnO component was increased by N_2 annealing from the deconvoluted O 1*s* spectra. This can be understood by chemical shift to SnO bonding states because N atoms support reduction reaction to take away O atoms from weakly-bonded Sn-O binding [6]. Such weak binding sites are included in an amorphous structure. The reaction model is shown in Fig. 2. Since the fabricated SnO_2 has an amorphous structure, many Sn^{2+} components were also observed in the Sn $3d_{5/2}$ spectrum. We speculate that this was also caused by the change in the chemical bonding states because of Madelung potential [7]. The SnO component showed dominant is consistent with increasing in p-type yield based on the Hall measurement. This suggests that one of the roles in N atom is to dissociate and reduce weakly-bonded O atoms from SnO_2.

Figure 3 shows the Tauc plots of the same sample as the XPS characterizations. The plot was estimated by the optical transmission spectra in the

wavelength ranging 220 to 2600 nm. The optical bandgap (E_g) was obtained by extrapolating the linear plot, as shown in Fig. 3, which are 3.89 and 3.99 eV for the as-deposited and N_2 PDA SnO_x films, respectively. Basically, nitridation makes the E_g narrow due to upward the VBM of an oxide material, however, E_g of the N incorporated SnO_x was wider than that of as-deposited film. This is because the reduction of tail states owing to the crystallization. The plots also suggest that V_O density located around at 2.7 eV was suppressed by nitrogen incorporation [8]. This is the same tendency that V_O ratio in the O 1*s* spectra is reduced (Fig. 4). Thus, we found that the subgap defects originating from V_O were suppressed by incorporation of N atoms. We suppose that this is another role of N atoms during annealing.

4. SUMMARY

We analyzed the XPS spectra of N_2-annealed SnO_x thin-films to determine the chemical bonding states and discuss the correlation between change in carrier density by N_2 annealing and the bonding states in the film. We found that the SnO component increased from the peak area ratio of O 1*s* (SnO/SnO_2). Furthermore, the Tauc plots indicated that the suppression of V_O due to the incorporation of N was observed. Thus, we suggest that the role of N in n-type SnO_x is both dissociation of weakly-bonded O for the SnO2 reduction, and V_O passivation for hole generation.

References:

[1] R. Barros, et al., Nanomaterials, 9, p.320 (2019).
[2] I.-C. Cheng. et al., SSDM 2021, 2021, Sep.8, J-5-01.
[3] M. Chiesa. et al., Chem. Sci., 11, p.6623 (2020).
[4] Y.-M. Lee, et al., J. Appl. Phys., 109, p.124316 (2011).
[5] K. Watanabe. et al., AIP Advances 12, 105102(2022).
[6] D. Maestre. et al., Eur. J. Inorg. Chem., 11, 1544-1548 (2007).
[7] S. Sallis. et al., Appl. Phys. Lett. 104, 232108 (2014).
[8] F. Stavale, et al., J. Phys. Chem. C, 118, p.13693 (2014).

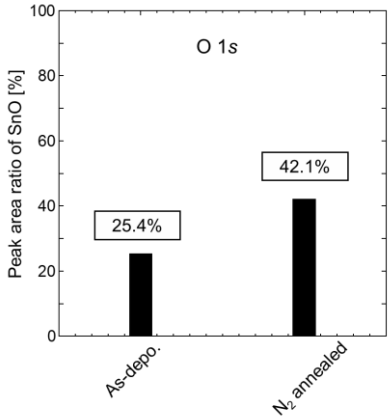

Fig.1 Comparisons of peak area ratio of O 1*s* before and after N_2 PDA.

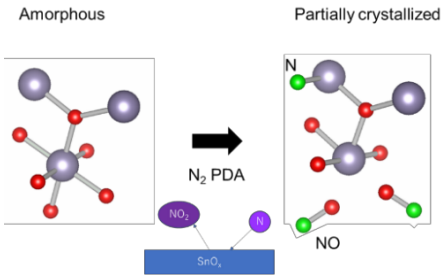

Fig. 2 Schematic illustration of partial reduction of amorphous SnO_x by N_2 PDA.

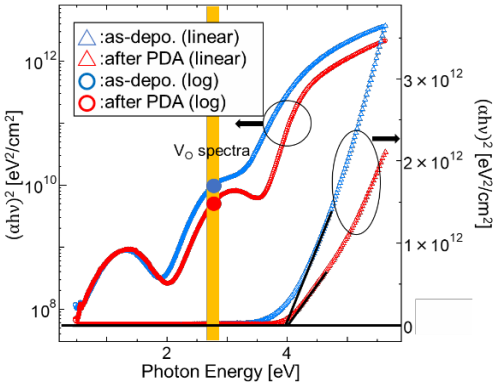

Fig. 3 Tauc plot of the SnO_x thin film (O_{pp}: 10%) before and after N_2 annealing. The film was annealed at 600 °C in N_2. The both semi-log and linear plots are shown for comparison.

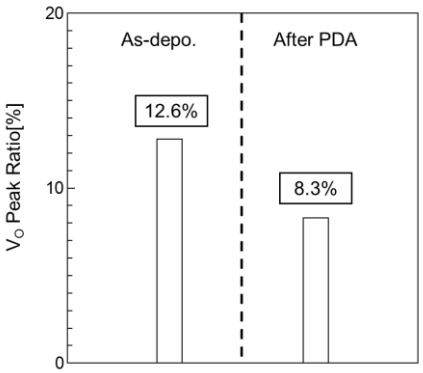

Fig. 4 Comparisons of peak area ratio of oxygen vacancy for O1s before and after N_2 PDA.

Breakout Room #2

Education and Human Studies & Architectural and Civil Engineering

Chairperson: Dr. Hoang Van Thanh, DUT

A Study on Vehicle Body Acceleration and Body Motion of a Rider during Riding a Bicycle

Rintaro Omiya*, Motoki Tsukada, Yusuke Kurasaki, Satoru Kizawa, Ayuko Saito
Department of Mechanical science and Engineering, Kogakuin University, Japan
E-mail: s520014@ns.kogakuin.ac.jp

Abstract

This study evaluated the relationship between the acceleration of a bicycle and the motion of a rider while riding a bicycle. By using the singular value decomposition of the acceleration, we determined that the trunk was mainly used to keep balanced on an uneven road.

Bicycle is a vehicle with two wheels or with more wheels which a person rides by sitting on it and pushing two pedals with his feet. Bicycles are used by millions of people, from young children to the elderly. One has to keep balance when he rides on a two-wheeled vehicles, which are widely used in general. Training wheels are often used when children begin to ride a bicycle for the first time. Clarifying how to keep balance of left-right when stepping on the pedals enables to develop an efficient method to practice riding a bicycle. Several studies on operating handlebars have described that a rider could keep balance while riding at high speeds without operating handlebars periodically [1]. However, there are many uncertainties regarding the mechanism of keeping balance while riding a bicycle. Therefore, this study evaluates the relationship between the acceleration of a bicycle and the motion of a rider while riding a bicycle. We clarify how to keep balance by using the coordinated relationship between the acceleration sensor outputs attached to body parts of a rider.

A healthy adult male (height 1.73 m, weight 75 kg) participated in the experiment. The measurement was conducted at two locations in Hachioji City, Tokyo. Following an explanation of the purpose and requirements of the study, the participant gave his written informed consent to participate in the study. Study approval was obtained from the Research Ethics Board, Kogakuin University. Fig. 1 shows the sensor positions. The analysis was conducted focusing on the acceleration of a bicycle and the acceleration of each body part of a rider. [1]. The singular value decomposition was performed on the three-axis synthetic acceleration for each sensor.

Figure 2 shows the results of spatial basis patterns obtained by singular value decomposition. Fig. 2(a) shows the results of the first mode on a flat road

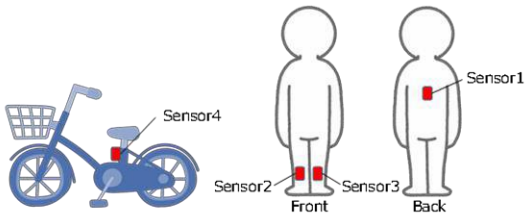

Fig.1 Sensor positions

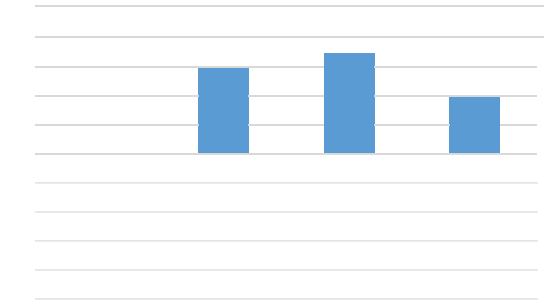

(a) Flat condition

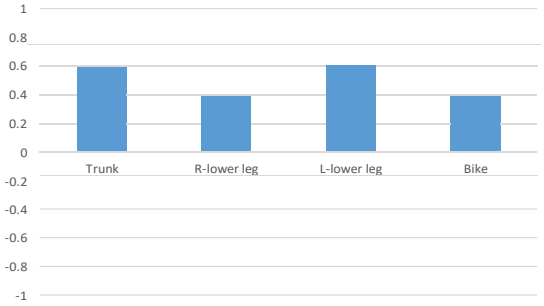

(b) Unevenness condition
Fig. 2. Results

surface (contribution rate of 94%), and Fig. 2(b) shows the results of the first mode on an uneven road surface (contribution rate of 93%). The results indicate that stepping on the pedal with the left and right legs is dominant on a flat road and almost no acceleration of the trunk is generated. While, the acceleration of the trunk was generated greatly on the uneven road, suggesting that the trunk was mainly used for keeping balance.

This study evaluated the relationship between the acceleration of a bicycle and the motion of a rider while riding a bicycle. By using the singular value decomposition of the acceleration, we determined that the trunk was mainly used to keep balanced on an uneven road.

References:

[1] Y. Usami, K. Ishikawa, T. Takayama, M. Yanagisawa, N. Togawa, *Proceedings of Multimedia, Distributed, Cooperative, and Mobile Symposium*, I. Syuhei, C. Aoki, *Physical Therapy Science*, 1670-1675 (2019).

Research on the Acceleration and Trunk Posture while Riding a Bicycle

Motoki Tsukada*, Rintaro Omiya, Yusuke Kurasaki, Satoru Kizawa, Ayuko Saito

Department of Mechanical Science and Engineering, Kogakuin University, Japan
E-mail: s520039@ns.kogakuin.ac.jp

Abstract

In this study, we measured the acceleration of a bicycle and the trunk posture of a rider are measured using the 9-axis motion sensor. The results indicate that the rider consciously maintains the trunk posture the uneven road surface. In future, we will analyze the cooperation between maintaining trunk posture of a rider and the acceleration of a bicycle.

People enjoy cycling because they can travel under their own power, at their own pace, in a way that is both stimulating and relaxing. Bicycle competition includes racing [1], BMX racing, track racing [2], criterium, roller racing, sportives and time trials. A rider receives constantly vibration transmitted from a road surface while riding a bike. Since the vibration increases on a road with rough surface, maintaining an appropriate posture enable to apply force to the pedal.

From the above, evaluating the relationship between the vibration transmitted from a road surface and the trunk posture of a rider enables to clarify how a rider keeps balance while riding a bike. Therefore, in this study, the acceleration of a bicycle and the trunk posture of a rider are measured using the 9-axis motion sensor. The acceleration of a bicycle and the trunk posture of a rider on two different road surfaces are compared.

A healthy adult male (height 1.73 m, weight 75 kg) participated in the experiment. The measurement was conducted at two locations in Hachioji City, Tokyo. Following an explanation of the purpose and requirements of the study, the participant gave his written informed consent to participate in the study. Study approval was obtained from the Research Ethics Board, Kogakuin University. Fig. 1 shows the sensor positions. The analysis was conducted focusing on the acceleration of a bicycle and the trunk posture.

The flexion - extension of the trunk and the acceleration of a bicycle are shown in Figs. 2 and 3, respectively. On a flat road, the acceleration in the riding direction fluctuates within ±0.5 [G] and the

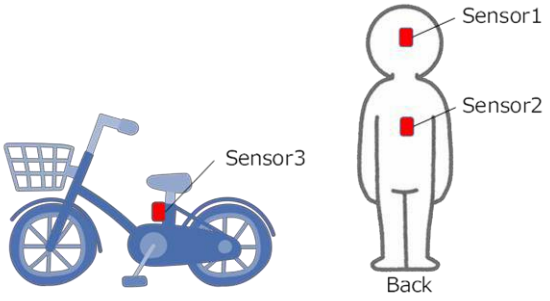

Fig. 1. Sensor positions

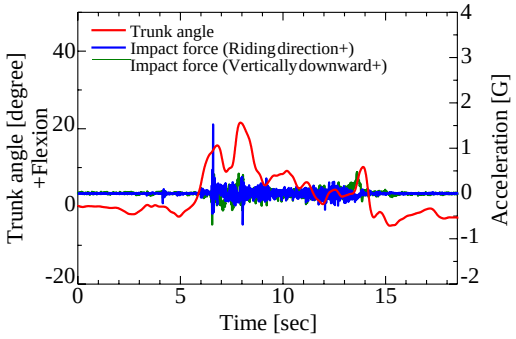

Fig.2 Flat condition

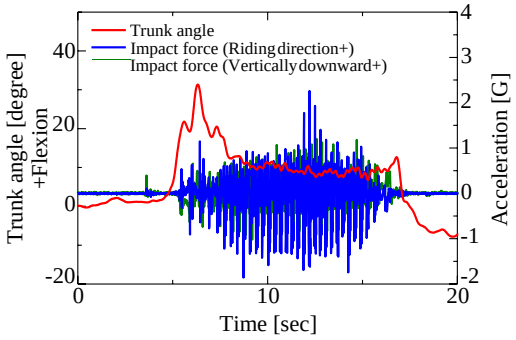

Fig.3 Unevenness condition

trunk posture fluctuates around 0 degrees roughly except the time when the rider begins to ride. While the acceleration in the traveling direction fluctuates greatly within ±2.0 [G] and the trunk posture consciously maintains the bend of about 10 degrees thereafter on uneven road surfaces.

References:

[1] Y. Ochi, *Transactions of Japanese Society for Information and Systems in Education*, **31**, 91-103 (2017).

A Study on Gaze Control while Riding a Bicycle

Yusuke Kurasaki*, Rintaro Omiya, Motoki Tsukada, Satoru Kizawa, Ayuko Saito

Department of Mechanical Science and Engineering, Kogakuin University, Japan
E-mail: S520022@ns.kogakuin.ac.jp

Abstract

This study investigated the differences of gaze control in the different road conditions while riding a bicycle. The participant often looked at the space in front while riding uphill. The results indicate that the participant might not be fully aware of road signs and pedestrians compared to the other two conditions.

Bicycle is a vehicle with two or more wheels which a person rides by sitting on it and pushing two pedals with his feet [1]. As of 2019, the number of bicycles owned by Japanese is approximately 68 million which is about half of the population [2].

Humans obtain most of their information about the external environment from the sense of sight during daily life and sports activities. Visual information is especially important to sense danger while riding a bicycle because we move faster than while walking. Several studies have described that a person looks far away while riding a bicycle with high speed and he looks closer with low speed. The range of eye movement tends to be narrower in the horizontal direction and wider in the vertical direction while moving with high speed. The range of eye movement tends to decrease in the direction of both horizontal and vertical while riding a bicycle with off-balance [3].

Clarifying the characteristics of gaze control while riding a bicycle enables to determine the appropriate location of signs, which contribute to reduce the number of accidents caused by missing road signs. Therefore, this study investigates the differences of gaze control in the different road conditions while riding a bicycle.

A healthy adult male (height 1.76m, weight 65kg) participated in the experiment. The measurement was conducted at two locations in Hachioji City, Tokyo.

Fig. 1. Eye tracking system (EMR-9)

Table1 View point locations

A	Automobile
B	Road sign, Utility pole
C	Pedestrian
D	Ground
E	Forward space
F	Own bike

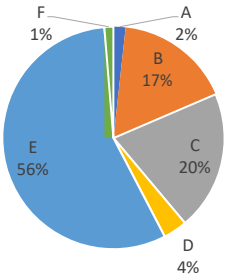

(a) Flat

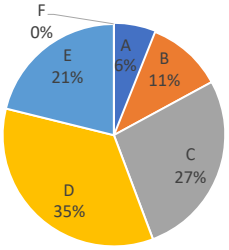

(b) Downhill

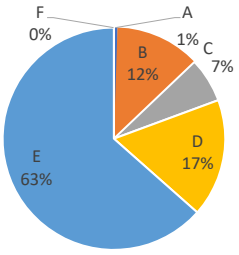

(c) Uphill

Fig. 2. Measurement results

Following an explanation of the purpose and requirements of the study, the participant gave his written informed consent to participate in the study. Study approval was obtained from the Research Ethics Board, Kogakuin University.

The participant wore the eye tracking system on his head shown in Figure 1 while riding a bike. The participant rode a bicycle on "flat roads", "sloping roads" in the urban area of Hachioji City, Tokyo. The sampling frequency of the eye tracking system was 60 Hz. Table 1 shows the grouping results of gaze point, and Figure 2 shows the results of the measurement. The analysis distance is approximately 100 m for each condition. The results indicate that the

participant looked at the ground and the space in front most frequently on a flat road. The participants looked at pedestrians and bicycles more frequently on a downhill slope. On an uphill slope, the participant looked at the space in front more frequently than other two conditions.

References:

[1] Japanese Law Translation, web site, https://www.japaneselawtranslation.go.jp/en/laws/view/2962/ja, (2015).

[2] Ministry of Land, Infrastructure, Transport and Tourism, web site, https://www.mlit.go.jp/road/ir/ir-council/bicycle-up/06pdf/02.pdf , (2020)

[3] T. Okawa, N. Yoshida, Y. Hino and T. Uchida, *Infrastructure Planning and Management*. **30**, 571-578 (2013).

A Research on The Development of Walking for a Healthy Toddler

Ryu Katsuhara*, Kei Hoshino, Ayuko Saito, Shinichiro Morichi, Satoru Kizawa

*Department of Mechanical Science and Engineering School of Advanced Engineering Kogakuin University, Tokyo, Japan
E-mail: s520015@ns.kogakuin.ac.jp

Abstract

The gait measurement was conducted for a toddler. The results indicated that the proportion of the stance phase increased during the developmental process from two to three years old. In future, we will show the significance of walking evaluation by following the individual developmental processes of young children.

Walking is a basic movement that humans perform on a daily basis. Evaluation of gait can be used to confirm developmental status of children and to diagnose frailty in the elderly.

Several studies on walking have been conducted from various viewpoints. For example, observational gait analysis has been used to confirm developmental status of children1). Since young children can't understand the instructions given by a doctor, however, the gait test does not seem to be an appropriate method for evaluating gait of the toddler. Otherwise, gait analysis is being performed from an engineering point of view. An optical motion capture enables to evaluate joint angles during walking. It has also been used in large-scale surveys in which the gait of 97 toddlers were evaluated2). However, very few studies which focus on the development of individual gait. Tracking the development of individual gait leads to clarify the development process of young children3).

In this study, the lower limb joint angles of a healthy toddler (at two and at three years old) are measured using an optical 3D motion analysis system. Then, the development of walking is described from changes in joint angles.

A healthy boy participated in the experiment. The gait measurement was conducted twice when he was two years and one month old and three years and ten months old. His height was 0.86 m and his weight was 11 kg when he was two years and one month old. His height was 0.98 m and his weight was 15 kg when he was three years and ten months old. Study approval was obtained from the Research Ethics Committee, Kogakuin University. Informed consent was obtained from the participant and his parent in advance.

The sampling frequency of the optical 3D motion analysis system was 100Hz. Before the measurement, 19 reflective markers were attached to the lower limbs of the participant with reference to the Helen Hayes marker set as shown in Fig. 1. The subject walked with a natural stride and speed.

Fig. 2 shows the results of the left hip joint angles. The positive direction in the vertical axis is flexion. The horizontal axis is 100% for one gait cycle, where

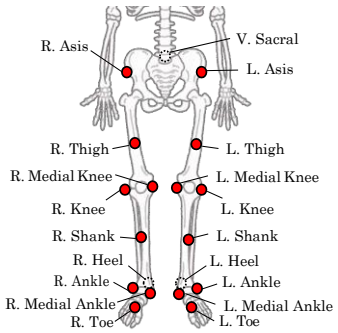

Fig. 1. Marker position

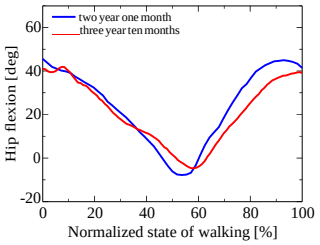

Fig. 2. Hip flexion

0% is the beginning of the stance phase. Both results gradually extend from the beginning of the stance phase and reach the peak of extension at the end of the stance phase. After that, they begin to extend in the swing phase. The results are similar to those of normal adult gait. The distinction between the two results is the length of the stance phase. The stance phase occupies about 50% of the total gait cycle when he is two years old, whereas it occupies about 60% when he is three years old. With growth, the ratio of the stance phase and the swing phase is becoming similar to that of normal adult gait.

References:

[1] I. Syuhei, C. Aoki, *Physical Therapy Science*, **32**,1,81-84(2017).
[2] Kao Corporation, web site, https://kyodonewspr wire.jp/release/202010065331, (2020).
[3] C. Nishio, K. Kudo, M. Sasaki, *The Japanese journal of developmental psychology*, **29**, 2, 73-83(2018).

A Study on Estimation of Lower Limb Muscle Forces during Squatting

Kazuya Inoshita*, Shinichiro Morichi, Yoshikazu Kobayashi, Satoru Kizawa, Ayuko Saito

Department of Mechanical Science and Engineering, Kogakuin University, Tokyo, Japan
E-mail: s520009@ns.kogakuin.ac.jp

Abstract

This study estimated the lower limb muscle forces during two types of squatting by using OpenSim. The results indicate that the muscle forces of the hamstrings, including the biceps femoris muscle, increases as the foot width increases.

A squat is a strength exercise in which a person lowers his hip from a standing position and then stands back up [1]. It is one of the most popular exercises for strengthening the leg and back muscles without using any special equipment. Since incorrect posture during squat exercise causes injury, physical therapists teach patients correct posture during squatting in rehabilitation. The effect is, however, evaluated by follow-up observation. The load on each muscle for each training is not quantitatively evaluated.

Therefore, this study, the lower limb muscle forces during squatting were estimated using the musculoskeletal software OpenSim [2]. Muscle force estimation using OpenSim, which is based on optical motion analysis, is used in various analyses as a non-invasive method. The two types of squat exercises including “normal squat” and “wide squat” were measured during the experiment. A person performs a squat with his legs about shoulder-width apart during “normal squat”, which trains the quadriceps and hamstrings. A person performs a squat with his legs wider than “normal squat” during “wide squat”, which trains the gluteus maximus and gluteus medius muscles. This study estimates the lower limb muscle forces during two types of squatting by using OpenSim and compares the results.

A healthy adult male (height 1.75 m, weight 67 kg) participated in the experiment. The measurement was conducted at National Institute of Technology, Akita College. Following an explanation of the purpose and requirements of the study, the participant gave his written informed consent to participate in the study. Study approval was obtained from the Research Ethics Board, Kogakuin University and National Institute of Technology, Akita College. Fig. 1 shows the sensor positions. The analysis was conducted focusing on the acceleration of a bicycle and the trunk posture. An optical 3D motion analysis device (Bonita10, Vicon) and a floor reaction force plates (Kistler) were used to obtain the kinematic and dynamic data of the lower limbs. The sampling frequency of both systems were 100 Hz. The software OpenSim 3.3 was used to estimate the lower limb muscle forces during squatting. The model used in the analysis was Gait2392, which has 23 degrees of freedom and 92 musculotendon actuators.

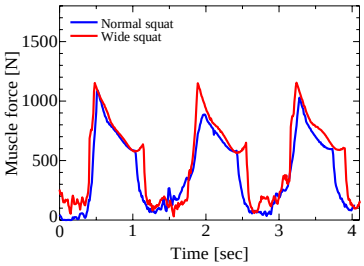

Fig. 1. Muscle force results

Figure 1 shows the result of the biceps femoris long head of the right leg obtained by static optimization calculations. Figure 1 shows the results of three repetitions. The horizontal axis represents the time and the vertical axis represents the estimated muscle force. The waveforms of the results during the two types of squats tended to be similar, indicating that there was no difference in how muscles were used. While the maximum force during wide squats was about 20% higher than normal squats, indicating that widening the stance increases the load on the hamstrings.

References:

[1] Y.Ochi, *Japanese Society for Information and Systems in Education*, 30, **1**, 98-103(2013).

[2] Delp, S. L., Anderson, F. C., Arnold, A. S., Loan, P., Habib, A., John, C. T., Guendelman, E. and Thelen, D. G.: OpenSim: *Open-source software to create and analyze dynamic simulations of movement, IEEE Transactions on Biomedical Engineering*, 54(11), 1940-1950, (2007).

A Study on Gaze in Passing a Ball

Takato Abe*, Wataru Ichikawa, Satoru Kizawa, Ayuko Saito

Department of Mechanical Science and Engineering, Kogakuin University, Japan
E-mail: s520003@ns.kogakuin.ac.jp

Abstract

This study investigated the gaze during a game 3 vs 1 which is called “pig in the middle”. Since the gaze characteristics of a skilled player and an inexperienced player are significantly different, we will analyze the coordination between movements and gazes in future work.

Soccer is a family of team sports that involve kicking a ball to score a goal. A team consists of 11 players. Since soccer eliminates the use of hands, the most basic movement is passing using legs. When a player moves his body in a soccer game, recognizing the positional relationship between space and a ball using vision is needed. Analyzing a player's gaze enables to elucidate how he feeds back the information obtained from vision to his movement[1]. Humans obtain most of their information about the external environment from the sense of sight during sports activities. External environmental information obtained from vision has a great influence on determining motor commands during reaching movements. Therefore, analyzing the line of sight during passing a ball enables to develop an efficient training methods for soccer. Therefore, in this study, as a first step to analyze the gaze trajectory of players in soccer, we measure their gaze trajectories while passing a ball.

Two healthy adult males participated in the experiment. One is a professional soccer player, and the other is an inexperienced player. Study approval was obtained from the Research Ethical Committee, Kogakuin University. The participants received an explanation of the purpose and requirements of the study and gave their written informed consent to participate. The participants played a game 3 vs 1, which is called “pig in the middle” (Fig. 1). They wore an eye tracking system (EMR-9; nac image technology Co., Ltd.) on their heads. The sampling frequency of the system was 60 Hz.

We determined the two analysis time intervals. One was set from the time the participant kicked the ball until the ball was caught by one of the players. Another was set from the time one of the players kicked the ball until the ball was caught by the participant. Figure 2 shows the time ratio of eye gaze. The professional player never looked at his feet until the ball came to his feet and kept his eyes on the ball only when receiving the ball. While, the inexperienced player looked at the ball and his feet half of the time. In addition, when passing the ball, the professional player switched his viewpoints more often than the inexperienced player.

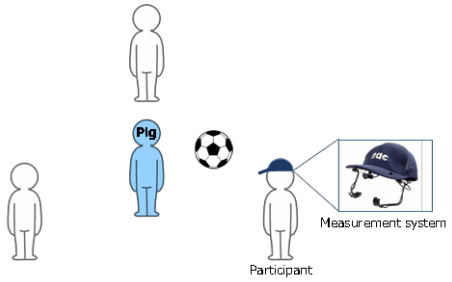

Fig.1 Schematic of pig in the middle 3vs1

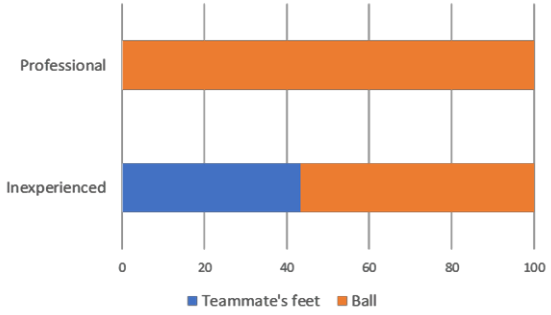

(a) When receiving a ball

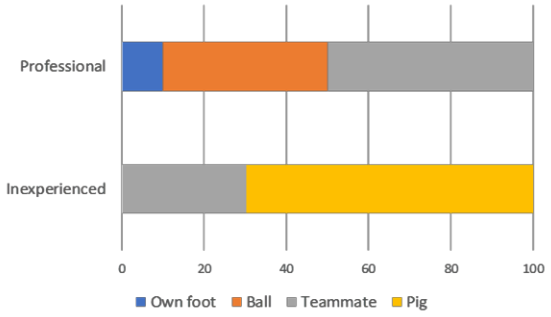

(b) When kicking a ball
Fig.2 Results

Reference

[1] K . Ikeda, S . Sakamoto, *Sports performance research*, 164-176 (2022)

A Study on Person Dependency in Person Identification by Acceleration

Yoshihaya Takahashi*, Takeshi KAMIYAMA, Masato Oguchi***, Saneyasu Yamaguchi***

*Electrical Engineering and Electronics, Kogakuin University Graduate School
E-mail: {cm21031@ns, sane@cc}.kogakuin.ac.jp

** School of Information and Data Sciences Nagasaki University
E-mail:kami@nagasaki-u.ac.jp

*** Department of Information Sciences Ochanomizu University
E-mail:oguchi@is.ocha.ac.jp

Abstract

Methods for identifying persons by analyzing the acceleration obtained from the accelerometer of a smartphone using deep learning have been studied. We proposed a method to identify the user by having the user draw shapes in the air with a smartphone. We then showed that the method could identify users with high accuracy. However, the dependence of the accuracy on the person has not been discussed. In this paper, we focus on the accuracy of each user and discuss the dependency of the accuracy of the method on the user.

Introduction: Recent improvement of deep learning enables a variety of types of estimation from sensed data. In our previous work, we proposed a method for identification of person identification by DeepConvLSTM [1] based on accelerations sensed in a smartphone[2]. We then showed that the method could identify persons accurately in average. However, the accuracy's dependency on persons was not discussed. In this paper, we investigate the dependency on individuals of the method and show that the dependency is not strongly.

Related Work: In the work of [2], we proposed a method for identifying a person from a given set of persons. A person draws some figures in the air using a smartphone with recording the acceleration. The method then analyze the acceleration with DeepConvLSTM and infers the person who drew the figure. The method was composed of three phases. In the first phase, every user draws figures such as circle and the letter N in the air with a smartphone and the acceleration at these drawing is recorded. In the second phase, the method creates the model for identification using DeepConvLSTM from the sensed acceleration. In the third phase, a person to be identified draws a figure in the air, the recorded acceleration is analyzed by DeepConvLSTM using the model, and the method infers the person from the previously given set of persons based on the recorded acceleration.

Dependency on accuracy on person: We identified persons with the proposed method [2] and measured the accuracy of each person. The identification was seven-class classification from seven subjects. We asked the subjects to draw the letter N in the air ten times using Nexus 5X. The results of are shown in Fig. 1. A to G indicate the subjects. The average represents the average accuracy of all the subjects. The figure shows that the accuracy does not strongly depend on the person. In the least case (person B, C, and D), the accuracy was less than the average by around 20%. On the other hand, in the largest case (person A), the accuracy was greater than the average around 30%. In many cases, a remarkably high accuracy is not important.

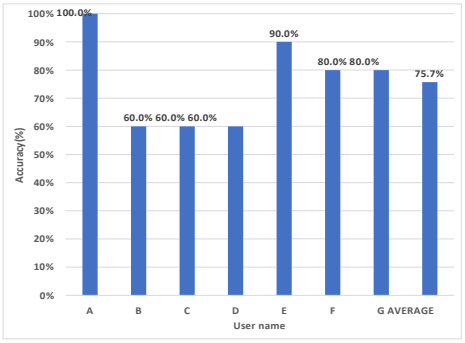

Fig. 1. Accuracy for each user in the 7-class classification

Conclusion: In this paper, we focused on a method for identification of persons from acceleration by DeepConvLSTM, and investigated that dependency of its accuracy on person. We then showed that the dependency was not strong and the method could identify person independent on users.

References:

[1] Ordóñez, F.J.; Roggen, D. Deep Convolutional and LSTM Recurrent Neural Networks for Multimodal Wearable Activity Recognition. *Sensors* 2016, *16*,115. Doi: 10.3390/s16010115

[2] Y. Takahashi, A. Sonoyama, T. Kamiyamaton, M. Oguchi and S. Yamaguchi, "Person Identification Based on Accelerations on Drawing Figures with a Smartphone," 2022 16th International Conference on Ubiquitous Information Management and Communication (IMCOM), 2022, pp. 1-4, doi: 10.1109/IMCOM53663.2022.9721744.

Acknowledge

This work was supported by JSPS KAKENHI Grant Numbers 21K11854 and 21K11874.

Research on Inter-joint Coordination in Abnormal Gait

Kei Hoshino*, Ryu Katsuhara, Shinichiro Morichi, Satoru Kizawa, Ayuko Saito

Department of Mechanical Science and Engineering, Kogakuin University, Japan
E-mail: s520055@ns.kogakuin.ac.jp

Abstract

This study investigated the kinematic characteristics of a case of gait disturbance caused by spastic paraplegia. From the results of the joint angles, we determined the asymmetry between the left and right sides.

Spasticity is a symptom that is characterized by tight or stiff muscles and an inability to control those muscles. It is caused by diseases of the spinal cord and nerves. Spasticity is one of the most common manifestations of cerebral palsy (CP). CP is a nonprogressive disorder, often congenital, caused by brain damage during pregnancy, before and after childbirth, or within the first 4 weeks of life.

CP is difficult to diagnose during early infancy. A comprehensive diagnosis is made by monitoring motor milestones. A doctor would observe the gait as children walk and run in the Health Checkup for Infants. If a child's symptoms are mild, it is sometimes difficult to make a diagnosis until the child is a few years older. Early rehabilitation for children with CP can bring their latent potential and promote growth. Therefore, in this study, as the first step in proposing a new gait evaluation method for children, we extract gait features in spastic gait.

The three healthy adult males (height 1.73±0.03 m, weight 57.3±3.05 kg), a healthy 2-year-old boy (height 1.04 m, weight 16 kg), a spastic 4-year-old girl (height 1.04 m, weight 16 kg) participated in the experiment. Study approval was obtained from the Research Ethics Review Committee, Kogakuin University, and the National Institute of Technology, Akita College. The optical 3D motion analysis system captured the participants during walking. The sampling frequency of the system was 100Hz. The participants walked with natural stride length and speed. The coordination between the joint angles of a person walking was examined by applying singular value decomposition. First, the joint angles obtained in the experiment were normalized from -1 to 1. Then, an observation matrix was constructed using normalized joint angles. Finally, singular value decomposition was performed on the observation matrix to obtain the dominant motion modes defined as the main coordination patterns.

One gait cycle including one stance phase and one swing phase was defined as 100%, and 0% was the beginning of the stance phase. Although the toe-off (TO) in adult males and a 2-year-old boy were 60% and 55%, respectively, that of 4-year-old girl with gait disturbance was 70% for left and 65% for right.

The results indicate that the tendency of joint angle changes of adult males and the 2-year-old boy were bilaterally symmetrical movements, while the joint angles of the 4-year-old girl showed bilaterally asymmetrical except for the hip joint. The results of 4-year-old girl describes that the internal rotation of the left hip joint increased during the stance phase of the left leg. During the stance phase of the right limb of 4-year-old girl, the right hip abduction increased, the right hip joint internally and externally rotated, and the right ankle joint internally and externally rotated.

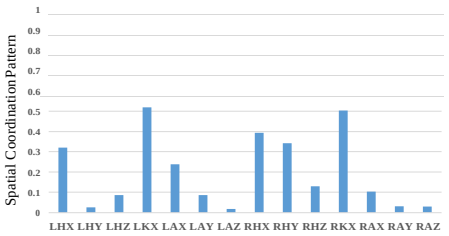

(a) Results of mode 1 during the left gait cycle

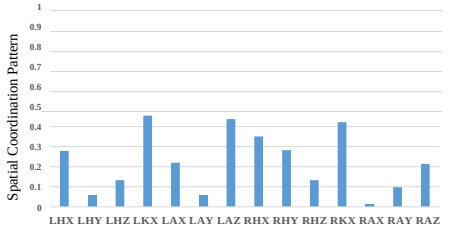

(b) Results of mode 1 during the right gait cycle

Fig. 1. Spatial coordination patterns

In addition, we evaluated the inter-joint cooperation of each subject by applying the evaluation method [1][2] of inter-joint cooperation based on the singular value decomposition of the measurement results. The spatial basis results, which represent the coordination patterns of the 4-year-old girl, are shown in Fig. 1. Fig. 1 shows the result was left-right asymmetric. The results indicate that the joint coordination of the 4-year-old girl was clearly different from that of a healthy person.

References:

[1] T. Funato, S. Aoi, K. Tsuchiya, *Quantitative evaluation of whole-body joint coordination during human walking, Journal of the Robotics Society of Japan*, **Vol. 28, No. 8**, 996−1003 (2010).

[2] A. Saito, S. Morichi, N. Sai, T. Yagi, S. Kizawa, *Study on kinematic evaluation of gait*

disturbance caused by spastic paralysis, *Dynamics and Design Conference 2022 Proceedings*, **506**, (2022).

A Proposal for adaptive advertising media using viewers' preferences and person recognition

Miho.Mizutani, Yoshio.Miki
Kogakuin University of Technology and Engineering
Email:j319270@g.kogakuin.jp

Abstract

We propose adaptive advertising media technology that optimizes the display content according to the preferences of viewers for signage in the city where content can be freely changed using 5G high-speed communication. In experiments using a test system, we confirmed the correspondence between the subject's features and the highly rated advertising content, and confirmed the effectiveness of the method of this research.

Recently, installing signage is progressing as a device that can interactive advertise. By using this medium, it becomes possible to change the displayed content in real time and obtain information about the person operating the device. Therefore, in this research, we propose a technology for recognizing a person using a device with a camera, estimating the person, and using the results to display content. In addition, we believe that this technology will make it possible to know what kind of demand there is in the area where the signage is installed, and based on that information, it will be possible to make highly accurate product and website recommendations.

Previous research[1] estimates a person using a camera and displays advertisements for each person. In that research, however, the same advertisement will be displayed for the person who has the same profile that advertiser decided. To solve this problem, in our research, we extract features from the operation history of the person who operated this device in the past, and make it possible to generate more accurate recommendations.

In the method of this research, the viewer's gender and age are obtained as feature values by person recognition using a camera. In addition, we analyze what the operator was paying attention to by interactive operation from the number of contents browsed, the browsing time for each content, the total browsing time, and the number of browsed contents for each category. If the information on the page is useful, the viewer presses the "Like" evaluation, which enables us to obtain the final interest and evaluation information of the viewer. Finally, based on this information, the feature values are associated with the highly rated browsed pages, and thereafter, the highly rated pages that have already been associated are presented as recommendations to the viewers who have the same feature value.

To confirm the effectiveness of this study, we created an html file corresponding to 36 places that can be divided into one of five categories such as restaurants, cafes, bookstores and art supply stores, parks, and taverns within a 20-minute walk from Kogakuin University Shinjuku Campus. We asked 5 women and 7 men to view the content they were interested in and operate the test system.

In order to generate recommendations, the following two points must be satisfied: "Operator differences can be clearly separated and grouped according to operator characteristics" and "the groups must correspond to the contents that have been rated as "Like". Therefore, we did a principal component analysis(Fig.1.). The data is mainly composed of IDs which are assigned to each subject vertically, number of viewed contents by category horizontally, total viewing time, viewing time of each content, number of viewed contents, whether or not the "Liked" or not for each content. The left figure shows the distribution of IDs, and the right figure plots the amount of content load that has been given a "Like" rating. The correspondence with the content on the right is also clear. Furthermore, it can be inferred that the horizontal direction of the content is whether or not there is an interest in restaurants where multiple people go, and the vertical direction is whether or not there is an interest in a place where you can stay long. From this result, we propose that to recommend to the people browsed in the past, content that has a high like rate among the people in the group who belonged.

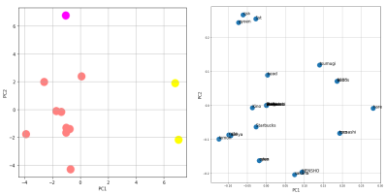

Fig.1. Result of Principal component analysis

Figure 2 is the left figure of Figure 1 with different markers depending on gender. The pink marker indicates female data, and the yellow marker indicates male data, indicating that gender separation has been achieved. This suggests that the upper left content in the right of Fig. 1 can be recommended for women, and the lower right content can be recommended for men.

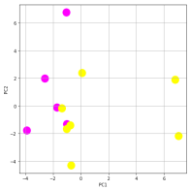

Fig.2. Results of colored by gender

References:

[1] K.Nishitani, K.Hashitani, Information Processing Society of Japan, **3**, 229−230 (2019).

Relationship between plaster density and mechanical properties by unit water content of plaster mixture

Aoba Sakai[*1] Kentaro Oka[*2] Masaki Tamura[*3]

***1 Master Course student, Dept.of Arch.,Graduate School of Engineering,Kogakuin Univ.,Tokyo,Japan**

***2 Assis. Prof., Faculty of Human Resources Development, Polytechnic Univ. M. Eng.**

Head Researcher, Dept. of Arch., Kogakuin Univ., Tokyo, Japan

***3 Kogakuin University, Dr.Eng, School of Architecture Department of Architecture,Tokyo, Japan**

dm21025@ns.kogakuin.ac.jp

1. Introduction

The plaster construction specifications for many heritage buildings do not specify the amount of water. This is still the case today, and there are no general or clear standards for kneading water for plaster used in buildings, leaving it to the discretion of the skilled plasterer.

Therefore, we decided to investigate how physical properties are affected in plaster kneaded with the amount of water determined by individual technicians' senses. Experiments were conducted using unit water and hemp as parameters.

2. Designation of water volume by age

We researched for documents describing plaster mixture by period and investigated for clear descriptions of the amount of water used in the plaster kneading process. There were many references in the documents with descriptions of water quality, such as salt and iron free, as well as plaster mixture tables and mixture. However, we could not find any documents that explicitly states how much water to use. Thus, it can be seen that the amount of water used for plaster has been determined at the discretion of the technicians up to the present day.

3. Experiment Summary

3.1 Plaster density based on the amount of water used in the plaster

Investigate the effect of changes in the amount of water used for plaster on plaster density. Plaster with varying amounts of plaster water and hemp were kneaded with the materials used in Table 1 and the factors, levels and mixture in Tables 2 and 3. We checked how the fresh density and the density during curing changed.

3.2 Plaster mechanical properties by amount of water used in plaster

The same plaster as in 3.1 was kneaded using the same parameters of unit water and hemp volume, and a square column specimen was prepared. After curing and hardening for 8 weeks, the plaster was tested for flexural, compressive, and shear strength by an Amsler tester. We decided to investigate how the physical properties of plaster with different amounts of water and hemp would change.

Table 1 : Materials used for tests

Material	Symbol	Contents
Slaked lime	C1	Natural weathered slaked lime (binder)
Shell lime	C2	Shell lime for plastering made from edible shells (binder)
Seaweed	—	Seaweed extract (water retention , improve workability)
Sand	S	River sand (hardener, anticrack)
Fiber	F	Hemp (reinforcing binder)
Water	W	Water

Table 2 : Factors and levels of plaster mixture with varying amounts of water

Factor	Levels
Mixture	Standard mixture, Hemp+4% mixture (F/P, mass ratio)
Slaked lime	471.4
Shell lime (g)	471.4
Seaweed (g)	57.1
Sand (g)	229.6
Hemp (g)	46.4(F/P=4.9wt%, standard) 84.2(F/P=8.9wt%, standard +4%)
Water(g)	1200, 1300, 1400, 1500, 1600, 1700

Table 3 : Blends with varying hemp and water

Mixture	Slaked lime (g)	Shell lime (g)	Seaweed (g)	Sand (g)	Fiber (g)	Water (g)	W/P (%)
Standard mixture	471.4	471.4	57.1	229.6	46.4 (F/P=4.9wt%, standard) Note 1)	1200	127
						1300	138
						1400	148
						1500	159
						1600	170
Hemp +4% mixture (mass ratio)	471.4	471.4	57.1	229.6	84.2 (F/P=8.9wt%, standard +4%) Note 2)	1300	138
						1400	148
						1500	159
						1600	170
						1700	180.3

Remarks: Note1)F/P(wt%)=F/(C1+C2)*100, Note2)W/P(wt%)=W/(C1+C2)*100

a) When fresh density is measured

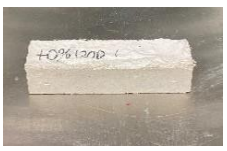

b) When measuring the density of a cured specimen

Photo 1 : Plaster by state

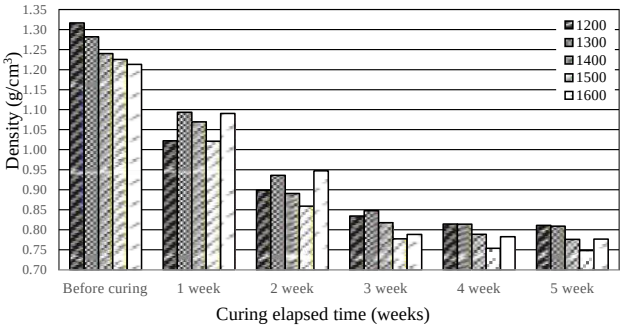

a) Plaster density as a function of elapsed time in standard mixture

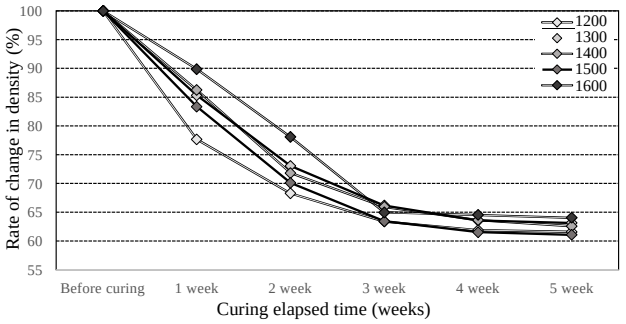

b) Percentage change in plaster density in standard mixture

Figure 1 : Plaster density as a function of elapsed time in standard mixture

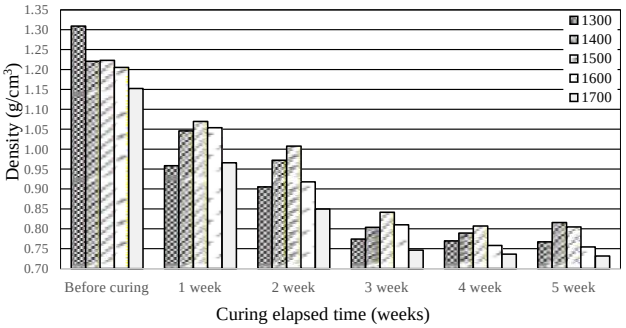

a) Plaster density by elapsed time for +4% mixture

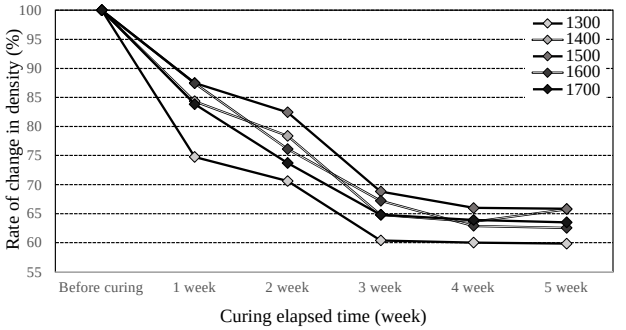

b) Percentage change in plaster density in +4% mixture

Figure 2 Plaster density by elapsed time for +4% mixture

4. Experimental results

4.1 Plaster density by amount of water used for plaster [Results].

Figures 1 and 2 shows plaster density decreased with time. This is thought to be due to the gradual loss of water from the fresh state and the formation of voids in the plaster.

Focusing on plaster in the fresh state, plaster with a higher water content tends to have a lower density. In the fresh state plaster, the density is considered to be lower because for the same mixture, the higher the amount of water in the plaster, the higher the ratio of water in the plaster and closer to 1, which is the density of water.

Focusing on the hemp, the density decreased significantly in one week. It is thought that the hemp in its dry state absorbed the moisture in the plaster paste, resulting in a rapid decrease in the moisture in the plaster paste and a decrease in density.

4.2Plaster mechanical properties for each amount of water used in plaster [Results].

From Figure 3, the maximum stress became slightly smaller as the amount of water used increased. Since the compressive strength test was less affected by the stickiness caused by hemp than other tests, the difference in compressive strength due to the amount of water used was easily seen in the results. Focusing on the hemp, the mix with more hemp was stronger. We confirmed that hemp has a significant effect on plaster strength, regardless of whether the amount of water is increased or decreased.

Next, Figure 4 shows the results of the shear strength test. In the shear strength test, the strength remained generally unchanged as the amount of water used changed. Shear stresses were lower than compressive and flexural stresses, likely due to the fact that the cross-linking effect of the hemp did not act.

Next, Figure 5 shows the results of the bending strength test. Again, no change in strength with increasing water content was observed. Focusing on hemp, the hemp + 4% blend was high strength and the influence of the cross-linking effect of hemp was pronounced.

When there is more hemp in the plaster in the longitudinal direction, it is considered favorable for bending tests. On the other hand, the shear test under the same conditions showed a 90° change in the way the force was applied, and the apparent strength of the plaster also changed due to the change in the apparent direction of the hemp, resulting in a smaller shear strength.

a) Bending strength test *b) Shear strength test*

Photo 2: Plaster strength test

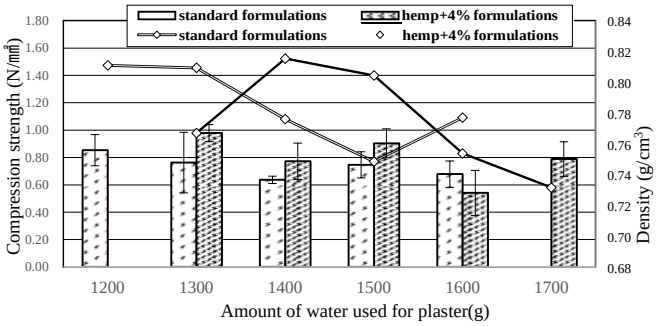

Figure 3 Compressive strength test results

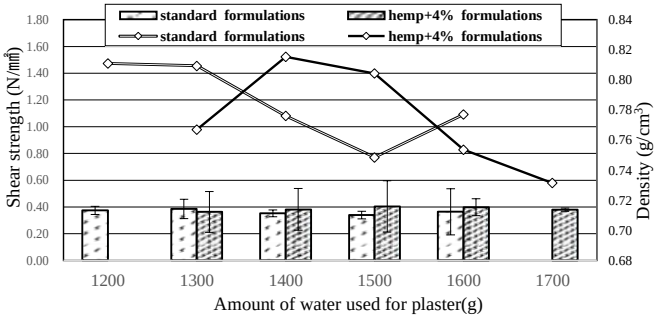

Figure 4 Shear strength test results

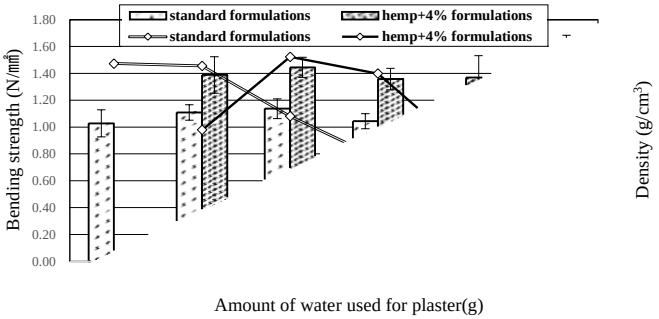

Figure 5 Bending strength test results

5. Conclusion

Looking at the correlation between density and stress, no change in strength with density was observed in this test in both compression, shear, and bending tests. However, if the amount of water is increased in the fresh condition, the plaster may become loose, and if it is a wood-slip base, the hooking may become loose and weak when combined with the base, when viewed as a whole component. Therefore, care should be taken in determining the amount of water at the discretion of the technician.

REFERENCES

[1] Aoba Sakai, Kentaro Oka, Masaki Tamura , Osamu Goto, 2021.10 , Development of Maintenance and Conservation Methods for Historical Architecture Using Plaster Wall Materials Part9 Plaster Fresh Properties of Wooden Lath and Plaster Celling in Historical Architecture

[2] Aoba Sakai, Kentaro Oka, Masaki Tamura , Osamu Goto, 2022.10 , Development of Maintenance and Conservation Methods for Historical Architecture Using Plaster Wall Materials Part12 Relationship between plaster density and mechanical properties according to unit water volume

Analysis of Concentration During Reading by Saccadic Amplitude and Blink

Ryota Shimizu and Hisaya Tanaka

Department of Informatics, Graduate School of Kogakuin University, Japan
E-mail: em21012@ns.kogakuin.ac.jp

Abstract

A study was conducted to determine the relationship between gaze data and concentration during reading. Analysis revealed a correlation of r=.505 between saccadic amplitude and total score on the concentration questionnaire. There was also a correlation of r=.499 between blink frequency and subjective elapsed time.

In this study, we will perform a reading task and acquire gaze data during the task. The goal is to estimate the concentration from the gaze data.

We used a Tobii Pro TX300 to measure gaze at 300 Hz. Fig.1 is an example of acquired gaze data. We used our own questionnaire (Q're) to evaluate the concentration. The Flow proposed by Csikszentmihalyi was used as a reference when creating the Q're. The Q're consisted of 32 questions, each of which was rated on a 5-point scale [1].

In the experiment, subjects were asked to read three books. They were asked to read for 10 minutes per book and to rate a prepared Q're after reading. Subjects were not informed of the reading time. In addition, the reading was done in a quiet environment, with the subjects alone in the room. There were 9 subjects, with a mean age of 22.7 years.

A correlation analysis was performed on the gaze data and the information obtained from the Q're. The results showed that there were strong correlations between some of the data. Fig.2 shows the correlation between saccadic amplitude and total score on the concentration Q're. The correlation coefficient was *r*=.505. This result suggests that the higher the value of Saccadic amplitude, the more concentrated the respondent is in reading. We consider that this is because the more concentrated one is, the greater the amount of text one can comprehend at a time. Fig.3 shows the correlation between blink frequency and subjective elapsed time. The correlation coefficient was *r*=.499. This result indicates that the fewer the blink frequency, the shorter the subjective elapsed time tends to be evaluated. We hypothesize that this is because the more a person concentrates on reading a text, the more information he or she obtains, and thus the shorter the subjective elapsed time.

In this study, we analyzed the relationship between gaze data obtained using an eye tracker and concentration. The results showed that there is a correlation between saccade amplitude and the total score of concentration Q're created, and between the blink frequency and subjective elapsed time. This allowed us to clarify to some extent the relationship between gaze data and concentration during reading.

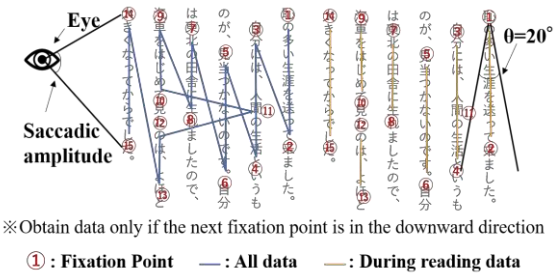

Fig. 1. Example of acquired gaze data and explanation of saccadic amplitude

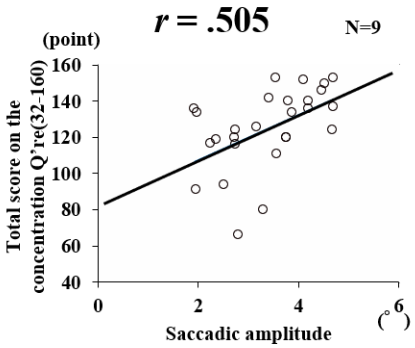

Fig. 2. Correlation between saccadic amplitude and total score on the concentration questionnaire.

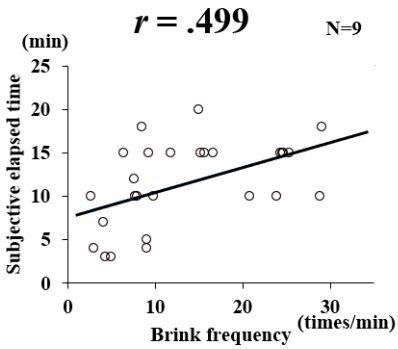

Fig. 3. Correlation between blink frequency and subjective elapsed time

References:

[1] Ryota Shimizu, Hisaya Tanaka, "Analysis of Deep Flow States During Reading by Eye Tracking", Proceedings of 17th JSKE conference, 1CP-01, pp.1-5, (2022-3-25)

Will blockchain technology create a leap forward in the construction industry?

Anh-Tuan Nguyen, Assoc. Prof. PhD

Faculty of Architecture, University of Science and Technology – The University of Danang
Email: natuan1@dut.udn.vn

Abstract

Blockchain technology is still new and there are certainly some initial challenges and controversies to be resolved, the impact of blockchain on the current world is undeniable, but we need a while to see how important blockchain is in the construction industry, although it is difficult to predict how much of an impact it will have. Blockchain is forecasted to have a strong impact on 7 industry-related fields, including: BIM and CAD, smart contract management, smart cities – smart buildings, project management, supply chain management, real estate, and construction product copyright. This article is based on existing information and data to make predictions about the impact of the blockchain technology on the construction industry (mainly focusing on the architecture sector) in the near future. The article also clarifies some challenges and inadequacies that this technology needs to overcome in order to occupy a more important position. The architecture industry's digital transformation will not be separated from technology, and blockchain drives that transition faster and more efficiently.

Keywords - blockchain; digital currency; metaverse; the construction industry; smart contracts; BIM

1. Technology and architecture development context

From the 1990s to now, the construction industry has benefited greatly from the results of the industrial revolution 4.0 with the application of a series of popular technologies, such as Artificial Intelligence (AI), Internet of Things (IoT), Virtual Reality (VR), Geographic Information Systems (GIS), digital imaging, Building Information Modeling (BIM), 3D printing, laser scanning, global positioning system (GPS), radio frequency identification devices (RFID), augmented reality (AR), sensors, automated robots, big data management and other technological devices.

Recently, the world was surprised when AI performed a transcendent intelligence, producing architectural design products so quickly and so similar to human solutions that it was difficult to distinguish in a very short span of time, just in a few seconds (example in Figure 1).

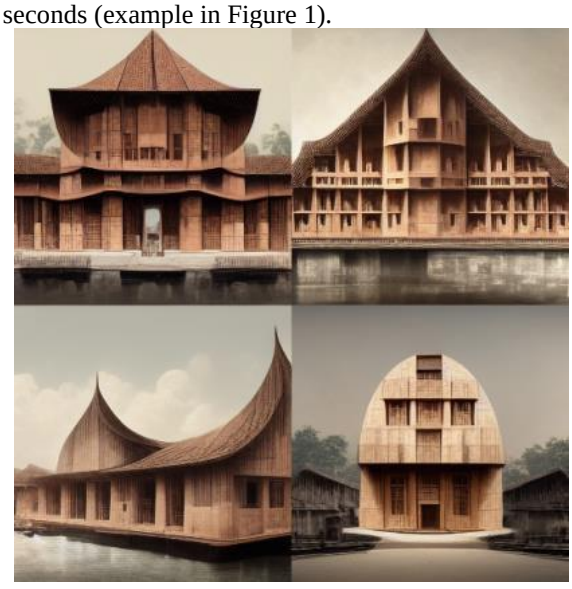

Figure 1: Louis Kahn's stylistic designs created by AI with the command: "a Louis Kahn building reimagined as Burmese vernacular architecture". From the sketches, we can choose the best options for further detailing by AI. Do architects need to do it anymore?

Technologies are increasingly involved in the lifecycle of architectural products and bring many benefits to project stakeholders. They lead to more efficient project management, faster and smarter building design, enhanced building performance, greater sustainability and resilience, high adaptability, and reduced environmental impact of buildings, improving information sharing among stakeholders…

Historically, critics have generally argued that the construction industry as a whole has been one of the slowest sectors to adapt to new technologies. Around the end of the 2010s, blockchain, another innovative digital technology, was born. Blockchain is drastically changing the way people conduct transactions, keep records, authenticate data, and

increasingly influence. For many people, blockchain is seen as a new core technology that can completely change the lives of mankind today. The emergence of blockchain technology once again raises the question of whether it is time to apply blockchain to different areas of the construction industry, and what can we now do with this new technology?

The most prominent and earliest application of Blockchain is the cryptocurrency Bitcoin, created by a person (or group of people) with the codename Satoshi Nakamoto (2008). Bitcoin's built-in blockchain technology allows users to exchange bitcoin's values in a decentralized network securely and independently without the intervention of an intermediary, and allows it to exist completely independently with existing power institutions. Bitcoin has proven that programs running on a computer network can be mined to securely conduct payments, within and between countries, without the reliance on high-fee mercenary financial institutions.

Although the age of blockchain is still very nascent, their applications and influence are already widespread and could have the potential to play an important role in the architecture & construction industry in the future, or even reshaping it drastically for the better (Shojaei 2019). Architecture is also entering the 4.0 era with a lot of changes. Architects face new opportunities, along with challenges that they themselves must change drastically to access and integrate 4.0 technologies into their design products in a process in which blockchain is considered as one of the focus of the 4.0 technology.

2. The scientific basis of applying Blockchain to architecture

Blockchain is a type of Digital Ledger Technology (DLT) consisting of a chronological and growing list of records, called blocks, which are securely linked together using data encryption technique (Figure 2). Blockchain transactions are irreversible in that, once they are recorded, changing the data in any given block must change all subsequent blocks – this is practically impossible in a large network (theoretically it may happen with a 51% attack).

Blockchain is said to have only been created by a person (or a group of people) using the name (or codename) Satoshi Nakamoto in 2008 (i.e. 14 years ago), but so far it has grown strongly and made change in many aspects of the contemporary society. The most important and prominent applications of blockchain are cryptocurrency and NFT (non-fungible token).

Blockchain technology has special characteristics that can solve some of the problems/issues of the architectural world, construction and investment in general, and real estate investment in particular, including but not all:

- Information transparency, anyone can know and admit: copies of the ledger distributed to all participants, for complete transparency; every block in the blockchain chain and every transaction has a timestamp,
- Information authenticity, authenticated records cannot be deleted or changed as they are irreversible,
- Ability to confirm the ownership and the originality of products or work through NFT technology,
- Ability to split the value of a block in the chain into almost infinitely smaller fragments and distribute their ownership to many different people,
- The parties joining the exchange transaction are completely anonymous, all transaction records are encrypted,
- Programmable: relying on blockchain, a contract can be programmed to enforce specific smart contract terms,
- There is no need for intermediaries when transacting between person A and person B.

Blockchain is based on core techniques, including: asymmetric cryptography, cryptographic hash functions, and the principle of decentralized consensus and the "Proof of Work" (PoW) concept. These techniques and principles make the blockchain very secure, fidelity and transparent, while ensuring the principle of anonymity and eliminating the role of third parties in transactions (banks, brokers…).

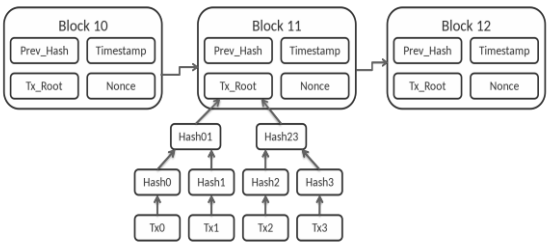

Figure 2: Blockchain diagram with the information content in each block locked with a timestamp (source: Matthäus Wander, CC permission to use).

With these preeminent properties, blockchain is considered as the first foundational digital technology for value exchange, just as the internet is the first digital medium for information exchange. The future development of blockchain is difficult to predict but it is very possible that blockchain will revolutionize online purchases and payments, record keeping, information and online gaming platforms, metaverse.

The applications of blockchain in the construction industry can be expanded further if combined with other technologies such as AI, NFT, BIM or metaverse.

3. Potential applications and developments of blockchain in the construction industry

Blockchain technology has had an impact on financial services, and many applications across industries have been implemented it. Cryptocurrency is changing the way of payments, foreign exchange, remittances, etc.

Architecture, or more broadly, the real estate industry does not seem to be affected by blockchain

and its applications. Traditionally real estate transactions have been done using conventional contracts and payment methods. However, blockchain can change this in a more secure way with smart contracts. More specifically, if real estate such as a plot of land, or a building is tokenized into a digital asset, it can be broken down into smaller fragments for exchanging values, and there can be many investors with a modest amount of capital being able to join. Transactions are secure and can be completely anonymous.

(Li et al., 2019) seeks to explore the challenges that have recently emerged in the construction industry. The results have shown that blockchain could become a solution to some of these challenges. This study suggests that there are seven clear application areas, namely: Smart Cities and Sharing Economy; Smart energy; Smart home; Smart government; Smart traffic; BIM and construction management; Business model and organizational structure.

With anti-tamper and information transparency characteristics, blockchain gives us an ability to access the origin of materials and energy, allows users predicting about the recycling and reuse of material and manufacturing products which are used in the built environment. Therefore, blockchain is an emerging idea technology in the construction industry toward a circular economy (CE). This was clearly shown in the study of Shojaei et al (2021).

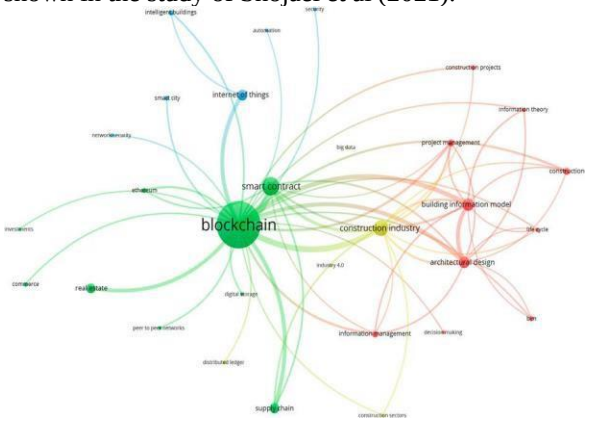

Figure 3: Bibliographic map of the co-occurrence of the top 30 keywords in studies covering blockchain in the construction industry (source: Plevris et al., 2022).

Plevris et al (2022) surveyed on Scopus from 2017 to 2022 using the keyword "blockchain" in combination with some other keywords of the construction industry, resulting in many related studies with other important keywords. The frequency of occurrence of those keywords is represented as a weighted network graph. In which, "blockchain" is the most popular keyword, appearing in the center of the network with the largest diameter (280 occurrences), followed by "smart contract" (91), "construction industry" (76), "building information modeling" (56), "architectural design" (50), "internet of things" (49), "supply chain" (45) and "project management" (28). This chart shows the importance of blockchain in the ecosystem of the construction industry, almost as a central bridge of smart contracts, construction industry, BIM and architectural design (Fig. 3).

If we consider the metaverse as a new arena of the construction industry, in our opinion, blockchain has an impact on 8 work groups: BIM and CAD, smart contract management, smart cities – smart buildings, project management, supply chain management, real estate, product copyright, construction architecture, and metaverse (see Fig. 4).

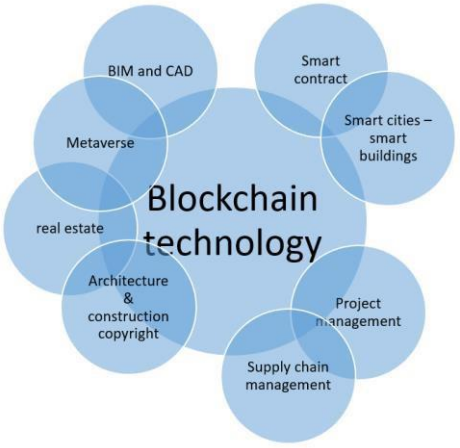

Figure 4: Blockchain and 8 potentially affected sectors in the construction industry

Blockchain technology can solve the problems of these sectors in the following ways:

- It is possible to digitalize real estate into digital assets, thereby increasing the ability to divide ownership, increasing liquidity due to transactions anytime, anywhere, and promoting smart contract adoption in the construction product business. Currently, smart contracts are not really common due to the lack of legal protection, the budding of e-wallets and digital signatures. But in the very near future, this will be a mainstay in the architecture - construction industry. Traditionally, real estate transaction records have been managed and stored by a single administrative point – typically the local government. With blockchain, all real estate ownership and transaction records can be publicly stored in the cyberspace as a digital record with tamper resistance, in a decentralized manner. Therefore, real estate records and transactions are transparent, immutable and irrevocable. The immutability and transparency of blockchain support transparency of ownership and thus enhance real estate transactions. In addition, verifying information related to real estate becomes an easy task, without requiring lengthy, high-cost and intermediary procedures.
- The spread of NFT (Non-fungible token) deployment to almost all fields of art and entertainment such as music, movies and video games, is providing an opportunity to raise public investment capital worldwide for projects. Projects

with clear applicability and value to the community will attract capital more easily through NFT. NFT is also applicable to real estate, digital buildings in a virtual metaverse. Virtual reality has long been used in real estate for home tours and virtual exhibition - conference, and the development of the metaverse could expand that functionality. A person who is very poor, homeless, but can still have a virtual house in the metaverse, where he can freely decorate, take care of and enjoy the space of his house. This is already very common in DeFi games such as DECENTRALAND, UPLANDS. For example,
Uplands is not a popular metaverse game but more of a business and real estate transaction. Real estate locations in the metaverse correspond to real-world locations. Once you own a piece of land in the game, you can sell it for profit every few hours. You can also sell or buy other properties on the Uplands marketplace. However, in-game transactions do not reflect real-life transactions. Uplands operates trading through its internal currency - UPX. This is a relatively new game with a unique concept.

- Architectural design copyright through NFT solution: Prototype designs sold as NFT help design teams save time and effort... 3D building design model can be built in the metaverse, help construction design companies earn money quickly without physicalizing these intellectual assets. Until now, this is still an idea, but with the rapid development of the metaverse, this idea will become an economic pillar of the metaverse, and architects can have a completely new working arena (Fig. 5).
- Eliminate middlemen or middle agents: blockchain technology is characterized by centralized charging, so the role of the middleman is no more valid. The validation of transactions is entirely done by the decentralized network. This feature benefits both buyers and sellers, as commissions and transaction fees have been eliminated (although blockchain transaction fees are still applied). Once buyers and sellers can connect directly and without any middlemen, the transaction is also faster, more convenient and transparent than the traditional way.
- The BIM protocol requires the collaborative work of many people and sectors, thereby posing a requirement to store and trace the work. By providing a reliable data management and storage solution, enhancing network security, and ensuring data ownership and change tracking, blockchain can help perfect the BIM environment and BIM management. Using blockchain technology, the BIM system can track, authenticate and prevent tampering of historical data related to BIM processes…
- It has been established that blockchain can indeed assist in all key areas of project management, including: 1) contract management, 2) purchasing management, 3) financial management, 4) asset and inventory management, and 5) management subcontractors in many ways: increasing the reliability of construction records, construction sales contracts, combating tampering of activity records, etc., and at the same time motivating stakeholders to provide timely records of their activities without any privacy risk.

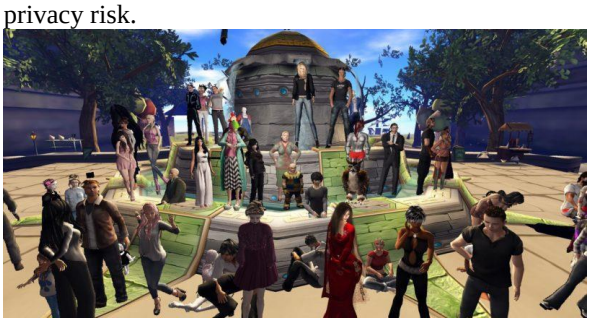

Figure 5: Virtual people (avatar) gather in a virtual world where blockchain technology ensures transparency, ownership and smooth transactions. (source: https://www.gameslikezone.com/)

- Smart city - smart building: A smart city is a city built on an information technology foundation that helps to connect and create an overall organic system connected from many component systems with an artificial intelligence system, taking advantage of potential opportunities and limit any associated threats arising from urbanization. Once the foundation is firmly established, the role of blockchain emerges. It is distributed ledger technology that will help smart cities solve 6 key problems of increasing security, improving healthcare, managing waste, simplifying education, saving energy and optimizing traffic. For example, effective waste management is an urgent issue in many major cities around the world. Blockchain can help maintain a clean and beautiful environment by transparently tracking real-time waste collection and recycling.

In addition, urban engineering-related malpractices can be avoided if there is a transparent, timely and immutable record of the activities involved, based on the blockchain network.

Blockchain technology and smart contracts can be used for flexible, decentralized access control of smart buildings. Based on blockchain and smart contracts, we can securely and flexibly manage building access privileges for long-term residents and visitors in an efficient, decentralized manner. They also limit the risks associated with one person having access to one or more spaces in the building.

4. Contradictions

The heart of the controversy is that unlike banking transactions, cryptocurrency transactions need to be authenticated by the respective blockchain network, which consumes huge amount of electricity. Many studies have estimated that the energy required for one Bitcoin transaction can be equivalent to the energy required for several hundred thousand VISA card transactions. As such, blockchain-based cryptocurrency is a technology with a serious environmental impact due to high CO2 emission. The current solution to this problem is to move the transaction validation system from PoW to PoS to

reduce the energy of validating transactions like the Ethereum network is trying to do. The successful the Merge event marks that transition for Ethereum, cutting almost all of the carbon emissions caused by Ethereum transaction validation. But this process is not easy and faces many security risks.

The blockchain-based cryptocurrency is labeled by some investors and economists with something similar to a speculative bubble, illicit money or even an advanced Ponzi scheme. Cryptocurrencies are mostly used in illegal transactions, supply scalability issues, huge power consumption, long transaction times, and highly volatile values. Many countries still ban or do not recognize the legality of cryptocurrencies.

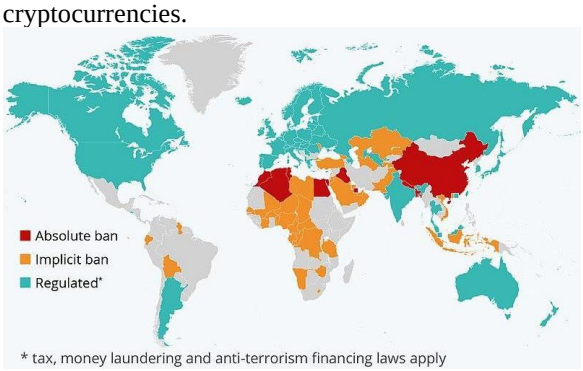

Figure 5: The legality of bitcoin until 2022 - Source: Law Library of Congress - License to use: CC 4.0

Blockchain and metaverse have a very close relationship, in which blockchain technology allows users to own digital assets in a virtual world through NFT. Metaverse is in its infancy, but big businesses have high hopes for it, such as Facebook which has changed its company name to Meta. Things seem a bit hazy at the moment due to its newness, but the metaverse will have many applications in Architecture in the very near future. With that, many scientists fear that the metaverse could be used negatively to address social challenges, such as using the virtual universe as an escape from the real world.

5. Conclusion

While blockchain technology is in its infancy and there are certainly some initial challenges and controversies to be resolved, the impact of blockchain on the current world is undeniable, but it takes some further patience to see how important blockchain is in the construction industry, although it is difficult to predict how much of an impact it will have. Blockchain is forecasted to have a strong impact on 7 industry-related fields, including: BIM and CAD, smart contract management, smart city – smart building, project management, chain management supply, real estate, construction product copyright.

Blockchain has great potential to be an extremely positive change driver in the construction industry. The digital transformation of the construction industry will not be separated from technology, and blockchain drives that transition faster and more efficiently.

What have we done to embrace the blockchain technology revolution? Perhaps what we should do is open up and wait to be accompanied with it to change our built world in a more positive way, instead of thinking it is too far away.

References:

[1] Li, J., Greenwood, D., and Kassem, M. (2019). Blockchain in the Built Environment and Construction Industry: A Systematic Review, Conceptual Models and Practical Use Cases. Automation in Construction 102, 288–307

[2] Shojaei, A., Ketabi, R., Razkenari, M., Hakim, H., and Wang, J. (2021). Enabling a Circular Economy in the Built Environment Sector through Blockchain Technology. J. Clean. Prod. 294, 126352.

[3] Plevris, V., Lagaros, ND and Zeytinci, A., 2022. Blockchain in Civil Engineering, The construction industry Industry: State of the Art, Evolution, Challenges and Opportunities. Frontiers in Built Environment, p.49

[4] Ankit Singh (2021). How can Blockchain Technology impact Architecture?. (See at: https://customerthink.com) Accessed September 8, 2022.

Breakout Room #3

Information and Communications Technology (ICT) & Intelligent and Secure Systems

Chairperson: Dr. Phan Tran Dang Khoa, DUT

A Study on a Trunk Reservation Control Method with Waiting Queue for Priority Calls in Emergency Situation

Yoichiro Arii[1], Katsunori Yamaoka[2], and Ken-ichi Baba[1]

[1]Graduate School of Electrical Engineering and Electronics, Kogakuin University, Japan
E-mail: cm21002@ns.kogakuin.ac.jp, baba@cc.kogakuin.ac.jp
[2]Department of Information and Communications Engineering, Tokyo Institute of Technology, Japan
E-mail: yamaoka@ict.e.titech.ac.jp

Abstract

In case of emergency, a huge number of call requests cause congestion in the network including subscriber telephones, VoIP and mobile phones. In order to increase the number of calls that can be accommodated in such an emergency, a trunk reservation control method that reserves a part of communication resources exclusively for priority calls and a holding time control method for general calls have been proposed. However, in these line reservation controls, it is necessary to secure network resources that are greater than the call volume of priority calls that are predicted to prevent call loss of priority calls. In this paper, we proposed a trunk reservation control by allowing priority calls to waiting to reduce the call blocking probability.

In an emergency situation, a large number of safety confirmations and important calls are made. We should distinguish between telephone calls that priority calls and general calls to maintain relief, recovery, and public order during disasters. And we want to accommodate as many general calls as possible while securing priority calls. As a method to solve the congestion problem in an emergency, Ref. [1] proposed a call admission control method using trunk reservation control and holding time control. However, since priority calls should not be lost, this line reservation control had to reserve a large number of lines according to the threshold value, so that network resources cannot be fully utilized.

In this paper, we study a trunk reservation control method that reduces the number of reserved lines to make effective use of network resources and keeps priority calls on hold so that priority calls are not lost. In the proposed method, the number of reserved lines for priority calls is reduced to the minimum necessary. When a call request for a priority call occurs and cannot be accommodated, it was inserted into the waiting queue instead of immediately dropping the call, so that the call blocking probability for general calls is reduced by reducing trunk reservation for priority calls. Figure 1 shows a conceptual diagram of the proposed method.

In order to evaluate the performance of the proposed method, we compare the call blocking probability between the conventional method and each reduction rate of reserved lines the proposed method. Figure 2 shows the relationship between h_g and general call blocking probability. β represents the reduction rate of the number of reserved lines compared to the existing method. From Fig. 2, it can be seen that the call blocking probability of the proposed method is lower than that of the existing method. And, the call blocking probability decreases as the number of reserved lines decreases. Although not shown in the figure due to space limitation, the waiting time for priority calls in the proposed method was also reduced significantly.

In conclusion, it was shown that the call blocking probability can be reduced by reducing the number of reserved lines in the proposed method and using queues for priority calls.

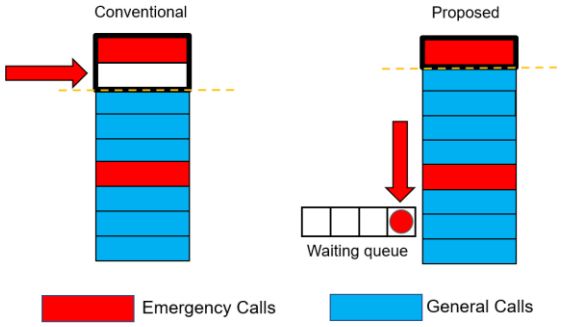

Fig. 1. Proposed Method

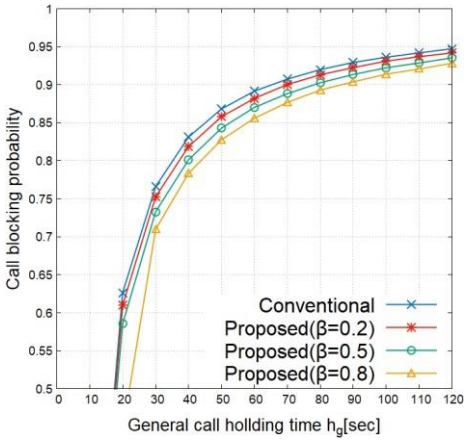

Fig. 2. Call blocking probability

References:

[1] K. Tanabe, et al., "Threshold relaxation and holding time limitation method for accepting more general calls under emergency trunk reservation", *IEICE Trans. Fundamentals*, vol. E99.A, no. 8, pp. 1518–1528, August 2016.

Method of Quantitative Assessment of Media Influence on Twitter

Yuki Sakurai, Aki Kobayashi*

Department of Information and Communication Engineering, Faculty of Informatics, Kogakuin University
E-mail: j019142@g.kogakuin.jp, aki@cc.kogakuin.ac.jp

Abstract

The influence of social networking services (SNS), such as Twitter, on the formation of public opinion, is growing. In this paper, we propose a method to quantitatively assess the impact of external media such as newspaper articles on the formation of topics on Twitter.

1. Introduction

Twitter, one of the famous social networking services (SNS), is widely used as a tool to transmit and collect information as well as for entertainment purposes such as passing the time [1]. In this study, we proposed a method to quantitatively assess the influence of each external media on the topics on Twitter.

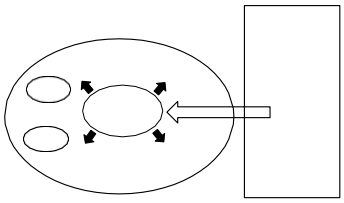

Fig. 1. Impact of External Media on a Topic.

2. Proposed Method

The target of analysis is the set of tweets that constitute a topic on Twitter. The impact of each external media on this tweet set is quantitatively assessed. In this paper, as an initial study, we define a tweet that directly refers to an external media as a tweet influenced by the external media. We then quantify this as the ratio of the influenced tweets to the set of tweets constituting the topic and define this as the degree of influence of the referenced external media on the topic. Data processing procedures and computational methods are shown below:

Using a sample stream of the Twitter streaming API, we obtained tweets containing Japanese in the tweet body, of which the set of tweet t_i containing the word w posted within 24 hours on a calendar day basis, is called T(w) (Eq. 1).

$$T(w) = \{t_i \mid w \in t_i\} \quad (1)$$

The method selects the topics as the trending words in Japan published by Twitter as of midnight at the end of the collection period. Therefore, a set of tweets containing a certain trending word W_t is denoted as $T(W_t)$ as in eq. 2.

$$T(w_t) = \{t_i \mid w_t \in t_i\} \quad (2)$$

Media-referenced tweets consist of the followings:
retweets or quoted tweets of tweets posted by the official Twitter account of each external media. and tweets including URLs of articles from external media. The influence of each media on the topic W_T is first determined by whether or not each tweet that constitutes the tweet set $T(W_T)$ has a media reference. When we denote that a tweet t has a reference to media m as m \in t, we define the formula for determining the reference of a tweet t to media m as in Equation 3.

$$L(t, m) = \begin{cases} 1 & (m \in t) \\ 0 & (\text{otherwise}) \end{cases} \quad (3)$$

Then, the number of tweets referring to media m in T(W_T) can be expressed as in Equation 4.

$$M(w_T, m) = \sum_{t_i \in T(w_T)} L(t_i, m) \quad (4)$$

Using this, we define the influence R_m of media m on topic W_T as in Equation 5.

$$R_m = \frac{M(w_t, m)}{|T(w_T)| - M(w_t, m)} \quad (5)$$

3. Experimental results

On October 15, there were 1,212 tweets that included “orix,” one of the trending words. Among them, there were 24 tweets referring to any media, so that $R_m \approx 0.02$. On October 19, there were 45 tweets that included “Nakamoto-san” and 9 tweets referring to any media so $R_m \approx 0.25$. These are the maximum value of R_m for any one media.

4. Conclusion

We have proposed an assessment measure of media influence on Twitter. We are addressing measuring various trend words and reviewing the assessment measure.

References:

[1] Yoshie Tani, Katsuyuki Matsumura, *A Model to Estimate the Impact of Sales Considering Information Diffusion on Twitter*, Proceedings of JSPE Semestrial Meeting,-**2016A**, A02(2016).

Table 1. Table captions should be centered and placed above the figure.

Date	W_T	influenced	Not influenced	R_m
2022.10.15	"orix”	24	1212	0.02
2022.10.19	"Nakamoto-san”	9	45	0.25

Influence of importance falsification in DTN

Hikaru KONDO , Osamu MIZUNO, Sakurai YUUDAI

Department of Information and Communications Engineering, Infomatic of Engineering, Kogakuin University, Tokyo, Japan
E-mail: j019132@ns.kogakuin.ac.jp, omizuno@cc.kogakuin.ac.jp

Abstract

Delay Tolerant Networking (DTN) allows data without end to end paths, are at high risk of attacks such as data eavesdropping and interference with data propagation. In previous studies, priority control was based on the importance assigned to data. However, in the presence of an attacker, it is possible to falsify the importance level and disseminate fake data. This paper investigates the impact of this attack and proposes a scheme to address it.

1. Introduction

DTN[1], nodes stores the received data its buffer. When it is ready to communicate with other nodes, the nodes sends duplicates of the data when they are ready to communicate with other nodes. However, the communication resources of nodes are very limited and it is difficult to take perfect measures in terms of security. Therefore, DTN communications are highly vulnerable to many attacks.

2. Influence of Fake Importance Data

We proposed Moderated Attribute based Transmissions Order Control(MATOC)[2] as a priority-based data transmission on DTN. MATOC assigns the high/low/ importance to each data. It controls that the high priority data will spread all nodes and the low priority of data will reach a specified node.

If an attacker to preferentially propagate fake importance data , true importance data may not sread as normal.We evaluate impact of the attack by simulation. In the simulation, attackers are 10% if the total number of users. Both of the priority data generated by the server and the fake priority data ganerated by the attacker are extracted ever hour. In addition the low priority data generated by normal nodes every minute.

Other simulation parameter shows in the Table 1. In the simulation, normal nodes and attacker move in 500×500m^2 field. The server generates high priority data and delivers it at middle of the field. When the normal nodes receive a high/low data from server or other normal node, re-deliver these data to other nodes using MATOC.

The result of simulation is shown in Figure 1. Vertical axis shows the propagation rate of each data. Horizontal axis shows data number generated at hour by hour. The result show that a certain amount of fake data is propagated along with the high priority data.

3. Countermeasures

When the server generates data with a high priority, it calculates a hash value from the data and sends it together with the encrypted data. The node that receives the data calculates the hash value from the data and discards it as invalid if it does not match.

Table1.Simulation parameter

Parameters	Value				
	Group1 (ID : p)	Group2 (ID : c)	Group3 (ID : lp)	Group4 (ID : lc)	Group5 (ID : server)
Simulator	the ONE				
Number of Simulations	30				
Simulation time[sec]	43200				
Number of nodes	270	270	30	30	1
Communication speed[Mbit/sec]	2				
Buffer capacity[Byte]	20M	20M	60M	60M	50G
Node speed [m/s]	0.5-1.5	2.7-13.9	0.5-1.5	2.7-13.9	0
Standby time [sec]	0-120				-
Routing method	MATOC	MATOC	Epidemic Routing	Epidemic Routing	MATOC

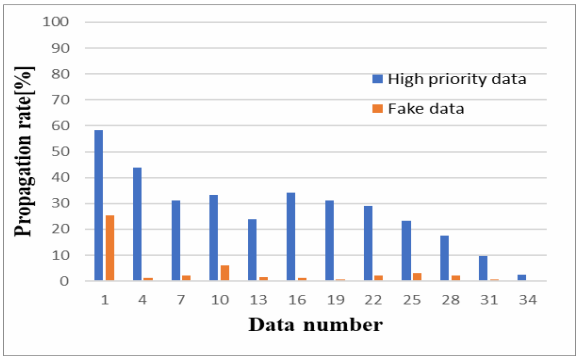

Fig1.Transmmision progration of priority data

4. Conclusion

In this paper, we evaluated influence of attacks in DTN. To protect such attack is future study.

References:

[1] M. Tsuru, M. Uchida, T. Takine, A. Nagata, T. Matsuda, H. Minami, and N. Yamamura, "DTN Technology: Status and Outlook," Communications Society Magazine, Spring Issue, No. 16, pp. 57-68, 2011.

[2] H. Suzuki and O. Mizuno, "Evaluation of Transmission Characteristics of Transmission Control Scheme by Moderated Data Attributes in DTN," IEICE Technical Report, NS2021-97, vol. 121, no. 301, pp. 7-12, Dec. 2021.

Recommending Tourist Destinations based on the Distribution of Attributes in Travel Planning via Chatbot

Junsaku Takada, Daisuke Kitayama

Department of Informatics, Graduate School of Engineering, Kogakuin University, Tokyo, Japan
E-mail: em21015@ns.kogakuin.ac.jp,kitayama@cc.kogakuin.ac.jp

Abstract

Planning group travel or tourism events can be challenging for participants with ambiguous wishes or who may have difficulty clearly expressing their opinions. In this study, we developed a chatbot designed to support travel planning by collecting candidate genres and destinations from users at arbitrary times and submitting the candidates to a vote among users. The output is a set of candidates based on the users' inputs. The candidates to be added are determined by estimating the attributes of the input on which users disagree. Because the voting results reflect the implicit wishes of each user, the proposed method captures the opinions of users who are less likely to express their preferences explicitly. By repeating this process while discussing their plans, users can select tourist destinations to visit. The results of a single test run of our proposed approach show that the number of genres recommended fell with the number of genres entered.

1. Introduction

Travel planning is often performed using group chat applications such as Whatsapp or Slack. However, understanding others' perspectives using such messaging applications may be difficult. In addition, some people may experience social difficulty expressing their opinions in a conversation with several other people. For example, a person might struggle to express an ambiguous request such as "I want to see a waterfall" after someone else provided a concrete proposal such as "I want to go to the Sai-no-Kawahara Open-air Bath". Furthermore, some people may struggle to suggest their ideas while planning is already in progress for a different destination or time. Below, we summarize the problem and outline the design requirements for the chatbot developed in this work.

Requirement 1: We consider the problem of users expressing strong or weak preferences or reservations depending on conversational timing. To solve this problem, we propose a system designed to collect opinions for a certain period of time and enable users to vote on candidates to coordinate the timing of the expression of opinions.

Requirement 2: The specificity of participants' wishes may vary. To solve this problem, the proposed system includes a function to present destinations as examples, which may be requests for genres or areas.

Requirement 3: Some users may be reluctant to express their opinions. To solve this problem, the proposed approach anonymizes the specific recommendations of travel destinations and presents all candidates to the users without identifying which user made a given suggestion.

Therefore, in this study, we propose a chatbot system designed to support travel planning by collecting users' wishes at arbitrary times, recommending candidate destinations, and allowing users to vote on the candidate travel plans. We assumed that travel planning could be divided into the following three phases, and thus collected a set of types of destinations, referred to as genres, as well as travel locations and areas.

(1) First, users must decide what to do on the trip (genre determination).
(2) They must select a destination region (area determination).
(3) Finally, they select a destination that satisfies (1) and (2) (location determination).

Our proposed system makes recommendations based on the genre and area distribution entered. The distribution of the dimension of the feature vector of genres represents the distribution of the genres. The latitude and longitude distributions of destinations within an area were used for the area distribution. The locations recommended by the chatbot in this study are not necessarily intended to be suitable as realistic potential travel destinations. The objective is to recommend locations that contribute to the determination of areas and genres, or to the expression and consideration of the opinions of reluctant users, even if they are not ultimately selected.

The remainder of this study is organized as follows. Chapter 2 introduces some related studies, and Chapter 3 presents our proposed approach. In Chapter 4, we describe and discuss an example. Chapter 5 summarizes our conclusions and suggests some potential avenues for further research.

2. Related Works

2.1 Recommendation of tourist information

Many studies have been conducted on recommending tourist information, such as tourism plans, destinations, and information on tourist travel locations.

Li [1] combined new techniques in data mining and operations research to recommend multi-day, multi-stay travel plans based on geotagged photos.

Yamazaki et al. [2] used Bayes' theorem to express the differences in the popularity of travel routes depending on the season and time of day in geotagged

photos, and incorporated this information into a Markov model to recommend intra-city travel plans that considered seasons and times of day.

Lao et al. [3] proposed a system to provide travel information with high regional characteristics by extracting regional features. Their proposed system provided travel recommendation information to users by satisfying two conditions, including a localized score and the content category of a given travel blog.

Cheng et al. [4] focused on personalized travel recommendations using photos posted in freely available communities. Furthermore, they proposed a personalized travel recommendation by considering the profile and attributes (gender, age, race, etc.) of individual users.

Kurashima et al. [5] extracted a photographer's travel history from geotagged photos and proposed a travel route recommendation.

While these methods may work well for a single person traveling alone, they are not intended for use by more than one person. In this study, we consider selecting travel destinations for multiple people.

2.2 Supporting decision-making among multiple people

Here, we introduce research on multi-person decision support.

Kim et al. [6] developed a chatbot for a group chat to manage discussion time, encourage uniform participation, and organize diverse opinions.

Lanyun [7] stated that group tourists are increasingly likely to engage in frequent group communication using digital applications instead of doing it face-to-face. Therefore, the authors explored ways to implicitly understand group preferences through an analysis of online in-group behavior by using a questionnaire to extract group preferences.

Amra et al. [8] proposed an approach to group recommendations from group dynamics perspective and analyzed a group's decision-making process for travel planning.

Shabnam et al. [9] evaluated aggregation strategies in terms of their ability to recommend a set of POIs to a group of tourists. In particular, they focused on groups with members with different travel preferences (high divergence) and similar preferences (low divergence).

Inma et al. [10] implemented an individual or group tourist destination recommendation system as an extension to e-Tourism, an application that allows users to plan sightseeing and leisure activities.

Kim et al. [6] implemented a chatbot designed to manage chat discussions by activating and managing time.
Their chatbot was designed to support reluctant users in expressing their opinions by allowing a third party to enter their preferences and recommend destinations.
Lanyun [7] studied group preferences. However, they did not consider group decision-making.

Reluctant users may encounter difficulty expressing their opinions with the system proposed by Amra et al [8].
Shabnam et al. [9] also did not consider group communication.

Similarly, Inma et al.'s recommendation system [10] was not designed to reflect the opinions of travelers with a preference or intention to visit certain destinations soon.

3. Proposed Method

In this paper, we used data obtained from Jalan.net. Genres, areas, and locations were obtained from general tourist information sites. The proposed method recommends locations based on the distribution of genres and areas from the genres, areas, and locations input by the users. As a data structure, locations are associated with areas and genres. Therefore, when a user enters a location to visit, the area and genre associated with that location are automatically entered as well. The candidate locations presented after the requests are received include the following.

(1) If the input is a location, that location is provided.
(2) If the input is an area or genre, a location that satisfies the input condition along with the recommended condition is selected as a condition that was not input by any user.
(3) Locations that meet the recommended criteria for both area and genre are selected.

The locations selected via method (2) are designed to achieve requirement 2 as indicated in Section 1. The locations selected via (3) allow the realization of requirement 3 by presenting locations who are not the input of any user, but who are considered relevant to each of their wishes.

The method consists of the following steps.

(1) Each user inputs a genre, area, and location. They may omit one or more of these if their preferences are ambiguous.
(2) Based on the latitude and longitude of the location in the input area, the system creates a recommendation condition for the area.
(3) Based on the input genres, the system determines the genre recommendation conditions.
(4) The system recommends candidate locations using conditions (2) and (3).

3.1 Area Recommendation Conditions

A minimum bounding rectangle (MBR) is created from the latitude and longitude of all locations belonging to each input area, and the center of gravity is created from the latitude and longitude of the vertices of all MBRs. Let $a_{!"\#}$ be the latitude and $a_{!\$\%}$ the longitude of the vertex of the MBR, and let $g_{!"\#}$ be the latitude and $g_{!\$\%}$ the longitude of the center of gravity. $g_{!"\#}$ and $g_{!\$\%}$ are obtained using Equations (5) and (6). We calculate the standard deviation from the latitude and longitude of all vertices used to create the MBR, respectively. The range of

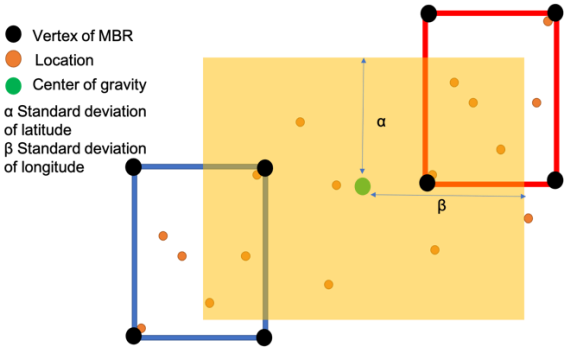

Fig. 1. Scope of Recommendation.

recommendations is created by the center of gravity of the latitude and longitude and a weighted standard deviation. The weight of the standard deviation is determined by the number of users who did not provide input regarding their preferred area. The more the users who did not provide specific input, the more ambiguous the group's requirements, and thus, the higher the weight and the larger the recommendation range. Let the range of the recommendation targets be given by Equations (1), (2), (3), and (4), and let n be the number of users who provided input and m be the number of users who did not provide input. $n + m$ is thus the number of users. This approach is illustrated in Figure 1.

$$noth = g_{!"\#} + 4\&'\$ \times \sqrt{\frac{1}{4n} \sum_{"\in +} (a_{!"\#} - g_{!"\#})} \quad , (1)$$

$$south = g_{!"\#} - 4\&'\$ \times \sqrt{\frac{1}{4n} \sum_{"\in +} (a_{!"\#} - g_{!"\#})} \quad , (2)$$

$$east = g_{!\$\%} + 4\&'\$ \times \sqrt{\frac{1}{4n} \sum_{"\in +} 8a_{!\$\%} - g_{!\$\%}9} \quad , (3)$$

$$west = g_{!\$\%} - 4\&'\$ \times \sqrt{\frac{1}{4n} \sum_{"\in +} 8a_{!\$\%} - g_{!\$\%}9} \quad , (4)$$

$$g_{!\$\%} = \frac{\sum_{"\in +} a_{!\$\%}}{4n}, \quad (5)$$

$$g_{!"\#} = \frac{\sum_{"\in +} a_{!"\#}}{4n}. \quad (6)$$

Locations within the range of recommendation targets created by these methods are considered as candidate locations to be recommended. If no area is entered, all locations are considered candidate locations.

3.2 Genre Recommendation Conditions

First, a genre feature vector was created for each input genre. We used a 200-dimensional model trained on Wikipedia using word2vec to create a feature vector for genres. The genres of the locations in the data from Jalan were divided into 329 categories, and each location was assigned a main genre and a

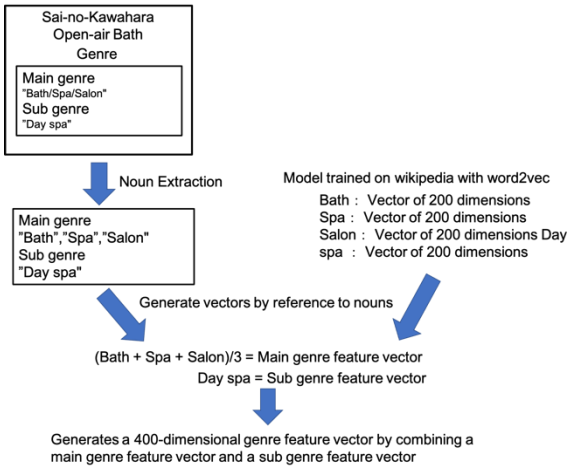

Fig. 2. Feature vector generation for genres

subgenre. For example, the major genre of a location called "Sai-no-Kawahara Open-air Bath" in the data was "bath/spa/salon," and its major genre was "day spa". Nouns were extracted from the major and minor genres using MeCab. For example, the nouns "bath", "spa", and "salon" can be extracted for "bath, spa, and salon", and "day spa" can be extracted for "day spa". The average vector of nouns extracted from the main and sub-genres was used as the vector for each. The main genre vector and subgenre vector were combined to form a 400-dimensional vector of genres, which is the feature vector used to model genres, as shown below in expression 7, where g is the name of the genre. An example of these conditions is shown in Figure 2.

$$V_g = @v_{g_1}, v_{g_2}, \ldots, v_{g_{400}} \ \text{A}. \quad (7)$$

When two or more users input genres, the mean and standard deviation are calculated for each dimension of the feature vector of the genre, and a range of dimension values is determined based on this mean and weighted standard deviation. As with area, the weight of the standard deviation is determined by the number of users who did not provide input on the genre of their preferred destination. However, because the value of the genre dimension is limited between -1.0 and 1.0, the weight is set smaller than for area. The input genre set is G, and the range is obtained by adding or subtracting the value of expression (8) to or from the mean. Let n be the number of users who provided input and m be the number of users who did not provide input. If the value of each dimension of the genre vector of a candidate location is within the range of the calculated dimensions, it is recommended. This process is illustrated in Figure 3.

$$std_{@} = 2\&'\$ \times \sqrt{\frac{1}{n} \sum_{\%\in 1} 8v_{\%_!} - \bar{v}_{@}9} \quad , \quad (8)$$

The standard deviation may be zero for only a single input location. In this case, Equation (9) is used instead

Table 1. Input Example 1

User	A	B	C	D
Location	Kusatsu Hot Spring	-	-	-
Main genre	Bath/Spa/Salon	-	-	-
Subgenre	Health spa/super public bath	-	-	-
Area	Kusatsu Town (Agatsuma-gun)	Chichibu City	Nikko City	-

Table 2. Input Example 2

User	A	B	C	D
Location	Kusatsu Hot Spring	-	-	-
Main genre	Bath/Spa/Salon	Bath/Spa/Salon	-	-
Subgenre	Health spa/super public bath	Health spa/super public bath	-	-
Area	Kusatsu Town (Agatsuma-gun)	Chichibu City	Nikko City	-

Table 3. Input Example 3

User	A	B	C	D
Location	Kusatsu Hot Spring	Chichibu Shrine	-	-
Main genre	Bath/Spa/Salon	Shrine/Jingu/Temple	-	-
Subgenre	Health spa/super public bath	Shrine/Jingu Tour	-	-
Area	Kusatsu Town (Agatsuma-gun)	Chichibu City	Nikko City	-

Table 4. Input Example 4

User	A	B	C	D
Location	Kusatsu Hot Spring	Chichibu Shrine	-	-
Main genre	Bath/Spa/Salon	Shrine/Jingu/Temple	Natural Landscape/Spectacular Views	-
Subgenre	Health spa/super public bath	Shrine/Jingu Tour	Canals/riverscapes	-
Area	Kusatsu Town (Agatsuma-gun)	Chichibu City	Nikko City	-

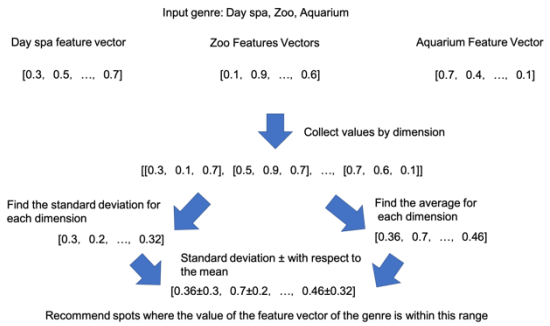

Fig. 3. Standard deviation vector

of Equation (8). Instead of the standard deviation, we used the value $0.03 \times 4^{\frac{\text{‥\#\$}}{\text{‥\%\&}}}$, which varies with the number of users who did not provide input.

$$std_{0} = 2^{\frac{\&\text{‘(}}{\&\text{‘\$}}} \times 0.03 \times 4^{\frac{\&\text{‘(}}{\&\text{‘\$}}}. \quad (9)$$

If no input is received, a genre is selected at random.

4. Execution Results and Discussion

The inputs are summarized in Tables 1, 2, 3, and 4, assuming travel planning for four people. In the table, "-" indicates no input. A total of 5,753 candidate locations were recommended, with "Kusatsu-cho (Agatsuma-gun)," "Chichibu City," and "Nikko City" as area input. Table 1 shows example inputs: one person specified a location, two people specified an area, and one person did not specify a location. Table 2 lists example inputs; one person specified a location, one person specified a genre and area, one person specified an area, and one person did not specify their preferences. Table 3 lists example inputs, in which two people specified a location, one person specified an area, and one person did not specify a location. Table 4 shows an example of inputs, in which two people specified a location, one person specified a genre and an area, and one person did not specify anything.

Table 5. Recommendation results for input example 1

Number of recommended locations	5769
Number of locations in the genre entered by A	291

4.1 Consideration of recommendation conditions by area

The results of these recommendations are summarized in Tables 1, 2, 3, and 4. The input in Table 1 is based on the number of people who have not yet entered a genre. The content demonstrates that the range of recommended genres may be relatively broad. Table 5 shows that 5,769 locations were recommended, whereas 291 locations were provided in the entered genres. The results of the proposed method allowed us to considerably expand the genres beyond those we

Table 6. Recommendation results for input example 2

Number of recommended locations	302
Number of locations in the genre entered by A and B	291

Table 7. Recommendation results for input example 3

Number of recommended locations	331
Number of locations in the genre entered by A	291
Number of locations in the genre entered by B	40

entered. The inputs in Table 2 were the same for the two genres, and two people had not yet entered a genre, which shows that the range of the recommended genres was slightly wider. Table 6 shows that 302 locations were recommended, whereas 291 locations were included in the genres entered. From these results, we were able to expand the genres slightly beyond those we had entered. Two more genres were added, both with the major genre of "bath/spa/salon" and the minor genres of "day spa" and "bedrock baths.

The inputs in Table 3 differ for the two genres and two users had not yet entered a genre, suggesting that the range of the recommended genres were slightly wider. Table 3 shows that 331 locations were included in the genres entered, compared to 331 recommended locations. Based on these results, it was not possible to expand the genres beyond those entered. The inputs in Table 4 differ among the three genre inputs, and a single user had not yet entered a genre, suggesting that the range of recommended genres was not very broad. Table 8 shows that the total number of locations for the genres entered was 585, compared to 585 recommended locations. The genres did not expand beyond the genres entered from this result.

These results show that the number of genres subject to recommendation conditions decreased with the number of genres entered. However, no genres were recommended in the data shown in Tables 7 and 8 other than those entered. The proposed method determines the allowed width for each dimension of the input genre feature vector. If the standard deviation of a dimension is extremely small, the width of that dimension becomes small as well, and the value of that dimension in the genre vector of the candidate locations for recommendation does not satisfy the condition. Instead of using a width threshold condition, the condition must be relaxed by penalizing the scores of the outliers.

The results showed a problem with the genres associated with some locations. For example "Kegon-no-taki" was classified in the subgenre of "Canals and river scenery," instead of "Waterfalls/valleys," and "Kusatsu-Shiranesan" was classified in the subgenre of "Others," instead of "Mountains" or "Trekking/climbing". To solve these problems, genre vectors must be created to reflect the characteristics of the locations to which they belong.

Table 8. Recommendation results for input example 4

Number of recommended locations	585
Number of locations in the genre entered by A	291
Number of locations in the genre entered by B	40
Number of locations in the genre entered by C	254

Table 9. 3 Area inputs

	Noth	South	East	West
Kusatsu Town (Agatsuma-gun)	36.6542	36.5794	138.6050	138.5280
Chichibu City	36.1075	35.8662	139.1420	138.7130
Nikko City	37.0851	36.6228	139.8220	139.3370
Recommendation range	37.2783	35.6933	139.9435	138.1054

Table 10. 1 Area input

	Noth	South	East	West
Kusatsu Town (Agatsuma-gun)	36.6542	36.5794	138.6050	138.5280
Recommendation range	36.7664	36.4671	138.7205	138.4125

4.2 Consideration of recommendation conditions by area

Table 9 summarizes the MBR and recommendation ranges for the input areas, and Table 10 summarizes the results of the recommendation ranges with three input areas and one input area. Table 9 shows that the recommended range was larger than the MBR of all the areas entered, which suggests that the range was appropriately created. Table 10 shows that the latitudinal range of the recommended area was approximately three times wider than the latitudinal range of the MBR for the town of Kusatsu (Agatsuma County). The longitudinal range of the recommended area was approximately three times wider than that of the MBR of Kusatsu-cho (Agatsuma-gun). This shows that the range of the recommendations offered was extended by the number of users who had not yet provided specific locations.

5. Conclusion

In multi-person tourism and travel planning, some individuals may struggle to adequately express their opinions owing to vague preferences or being excluded from a discussion. To solve this problem, we developed a chatbot designed to support planning by collecting candidate genres and locations from users and submitting them for a vote. The results showed that the recommended number of genres was reduced with the number of genres entered. Future research may consider creating genre vectors to reflect the characteristics of the locations to which they belong. The conditions can also be relaxed by scoring the genres to penalize those who fall outside the range of acceptable conditions for a given genre. The present work is a discussion based on the results of a single example run. In the future, we plan to implement a

voting function in the chatbot and evaluate the system with users.

Acknowledgments

This work was supported by ISPS KAKENHI of Grant-in-Aid for Scientific Research(C) Grant Number 21K12147.

References:

[1] X. Li, “Multi-day and multi-stay travel planning using geotagged photos,” Proceedings of the Second ACM SIGSPATIAL International Workshop on Crowdsourced and Volunteered Geographic Information, pp.1–8, GEOCROWD ’13, Association for Computing Machinery, New York, NY, USA, 2013.

[2] T. Yamasaki, A. Gallagher, and T. Chen, “Geotag-based travel route recommendation featuring seasonal and temporal popularity,” 2013 9th International Conference on Information, Communications Signal Processing, pp.1–4, 2013.

[3] Y. Lao, Y. Wei, and D. Han, “A method for discovering local travel information from travel-blogs,” Proceedings of the 2020 The 6th International Conference on Frontiers of Educational Technologies, p.212–216, ICFET 2020, Association for Computing Machinery, New York, NY, USA, 2020.

[4] A.-J. Cheng, Y.-Y. Chen, Y.-T. Huang, W.H. Hsu, and H.Y.M. Liao, “Personalized travel recommendation by mining people attributes from community-contributed photos,” Proceedings of the 19th ACM International Conference on Multimedia, p.83–92, MM ’11, Association for Computing Machinery, New York, NY, USA, 2011.

[5] T. Kurashima, T. Iwata, G. Irie, and K. Fujimura, “Travel route recommendation using geotags in photo sharing sites,” Proceedings of the 19th ACM International Conference on Information and Knowledge Management, p.579–588, CIKM ’10, Association for Computing Machinery, New York, NY, USA, 2010.

[6] S. Kim, J. Eun, C. Oh, B. Suh, and J. Lee, “Bot in the bunch: Facilitating group chat discussion by improving efficiency and participation with a chatbot,” p.1–13, Association for Computing Machinery, New York, NY, USA, 2020.

[7] L. Zhang, “Supporting group tourists’ planning: Understanding group preferences through ubicomp systems,” Adjunct Proceedings of the 2015 ACM International Joint Conference on Pervasive and Ubiquitous Computing and Proceedings of the 2015 ACM International Symposium on Wearable Computers, p.483–488, UbiComp/ISWC’15 Adjunct, Association for Computing Machinery, New York, NY, USA, 2015.

[8] A. Delic, J. Neidhardt, T.N. Nguyen, F. Ricci, L. Rook, H. Werthner, and M. Zanker, “Observing group decision making processes,” Proceedings of the 10th ACM Conference on Recommender Systems, p.147–150, RecSys ’16, Association for Computing Machinery, New York, NY, USA, 2016.

[9] S. Najafian, D. Herzog, S. Qiu, O. Inel, and N. Tintarev, “You do not decide for me! evaluating explainable group aggregation strategies for tourism,” Proceedings of the 31st ACM Conference on Hypertext and Social Media, p.187–196, HT ’20, Association for Computing Machinery, New York, NY, USA, 2020.

[10] I. Garcia, L. Sebastia, and E. Onaindia, “On the design of individual and group recommender systems for tourism,” Expert Systems with Applications, vol.38, no.6, pp.7683–7692, 2011.

The Effect of Timing the Initiation of Active Interaction on Smart Speakers Based on Human Activity

Kanta Ito[1,a] and Daigo Misaki[1,b]

[1]Graduate School of Engineering, Kogakuin University, Tokyo, Japan
[a]am22007@ns.kogakuin.ac.jp, [b]misaki@cc.kogakuin.ac.jp

Abstract

Attention to the user's state is necessary for devices with voice assistants, such as smart speakers, to perform active interactions that are acceptable to the user. In this study, we conduct basic experiments on the attention capacity used for each user's social behavior and the timing of starting interaction. We propose a method for determining the appropriate timing of attention.

Recent advances in Internet and voice identification technology have led to the emergence of voice assistants such as Alexa and google assistant. Devices equipped with voice assistants, such as smart speakers, currently interact passively, responding to user inquiries. This research considers active interaction that is acceptable to the user by using artificial intelligence and sensing technology. They have evaluated the acceptability of active interactions using storyboards [1] and the response rate of interactions initiated at random times [2]. The above studies have shown that the acceptability of interactions is related to the attention used in the user's activity and that the attention used in the user's social behavior is related to the attention used in the user's activity. In this study, we examined the attention capacity used for each user's social behavior and the timing of initiating interaction.

METHODOLOGY

We propose a system that notifies information when a user moves. The system is equipped with acceleration sensors attached to the user's feet and notifies information when the user stands up.

Using an intelligent speaker that actively notifies the user, we evaluated the subjective and quantitative cognitive load caused by the timing of notification. Figure 1 shows the situation. Subjects were asked to assume they lived at home, studied, walked, and read. Information was notified only once per experiment, and three experiments were conducted per subject at three different times: Walking, studying, and reading. Subjective cognitive load was assessed by a 7-point questionnaire on how frustrated they felt. Quantitative cognitive load was compared by measuring the time to reconvene for interrupted activities when the notification was given.

Figure1: Interaction from the speaker in the test

RESULTS AND DISCUSSION

As shown in Figure 2, subjective frustration was lowest during Walking, but there was no predominant difference in mean values. Quantitative evaluation could not measure activity reunion time in the reading, so only Walking and studying were compared. Activity reacquaintance time with notifications was shortest during Walking compared to studying, with a mean value twice as long. We plan to construct a system that takes into account the timing of actions and interactions in the home, as shown in Figure 3, and test whether it can encourage users to change their behavior.

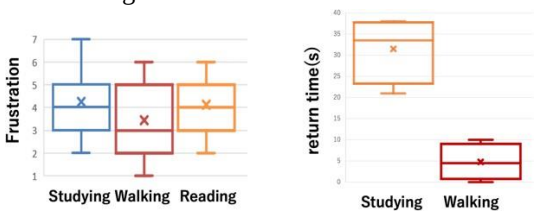

Figure 2: Interaction frustration, the time required to resume activities

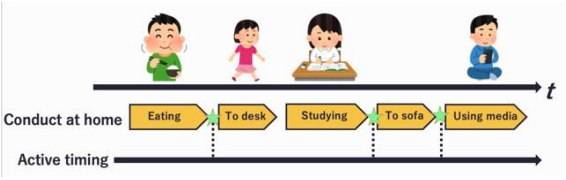

Figure 3: Notification system tailored to user activity

References:

[1] Zargham, Nima, et al. "Understanding Circumstances. for Desirable Proactive Behaviour of Voice Assistants: The Proactivity Dilemma." 4th Conference on Conversational User Interfaces. 2022.

[2] Cha, Narae, et al. "Hello there! is now a good time to talk? Opportune moments for proactive interactions with smart speakers." *Proceedings of the ACM on Interactive, Mobile, Wearable and Ubiquitous Technologies* 4.3 (2020): 1-28.

Route Finder Interface with Route-Piece Assembly on a Map

Jumpei Toyofuku † [a] and Aki Kobayashi † [b]

† Graduate School of Engineering, Kogakuin University, Japan
Department of Information and Communications Engineering, Faculty of Informatics, Kogakuin University, Japan
E-mail: a) cm22035@g.kogakuin.jp, b) aki@cc.kogakuin.ac.jp

Abstract

Existing route finder services can't search for "detour" routes that aren't direct trips to a destination such as for tourist purposes. On the other hand, tourists are often not familiar with the geography. Therefore, this study proposes a search support interface that searches for and presents "detour" routes with less effort to passengers who aren't familiar with the geography. After displaying candidate routes on a map, our method provides users with a function to change part of the routes on the map. We measured the time required for the user to assemble the desired route and found that the proposed method is efficient.

1. Introduction

Existing route finder services don't allow users to change a part of the proposed route when the user doesn't like it after the candidate route is displayed. However, most of the services don't allow users to change part of the proposed route when the user doesn't like it after the candidate route is displayed. Only a few services offer an interface for changing a part of the candidate route on a map. However, it looks like a graphical rerouting function on a map and doesn't provide an efficient route as it did in the initial search. In this paper, we propose an interface that displays some initial candidate routes on a map and replaces the partial route (or route pieces) with search results of efficient routes according to the user's directions. Our method provides support that enables a user without geographical knowledge to freely assemble the desired detour route.

2. Proposed method

Initial retrieve: As in general services, the system created by the authors displays candidate routes on a map.

Route selection and re-retrieve command: The user looks at the map and selects a starting station of the partial route that the user wants to "go around". The selected starting station becomes a transfer station. The system re-retrieves the route from the transfer station to the final station and displays candidate routes as well as the initial retrieve. The user selects the desired route from the candidate routes. This re-retrieve action can be repeated recursively as necessary until reached the final destination station.

The interface of this system achieves the selection of a re-retrieve section and the selection from its re-retrieve result candidate routes, each in a single action. In addition, the system doesn`t require geographical background knowledge from the user because all operations are performed while viewing candidate routes on a map.

Figure 1. Route display screen of the proposed method

3. Evaluation

We have made a comparison and evaluation using the proposed method and comparative method (Google Maps [1]). The comparison is the time it takes to accomplish a route search based on certain scenarios. The result is shown in Table1. It is shown that the proposed method can accomplish the search in less time than the comparative method.

Table 1. Route search time [s]

A participant	Comparative method	Proposed method
A	209	64
B	97	112
C	134	62
D	145	117

4. Conclusion

We have proposed an interface to support users without geographical knowledge to assemble a route for tourism using geographical information as a clue. Experimental results showed the effectiveness of the proposed interface.

References:

[1] Google Maps https://www.google.co.jp/maps (Reference 2022-10-17).

[2] S. Yamazaki, S. Nakajima, J. Mitera, *A Study on Window Views and Perception of Scenery in Local Railways*, Journal of the City Planning Institute of Japan Chubu Branch, **32**, 61-64 (2021).

Hand Motion Imagery EEG classification using Deep Learning CNN models for Brain-Computer Interface

Yuma Kadowaki and Hisaya Tanaka

Department of Informatics, Graduate School of Kogakuin University, Japan
E-mail: em21004@ns.kogakuin.ac.jp

Abstract

Experiments were done comparing two hierarchical structure CNN models and Input Data with difficult conditions for classification of Motor Imagery EEG data. The classification results showed that 89.29% was achieved with WVD, 70 x 100 input images, trained with a two-block CNN structure.

MI-BCI (Motor Imagery-Brain Computer Interface) is a technology for detecting characteristic brain waves emitted from the brain during motor imagery. Recent studies have used deep learning to improve the accuracy of feature extraction from EEG data. However, few studies using deep learning for classification of motor imagery have compared parameters in detail. In this study, we focused on time-frequency analysis and used a CNN (Convolution Neural Network) to classify motor imagery in order to examine under the conditions which high classification accuracy can be achieved.

CNN is a type of deep learning. It is a model of deep learning based on the human visual area. In this study, we focus on the convolutional layer and the pooling layer.

Time-frequency analysis is an analysis method that can visualize the power value of each frequency component in each time period. In this study, we use STFT (Short Time Frequency Transform), CWT (Continuous Wavelet Transform), and WVD (Wigner Ville Distribution), which are representative among time-frequency analysis methods. Time-frequency analysis can be used to confirm the occurrence of ERD (Event-Related Desynchronization), an EEG response to motor imagery. ERD is a phenomenon in which μ waves, one of the frequency bands in the EEG, are attenuated. Left and right movements of the body generate ERD in the opposite left and right motor cortices. Time-frequency analysis using STFT is shown in Figure 1. Figure 1 shows the spectrogram of the right hand motor imagery EEG. Subjects performed motor imagery between 3 and 9 seconds. Figure 1 shows that there is a trend toward ERD in Figure 1(a) and less ERD in Figure 1(b).

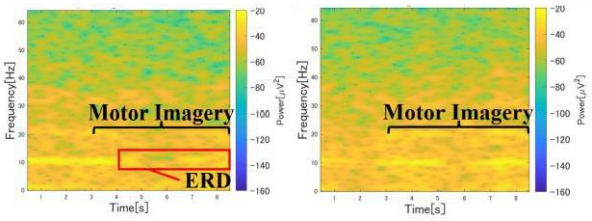

(a) Left Brain Wavepawer (b) Right Brain Wavepawer.

Fig. 1. Spectrogram of right hand motor imagery Brain wave.

Table 1. Comparison of preprocessing methods for motor imagery EEG classification by CNN.

(a) 2Blocks CNN result.

TF	Input Image Size			
	70×100	**140×200**	**200×300**	**280×400**
CWT	85.71%	82.14%	82.14%	82.14%
STFT	71.43%	82.14%	82.14%	89.29%
WVD	89.29%	89.29%	85.71%	85.71%

(b) 4Blocks CNN result.

TF	Input Image Size			
	70×100	**140×200**	**200×300**	**280×400**
CWT	92.86%	89.29%	89.29%	Error
STFT	71.43%	78.57%	85.71%	Error
WVD	82.14%	92.86%	89.29%	Error

In this experiment, the number of feature extraction layers, the method of time-frequency analysis on the data, and the size of the input image data were changed and compare the result. The input data used was BCI Competition II dataset III provided by BCI Competition[1].

The results of the experiment are shown in Table 1. TF stands for Time-Frequency analysis. 3 different time frequency analysis, input image size, and number of feature extraction layers were compared under different conditions. As a result, the highest accuracy was achieved 92.86% with CWT, 70×100 input image, and WVD, 140×200 input image, with 4-block structure CNN model.

In summary, the highest accuracy of 92.86% was achieved with the 4-block CNN model. However, the 4-block structure requires approximately 75 to 440 minutes of training time. Considering accuracy and training time, the 2-block structure CNN model and WVD, 70×100 input image achieved 89.29% in approximately 5 minutes.The results suggest that a 2-block structure, WVD, and 70×200 input images are suitable for the BCI Competition II dataset III.

References:

[1] Yuma Kadowaki, Hisaya Tanaka, "Study of Hierarchical Structure of Deep Learning to Improve Classification Accuracy of Brain-Computer Interfaces", IEEJ IM21030, PI21068, Reference material pp.29-34, (2021/12/16).

GPS Positioning Error Improvements by Pseudo Range Correction in Shinjuku Area

Koichi Saito, Takatoshi Sugiyama

Graduate School of Engineering, Kogakuin University, Tokyo, Japan
E-mail: cm21025@ns.kogakuin.ac.jp

Abstract

There is problem that it makes GPS positioning errors larger when reflected GPS signals are used unfortunately. To solve this problem, the pseudo range correction has been previously proposed. In the previous studies, in a simple east-west symmetrical simulation model the proposed method is effective to reduce the GPS positioning errors.

In this paper, we evaluate the GPS positioning errors improvements by proposed pseudo range correction in the simulation model established by Shinjuku area for feasibility study. The distances from the building reflection surface are actually measured by a commercial laser range finder in Shinjuku area. It is clarified that the proposed pseudo range correction can improve GPS positioning errors in Shinjuku model.

INTRODUCTION

GPS positioning calculations use the pseudo range between a GPS satellite and a GPS reception point calculated from the propagation time [1], but when reflected signal is received by building walls, the pseudo range is longer than the original linear distance, then GPS positioning accuracy deteriorates. One solution to this problem, the pseudo range correction is proposed [2]. The pseudo range correction needs the numbers of reflections and the incident angles, and the distances from the building reflection surface at GPS reception points. In Ref. [2], [3], in a simple east-west symmetrical simulation model, the numbers of reflections and the incident angles were estimated using the received GPS signal powers and the pseudo ranges before the correction, and the distances from the building reflection surface were treated as known values because they are relatively shorter.

In this paper, as a feasibility study of the pseudo range correction, we estimate the numbers of reflections and the incident angles in the simulation model established by Shinjuku area, and the distances from the building reflection surface is actually measured with a commercial laser rangefinder in Shinjuku area. We evaluate the GPS positioning errors by the pseudo range correction and show that the pseudo range correction can improve the GPS positioning errors.

THE PSEUDO RANGE CORRECTION

The pseudo range correction [2] is shown in Fig.1. GPS satellites A, GPS reception points B, and reflection points D are defined, respectively. Temporary GPS reception points C is also defined. A is intentionally transformed from three-dimensional coordinates to a two-dimensional plane [5] and A is placed on the same plane as B, D [2]. Since DB equals DC in triangle BCD, using the cosine theorem in triangle ABC, the original linear distance AB between the GPS satellite and the GPS reception point can be obtained from the observed pseudo range AC by using r and θ, as shown in Equation (1). r is defined as the distances from the building reflection surface at GPS reception point, n is defined as the numbers of reflections, and θ is defined as the incident angles respectively.

$$n = 1: \quad AB^2 = AC^2 + (2r)^2 - 2AC(2r)\cos\theta \qquad (1)$$

n = 2 to 3 can be calculated in the same way [2]. In this paper, r is actually measured with a commercial laser rangefinder in Shinjuku area.

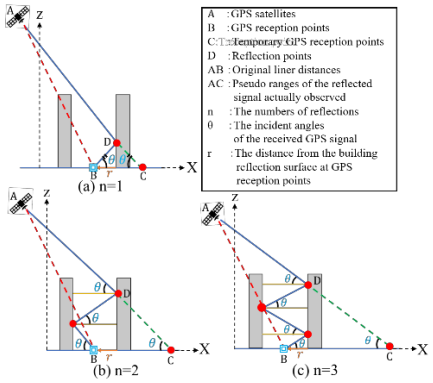

Fig. 1. Pseudo range correction.

SIMULATION PARAMETERS

Fig.2 shows the flow chart of Shinjuku area.

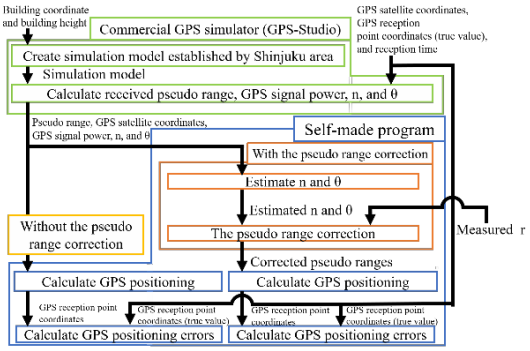

Fig. 2. Flow chart of Shinjuku area.

GPS-Studio is a GPS commercial simulation software [4]. The pseudo range correction and GPS positioning errors are self-made programs.

First, a simulation model is established by Shinjuku area using building coordinate and height in actual Shinjuku area. GPS-Studio uses simulation model, GPS satellite coordinates, GPS reception point coordinates (true value), and reception time to calculate information of received pseudo range, GPS signal power, n, and θ.

Next, n and θ are estimated. r is actually measured. The pseudo range correction of the self-made program calculates corrected pseudo ranges using pseudo ranges, n, θ, and r.

Finally, corrected pseudo ranges, and GPS satellite coordinates are used to calculate GPS positioning. GPS positioning errors are calculated by comparing the GPS reception point coordinates (true value) with the GPS reception point coordinates calculated by GPS positioning.

Fig.3 shows the simulation model of bird's-eye view. Table 1 shows the major simulation parameters. GPS satellite orbits are based on 24 hours from January 15, 2016 00:00:00 to January 16, 2016 00:00:00 [2], [3].

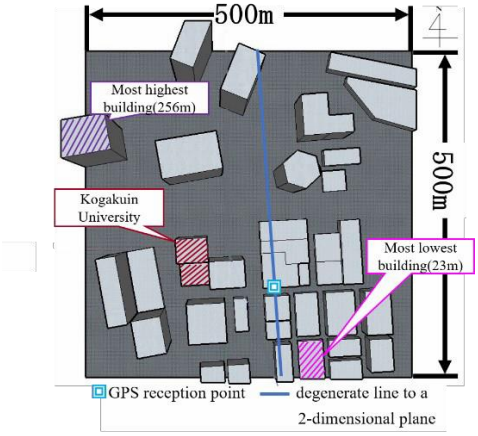

Fig. 3. Simulation model of bird's-eye view.

Table 1 Major simulation parameters.

Parameter	***Value***
Number of GPS satellites	32
Positioning simulation time	24 hours
Positioning interval	10 minutes
Number of reflections n	1～3
Building height	23m~256m
Building material	concrete

First, estimation model for n is created as same as Ref. [5]. Fig.4 shows the estimation model for n. The horizontal axis is the received GPS signal powers and the vertical axis is the pseudo ranges before the correction. If the received GPS signal power is observed as -160dBm and the pseudo ranges before the correction is calculated as 22000km, n can be estimated as 3.

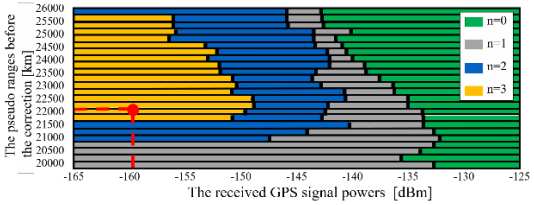

Fig. 4. Estimation model for n.

Next, estimation model for θ is also created as same as Ref. [5]. Fig.5 shows the estimation model for θ. The horizontal axis is the pseudo ranges before the correction and the vertical axis is θ. If n is just estimated to be 3 in Fig.4 and the pseudo ranges before the correction is calculated as 22000km, θ can be estimated to be 42° by using the approximation curve for n=3 in Fig.5.

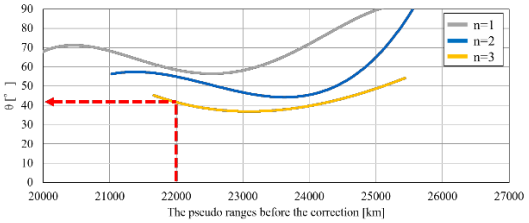

Fig. 5. Estimation model for θ.

SIMULATION RESULT

Fig.6 shows the CCDF (Complementary Cumulative Distribution Function) of GPS positioning errors. The horizontal axis is GPS positioning errors and the vertical axis is CCDF of GPS positioning errors.

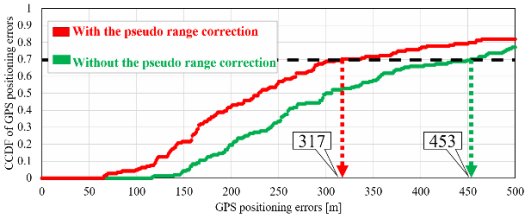

Fig. 6. CCDF of GPS positioning errors.

In this figure, the red line is GPS positioning errors with the pseudo range correction. The green line is GPS positioning errors without the pseudo range correction.

The pseudo range correction improves GPS positioning errors compared to the case without the pseudo range correction. For example, when CCDF of GPS positioning errors equals 0.70, the GPS positioning errors without the pseudo range correction has become 453m. The GPS positioning errors with the pseudo range correction has become 317m. Thus, the pseudo range correction can improve the GPS positioning errors by 136m.

CONCLUSION

When reflected GPS signals are received, pseudo ranges longer than original linear distances are observed, so they would degrade GPS positioning accuracy. To solve this problem, the pseudo range correction has been previously proposed. In this paper, as a feasibility study of the proposed pseudo range correction, the numbers of reflections and the incident angles were estimated using a simulation model established by Shinjuku area, and the distances from the building reflection surface at a GPS reception point has actually been measured with a commercial laser rangefinder in Shinjuku area. The pseudo range correction improves GPS positioning errors compared to those without the pseudo range correction. For example, when CCDF of GPS positioning errors equals 0.70, the GPS positioning errors without the pseudo range correction has become 453m. On the other hand, the GPS positioning errors with the pseudo range correction has become 317m. Therefore, the pseudo range correction can improve the GPS positioning errors by 136m.

References:

[1] Pratap Misra and Per Enge, "Global Positioning System: Signals, Measurements, and Performance," Syoyo Bunko, 2004.

[2] Toshinari Hayakawa and Norifumi Murai and Takatoshi Sugiyama, "Pseudo Range Estimation Model Based on Received GPS Signal Power in Many Skyscrapers Environments," KICS ICTC2018, pp.329-331, Oct. 2018.

[3] Toshinari Hayakawa and Norifumi Murai and Takatoshi Sugiyama," GPS Calculated Distance Error Improvement by Planar Approximation of Pseudo Range in Many Skyscrapers Environments," IEEE VTC2019, pp1-5, Sep. 2019.

[4] GPS-Studio, http://network.kke.co.jp/products/gps-studio/, Oct. 2022.

[5] Koichi Saito and Takatoshi Sugiyama," GPS Pseudo Range Correction by the Number of Reflections and Incident Angle Estimations," KICS ICTC2021, pp1014-1018, Oct. 2021.

A Novel Automatic Capturing Tool For Data Collection in Fish Freshness Determination

Nguyet Ha T. Tran [1], Dat Xuan Ho[1], Hoang Duc V. Le[1], Liem Thanh Nguyen[1], Hoang Hong Ngo[1], Ba Hoang Nguyen[2], Tuan V. Pham[1,2], Anh Thu T. Nguyen* [1,2]

[1]Faculty of Advances Science and Technology, University of Danang - University of Science and Technology
[2]L.Y.D.I.N.C Co. Ltd., Vietnam
E-mail: ttnguyetha2001@gmail.com, vailvy225@gmail.com, levhoangduc@gmail.com, honghoangngo@gmail.com, liem1762001@gmail.com, bahoang271199@gmail.com, pvtuan@dut.udn.vn, ntathu@dut.udn.vn.

Abstract

The need for high-quality food is increasing, and one specific illustration of this is customer's interest in diagnosing fish freshness. This paper presents a development of our previous research with a novel design of the capturing tool to collect a large fish image dataset. This comprehensive data is built to reflect fish freshness changed, from very fresh to very stale status, over 24 hours per fish sample. An automatic segmentation has also been developed to segment accurate fisheye regions where the biological and physical characteristics features of the fish will be extracted. The feature set includes 12 Intensity Slices, Minimum Intensity, Histogram, and Standard Deviation in 12 intensity slices. Notably, the qualitative and quantitative results of the features extracted from this automatically built database are similar to those that were presented in our previous studies.

Keyword : fish freshness determination , automatically capturing system , physiological features

I. Introduction

Fish nutrition has important substances such as protein, vitamin D, etc. and an excellent source of omega-3 fatty acids, which are extremely important for the body and brain. Therefore, the demand for fish products is increasing, identifying fresh fish is extremely important because freshness is not only a quality element of fish but it also ensures that no food poisoning occurs due to eating spoiled fish. Normally, raw or freshly caught fish are free of bacteria. When the fish dies, the immune system is weakened and the bacteria are free to grow. So far, most consumers generally distinguish the freshness of fish through intuition as well as personal experience.

However, with the advancement of computer science and image processing technologies, some researchers have suggested a method to identify fish disease by extracting fish skin tissue using image processing methods in order to assess the freshness of the fish [1]. Fish freshness reduction was analyzed using the HSV color model to establish its pattern [2]. Another study from the Dokuz Eylül University of Natural and Applied Sciences in Turkey [3] in 2013 used an automated data collection system with a smartphone and a set of stands with the data acquired is the image of fish observed from above. Although there is only one fish sample in each image, this method is still constrained by the camera angle and data collection capacities. A design has been applied in a paper in 2018 [4] with automatic identification and segmentation, but there are still disadvantages when it has to be collected manually by phone.

In the studies using the imaging modality, images of fishes have been collected from available online image sources or own-built [2]. In our previous studies [6], data collected manually and captured using an iPhone. Images captured from the iphones were in high resolution and revealed some results in fish freshness determination. However, when attempting to build a method for determining fish freshness that would function for the majority of devices, including low-cost ones, the achieved results from high-resolution images would not be appropriate. Additionally, manual data gathering techniques would become infeasible when this study is implemented and a substantially bigger amount of data is collected.

Our final target is to build a mobile low-cost fish freshness determination system that could be applicable on any types of image quality captured from different types of smartphone but reveal the same results. In addition, a large amount of data should be collected in the same scenario of imaging setting for testing. In this article, we introduce an automatic self-built rotating imaging system suitable and consistent for large amounts of data collection of medium quality images. Then, we conduct a testing of the performance of the system on feature extraction for freshness determination in comparison with the previous performance of Iphone [6].

II. Methodology and Materials

1. System design

In order to ensure uniform lighting and shooting angles, light intensity was maintained during data collection. For each sample, we have created an

automatic rotating image collection system with 5 equal corners at 72 degrees and a circular table top with a diameter of 50 cm coupled to a fixed-angle with step-motor. The system comprises a controller of Raspberry Pi 3B board, connecting to peripherals including one camera, a computer, and a cooling fan to control all the automatic imaging process. Rapoo camera specifications include a maximum resolution of 1280 x 720 and 1080p/30fps (up to 1920 x 1080), as well as beauty lights. Reduce reliance on PCs and other network sources with 3 levels of touch, support for H.264 with Scalable Video Coding, and UVC 1.1 encoding. The camera was positioned 10-15 cm vertically from the fish sample to capture the whole fish, as shown in Fig. 1 with outside view with black covering for unexpected light avoiding (a) and inside structure (b) (see Appendix 1). Five different fish samples were placed in the system and were photographed every hour for 25 hours after death. The table was rotated every 48 degrees and paused for 35 seconds for every sample imaging. Each shot lasted in two minutes to finish.. Together with an automatic hardware system, an algorithm was built to automatically save data to the cloud service. The automated system performed well and has satisfied the established objectives for collecting image datasets in terms of stability, durability, accuracy, and low cost.

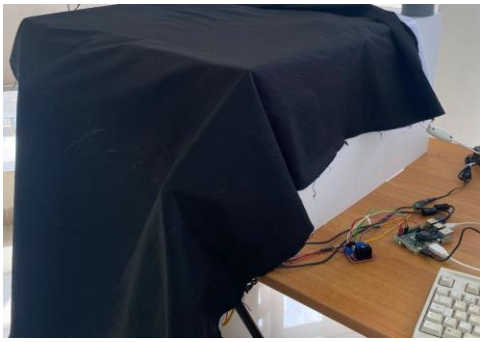

(a)

(b)

Fig. 1. The automated data collection system (a) outside, (b) inside.

2. Data collection

The five live Crucian carp fish were collected from the market. A dataset of 125 images of 5 fish samples were taken and labeled. Similar to our previous definition in classification of fish freshness [6], the acquired images are classified as "Fresh" during the early hours (0h-5h), "Neutral" during the middle hours (6h-19h), and "Stale" after around 20 hours (20h-24h).

3. Image pre-processing

With the purpose of significantly saving time and automatically capturing fisheye images on a large amount, a machine learning model has been built to automatically segment data for image preprocessing. Firstly, from raw-image as Fig. 2a, automatic fisheye position identification was conducted to crop into a smaller image as Fig.2b to facilitate the next step. Then, image segmentation based on YOLO's network model was used with Instance Segmentation technology from the recognized eye area in the image as Fig 2c. Fig.2d is the final result of this automatic process.

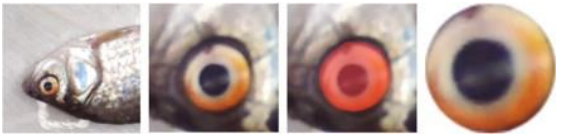

(a) (b) (c) (d)

Fig. 2.Automatically segment data process.

Fisheye photos of 125x125 pixels were segmented for the pupil and iris regions, cropped, and made grayscale. In order to verify the performance of the imaging method using the automatic low-cost photography system in comparison to the previous manual iphone imaging method, a set of four previously defined fisheye features (F0, F1, F2, F3) were extracted and analyzed. Particularly, the feature F0, which consists of 12 intensity slices, was extracted from the fisheye photos in a manner similar to the earlier study [6] by cutting straight lines across the image every 15 degrees, from 0 to 180 degrees. Minimum values of 12 intensity slices were taken for feature F1. With a step size of 1, the histogram of each gray fisheye picture was chosen to represent the intensity distribution of the image pixels for feature F2. The calculated standard deviation at each pixel point pertaining to the 12 slices makes up feature F3, which is the final feature.

4. Mobile Application Design

With the target of building a fish freshness assessment mobile application that is appropriate for all users, including those using low-cost devices that cannot capture images with high resolution, a mobile application has been designed for capturing fisheye images, automatically segmenting the fisheyes and

freshness determining. All the processing steps were conducted on a server following the flowchart in Fig.3.

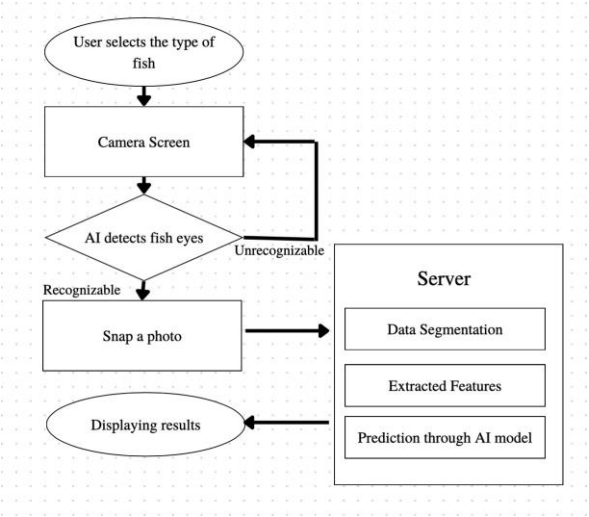

Fig. 3. Flowchart of the application's processing

III. Results and Discussions

1. Data Visual Analysis

From our visual observation, when a fish was fresh, fisheyes had entirely black pupils and were transparent, brilliant, convex, clear, and glossy in the early stages. After around 20 hours, fisheyes became opaque, submerged, shrouded in a haze layer and the size of pupils increased as Fig.4.

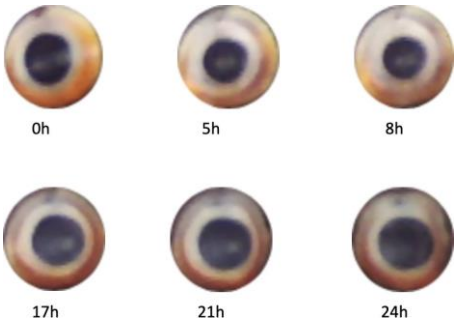

Fig. 4.Eye images of Crucian Carp at several typical time points (0-24 h after death)

2. Results on Extracted Features

Four features including F0 (12 Intensity Slices), F1 (Minimum Intensity), F2 (Histogram), and F3 (Standard Deviation) of Crucian carp were derived and classified into three groups (group 1: 0-5h; group 2: 6-19h; group 3: 20-24h). The average feature vector for fish was calculated and presented in blue bars for minimum values (Fig. 3b); purple, yellow and red color curves with surrounding purple, yellow, and red areas for standard deviation values (Fig. 3a, c).

From Figure 5a, the average value of F0 shows the decrease in the intensity values over the iris region, which is approximately from pixel 0 to 30 and 100 to 125 (see Appendix 2) when the fish becomes stale. Moreover, the F1 minimum intensities which are derived from the 3 groups are also sequentially increased as shown in Fig. 5b. For the F2 histogram feature, there is a movement from the low-intensity to high-intensity zone of group 1 to group 3, respectively. In addition, from Fig 5a, the F3 feature reveals a variation in the standard deviation of 12 intensity slices over time.

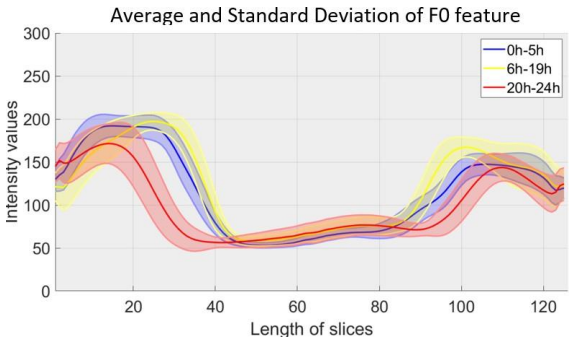

(a)

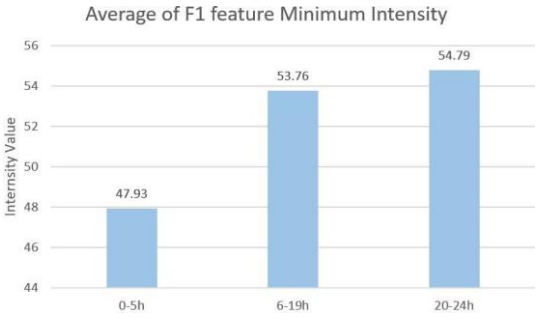

(b)

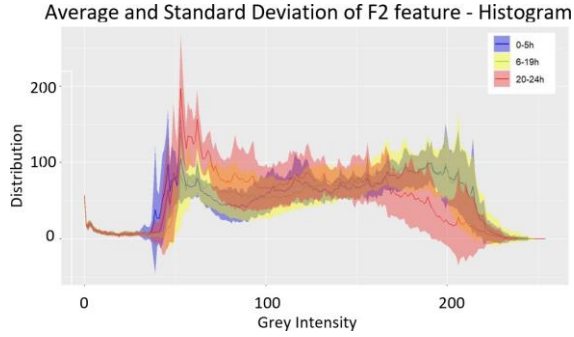

(c)

Fig. 5. Average values of (a) F0 features, (b) F1 features (c) F2 features of Crucian Carp

In order to determine efficiency of the novel automatic fish photo capturing system, comparison of changes over 25 hours of the 2 sets of four fisheye's features were presented in Table 1. The first set was extracted from the manual system of the previous work [6]. The second set was extracted from the

automatic system in this research. Table 1 shows that only the F2 feature graph is slightly different due to the changing of Crucian carp's physiological characteristics from visual analysis. In general, it shows a good match with the proposed assumptions, which is the evidence of the effective automatic system as well as the previous features.

Table 1. The comparison of data value trends over three groups between two datasets collected by two different approaches

Proposed features	**Manual and high resolution imaging method (proposed in [6])**	**Automatic and low resolution imaging method (novel proposal)**
Average values of the feature F0 (Fig. 5a)	Decreased in iris area (from group 1 to group 3)	Decreased in iris area (from group 1 to group 3)
Feature F1 - Minimum Intensity (average values)	Increased in pupil area	Increased in pupil area
Feature F2 - Histogram	Shifting to the right of graph	Slightly moving to higher intensity zone
Feature F3 - Standard deviation of the feature F0 (Fig. 5a)	Changing randomly	Fluctuation

3. The designed mobile application

The application with a user-friendly interface for mobile users has been developed using JavaScript programming, as shown in Fig. 6. It was designed to allow users to select different types of fish for freshness prediction. In order to guide users in taking fisheye images, a simulated fisheye image was created for localization and artificial intelligence was then utilized to prompt the user to take a photo. The taken image was stored automatically in the server for processing. Result of the prediction was then finally displayed on the screen. In addition, the application also included some user supporting functions such as searching history, guidance information. Furthermore, user's experiences and feedback on the prediction results have also been submitted to the server to aid in the development of the AI system.

On the server, we developed a system using Python programming and the MongoDB database that could interact with the user interface and process requests for determining the freshness of fish by image through the use of automatic segmentation, data extraction algorithms, and an AI set based on four proposed features. The server system also stored the user's evaluation findings, which helped to identify algorithmic flaws or gather data for further improvement.

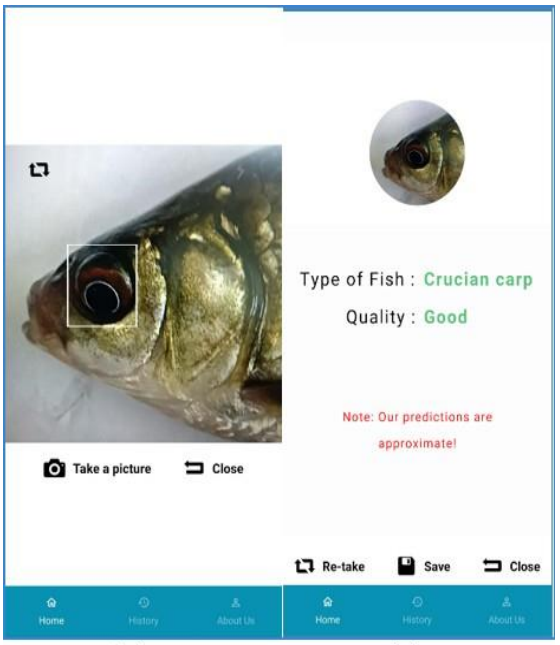

Fig. 6. (a) Camera screen, (b) Processing result screen

IV. Conclusion and Future Works

Our previous studies demonstrated high accuracy and efficiency, but were conducted in perfect circumstances of high-quality photographs. In order to extend the dataset as well as diversify operating conditions, and make it applicable to more real-world situations, we introduced an low-cost automatic imaging system for large amounts of medium-quality data collection. The system can automatically capture 125 images in 25 hours.

From the database of 125 Crucian carp's eye images, four features including 12 intensity slices, minimum values, histogram and standard deviation were extracted and proved a good match with the conclusion of the previous study [6]. Therefore, the automatic low resolution imaging method is evaluated as an effective, rapid technique for data gathering.

Furthermore, we have been extending our database taking into consideration large fish samples, different fish species. Moreover, new physiological features related to the eye such as curved cornea and skin could be studied and combined with the proposed

assumptions to increase the accuracy in fish freshness determination.

Acknowledgement

We would like to thank L.Y.D.I.N.C Co. Ltd. for expert guidance, technical support and funding sponsor for the study, and thank the University of Danang - University of Science and Technology for partly funding for the project.

Appendix:

1. Light condition of automatically capturing system

In order to extract and analyze correctly the alteration of physiological characteristics of the fish eye over time, the light condition should be fixed and uniform in one circumstance. The unexpected light element such as sunlight could cause some errors in the database which was constructed in 25 hours continuously. Therefore, we built an automatically capturing system including a white box and black covering to avoid the unpredicted factor. Fig.7a presents the method for capturing the fish by automatic system and the resulting image is as Fig.7b.

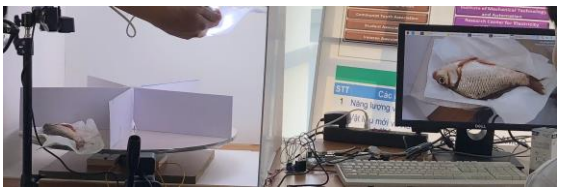

(a)

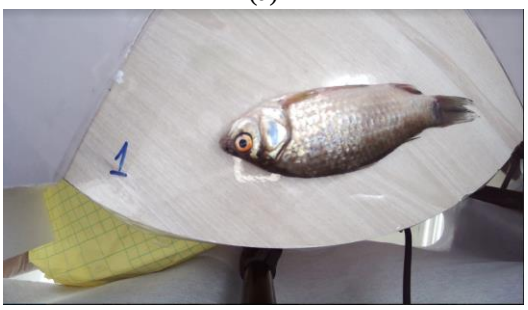

(b)

Fig.7. (a) Image capturing set-up and (b)the resulting image.

2. The fish's iris and pupil area

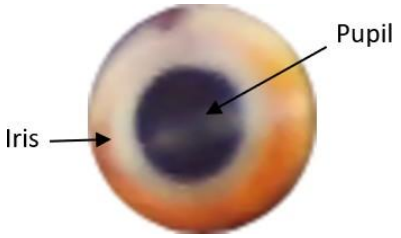

Fig.8. A fish's pupil and iris region.

In this study, feature F0- 12 intensity slices were cut across the image and had the length of 125 pixels. Therefore, the pupil which is the black circular part in Fig.7 is in the range of pixel 40 to 100 for fresh fish and 30 to 110 for stale ones. It is due to the increase in the pupil's size that is described in data visual analysis. Consequently, the iris starts from pixel 0 to 40, 100 to 125, and from pixel 0-30, 110 to 125, corresponding to the fresh and spoiled fish, respectively.

References:

[1] Namita Sengar, Varun Gupta, Malay Kishore Dutta , Carlos M. Travieso : Image Processing Based Method For Identification Of Fish Freshness Using Skin Tissue

[2] Shaveta Malik, Tapas Kumar, A. K. Sahoo : Image Processing Techniques for Identification of Fish Disease

[3] Aydoğan KARAGÖZ "Fish freshness detection by image processing", A Thesis Submitted to the Graduate School of Natural and Applied Sciences of Dokuz Eylül University In Partial Fulfillment of the Requirements for the Degree of Master of Science in Electrical and Electronics Engineering, pp. 24-25, 2013

[4] Ian C.Navotas, Charisse Nadine V.Santos, Earl John M.Balderrama, Francia Emmanuelle B.Candido, Aloysius John E.Villacanas and Jessica S.Velasco. "Fish identification and freshness classification through image processing using artificial neural networks". ARPN Journal of Engineering and Applied Sciences. vol. 13, no.18, Sep. 2018

[5] Jing Hu , Daoliang Li , Qingling Duan , Yueqi Han , Guifen Chen , Xiuli Si : fish species classification by color, texture and multi-class support vector machines using computer vision

[6] Anh Thu T. Nguyen, Nguyet Ha T. Tran, Phuong Dieu T. Nguyen, Dat Xuan Ho, Uyen Kim Hoang, Nguyen Ba Hoang, Thuong H.N. Nguyen, Tuan V. Pham."The Remarkable Enhancement in Fish Freshness Classification on Various Species using Neural Network on Physiological Characteristics Features". In: The International Conference on Intelligent Systems

and Networks. Lecture Notes in Networks and Systems, vol 471, pp 615-622

Revisit Attention Mechanism in Laplacian Pyramid Network for Artistic Style Transfer

Shenzhi. Wang, and Qiu. Chen

Graduate School of Engineering, Kogakuin University, Japan
E-mail: cm21061@ns.kogakuin.ac.jp, chen@cc.kogakuin.ac.jp

Abstract

As a very creative research direction in the field of deep learning, style transfer research has been attracted a lot of attention in the past two years, which can transform ordinary photos into artistic paintings. Existing methods can be divided in two categories: arbitrary style transfer and single style transfer. In this paper, we propose a novel arbitrary style transfer named LapAttN to optimize the single style transfer, which combines the advantages of LapStyle and AdaAttN. The experimental results on the COCO dataset show that the image quality of proposed method is superior to other SOTA algorithms.

Artistic style transfer is an optimization technique used to take two images—a content image and a style reference images (such as an artwork by a famous painter)—and blend them together so that the output image looks like the content image, but "painted" in the style of the style reference image.

Currently, the main methods are categorized to the following: Per-Style-Per-Model which can synthesize images with a single given style image; Multi-Style-Per-Model introduces various network architectures to simultaneously handle multiple styles, and Arbitrary-Style-Per-Model can transfer arbitrary styles.

These methods have achieved great stylization quality, but they still fail to synthesize complex styles when there are holistic global and local patterns and they are prone to unnatural output with unpleasing local distortions because these methods left shallow feature unexplored and without locally considered feature statistics.

We observed when painters handle complex style patterns, they always start with a draft to the capture global structure and then revise the local details gradually. Inspired by this, to alleviate the existing problems, we refer to LapStyle[2] and propose a novel feed-forward artistic style transfers framework, named Revisit Attention Mechanism in Laplacian Pyramid Network for Artistic Style Transfer(LapAttN), as shown in Fig.1.

In our framework, first, a drafting network is designed to transfer global style patterns in low-resolution by the fast arbitrary neural style transfer method(AdaAttN)[1]. A revision network is then used to revise the local details in high-resolution via hallucinating a residual image according to the draft and the textures extracted by Laplacian filtering. As illustrated in Fig. 2, appealing stylization results are achieved.

We compare our method with other SOTA methods, and the results on the COCO dataset areas shown in Fig. 3. In contrast to these methods, our method can simultaneously transfer simple local style patterns and complex global style patterns, retaining clear and clean structure of style patterns.

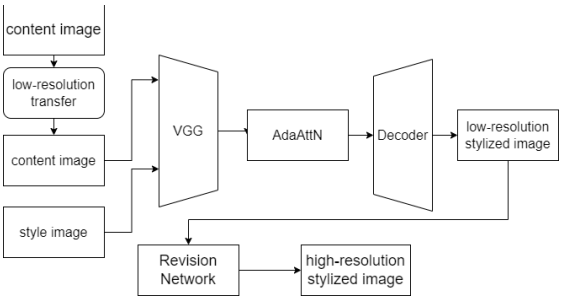

Fig. 1. LapAttN framework.

Fig. 2. Input and output.

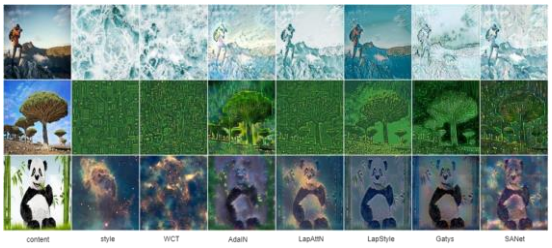

Fig. 3. Comparison with prior works.

References:

[1] S. Liu, "AdaAttN: Revisit attention mechanism in arbitrary neural style transfer," in Proc. the IEEE Conf. Computer Vision and Pattern Recognition, 6649-6658(2021).

[2] T.Lin, "Drafting and revision: Laplacian pyramid network for fast High-quality artistic style transfer," in Proc. the IEEE Conf. Computer Vision and Pattern Recognition, 5141-5150(2021).

Applying Blockchain Technology in IoT Data Distribution

Hayato Kumazaki[1)], Takafumi Taya[2)], Eishin Nagaoka[2)], and Osamu Mizuno[1)2)]

[1)]Department of Information and Communication Engineering, Faculty of Informatics, Kogakuin University, Tokyo, Japan
[2)]Graduate School of Electrics and Electronics Engineering, Kogakuin University, Tokyo, Japan
E-mail: j019113@ns.kogakuin.ac.jp, cm22032@ns.kogakuin.ac.jp, cm21037@ns.kogakuin.ac.jp, omizuno@cc.kogakuin.ac.jp

Abstract

Appearance of new IoT services with handling multiple types of IoT data is expected. To realize flexibility of data distribution, the infrastructure for multiple types of IoT data distribution is required. We proposed the Tag-ID-based Pub/Sub model with Ticket-based AC (Access Control). However, this method has a database system that causes the single point of failure. In this paper, we propose to apply Blockchain (BC) instead of the system for the conventional method.

1. Introduction

With the popularization of the Internet of Things (IoT), many types of IoT services are providing. It is expected that IoT services will use multiple types of data to realize service variation. IoT data distribution infrastructure is required to meet the needs of IoT data collection, analysis, scalability, and security. Therefore, we proposed the Tag-ID-based Pub/Sub model with Ticket-based AC (Access Control) [1].

This model includes a third-party system called TAAI (Ticket Authentication and Authorization Infrastructure) that authorizes and authenticates tickets. However, TAAI can be the single point of failure. In this paper, we propose applying blockchain to reduce the load on the TAAI and eliminate the single point of failure.

2.Applying Blockchain Technology

To solve the problem, we propose applying Blockchain technology (BC) for TAAI. By taking advantage of features of BC, the system can assure high availability, prevent ticket tampering, and guarantee the fairness of transactions. Fig.1 illustrate the overall operation flow. The Service Provider (SP) holds the Tag ID, which is distributed to devices by the User Fog Node (UFN). UFN selects a Tag-ID that is to be linked to the data related to privacy. Each Service Fog Node (SFN) and UFN participates in the BC. When SFN_n requests data held by UFN_1 with which it has no contractual relationship, it adds a block of ticket information including the requested Tag ID, ticket creator ID, etc. to SFN_n. Therefore, there is no risk of tampering. Besides, consensus can prevent malicious third parties from adding blocks. The UFN_1 refers to the data, then it checks whether the data is addressed to itself and whether it is a Tag ID to be hidden. If a Tag-ID to be hidden is included, UFN_1 reports the fact to SFN_1 of contracted SP_n. The traceability of the BC to confirm the authenticity of the contents reported by UFN_1 is used. If it is true, SP_1 impose a penalty to SP_n.

3.Conclusion

We proposed applying blockchain to address The problems in the previous study. After implementing the proposed scheme, we will conduct emulation and evaluate the results.

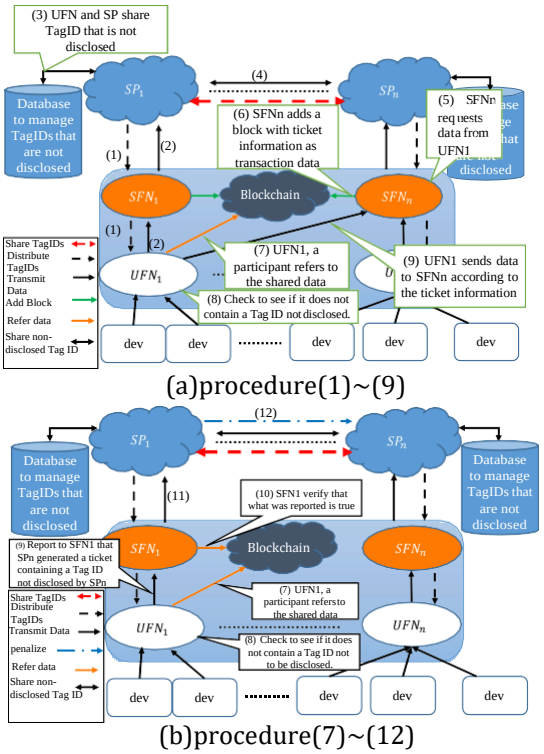

Fig.1. Overview of Blockchain Application Scheme

Acknowledgements

Part of this research was funded by Japan Society for the Promotion of Science (JSPS) research grant JP22K12014.

References:

[1] Masaki Yoshii, Ryohei Banno, Osamu Mizuno, “Performance and Security Evaluation of Table-based Access Control Applied to IoT Data Distribution Method”, IEICE TRANS. Of COM. DOI: 10.1587/transcom.2021TMP0007, 2022.

[2] M. N. M. Bhutta et al., "A Survey on Blockchain Technology: Evolution, Architecture and Security," in IEEE Access, vol. 9, pp. 61048-61073, 2021, doi: 10.1109/ACCESS.2021.3072849.

Interest Flooding Attack Countermeasures for Information-Centric Networking-based Wireless Sensor Networks

Tatsuya Ohsawa[1)], Takafumi Taya[2)], Eishin Nagaoka[2)] and Osamu Mizuno[1), 2)]
[1)]Department of Information and Communication Engineering, Faculty of Informatics, Kogakuin University, Tokyo, Japan
[2)]Graduate School of Electrics and Electronics Engineering, Kogakuin University, Tokyo, Japan
E-mail: {j019059, cm22032, cm21037}@ns.kogakuin.ac.jp, omizuno@cc.kogakuin.ac.jp

Abstract
We have proposed ICN-based Wireless Sensor Networks (ICSN). It is an application of Information-Centric Networking (ICN) to realize multiple IoT services in a single wireless sensor network. This paper addresses countermeasures against Interest Flooding Attack, a kind of DDoS (Distributed Denial of Service) attack, to a cluster head node in ICSN.

1. Introduction
In general, IoT services require individual sensor networks. It causes higher construction and operation costs when new IoT service is introduced. To solve this problem, we proposed ICSN (ICN-based Wireless Sensor Networks) that realizes multiple IoT services in single sensor network [1]. Here, ICN is Information Centric Networking. Unauthorized access to the sensors by a attacker may cause some of the sensors to functional outage. It can be a risk of availability and reliability for the ICSN service. The objective of this paper is to maintain a secure environment by addressing DDoS attack to nodes in ICSN.

2. Interest Flooding Attack
An ICN node has tables called PIT and FIB (Forwarding Interest Table), and an interface to next node is called “face”. Face of FIB is defined and PIT is written at the timing of entry based on it. In ICSN, a sink node sends Interest message to a sensor node via CH (Cluster Head node). The sensor node sends Data to CH as an answer of Interest.
This paper focuses on IFA (Interest Flooding Attack) in ICSN. IFA is a type of DDoS attack in which an attacker continuously sends Interests to a router. which causes a series of entries in the PIT (Pending Interest Table), making it impossible for normal users to obtain data.
We conducted a preliminary experiment to confirm the behavior of ICSN under IFA. In the preliminary experiment, Cefore [2] was used as OSS (Open Source Software) to realize the communication environment of ICSN. The assumed environment consisted of four sensors and a sink node. Fig. 1 shows an example of the preliminary experiment. The malicious sensor node executes an IFA toward CH_B. It set the upper limit of PIT entries to 2, and sent 10 simultaneous Interest messages. As a result, it was found that data could not be retrieved from the sink node, that all PIT entries were filled. Then IFA is succeeded.

3. Proposal Method
We propose to compare face data in PIT and FIB as countermeasures against IFA. Because a normal sensor node never sends Interest. Fig. 2 shows the operation of the proposed method. A malcious sensor

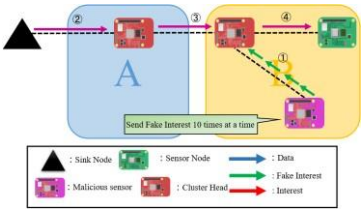

Fig.1.Preliminary Experiment

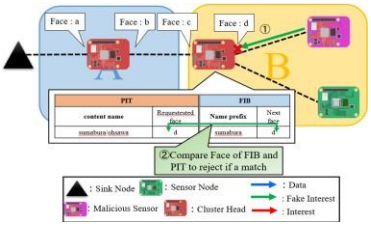

Fig.2.Compare Face of FIB and PIT

node in area B sends Interest to a CH. At that time, the CH compares face data in FIB and PIT. If the faces are match, the CH rejects all Interests and Data sent from the sensor node. The CH shares the blocked node information with other nodes. This allows other nodes to identify malicious nodes even when clustering is performed

4. Conclusion
We have proposed a countermeasure to DDoS attack in ICSN, which is a face confirmation method that intercepts an Interest from a sensor node by comparing its face.

Acknowledgements
Part of this research was funded by Japan Society for the Promotion of Science (JSPS) Research grant JP22K12014.

References:
[1] K. Kimura, K. Mochizuki, M. Koike and O. Mizuno, "Data Transfer Methods for Information-Centric Networking-Based Wireless Sensor Network Platform," 2019 International Conference on Information Networking (ICOIN), 2019,pp.336-341,10.1109/ICOIN.2019.8718137.
[2] Cefore, “https://cefore.net/” (accessed Sep. 2022).

Breakout Room #4

Advanced Functional Materials & Mechanical Engineering

Chairperson: Dr. Huynh Thanh Tung, DUT

TEM evaluation of *in-situ* nitrogen plasma irradiated GaInN

A. Tokushige[1*], S. Ohno[1], Y. Hayakawa[1], T. Honda[1, 2], T. Onuma[1, 2], and T. Yamaguchi[1, 2]

1. Department of Electrical and Electronic Engineering, Kogakuin University, Tokyo, Japan
2. Department of Applied Physics, School of Advanced Engineering, Kogakuin University, Tokyo, Japan

E-mail: cm22034@ns.kogakuin.ac.jp

Abstract

We evaluated *in-situ* nitrogen plasma irradiated GaInN film by the transmission electron microscope. Bright field images were observed for the sample at **g**=0006 and **g**=33-60, respectively. In-composition was expected to be low at the N* irradiated area. It is a phenomenon peculiar to the alloy crystals. Dark contrast was observed in the **g**=0006 image of the first GaInN layer (5 min.). The contrast was not observed above the first N* irradiated area.

Introduction

GaInN is used for blue and green LEDs, but GaInN-based red LEDs are not commercially available. By fabricating red LEDs with GaInN, miniaturization and integration of three-primary-color LEDs can be expected. However, lattice-matched GaInN substrate is hard to be realized at present. Consequently, misfit dislocations are formed at the GaInN/substrate hetero-interface. Dislocations deteriorate the devices through the carrier trapping, becoming the leakage path, and reducing the external quantum efficiency [1]. Therefore, a reduction of dislocation density in the film is required.

In previous study, one order of magnitude reduction of dislocation density has been achieved in InN regrown on an *in-situ* nitrogen plasma (N*) irradiated InN surface [2]. This is mainly due to the bending of the dislocations. Therefore, further reduction of dislocation density can be expected by repeating the N* irradiation and re-growth [2].

In this study, we evaluated GaInN film grown by employing the method using transmission electron microscope (TEM).

Experiment

GaInN was grown on GaN for 5 minutes using RF-plasma assisted molecular beam epitaxy (RF-MBE) with Ga flux of 5.0×10^{-7} Torr, In flux of 6.0×10^{-7} Torr, N_2 flux of 0.8 sccm and RF power of 200 W to achieve an In-composition of 30 %. Then, N* was irradiated with RF power of 400 W for 30 min., which was followed by GaInN regrowth for 20 min. The N* irradiation and regrowth were repeated three times. TEM-Bright Field (BF) images were obtained for the sample at **g**=0006 and **g**=33-60, respectively. TEM image of **g**=0006 mainly reflects screw or mixed dislocations, and that of g=33-60 reflects edge or mixed dislocations [3].

Result and Discussion

As shown in TEM-BF image of **g**=0006 in Fig. 1, N* irradiated areas turned white. Since heavier elements tend to blacken the image, In-composition is expected to be low at the N* irradiated area. It is a phenomenon peculiar to the alloy crystals, which has not been observed in previous study of InN[2]. In addition, the dark contrast was observed for the GaInN(5 min.) layer. Magnified image is shown in Fig. 2. The contrast was not observed above the first N* irradiated area. Note that the phenomenon was not observed for **g**=33-60.

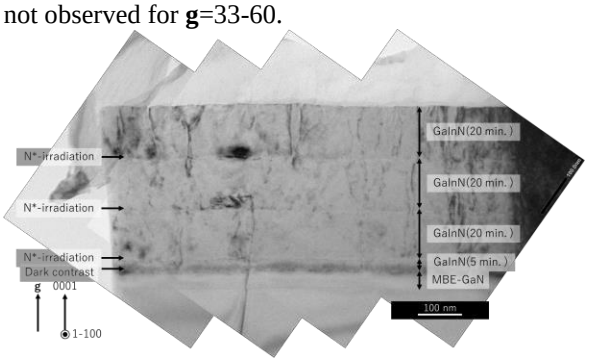

*Fig. 1 TEM-BF image of **g**=0006.*

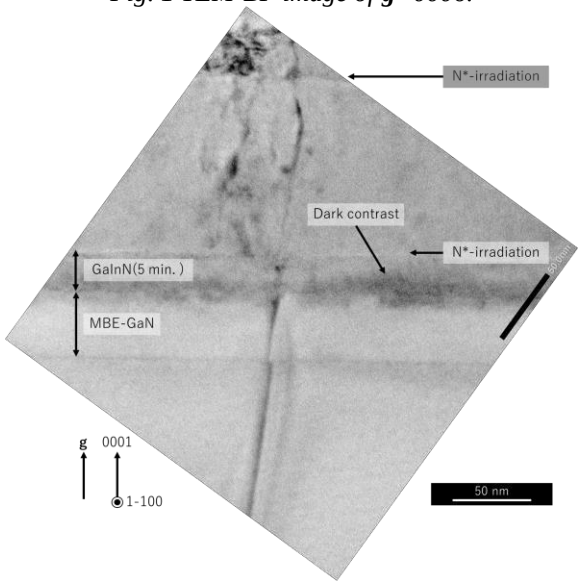

*Fig. 2 Magnified TEM-BF image of **g**=0006 near the dark contrast region.*

References:

[1] X. A. Cao *et al.*, J. Cryst. Growth **264**, 172-177 (2004).
[2] F. B. Abas *et al.*, Jpn. J. Appl Phys. **57**, 035502/1-4 (2018).
[3] Z. Liliental-Weber, Jpn. J. Appl Phys. **53**, 100205/1-14 (2014).

Adhesion of Cu thin films on PTFE surface modified by low-angle N^+ ion beam irradiation

First Y. Nakayama*, Second I. Takano*,

Graduate school of engineering, Electrical engineering and electronics, Kogakuin university, Tokyo, Japan
E-mail: cm21038@ns.kogakuin.ac.jp
Faculty of engineering, Department of electrical and electronic engineering, Kogakuin university, Tokyo, Japan
E-mail: ct97912@ns.kogakuin.ac.jp

Abstract

In order to utilize PTFE with various excellent properties as high-frequency printed wiring boards, the surface modification of PTFE was carried out by low-angle N^+ ion beam irradiation at an angle of 60°. In this study, adhesion of Cu thin films on PTFE modified by N^+ ion beam irradiation was evaluated by mechanical measurements with investigation of the surface morphology and chemical state.

PTFE has been attracting attention as one of substrate materials for the high-frequency band used in today's information and telecommunications society. Although PTFE is an excellent substrate material due to the strong bonding energy between the F and C atoms, its property makes it difficult to achieve sufficient adhesion with Cu films as a wiring material. Therefore, many researchers have studied the surface modification of PTFE.

While the ion beam used for impurity implantation in semiconductors is characterized by its low thermal effect, it is known to affect the surface morphology by the sputtering effect. The authors have investigated the low-angle ion beam irradiation as a technique for the surface modification. Using characteristics and directivity of ion beams, the PTFE surface could be smoothed and functional groups could be introduced by irradiating at low-angles. In this study, PTFE was irradiated with the N^+ ion beam with an incident angle of 60° to improve the adhesion of Cu films on PTFE.

PTFE samples were prepared by attaching the fluoroplastic adhesive tape (Nitto Denko Corporation, No. 903UL) on glass substrates (Matsunami Glass Slide S1126). N^+ ion irradiation and Cu film formation were performed using a multi-process coating system (ULVAC Co., Ltd.), and both processes were continuously carried out in a high vacuum chamber. After irradiating the PTFE surface by the selected N^+ ion beam through the mass analyzer, the Cu film of 50 nm in thickness was formed by sputtering.

Ion beam irradiation fluences were varied in the range of 0 ~ 244×10^{15} ions/cm^2, and the transition of roughness is shown in Fig. 1. The arithmetic mean height Sa and maximum height Sz, which are indices of surface roughness, decreased at initial irradiation and are maintained up to 122×10^{15} ions/cm^2, and finally the roughness increased.

Adhesion between PTFE and Cu thin film was examined using a 90° tensile tester (spring scale: 2-5 kg, Ohba Keiki Co.) and the samples were prepared using the epoxy resin adhesive (001401, Konishi) for bonding. The adhesion evaluation was shown in Fig. 2, which demonstrates that the high adhesion was

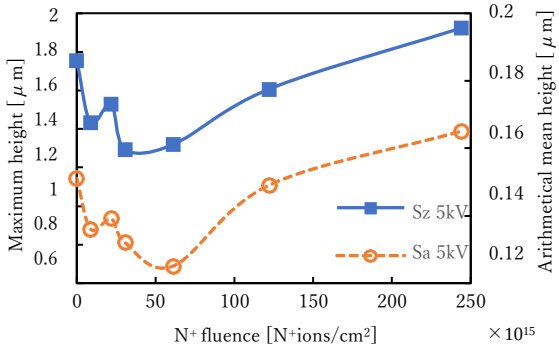

Fig.1. Surface roughness of ion beam irradiated PTFE for N^+ ion fluences

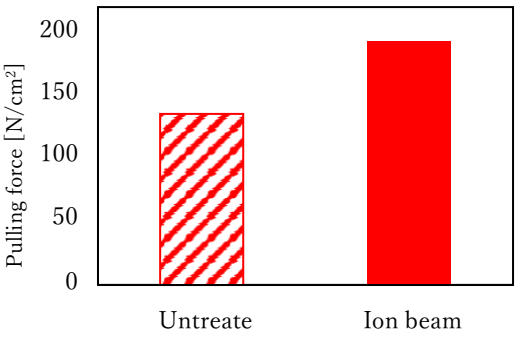

Fig.2. Adhesion evaluation of Cu thin films on untreated and ion beam irradiated PTFE by the tensile testing. (Fluence: 30.6× 10^{15} ion/cm^2)

obtained despite the PTFE surface smoothed of 30.6 × 10^{15} ion/cm^2 in fluence. This meant the chemical effect had the stronger influence than the mechanical effect.

The low-angle N^+ ion beam irradiation can smooth and introduce free bonds of C to improve the adhesion of Cu thin films on PTFE.

References:

[1] Koki Iesaka, Ichiro Takano : "Adhesive Improvement of Metallic Films onto PTFE Surface-modified by using Ar Plasma", IEEJ Trans. FM, Vol.141, No.1 pp34-39 (2016)(in Japanese)

Influence of Slot Angle of the Circular Cylinder on the Flow Characteristics of the Jets

D.Yaguchi[1] and K. Sato[2]

[1]Graduate School of Engineering, Kogakuin University, Tokyo, Japan
[1]E-mail: am21064@ns.kogakuin.ac.jp
[2]epartment of Mechanical System Engineering, Kogakuin University, Tokyo, Japan
[2]E-mail: at12164@ns.kogakuin.ac.jp

Abstract

Circulation control wings (CCWs) are high-lift devices used in aircraft applications. In this study, a tangential-blowout cylinder, a type of CCW, was used to elucidate the basic flow characteristics experimentally. Flow control of the primary jet using a tangential-blowout cylinder was performed, and the effect of the blowout slot angle on the deflection characteristics of the primary jet was discussed. In particular, the optimal conditions for jet deflection are discussed.

In a study using a tangential blowout cylinder, Okayasu and Zhang et al. verified the basic characteristics, hydrodynamic force, and vibration, using a single slot.[1]~[2] They also verified the effect of the single-slot angle on the deflection angle. [3]

However, the conditions in previous research directions were limited, and the results were not fully verified.

In this study, the influence of slot angle was examined, and the optimal slot angle that provided the maximum deflection angle was discussed.

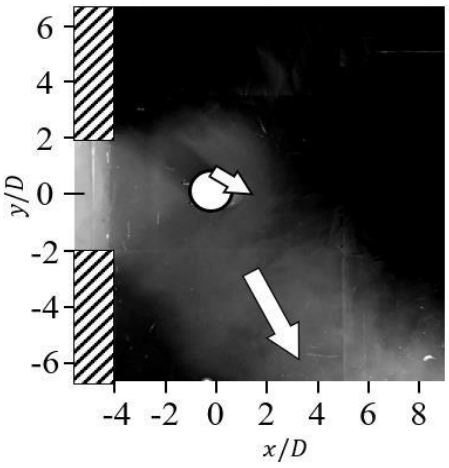

Up = 8.3 m/s, Vj = 60 m/s,

$C_\mu = 0.27$, W = 200 mm, θ j = 120°

Fig. 1. Experimental results from visualization

The test section of the experimental apparatus used in this study was 1000 mm × 1000 mm. A wind tunnel was used to generate the primary jet, and a tangential blowout cylinder was placed 200 mm from the mouth of the wind tunnel. The exit width and height of the wind tunnel were 200 mm each. The cylinder had a diameter of 50 mm and span the length of 200 mm. It was equipped with a slot of 1 mm width for blowing in the tangential direction. The working fluid was air, which was fed into a plenum tank using a blower and subsequently passed through a cavity in the center of the cylinder to generate a jet sheet from the slot. In this experiment, the main flow rate was maintained constant at 8.3 m/s.

Visualization was performed using a smoke generator to show the results. The smoke generated by the smoke generator flowed into the suction port of the wind tunnel.

Figure 1 shows the experimental results, when the slot angle was set to 120°, obtained via visualization . The velocity of the jet sheet was 60 m/s, and the momentum ratio of the jet sheet to the main flow was 0.27.

The maximum deflection angle for the same momentum ratio reported by Zhang et al. was approximately 60°, whereas it was 76° herein. This is attributed to the position of the detachment point around the mainstream cylinder. In the future, clarifying this by carefully examining the pressure distribution around the cylinder is necessary.

We herein suggest that an optimum slot angle exists for a cylinder.

References:

[1] S. Okayasu, K. Sato, T. Shakochi, and K. Furuya, “Flow around a Tangential Blowing Cylinder Placed near a Wall (2nd Report, Consideration of Unsteady Characteristics)”, *Proc. of JSME*, 74, no. 744, pp. 1725–1734, (2008)

[2] Q. Zhang, F. Takahashi, K. Sato, W. Tsuru, and K. Yokota, “Jet Direction Control Using Circular Cylinder with Tangential Blowing”, *Trans. Japan Soc. Aero Space Sci*., 64, no. 3, pp. 181–188, (2021)

[3] D.Yaguchi, T. Nakayama, and K. Sato, “Flow characteristics around double slotted circulation control wing” , *International Symposium on Advanced Technology* (ISAT20)

Influence of suction on the flow field under interference between a synthetic jet and a continuous jet

M. Mori[1], M. Takano[2], N. Ajino[3], K. Nisibe[4], and K. Sato[5]

[1] Graduate School of Engineering, Kogakuin University, Tokyo, Japan
E-mail: am21061@ns.kogakuin.ac.jp
[2] Mechanical Systems Engineering, Kogakuin University, Tokyo, Japan
E-mail: a219060@ns.kogakuin.ac.jp
[3] Graduate School of Engineering, Tokyo City University, Tokyo, Japan
E-mail: g2181001@tcu.ac.jp
[4] Department of Mechanical Engineering, Tokyo City University, Tokyo, Japan
E-mail: knishibe@tcu.ac.jp
[5] Department of Mechanical System Engineering, Kogakuin University, Tokyo, Japan
E-mail: at12164@ns.kogakuin.ac.jp

Abstract

Although studies have been conducted on the interference between synthetic and continuous jets, none have focused on the effect of a suction process on the flow field of synthetic jets. In this study, a pulsating flow without a jetting process was generated as an alternative to the synthetic jet, and the relationship between the suction and deflection characteristics of the continuous jet were clarified. Subsequently, we discovered conditions under which the continuous jet was deflected by approximately 180° and converted into a wall-attached jet.

Several studies have been conducted on the directional control of continuous jets using synthetic jets, and they have reported that the jets can be deflected by changing the momentum ratios of continuous and synthetic jets, or the dimensionless frequency of synthetic jets [1]-[3]. However, the mechanism of jet deflection is not sufficiently understood, and the influence of a suction process on synthetic jets remains unclear. In this study, a pulsating flow without a jetting process (that is, a pulsating flow with only a suction process) was generated as a fundamental experiment of the interference between a synthetic and continuous jet, to investigate and discuss the effect of the suction process on the flow field.

For experimental methods, please refer to the references [2, 3].

In this study, we attempted to elucidate the phenomenon by visualizing the flow. Fig. 1 shows examples of visualization observations acquired under the following conditions: $U_a = 5.00\text{m/s}$, $U_{c1} = 7.00$ m/s, $U_{c2} = 4.90$ m/s, $\xi = 0.73$, c = 1 mm, C = 0.33, $b_c = 3$ mm, $b_s = 3$ mm, $L_0 = 46.7$, $f = 50$ Hz, $f^* = 0.021$. These parameters were combined with the maximum flow velocity at suction to compare the results with the maximum velocity amplitude of the synthetic jet: $U_a = 9.90$ m/s. This figure shows that during the interference of the pulsating suction flow (with no jetting process) with the continuous jet, the continuous jet was significantly attracted toward the pulsating-suction side and converted into a wall-attached jet, despite the flow ratio is 0.83. Furthermore, the degree of deflection was larger than the interference between conventional synthetic and continuous jets, suggesting that the suction process was deeply involved in the deflection of the jet.

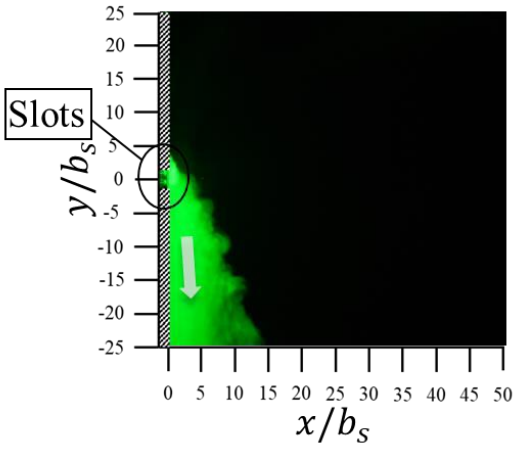

Fig. 1 Visualized typical flow pattern under the pulsating suction condition

($U_a = 5.00$ m/s, $U_{c1} = 7.00$ m/s, $U_{c2} = 4.90$ m/s, $\xi = 0.73$, c = 1 mm, C = 0.33, $b_c = 3$ mm, $b_s = 3$ mm, $L_0 = 46.7$, $f = 50$ Hz, $f^* = 0.021$)

References:

[1] B. L. Smith, and A. Glezer, 2002, "Jet vectoring using synthetic jets," J. Fluid Mech., 458, pp. 1–34.
[2] Y. Suzuki, R. Kobayashi, K. Sato, K. Nishibe, and K. Yokota, 2020, "Interaction between a continuous jet and synthetic jet," The 31st International Symposium on Transport Phenomena.
[3] M. Mori, N. Ajino, K. Nishibe, and K. Sato, 2022 "Influence of the momentum ratio between synthetic jets and continuous jets on flow fields,"

The 32nd International Symposium on Transport Phenomena.

Behavior of synthetic jets colliding with rectangular cylinders

M. Yasumiba [1], K. Sato [1]

[1] Mechanical Engineering Program in the Graduate School of Engineering, Kogakuin University, Tokyo, Japan, E-mail: am22068@ns.kogakuin.ac.jp

Abstract

This study attempts to elucidate the behavior of synthetic jets impinging on a prism placed near the slot exit. The flow field is visualized and observed using the smoke-wire method. Results are compared with those obtained using a continuous jet. It was found that the behavior of the synthetic jet impinging on the prism depends on the frequency and that the behavior may be similar to or different from that of the continuous jet depending on the frequency.

Continuous jets have mainly been used in research on impinging jets for object cooling and other applications[1]. However, the structure of continuous jets is complicated by components such as motors and propellers, making downsizing and weight reduction challenging. Synthetic jets have been widely used to replace continuous jets. Nishibe et al.[2] showed that the flow sufficiently downstream of a two-dimensional planar synthetic jet is similar to that of a continuous jet, where this similarity includes unsteady characteristics, confirming that synthetic jets can be a substitute for continuous jets. Yasumiba et al.[3] examined the collision problem between a continuous jet and synthetic jet by placing a circular cylinder downstream of the jet. However, to date, no studies have been conducted on the behavior of synthetic jets impinging on prismatic columns. In this study, we attempt to elucidate the effects of the aspect ratio and dimensionless frequency on the vortex structure and flow direction in a flow field through visualization experiments using square columns with various aspect ratios downstream of the jet.

References [2, 3] were the sources for the experimental method employed in this study. In the experiment, the relative distance from the slot to the wall was maintained at $X_w = 10$

Figure 1 shows examples of the flow pattern visualization observations for two types of square columns (aspect ratios of 2 and 1). Under condition (i), the continuous and synthetic jets formed similar flow fields, and a y-directional velocity component occurred between the slot and prism, forming two recirculation regions. Under condition (ii), in the case of the continuous jet, two jets were formed in the oblique direction after collision. In the case of the synthetic jet, a recirculation region was formed as under condition (i). In other words, when the aspect ratio exceeded a certain threshold value, a difference in the flow field between the continuous and synthetic jets was observed.

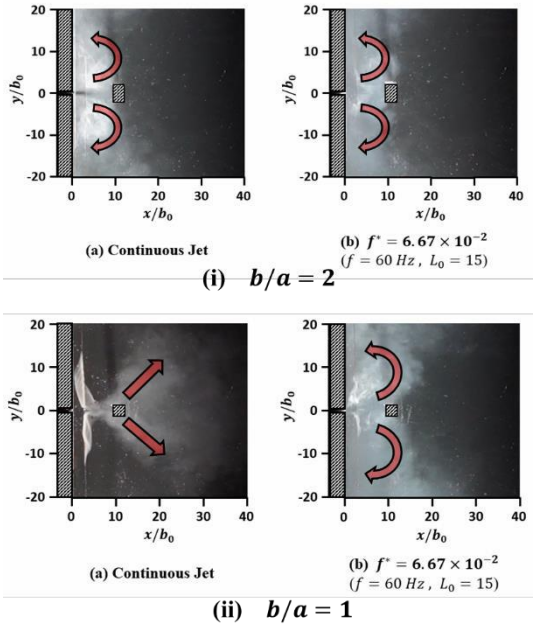

Fig. 1 Visualization of synthetic jet and continuous jet by smoke wire method.

$[U_{s0} = U_{c0} = 4.5\ m/s, X_w = 10]$

References:

[1] K. Tsujimoto, K. Ao, T. Shakouchi, and T. Ando, "Numerical Investigation on Flow Structures and Mixing Performances of Vector-Controlled Free Jet using DNS", Journal of Fluid Science and Technology, 6(4), 401–411 (2011)

[2] K. Nishibe, Y. Fujita, K. Sato, K. Yokota, and T. Koso, "Experimental and Numerical Study on the Flow Characteristics of Synthetic Jets", Journal of Fluid Science and Technology, 6(4), 425–436 (2011)

[3] M. Yasumiba, K. Sato, T. Ito, R. Kawahara, and K. Yokota, "Flow around bluff body downstream of synthetic jets", Proceedings of the 28th Annual Meeting of the Kanto Branch of the Japan Society of Mechanical Engineers (in Japanese) (2022)

Throughput Performance Improvements by Multiple Drones' Height Control in Non-Uniform Terminal Distribution Environments.

Keisuke Imamura, Takatoshi Sugiyama

Graduate School of Engineering, Kogakuin University, Tokyo, Japan
E-mail: cm22010@ns.kogakuin.ac.jp

Abstract

A multi-hop wireless network using multiple drones is one of the most effective approaches to construct a temporary communication infrastructure in an isolated disaster area. In order to improve the throughput performances in non-uniform terminal distribution environments, a single drone's height control has previously been proposed. In this paper, we propose a new multiple drones' height control to more improve the throughput performance. As a computer simulations result, the new proposed scheme achieves 280 [kbps] improvement of throughput per terminal compared to that with the conventional single drone's height control.

Introduction

In an isolated disaster area, a m multi-hop wireless network using multiple drones is needed to construct a temporary communication infrastructure. As shown in Fig.1, when the terminals on the ground are uniformly distributed, the same number of terminals can be accommodated equally to the drones with the same height, and equivalent throughput performances of the terminals are accomplished naturally. However, in the actual disaster areas, the distribution of terminals might almost be non-uniform. This would make throughput performances of the terminals worse. To solve this problem, a single drone's height control has previously been proposed and its thought performance improvents have been clarified [1]. However, as shown in Fig.2, if the height of one drone becomes much lower in the conventional control, its throughput performances degrade. In this paper, we propose a new multiple drones' height control. By computer simulations, it is clarified that the proposed height control improves the throughput per terminal compared to that with the conventional control.

Proposal

In our model, the disaster area is divided to four parts equally where each drone is allocated in the center of each part. The part is called "a cell". In order to simulate non-uniform terminal distribution environments, Cell 1 has larger numbers of terminals than the other cells. IEEE802.11a specifications are used assuming 5GHz band communications. The four drones communicate their terminals using independent 5GHz channels with 54[Mbps]. Fig.3 shows the transmission rate characteristics as the function of the distance between the drone and the terminal, similar to Ref.[2]. The throughput performances are obtained from Fig.3. As shown in Fig.4, the proposed scheme controls at the same drones' heights of Cell 2 and 3 in additon to Cell 1. Therefore, the drones in Cell 2 and 3 can accomodate the terminals out of Cell 1 communication range and it is expected the throughput per terminal can be improved.

Simulation Evaluation

In this paper, simulations are performed with 10 terminals in Cell 1, and 5 terminals in the other cells, assuming a non-uniform terminal distribution environment. The beam width of the drones' antenna is 45[°], and the terminal antenna is an omni-antenna. Fig.5 shows relationship between drones' height and the throughput per terminal. The green dots show that when each drone is at a height of 420[m], the throughput per terminal is improved by 1.700[Mbps]. In a conventional scheme, when the height of Cell 1 drone is only moved to 350[m], the throughput per terminal becomes 1.848[Mbps] as shown by bule dot. Moreover, in the proposed scheme, when the height of Cell 1 drone is set to 350[m] and the height of Cell 2 and 3 drones is moved to 360[m], the throughput per terminal becomes 2.128[Mbps] as shown by red dot. Therfore, the newly proposed scheme achieves 280 [kbps] improvement of throughput per terminal compared to that with the conventional single drone's height control.

Conclusion

In this paper, we have evaluated a new multiple drones' height control to more improve the throughput performance in non-uniform terminal distribution environments in disaster area. It is clarified that the proposed scheme was found to improve the throughput per terminal became 2.128 [Mbps], the height of the drone in Cell 1 was 350 [m] and the height of the drones in Cells 2 and 3 was 360 [m].

References:

[1] Miho Ishigami, et al, "A Novel Drones' Height Control Algorithm for Throughput Optimization in Disaster Resilient Network," IEEE Trans. on VT, vol. 69, no. 12, pp. 16188-16190, Dec. 2020.

[2] Ryu Miura, et al, "Research and development of technologies for coordination and sharing with ground networks utilizing unmanned aerial vehicles," 9th Research and Development for Expansion of Radio Resources Presentation of Results, Fen. 2017.

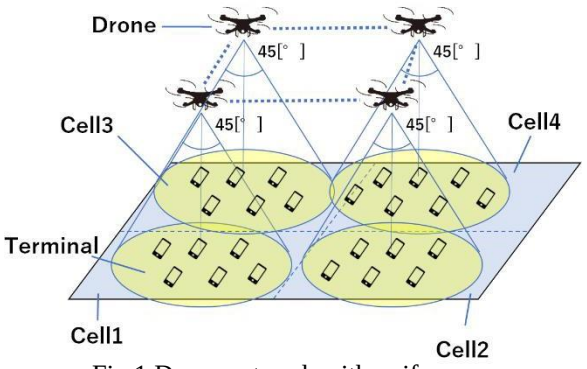

Fig.1 Drone network with uniform terminals distribution.

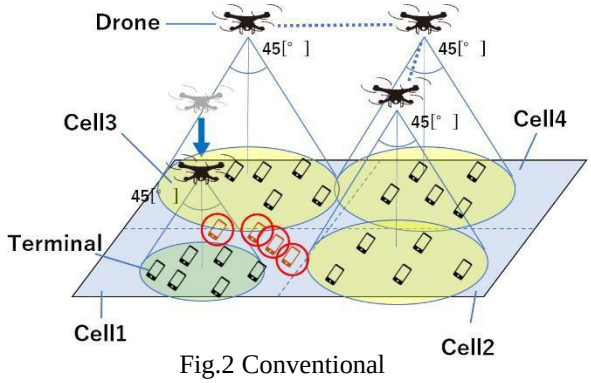

Fig.2 Conventional single drone's height control.

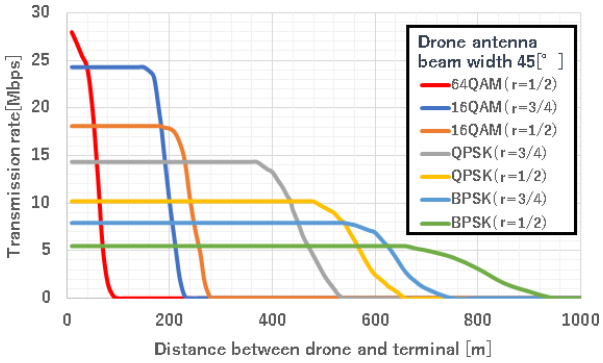

Fig.3 Transmission rate characteristics as the function of the distance between the drone and the terminal.

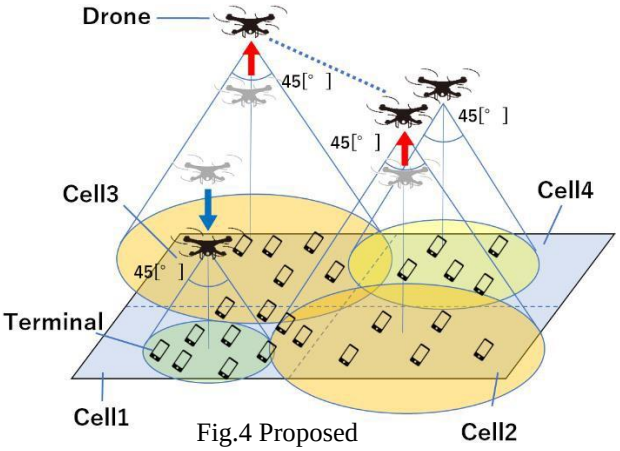

Fig.4 Proposed multiple drones' height control.

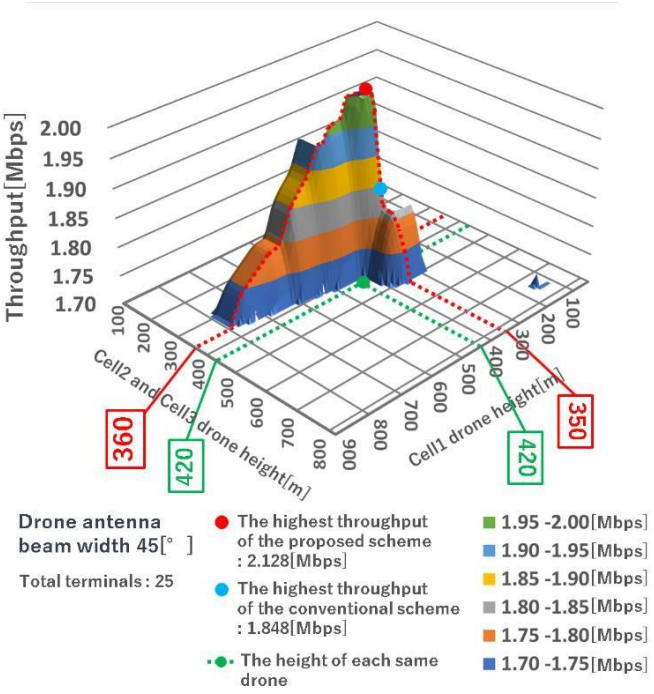

Fig.5 Relationship between drones' height and the throughput per terminal.

Drone's allocation optimization for concentric circle flight path in DTN

Yuki Kato, Takatoshi Sugiyama

Graduate School of Engineering, Kogakuin University, Tokyo, Japan
E-mail: cm22017@ns.kogakuin.ac.jp

Abstract

In this paper, we focus on a temporary communication network introducing the concept of DTN (Delay Tolerant Networking). We optimize drone's allocation for the concentric circle flight path previously proposed. It is clarified that the proposed flight path with one inner drone and three outer drones is the shorter information delivery time than that with both of two drones.

INTRODUCTION

In the event of a large-scale disaster, many people would become evacuees due to the collapse of lifelines and infrastructure. Therefore, a temporary communication network with drones is very effective[1]. Fig.1 shows temporary communication system using drones to introduce the concept of DTN[2]. We have previously proposed concentric circle flight path and it has been clarified that the propose flight path achieves shorter information delivery time than the conventional rebounding flight path[3]. In this paper, we optimize drone's allocation for the proposed flight path.

PROPOSED FLIGHT PATH

Fig.2 shows the proposed concentric circle flight path. In this paper, contact is defined as drones entering communication range each other just moment[3]. Since the drones fly in the same circular trajectory constantly and the drones on the outer are flying in opposite directions to the inner, it is expected to reduce the information delivery time due to the larger numbers of contacts among the drones comparing to the conventional flight path.

SIMULATION RESULTS

Table 1 shows the major simulation parameters. In this paper, the information delivery time for evaluation from a sending to a receiving terminal is defined as the sum of the times only taking drone's movements. In this simulation, pairs of sending and receiving terminals are randomly allocated. We define the limiting distance in order to eliminate some pairs communicating directly.

Fig.3 shows the relationship between limiting distance and average information delivery time. From Fig.3, the proposed flight path with one inner drone and three inner drones achieves shorter information delivery times than those with two inner drones and two inner drones in all of limiting distance. For an example of limiting distance 800[m], the information delivery time by the proposed flight path with two inner drones and two inner drones achieves 46.6[s]. On the other hand, those with one inner drone and three inner drones can reduce the information delivery time to 33.2[s] by 13.4[s].

CONCLUSION

In this paper, we optimize drone's allocation on the proposed flight path. The proposed flight path with one inner drone and three outer drones can reduce the information delivery time in the conditions of smaller numbers of drones more than the those with two inner drones and two outer drones.

References:

[1] Z. Fadlullah, et al., "A dynamic trajectory control algorithm for improving the communication throughput and delay in UAV-aided networks", IEEE Net., vol. 30, no. 1, pp. 100-105, Jan. 2016.

[2] A.Vahdat, et al., "Epidemic routing for partially connected ad hoc networks", Duke Tech. Rep. CS-2000-06, July 200.

[3] Y.Kato, et al., "New drone's flight path proposal to reduce information delivery time in DTN," ICTC 2022, Oct. 2022.

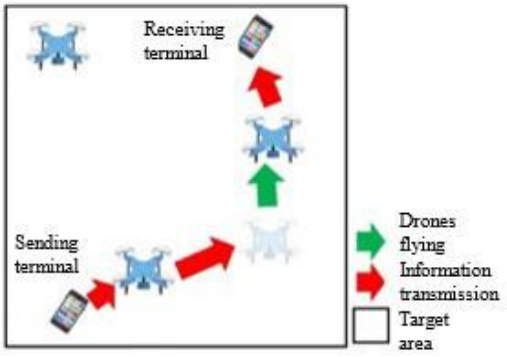

Fig.1 Temporary communication system using drones to introduce the concept of DTN.

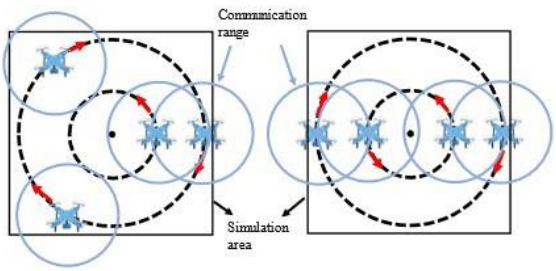

Fig.2 Proposed flight path.

Table 1. Simulation parameters.

Target area	1500[m]×1500[m]
Number of drones	4 (outer: inner = 3:1 or 2:2)
Drone's flight speed	10[m/s]
Communication range of the drones and terminals	500[m] (2.4GHz Wi-Fi base)
Information transmission time from the drone to the drone	0[s]
Sending terminal	1
Receiving terminal	1
Limiting distance	500~1000[m]

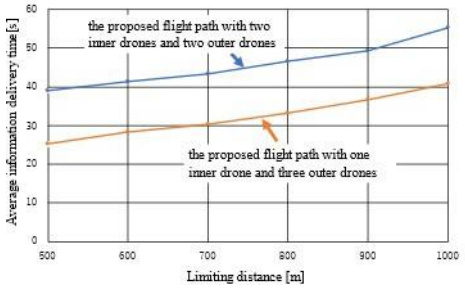

Fig.3 The relationship between limiting distance and average information delivery time.

Rubrics for University Calculus Courses

Satoru Takagi

Department of Mathematics, Global Education Center, Waseda University, Japan
E-mail: satoru@waseda.jp

Abstract

Rubrics are useful tools for evaluation of students' skills which are difficult to grade by examinations. On the other hand, rubrics are also useful for checking students' skills at that time by themselves. In this presentation, we show a revised flowchart-type rubric and report the activity of this rubric applying to the students in some university calculus courses.

The Ministry of Education, Culture, Sports, Science and Technology in Japan recommend utilizing rubrics. Rubrics are criteria for judging the degree of accomplishment of a learner by describing the standard of achievement degree on education in several stages separately. In mathematics subjects, it is not so hard to evaluate students' ability by examination. Therefore, we think that we do not need rubrics in math classes. However, rubrics have another good point that we can motivate students to make self-evaluation and self-improvement a habit in the classes. Actually, is it effective to use rubrics in calculus classes? In this presentation, we show a revised flowchart-type rubric and report the activity of this rubric applying to the students in some university calculus lectures. As to the method of evaluation in calculus classes by rubric, see [1]. We also considered the designing 1st year calculus course in [2] and the ways to improve our education in [3].

Table 1 is a normal rubric. However, we use a revised flowchart-type rubric developed by Professor Y. Hayashi mentioned in [4] because it is easy for students to estimate themselves (see Fig.1). We shall mention the evaluation viewpoints and skill levels of university calculus courses, and show the case study in our talk.

Table 1. A normal rubric.

	Level		
	1	2	3
Unit 1 Subject			
Unit 2 Subject			
Unit 3 Subject			

References:

[1] S. Takagi and T. Nikami, A method of evaluation in calculus classes by rubric, *ICIC Express Letters, Part B: Applications*, **9** (7) , 715−720 (2018).

[2] S. Takagi, S. Yamaguchi and R. Mizumachi, Designing 1st year calculus courses, *Proceedings of the International Workshop on Mathematical Education for Non-Mathematics Students Developing Advanced Mathematical Literacy*, 47–52 (2018).

[3] S. Takagi, Several ways to improve our education, *Proceedings of the 16th International Symposium on Advanced Technology (ISAT-16)*, 63 (2017).

[4] S. Takagi, T. Nikami and Y. Hayashi, Utilization of Revised Rubrics for Calculus Courses, in preparation.

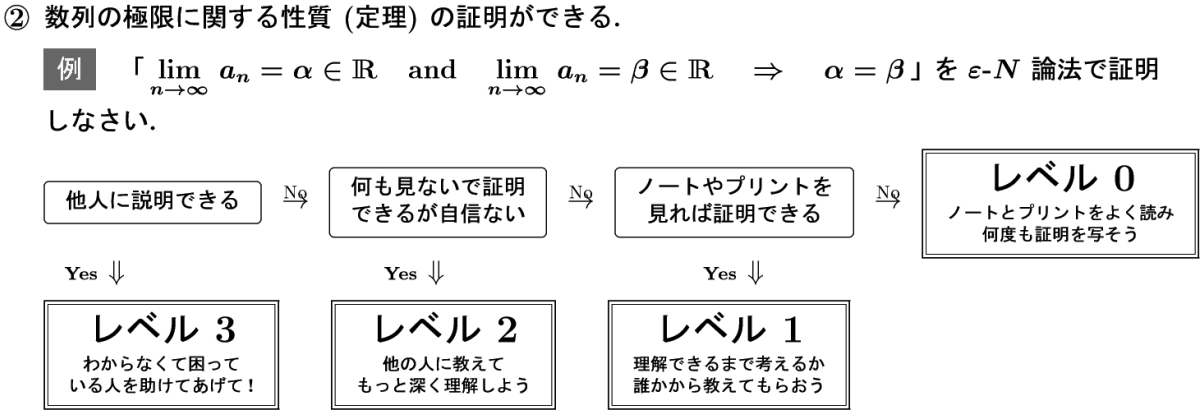

Fig. 1. A revised flowchart-type rubric.

Study on Acceleration Coordination during Dribbling in Soccer

Wataru Ichikawa*, Takato Abe, Satoru Kizawa, Ayuko Saito

Department of Mechanical Science and Engineering, Kogakuin University, Japan
E-mail: s520007@ns.kogakuin.ac.jp

Abstract

In this study, the singular value decomposition of acceleration was used to quantitatively clarify the coordination of the limbs during dribbling. The results showed that the coordination in the right and left forearms, thighs, and lower legs was confirmed.

Soccer is a sport in which players compete to score points by shooting the ball into the opposing team's goal. Currently, the number of soccer players in Japan is approximately 4.36 million, with about 800,000 active players. It is essential for players, both professional and amateur, to acquire various skills in order to be successful in the game. An evidence-based training method enables players to practice effectively and to prevent injury.

This study focuses on dribbling which is the basic motion during soccer game. In order to elucidate the mechanism of dribbling motion, several researches have been investigated the sprinting activities during dribbling [1]. This study investigates the acceleration of forearm, thigh, and lower leg during dribbling and analyze the acceleration coordination.

An adult male (height 1,8m, weight 68kg) participated in the experiment. After receiving an explanation of the purpose and requirements of the study, the participant gave his written informed consent to participate. Study approval was obtained from the Research Ethics Board, Kogakuin University.

As shown in Figure 1, a total of six 9-axis motion sensors were attached to the participants' forearms, thighs, and lower legs. He dribbled a ball through five cones placed at equal intervals on either side. After measurement, each acceleration sensor output was converted into dimensionless quantities of -1 to 1. The observation matrix consisted of dimensionless quantities of acceleration data. A singular value decomposition was performed and the observation matrix was decomposed into the basis vectors.

The results of the spatial basis patterns obtained by singular value decomposition are shown in Figure 2. Figure 2(a) shows the results for the first mode with a 97% contribution rate, and Figure 2(b) shows the results for the second mode with a 2% contribution rate. The results showed that the right and left forearms, thighs, and lower legs coordinated with each other. The right and left coordination was stronger in the order of lower legs, thighs, and forearms. The contribution of the second mode is 2%, which was not the dominant mode of motion for dribbling, suggesting that it is for fine-tuning the motion. The results described that the participant dribbled while fine-tuning the movements of their left and right forearms.

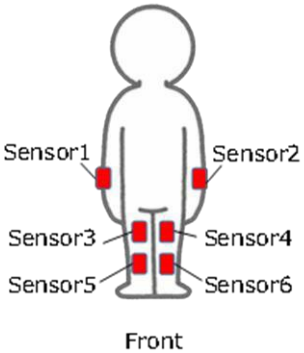

Fig. 1. Sensor positions

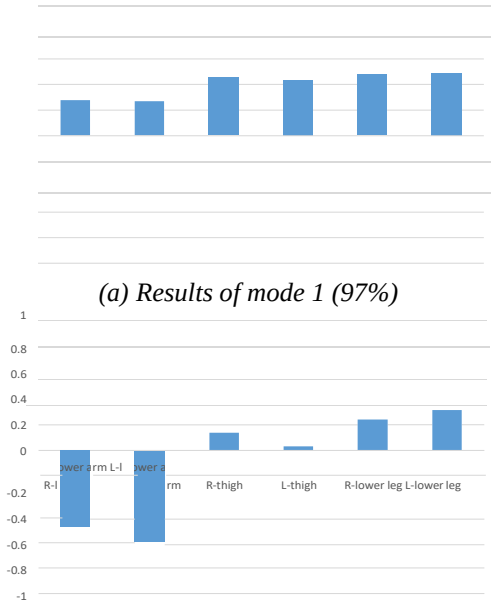

(a) Results of mode 1 (97%)

(b) Results of mode 2 (2%)

Fig.2 Spatial coordination patterns

In this study, the singular value decomposition of acceleration was used to quantitatively clarify the coordination of the limbs during dribbling. The results showed that the coordination in the right and left forearms, thighs, and lower legs was confirmed

References:

[1] Y. Muranoshi, S. Nakahira, T. Yamaoka, Y. Kitazima, R. Isano, K. Aoyama, *Study on the rising sprinting motion of dribbling in soccer*, **26**, 2 267-271(2013)

Research on Exercise Support by Auditory Information using Spatial Audio

Kota Yamamoto[1,a] and Daigo Misaki[1,b]

[1]Graduate School of Engineering, Kogakuin University, Tokyo, Japan
[a]am22072@ns.kogakuin.ac.jp, [b]misaki@cc.kogakuin.ac.jp

Abstract

As research on exercise support without visual information progresses, reducing the size and weight of support devices has become a challenge. We proposed an inexpensive and easy wearable exercise support system using spatial audio in this study. The validation results show that the spatial audio system is adequate for guiding walking and running without visual information.

In recent years, research without using visual information have progressed. Research have been conducted on exercise support without visual information using image processing and vibrating gloves for guidance[1] and magnetic force sensors for assistance[2]. However, reducing the size and weight of the devices used for assistance without visual information. Therefore, this study focuses on running exercises without visual information and research and proposes an inexpensive and easy wearable exercise support system using spatial audio.

METHODOLOGY

This study used spatial audio with dynamic head tracking[3]. Dynamic head tracking refers to using accelerometers and gyroscopes built into devices such as AirPods Pro to track the user's head movements. Head tracking also senses the six degrees of freedom of rotation and movement on the XYZ axis of how the human body moves in space. Using an iPhone and AirPods Pro, we propose an exercise system that is small, light, and has minimal impact on running. We also believe the system is convenient and easy to use because it uses widely used devices. When the user deviates from the direction of motion, the system corrects the direction of motion with sound feedback from the left and right. For example, if the user deviates to the left, the sound is heard from the right beside the user, allowing the user to correct the deviation in the forward direction. The sound that is heard when the user goes off to the left is the musical scale. This is so that the user can sense how far to the left he or she has deviated when he or she deviates to the left. This allows the user to move forward in the middle of the direction of motion by moving forward to the right by that sensation. In the basic experiment, users wore eye masks and were guided to walk blindly, as shown in Figure 1.

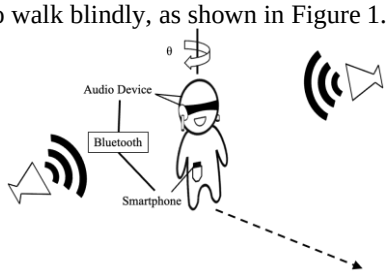

Fig. 1. Blind Walking Guidance Method in Support System using Spatial Audio

RESULTS AND DISCUSSION

Three subjects, A, B, and C, were asked to perform a 15m blind walk. The gait trajectory data of the subjects are shown in Figures 2.1 and 2.2. The data from Subjects A and B show that the spatial audio system used in this experiment effectively guides the user. In the data of subject C, the deviated values were larger for the data with assistance. The reason for the larger difference in the data with assistance is a problem with the initial value settings, indicating that the spatial audio system is capable of guiding the user in a straight line. In the future, it will be necessary to recognize the direction the user is facing at the start of the system.

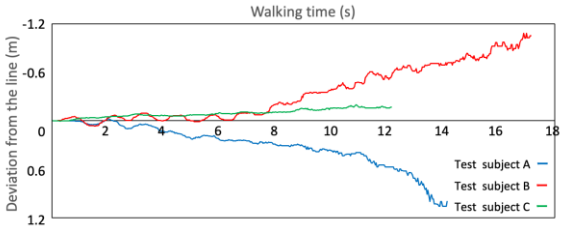

Fig. 2.1. Walking trajectory without support

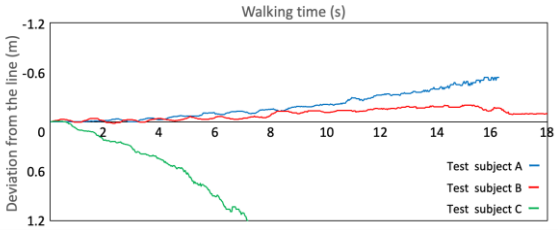

Fig. 2.2. Walking trajectory with support

References:

[1] Mancini, Adriano, Emanuele Frontoni, and Primo Zingaretti. "Mechatronic system to help visually impaired users during walking and running." *IEEE transactions on intelligent transportation systems* 19.2 (2018): 649-660.

[2] Pieralisi, Marco, et al. "An electromagnetic sensor for the autonomous running of visually impaired and blind athletes (Part II: The wearable device)." *Sensors* 17.2 (2017): 381.

[3] “ Immerse your app in spatial audio”. Apple Developer.https://developer.apple.com/videos/play/wwdc2021/10265/ ,(2022-10-19)

Preparation of the Side-chain Modified Peptides as Lysine-specific Demethylase 1 Inhibitors

Masaki Asakawa[1], Ayumu Agarie[1], Taeko Kakizawa[1*], and Takayoshi Suzuki[2]

[1]Graduate School of Materials and Life Sciences, Kanto Gakuin University, 1-50-1 Mutsuurahigashi, Kanazawa-ku, Yokohama, Kanagawa, 236-8501, Japan,
[2]The Institute of Scientific and Industrial Research, Osaka University, Mihogaoka 8-1, Ibaraki, Osaka 567-0047, Japan
E-mail: kg100683@kanto-gakuin.ac.jp

Abstract

In this study, peptidic lysine-specific demethylase 1 (LSD1) inhibitors were prepared. The inhibitors are substrate-based peptides that contains active moieties in the side chain of lysine residue. The preparation and characterization of the peptides are discussed.

Lysine-specific demethylase 1 (LSD1) is an enzyme which demethylates the fourth lysine residue (Lys-4) in the methylated form of histone H3. The development of LSD1 inhibitors has been a research focus because the enzymatic activity of LSD1 is suggested to be associated with various diseases. We have already reported several substrate-based LSD1 inhibitors including *trans*-2-phenylcyclopropylamine (PCPA) in the side chain of the Lys-4 residue [1]. The PCPA moiety reacts with the flavin adenine dinucleotide (FAD) moiety in the active center of LSD1.

In our synthetic studies, we found that several unnatural amino acids in substrate sequence are suitable to increase the inhibitory activity. For example, the peptidic LSD1 inhibitor which contains 1-aminocyclohexanecarboxylic acids (Acc) on either sides of the Lys-4 residue, is a good drug candidate (Fig. 1) [2]. In addition, we have been studied the modifications of the Lys-4 side chain [1, 3]. In this study, the peptides including the Acc were prepared with the moieties derived from 2,5-dihydro-1H-pyrrole (DHP) and 1,2,3,6-tetrahydropyridine (THP) in the side chain of Lys-4 instead of PCPA. The DHP or THP moiety is expected to react with FAD in LSD1 with use of the double bond.

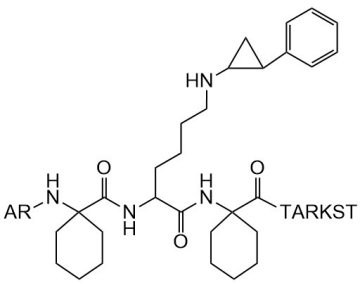

Fig. 1. Structure of LSD1 inhibitor including PCPA moiety.

The preparations of DHP- and THP- peptides were performed in a similar manner to previous reports [1-3]. Started from Fmoc-Thr(*t*Bu)-Wang-resin, the protected peptide chain was accomplished *via* Fmoc-based solid phase peptide synthesis. The 6-hydroxynorleucine residue was introduced at the forth position of the sequence. The side-chain modification was carried out for the hydroxyl group with mesylation using methanesulfonyl chloride and following replacement with DHP or THP in the presence of trimethylamine. The total cleavage was performed with TFA in the presence of H_2O, *m*-cresol, and thioanisole. Purification and characterization were performed with high performance liquid chromatography and matrix-assisted laser desorption ionization-time of flight mass spectrometry. The desired peptides are obtained in moderately low yield. The evaluations of inhibitory activities of these inhibitors are now in progress.

References:

[1] T. Kakizawa, Y .Ota, Y. Itoh, H. Tsumoto, T. Suzuki, *Bioorg. Med. Chem. Lett*., **25**, 1925-1928 (2015).
[2] Y. Ota, T. Kakizawa, Y. Itoh, T. Suzuki, *Molecules*, **23**, 1099-1107 (2018).
[3] T. Kakizawa, Y. Ota, Y. Itoh, T. Suzuki, *Bioorg. Med. Chem. Lett*., **28**, 167-169 (2018).

Synthesis of Short Peptides as Lysine-specific Demethylase 1 Inhibitors

Ren Inoue[1], Taeko Kakizawa[1]*, and Takayoshi Suzuki [2]

[1]Graduate School of Materials and Life Sciences, Kanto Gakuin University, 1-50-1 Mutsuurahigashi, Kanazawa-ku, Yokohama, Kanagawa, 236-8501, Japan,
[2]The Institute of Scientific and Industrial Research, Osaka University, Mihogaoka 8-1, Ibaraki, Osaka 567-0047, Japan
E-mail: kg100683@kanto-gakuin.ac.jp

Abstract

Lysine-specific demethylase 1 (LSD1) inhibitors have been studied as drug candidates because LSD1 is thought to be associated with various diseases. We have reported substrate-based LSD1 inhibitors. In this study, several short peptides as LSD1 inhibitors ware prepared.

Lysine-specific demethylase 1 (LSD1) inhibitors are now widely investigated by several research groups including ours because they are thought to be associated with various diseases. LSD1 removes methyl groups from the methylated lysine residue in the fourth position (Lys-4) of histone H3.

The peptide sequence of histone H3 can be used for the development of substrate-based inhibitors. We previously reported the LSD1 inhibitor, which includes a *trans*-2-phenylcyclopropylamine (PCPA) in the side chain of the Lys-4 residue in a 21-amino acid peptide sequence of histone H3 (Fig.1 (A)) [1]. We performed its truncation study in the C-terminal region and proved that the leaving of amino acids gradually reduces its inhibitory activity against LSD1[1]. After this research, we found that the introduction of unnatural amino acids that induce a γ-turn in the peptide chain increases inhibitory activity against LSD1 [2]. We designed the undecapeptide inhibitor comprising the 1-aminocyclohexanecarboxylic acid (Acc) on either sides of the Lys-4 residue (Fig.1 (B)). It showed better potency against LSD1. In this study, we performed a truncation study of the undecapeptide including two Accs beside the Lys-4 residue.

Several peptides shorter than eleven amino acids were synthesized. The peptide preparation was performed in a similar manner to previously reported procedures [1,2]. The peptide chain was elongated on 2-chlorotrityl chloride resin *via* Fmoc-based solid phase peptide synthesis. The introduction of PCPA moiety was carried out through mesylation of hydroxyl group of 6-hydroxynorleucine residue at fourth position in the sequence, and following treatment with PCPA·HCl. Peptides were cleaved from resin with TFA cocktail and precipitated with cold diethyl ether. The obtained crude product was adjusted to high performance liquid chromatography and the desired product was collected. After the lyophilization, desired peptide was obtained as a white powder. Peptides were characterized with matrix-assisted laser desorption ionization-time of flight mass spectrometry. These compounds were obtained in moderately low yield probably due to the steric hindrances of cyclohexyl group. Now further investigations are in progress.

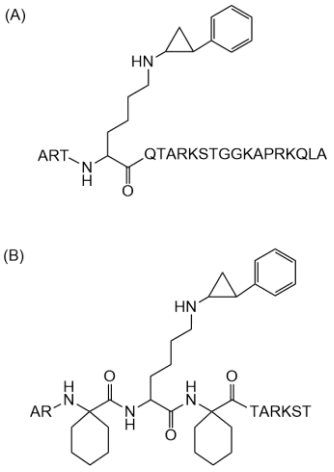

Fig. 1. Structures of (A) Substrate-based LSD1 inhibitor comprising 21-amino acids (B) The peptide including 1-aminocyclohexanecarboxylic acid.

References:

[1] T. Kakizawa, Y. Ota, Y. Itoh, H. Tsumoto, T. Suzuki, *Bioorg. Med. Chem. Lett.*, **25**, 1925-1928 (2015).
[2] Y. Ota, T. Kakizawa, Y. Itoh, T. Suzuki, *Molecules*, **23**, 1099-1107 (2018).

Breakout Room #5

Electric Engineering and Electronic Engineering

Chairperson: Dr. Vo Tuan Minh, DUT

Presentation No.	Title	Author	Page
EEEL1.	Analysis Malware Infection Of IOT Devices On Zero Trust Networks	Yudai Sakurai, Osamu Mizuno	186
EEEL2.	A Study Of Dynamic Routing Method In ICN-Based Wireless Sensor Networks	Kohei Yamamoto, Takafumi Taya, Eishin Nagaoka, Osamu Mizuno	187
EEEL3.	Affect Of Lorawan Network Parameters On The Performance Of The Network In Frequency Band In Vietnam	Tran Van Lic, Fang Yi Lee, Meng-Hsun Tsai	188
EEEL4.	Mutual Authentication Scheme In ICN-Based Wireless Sensor Networks	Takafumi Taya, Eishin Nagaoka, Osamu Mizuno	194
EEEL5.	Frequency Utilization Efficiency Improvement By Spectrum Suppressed Transmission With 16QAM	Teppei Kanke, Takatoshi Sugiyama	195
EEEL6.	A Study On Performance Of CPU Clock Rate Control Based On Application Monitoring	Kota Kumakura, Takeshi Kamiyama, Masato Oguchi, Saneyasu Yamaguchi	196
EEEL7.	A Study On A Modified Vision Transformer Model For Image Processing	Tatsuhiko Ikeda, Hidetoshi Saito	197
EEEL8.	A Study On Deletion Of Snis For Service Identification	Ryo Asaoka, Akihiro Nakao, Masato Oguchi, Saneyasu Yamaguchi	198
EEEL9.	A Study On Mutual Interference With Islanding Detection Function In Inverters With Inertia Function	Dehui Li, Yasuhiro Noro	199
EEEL10.	CO2 Gas Sensing By In2O3-Based Thin-Film Transistors	Ayumu Nodera, Shun Mori, Shinya Aikawa	200
EEEL11.	Electrical Property And Valence Band Offset In Conductive Mgnio On Sapphire Substrates	M. Murayama, A. Ishikawa, T. Yamaguchi, T. Honda, K. Sasaki, A. Kuramata, T. Onuma	203
EEEL12.	Growth And Characterization Of Algan And Multiple Quantum Wells With Varying III/V Ratios By RF-MBE	Mahiro Hayasaki, Tomoya Yamaguchi, Tomohiro Yamaguchi, Tohru Honda, Takeyoshi Onuma	204
EEEL13.	Structural Analysis In Epitaxial Growth Of Gainn By RF-MBE Using XRD-RSM	J. Takeuchi, T. Sasaki, H. Yokoyama, T. Onuma, T. Honda, T. Yamaguchi	205

Analysis malware infection of IoT devices on Zero Trust Networks

Yudai SAKURAI, Osamu MIZUNO

Department of Electrical Engineering and Electronics, Graduate School of Engineering, Kogakuin University, Tokyo, Japan
E-mail: cm22027@ns.kogakuin.ac.jp, omizuno@cc.kogakuin.ac.jp

Abstract

Cyber attacks targeting IoT (Internet of Things) systems are on the rise. IoT devices have small computing resources, so it is necessary to take security measures with less load. Therefore, we designed and built a system that applies Zero Trust Networks (ZTN) to the IoT system. In this paper, we focus on malware, which is the main security issue in IoT, and present a countermeasure for IoT-ZTN systems.

1. Introduction

Cyber-attacks targeting IoT (Internet of Things) systems are increasing. Threats exist in the internal network. In addition, IoT devices have only small computing resources and require security measures with less workload. We designed the IoT-ZTN (Zero Trust Networks) systems [1]. The IoT-ZTN system is capable of dealing with unauthorized access that occurs in the internal network. However, there are various cyber-attacks against IoT, and it is necessary to deal with them. In this paper, we list the security issues of IoT and discuss a method to deal with them in the IoT-ZTN system.

2. The IoT-ZTN system

We proposed an IoT system applying ZTN to solve the problem of internal fraud [1]. In the IoT-ZTN system, the control plane performs access control. It performs access control based on the policy of "being suspicious of unusual access". For example, access by an unusual IP address is considered suspicious, and therefore access is denied. Based on the concept of ZTN, this system can prevent unauthorized access that occurs in the internal network by verifying access information for all accesses. However, there are other attacks targeting the IoT devices that need to be addressed.

3. Malware Attacks for IoT devices

Malware attacks are the major threat to the IoT devices [2]. Attackers exploit a large number of infected IoT devices to launch large-scale DDoS attacks. There are three risks when IoT devices are infected with malware. The first is unauthorized data acquisition. The unauthorized acquisition of data may violate the confidentiality of users of the system. The second is data falsification. Data falsification may compromise the integrity of the system. Third is DDoS attacks that exploit a large number of IoT devices. DDoS attacks can disrupt system operation and compromise availability. Based on the above, it is necessary to deal with malware attacks.

4. Countermeasures for Malware Attacks

We present three countermeasures against malware attacks in IoT-ZTN systems. The first method is distributed detection. It denies access to infected IoT devices by increasing the variation of access information to be verified at the time of authentication and authorization. The second is continuous authentication of IoT devices to prevent access from the malware-infected IoT device, even if it has been authenticated once. The third method is traffic pre-monitoring. This method monitors the traffic toward the IoT gateway to detect suspicious behavior such as a large number of the same packets flowing through the gateway. Table 1 shows the qualitative evaluation of the coping methods. It shows that distributed detection methods are effective in coping with malware. The combination of the presented schemes can also cope with data tampering and DDoS attacks.

Table 1 Qualitative Evaluation of Coping Methods

	Security		Performance	
	Malware Detection	DDoS attacks	Load on IoT devices	Number of C-plane signals
Distributed Detection Method	○ Detectable at device registration and access	× Reduces likelihood of attack, but does not directly address the issue	× High load due to application	○ Increased signals at registration
Continuous Authentication Method	△ Detectable, depending on scanning accuracy	× Reduces likelihood of attack, but does not directly address the issue	△ Increased authentication requests	△ Increased by number of continuing certifications
Traffic Pre-monitoring Method	× Undetectable because the device is not monitored	○ Can be dealt with by refusing in advance	○ Normal load as devices are not monitored	× High load due to increase in number of devices to be monitored

Relatively good : ○ partially favorable : △ relatively inferior : ×

5. Conclusion

We identified security issues in IoT and analyzed countermeasures for the IoT-ZTN system. Design the proposed methods for the IoT-ZTN system and evaluations using it is future studies.

Acknowledgments

This work was supported by JSPS KAKENHI Grant Numbers 22K12014.

References:

[1] Y. Sakurai, et. al., “Construction of IoT System Based on Zero Trust Networks,” IEICE Technical Reports, NS2022-41, July 2022.

[2] N. Miyaho, et. al., “ Network and Security Technologies for IoT/5G/DX,” Morikitasyuppan Co., Japan, Tokyo, 2022.

A Study of Dynamic Routing Method in ICN-based Wireless Sensor Networks

Kohei Yamamoto[1], Takafumi Taya[2], Eishin Nagaoka[2] and Osamu Mizuno[1, 2]
[1] Department of Information and Communication Engineering, Faculty of Informatics, Kogakuin University, Tokyo, Japan
[2] Graduate School of Electrics and Electronics Engineering, Kogakuin University, Tokyo, Japan
E-mail: {j019302, cm22032, cm21037}@ns.kogakuin.ac.jp, omizuno@cc.kogakuin.ac.jp

Abstract
We proposed ICSN as a method to realize multiple IoT services. However, ICSN needs to set up the routing table in advance, so it is difficult to build up quickly. To solve this problem, this paper proposes the Hello Interest Method (HIM) and the Search in Mesh Network Method (SMNM) as dynamic routing methods. The quantitative evaluation results show that the construction time of HIM is 2.61 to 3.90 times faster than SMNM.

1. Introduction
To realize multiple IoT (Internet of Things) services on a sensor network, we have proposed an ICSN (Information-Centric Networking based Wireless Sensor Networks) [1] which is an application of ICN (Information-Centric Networking) [2]. To deploy ICSN, it is necessary to determine the route between nodes in advance. It makes difficult quickly deploy ICSN. The dynamic routing protocol builds the initial route. This paper, we compared the Hello Interest Method (HIM) and the Search in Mesh Network Method (SMNM) as proposed dynamic routing protocols.

2. Proposed Dynamic Routing Methods
2.1 Hello Interest Method
The HIM is a routing protocol using flooding of Hello-Interest packets from a sink node. Fig.1 shows overview of HIM. Initially, the node receives a Hello-Interest packet from a sink node. It sends its own Content ID to the sink node in Data packet. After the sink node receives the Data packet, it gets the Content ID from the Data packet and add to its FIB (Forwarding Interest Table). Each node repeats this procedure. To avoid network congestion, each node - doesn't receive the Hello-Interest packets more than twice. Then, a tree topology network will be built.

2.2 Serch in Mesh Network Meshod
The SMNM initially constructs a mesh topology network. After that, SMNM determines the final routes by search. In Fig.2, a sink node floods Hello-Packets. After the sensor node receives the packet, it adds the adjacent nodes to its neighbor node list. After this process is completed, a sink node starts to search reachable nodes. When the sink node founds route to some nodes, it adds to its own FIBs.

3. Qualitative Evaluation
Qualitative evaluation of the overall network number of signal counts, computational complexity, and network convergence time for the HIM and the SMNM was conducted. In addition, the convergence time of the network is the sum of the number of communications and the amount of computation. The total number of sensor nodes are 32 and number of neighboring nodes per node are evaluated under the condition that the number of neighboring nodes are increased from 1 to 32. As a result, the network convergence time for the HIM ranged from 160 to 2080 [unit time], while that for the SMNM ranged from 624 to 5424 [unit time]. Thus, the convergence time of the SMNM is 2.61 to 3.90 times longer than that of the HIM.

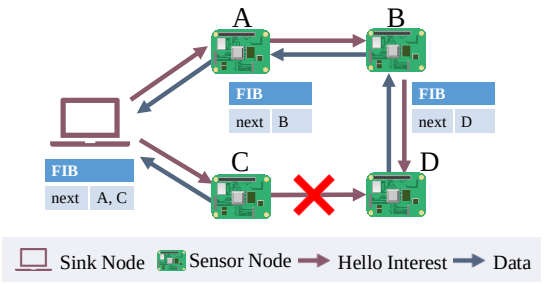

Fig. 1. Hello Interest Method (HIM)

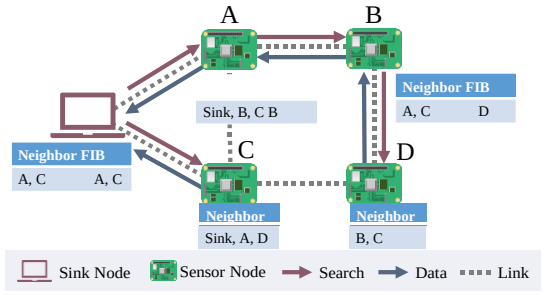

Fig. 2. Search in Mesh Network Method (SMNM)

4. Conclusion
We propose HIM and SMNM for dynamic routing protocol on ICSN.

Acknowledgements
Part of this research was funded by Japan Society for the Promotion of Science (JSPS) research grant JP22K12014.

References:
[1] K. Kimura, K. Mochizuki, M. Koike and O. Mizuno, "Data Transfer Methods for Information-Centric Networking-Based Wireless Sensor Network Platform," 2019 International Conference on Information Networking (ICOIN), pp. 336-341, 2019.
[2] B. Ahlgren, C. Dannewitz, C. Imbrenda, D. Kutscher, and B. Ohlman, "A survey of information-centricnetworking," IEEE Communications Magazine, vol. 50, no. 7, pp. 26–36, July 2012.

Affect Of Lorawan Network Parameters On The Performance Of The Network In Frequency Band In Vietnam

Tran Van Lic[1], Fang Yi Lee[2], Meng-Hsun Tsai[2]

[1]Department of Electronic and Telecommunication Engineering, The University of Danang - University of Science and Technology, Vietnam
E-mail: tvlic@dut.udn.vn
[2]Department of Computer Science and Information Engineering, National Cheng Kung University, Taiwan
Email: alicebear1203@gmail.com, tsaimh@csie.ncku.edu.tw

Abstract

In recent years, researchers have been studying and testing the Low Power Wide Area Network (LPWAN) protocol, which is generally LoRaWAN in Internet of Things (IoT) devices. In this study, we examine the LoRaWAN protocol by determining the impact of network setup settings on the network performance in the real world on the 920–923 MHz range. The frequency is approved for usage in Vietnam for IoT applications by the frequency administration. The study concentrates on the effects of the LoRaWAN parameters, such as Spreading Factor (SF), Payload Length (PL), Data Length (PL), Adaptive Data Rate (ADR), Frequency Channel (FC), and Distance. Using RSSI, SNR, Packet Delivery Ratio (PDR), and Time on Air, the LoRaWAN network's performance was assessed.

Keywords – LoRa, LoRaWAN, LPWAN, IoT, Performance.

1. Introduction

A low Power Wide Area Network (LPWAN) is a collection of wireless technologies with a large coverage area, low bandwidth, low operating power, and long battery life [1]. LPWAN provides connectivity for devices and applications with low mobility and low data transmission. For example, temperature-humidity sensors, measuring sensors in digital meters, are a significant part of the IoT system. Therefore, the future LPWAN will bring a new option for IoT data transmission, developed to meet the purpose of low energy consumption, prolonging the uptime of IoT terminal devices, with the ability to transmit capacity and long distances of kilometers [2].

Among low-power wide area networks (LPWAN), Long Range Wide Area Network (LoRaWAN) is one of the most popular technologies today, which will be analyzed and evaluated in this paper. LoRaWAN is an open standard launched by the LoRa Alliance organization to ensure interoperability between IoT devices [3]. The LoRa chip, the essential part needed to deploy a LoRaWAN network, is proprietary to US-based semiconductor chip maker SemTech.

LoRa uses the Sub-GHz spectrum (868 Mhz in Europe, 915 Mhz in the Americas, and 923 Mhz in Asia). This technology uses spread spectrum technology to transmit data on different frequency channels and speeds so that Gateways can adapt to changing conditions and optimize how data is exchanged with each device.

Data rates in LoRaWAN networks range from 300 bps to 50 kbps depending on the Spreading Factor (SF) and bandwidth (BW). The maximum Payload Length (PL) data length is 243 bytes and provides Efficient two-way uplink and downlink communication. Each packet is received by all gateways in the coverage area to ensure a successful transmission rate. Still, the requirement of multiple gateway stations can increase the cost of network deployment.

To ensure the efficiency and reliability of the LoRaWAN network, the LoRa End-nodes need to be configured with various communication parameters. For example, a LoRa device can be configured to be used with different parameters such as Spreading Factor (SF), Bandwidth (BW), Coding Rate (CR), Transmit Power transmission powers (TP), Adaptive Data Rate (ADR). The possible combination results in over 6720 possible settings [4]. Therefore, choosing the right configuration parameters to ensure energy saving and the LoRaWAN network performance is also a challenge.

Many foreign articles have evaluated the influence of these parameters on the performance of LoRaWAN networks. Typically, the study [5] by Davide Magrin, Martina Capuzzo, and Andrea Zanella used simulation software to analyze the interaction effects of configuration parameters in the LoRaWAN network on the performance of the LoRaWAN network. However, most studies mainly use simulation software to simulate these parameters and give computer simulation results for comparison. Therefore, the reality is not high because the background noise environment with the allowed frequency range in different countries is different.

In this paper, we do not simulate but test in real conditions with the actual background noise level in Vietnam and the allowed frequency band from 920-923 Mhz. By collecting data and analyzing it, evaluate it to see how it affects the real environment in setting LoRaWAN network parameters such as Spreading Factor (SF), length Payload Length (PL), Adaptive Data Rate (ADR), Frequency channel (FC)

and distance to LoRaWAN performance, namely SNR, RSSI, packet transmission rate Packet Delivery Ratio (PDR) and Time on Air (ToA). The rest of the paper is presented as follows. Part 2 presents the theoretical basis of the LoRaWAN network protocol and configuration parameters. Section 3 describes the empirical evaluation model. Section 4 presents the results of experimental implementation and evaluation. The conclusion of the paper is presented in section 5.

2. LoRaWAN parameter

In the LoRaWAN network, LoRa acts as the physical layer and is developed exclusively by Semtech cave. The LoRaWAN communication standard is open source and actively developed by commercial and industry partners [6].

2.1. Spreading Factor (SF)

LoRa uses Chirp Spread Spectrum (CSS) modulation and Forward Error Correction (FEC) to reduce noise [7]. Which, Spreading Factor (SF) is the main configuration parameter, which is the ratio between symbol rate and chip rate [8], [9]. The SF determines the number of chirp signals when encoding the frequency-modulated signal of the data specified from SF7 to SF12. For example, if SF is 12, 12 pulses of the chirp signal will encode one logic level of the chipped signal.

2.2. RSSI và SNR

Received Signal Strength Indication (RSSI), depicted in Figure 1, is the received signal power in mW and is measured in dBm. This value can be used as a measurement of how well the receiver can "hear" the signal from the sender. RSSI is one of the primary indicators of the LoRa network. Specifically, RSSI is an index that measures the level of power loss relative to the source. The RSSI is calculated based on the transmit power (of the LoRa End-node) minus the total loss on the path (material loss and distance loss).

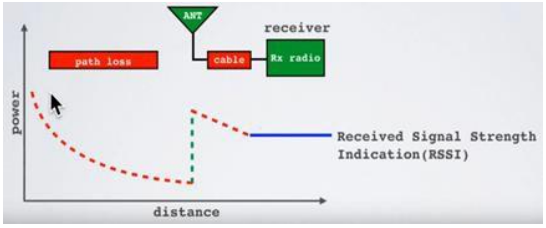

Figure 1. Illustration of RSSI [10]

The Signal-to-Noise Ratio (SNR), depicted in Figure 2, is a signal-to-noise ratio of the received signal to the noise floor. Background noise is an area of all sources of unwanted interference that can interfere with the transmitted signal, causing difficulty in decoding at the receiver.

If the SNR exceeds 0, the received signal will operate above the noise level. If the SNR is less than 0, the received signal will work under the noise layer.

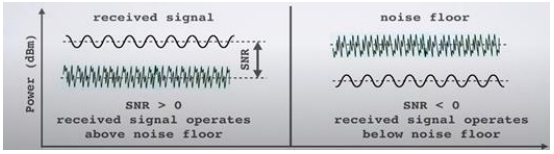

Figure 2. Image illustrates signal level and background noise [10]

2.3. Time on Air (ToA)

When a signal is sent from the sender, it takes a certain amount of time before the receiver receives the signal. This interval is called Time on Air (ToA) illustrated in Figure 3.

Figure 3. Illustration of ToA [10]

The total air transmission time of a LoRa packet called Time on air (ToA), also known as LoRa packet duration – Lora packet duration (Tpacket) is calculated as follows:

ToA = Tpacket = Tpreamble + Tpayload

In there:

Tpreamble is the time it takes for the receiver to receive the signal of a LoRa packet in the air.

Tpayload is the time it takes to transmit the outgoing data.

2.4. Adaptive Data Rate (ADR)

ADR is a mechanism that optimizes data rate, usage time, and capacity in a network. The LoRaWAN protocol defines Adaptive Data Rate (ADR) to control uplink transmission parameters of LoRa devices including:

- Spreading Factor (SF)
- Bandwidth (BW)
- Transmission power (Txpower)

Whether the ADR function is used or not is required by the End-nodes by setting (flag) ADR in the packet message sent to the Gateway (uplink). If ADR is enabled, the network server can control the transmission parameters of the End-node.

ADR should only be used in stable Radio Frequency (RF) situations where the End-nodes are not moving. Fixed mobile End-nodes for longer periods can enable ADR during that time.

Network server collects nearly 20 most recent uplink transmission data, such as data rate and Signal-to-Noise Ratio (SNR) from an End-node. Out of the 20 uplink packets received, the network server takes the maximum SNR value that is now called SNR-measured and the corresponding data rate.

After 20 frames of signal received, it calculates the SNRmargin using the data rate (DR: Data rate) of the last received message.

SNRmargin = SNRmax + requireSNR -margin (dB)

With:

SNRmargin is the maximum value of 20 received signals.

Margin is defaulted to 10

The requireSNR value is given in Table 1.

Table 1. Table of SNR values by SF and data rate

SF	SNR (dB)
DR5/SF12	-20
DR4/SF11	-17,5
DR3/SF10	-15
DR2/SF9	-12,5
DR1/SF8	-10
DR0/SF7	-7,5

2.5. Packet Delivery Ratio (PDR)

PDR is the ratio of the number of packets successfully received at the network host to the total number of packets transmitted by a terminal [11]. PDR is an important parameter to evaluate the stability of the network. To calculate the PDR, the End-node devices will be fixed to transmit 200 packets continuously, based on the number of packets received at the network server, the rate of successful packet transmission will be calculated.

3. Experiment system

The experiment system consists of 4 main parts: End-node, LoRaWAN gateway, Network Server using The Things Network (TTN) and Applicaton Server (TTN Mapper).

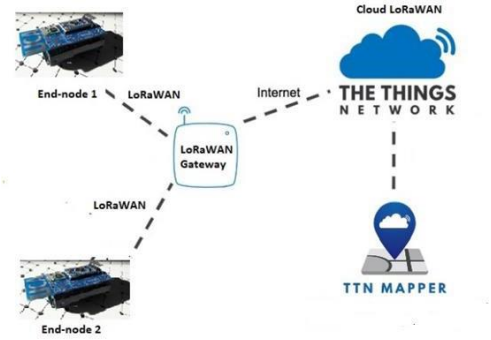

Figure 4. LoRaWAN test system connection diagram

End-node (or LoRa node) is an end device that uses LoRa chip to transmit and receive data to Gateway via LoRaWAN protocol. End nodes are often fitted with sensors that are used to detect changing parameters such as temperature, humidity, light intensity, and air quality.

LoRaWAN Gateway receives data transmitted from the End-node. The Gateway then uploads the data to the Network Server TTN over the Internet.

Finally, using TTN mapper software to collect data, LoRaWAN transmission and reception parameters for analysis and evaluation.

3.1. Hardware design

3.1.1. End-node

The end node used in the test is the UCA board developed by Prof. Fabien Ferrero, Université Côte d'Azur.

End-node hardware includes 1 Arduino Mini Pro used to control End-node operations, an RFM95 module responsible for modulating LoRa signal transmission, End-node using AA batteries, and the antenna part is integrated into the PCB board through the letter UCA. In addition, the End-node can attach sensors to collect data, as shown in Figure 5.

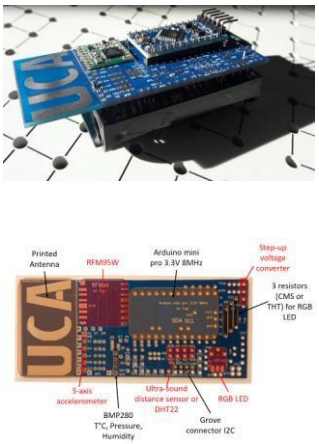

Figure 5. Layout PCB của End-node UCA board

3.1.2. LoRaWAN Gateway

LoRaWAN Gateway Rak7240 is used in the test. This is a Gateway designed to be installed outdoors (Outdoor Gateway) and can work with 8 frequency channels in the 920-923Mhz band.

The Gateway is connected to the Internet through an Ethernet port. The gateway device is always connected to a power source via a Power over Ethernet (PoE) port. The data transmitted to the Gateway is configured to forward to the Network Server, The Things Network (TTN), a free-to-use LoRaWAN cloud for testing.

Figure 6. Gateway installed for testing

Figure 6 depicts the Gateway installed on a high-

rise building to be able to transmit Line of Sight (LoS) to the End-nodes, ensuring data accuracy during the entire testing process.

3.2. Data collection

TTN Mapper software is used to collect data sent up from the End-node and the accompanying LoRaWAN network parameters for analysis, such as RSSI, SNR, SF, PL, ADR, and frequency channel. In addition, TTN Mapper can use GPS to calculate the distance from the End-node to the Gateway based on the map. The data is extracted in the form of a CSV file which is convenient for data analysis and evaluation.

3.3. Experiment method

In this test, the parameters SF, PL, ADR, FC, and transmission distance will be changed to evaluate their impact on the performance of the network, specifically here, the parameters RSSI, SNR, PDR, and ToA of the LoRaWAN network.

The experiment is set up as follows:

• The end node sends 200 packets continuously to the Gateway every 10 s.

• End-node is placed in 2 different locations in turn. In the first position, will place at a distance of 150 m from the Gateway and call here and near (Near). Far distance (Far) will place the node 450 m away from the Gateway.

The data obtained from the Gateway will be transmitted and stored in the database of the TTN mapper application. After collecting enough data, synthesizing, and analyzing the data, using Matlab software to display the data in the form of graphs.

To ensure accuracy, tests will be conducted based on Line of Sight (LoS) conditions, i.e., End-nodes will be placed in positions to clearly see gateways without obstructing the view.

Change the SF value from SF7 to SF12, respectively. For each SF, we change the PL parameter from 10 bytes to 50 bytes, respectively. Using 125kHz. BW bandwidth

The PDR value is calculated based on the number of packets successfully transmitted to the Gateway out of the total number of packets transmitted. To prevent nodes from being disconnected from the network while in operation, nodes can perform periodic network link checks by activating link checks (LCs) to confirm that they are still connected to LoRaWAN.

Enabling link check (LC) is done on the node through the lmic library. The node that transmits uplink data until the 12th packet will automatically activate LC and ask the Gateway to send the downlink to confirm whether it is still connected to the network. The tests are also performed at near and far distances and do the same with the Payload length evaluation.

4. Results

4.1. Effect of distance on RSSI and SNR

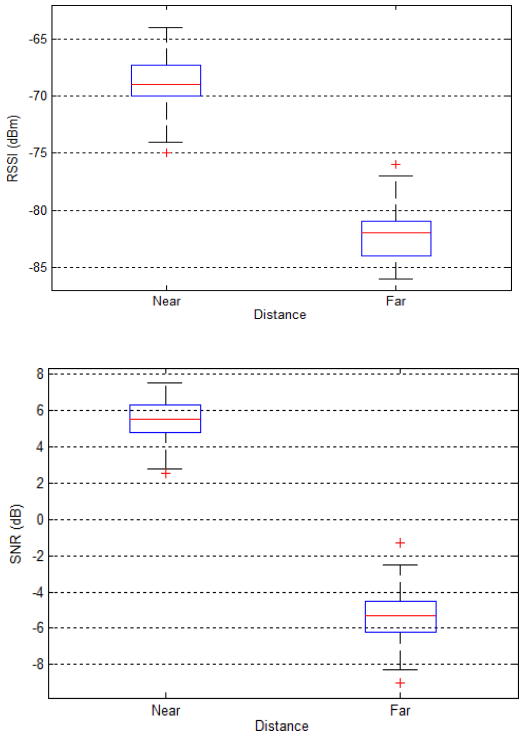

Figure 7. Experimental evaluation results with RSSI and SNR

The RSSI and SNR shown in Figure 7 have a significant decrease from the near distance (Near) to the far distance (Far). A positive SNR between 2 and 8 dB at close distances indicates good signal transmission and little interference. The common SNR value, in this case, is 5.5 dB. SNR in this case of long-distance (Far) is reduced quite a lot, from -8 dB to -2 dB and at most about -5 dB. Similarly, the received signal strength parameter RSSI is significantly reduced at near and far distances.

Thereby, distance effects on RSSI and SNR, the two main parameters to evaluate the quality of the signal. Near distances, the signal is good and less noisy, and conversely, at long distances, the signal is poor, and the noise is more.

Table 2. Test results with different frequency channels

Channel		0	1	2	3	4	5	6	7	LoRa std	FSK
Frequency (Mhz)		921,4	921,6	921,8	922	922,2	922,4	922,6	922,8	922,7	923
Payload length (PL)	10 bytes										
Distance (Line of Sight)	0.45 Km										
Number of packets		200									
	SNR	-3,5	-6,7	-4,5	-10,3	-9,5	-0,9	-5,5	-6,7	1,2	-2,2
	RSSI (dBm)	-99	-93	-90	-101	-96	-89	-95	-99	-88	-95
	PDR (%)	78	75	75	67	86	88	70	79	83	81
	ToA (ms)	42,216 ms									

4.2. Effect of SF to ToA

Figure 8 shows the ToA parameter for different SFs and PLs with a BW bandwidth of 125 kHz. With larger SF allows longer range of communication. However, according to the results in the figure, large SFs also increase the transmission time in the ToA space.

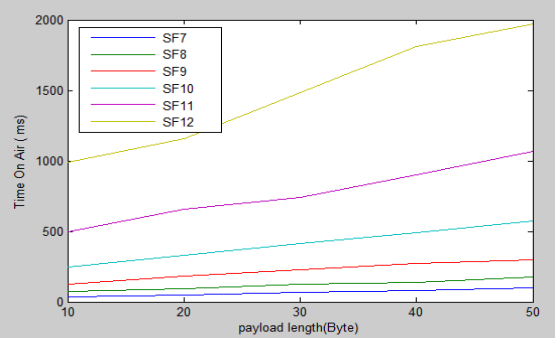

Figure 8. Effect of PL on ToA

For example, if the packet payload is 40 bytes for SF = 8, we get a ToA of 60 ms; if SF = 12, then a ToA obtained is about 1800 ms. One way to increase the transmission time of a LoRa End-node is to switch between the SFs of the allocated channel. This issue should therefore be considered in future practical applications since large SFs are used more often than small SFs.

4.3. Effect of PL to PDR

In general, payload length clearly affects packet transmission. PDR, in general cases, tends to decrease with packet length. However, Figures 9, and 10 also see cases (PL=20, Far), (PL=30, Near) or cases with ADR activation in Figure 10 like cases (PL=20, Far), (PL=30, Near), (PL=40, Far) gives results that do not follow this rule. These results can be affected by random noise sources in space, and more data is needed to increase the accuracy of the results.

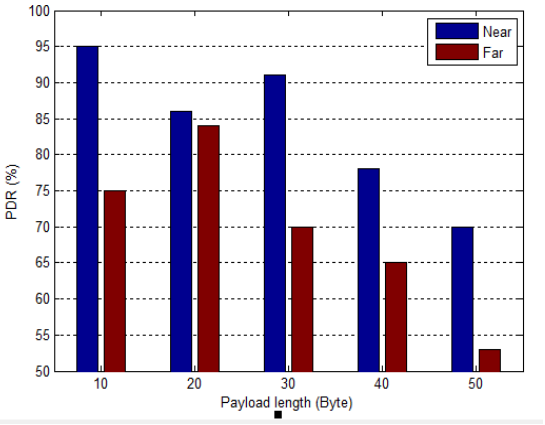

Figure 9. Effect of PL on PDR

With a length of 10 bytes, the transmission quality is quite good, PDR reaches 95% at close distance and 75% at long distance. PDR in payload length of 50 bytes gives 70% at close range (150 m) and 53% at long range (450 m).

4.4. Effect of ADR to PDR

Enabling Adaptive Data Rate (ADR) increased PDR in the proximal and distal groups, as shown in Figure 10. At most different payload lengths (PLs), ADR improved PDR by about 5%. Thereby it can be seen that the impact of ADR on the network's performance is yes but not significant.

4.5. Effect of Frequency channel (FC) to PDR and ToA

Table 2 shows that at frequency channels, the received signal strength of RSSI is almost the same, ranging from -88 dBm to -101 dBm. However, the PDR packet transmission rate in the 922 MHz frequency channel is significantly lower than other frequency channels. Through the results of PDR, SNR is different between channels. The influence of background noise on frequency channels is different. However, the propagation time is almost constant for the frequency channels. The frequency channels all send in 42.216 ms.

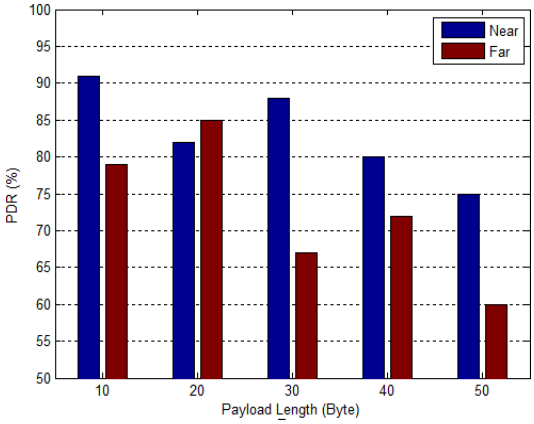

Figure 10. Effect of PL on PDR in case of ADR activation

5. Conclusion

In the framework of the paper, by setting up the actual LoRaWAN system in Vietnam and collecting data by changing the basic parameters of the LoRaWAN network, such as Spreading Factor (SF), Payload Length (PL), Adaptive Data Rate (ADR), Frequency channel (FC) and transmission distance. Through the results affecting LoRaWAN network performance, such as RSSI, SNR, PDR, and ToA, it is possible to change configuration parameters that can increase RSSI and SNR signal quality in the network. In addition, by surveying the influence of frequency channels on PDR and ToA, it will be possible to evaluate which frequency channel is better received to choose a potential frequency channel to deploy for LoRaWAN applications. Based on the results obtained in the article, further studies can suggest adding Machine Learning to select the parameters of the LoRaWAN network automatically and optimally in response to other actual environmental conditions.

Acknowledments:

This work is supported by 2022-2023 DUT-NCKU Joint Research Program

References:

[1] U. Raza, P. Kulkarni and M. Sooriyabandara, "Low Power Wide Area Networks: An Overview," in IEEE Communications Surveys & Tutorials, vol. 19, no. 2, 2017, pp. 855-873.

[2] Hoàng Lê Trung, "Mạng LPWAN cho các ứng dụng IoT", http://www.cuctanso.vn/, 02/2019.

[3] LoRa Alliance®, https://lora-alliance.org/

[4] M. Bor and U. Roedig, "LoRa Transmission Parameter Selection", 2017 13th International Conference on Distributed Computing in Sensor Systems (DCOSS), Ottawa, ON, Canada, 2017, pp. 27-34,

[5] D. Magrin, M. Capuzzo and A. Zanella, "A Thorough Study of LoRaWAN Performance Under Different Parameter Settings", in IEEE Internet of Things Journal, vol. 7, no. 1, Jan. 2020, pp. 116-127.

[6] U. Raza, P. Kulkarni, and M. Sooriyabandara,"Low Power Wide Area Networks: An Overview", IEEE Communications Surveys and Tutorials, vol. 19, no. 2, year 2017, pp. 855–873.

[7] M. Bor, J. Vidler, and U. Roedig, "LoRa for the Internet of Things", in Proceedings of the 2016 International Conference on Embedded Wireless Systems and Networks, Graz, Austria, February 2016, pp. 361–366.

[8] M. Bor and U. Roedig, "LoRa transmission parameter selection", in Proceedings - 2017 13th International Conference on Distributed Computing in Sensor Systems, DCOSS 2017, Ottawa, ON, Canada, 2018, pp. 27–34.

[9] A. Potsch, F. Haslhofer, P. Albert, and F. Haslhofer, "Practical Limitations for Deployment of LoRa Gateways", in 2017 IEEE International Workshop on Measurement and Networking (M&N), Naples, Italy, 2017, pp. 1–6.

[10] LoRaWAN, https://www.mobilefish.com/

[11] A. M. Yousuf, E. M. Rochester, B. Ousat and M. Ghaderi, "Throughput, Coverage and Scalability of LoRa LPWAN for Internet of Things", 2018 IEEE/ACM 26th International Symposium on Quality of Service (IWQoS), Banff, AB, Canada, 2018, pp. 1-10.

Mutual Authentication Scheme in ICN-based Wireless Sensor Networks

Takafumi Taya, Eishin Nagaoka, and Osamu Mizuno

Department of Electrical Engineering and Electronics, Graduate School of Engineering, Kogakuin University, Tokyo, Japan
E-mail: cm22032@ns.kogakuin.ac.jp, cm21037@ns.kogakuin.ac.jp, omizuno@cc.kogakuin.ac.jp

Abstract

ICSN (Information-Centric Networking based Wireless Sensor Networks) enable to provide multiple IoT (Internet of Things) services. ICSN realizes low-power consumption of sensor devices and load distribution methods at a sink node. In this paper, we propose a mutual authentication scheme in ICSN to prevent attacks from malicious devices.

1. Introduction

When new IoT services are introduced, new sensor networks need to be built. Whenever the number of sensor networks and devices increases with the number of services, it is costly to manage and operate them. To solve this problem, we have proposed ICSN (Information-Centric Networking based Wireless Sensor Networks). As a platform of ICSN, we have proposed ICSNP (ICSN Platform) [1]. ICSN retains the cache function in the sensor devices. Previous research has shown that retrieving sensor data from a cache reduces the number of communications and enables low-power consumption of sensor devices. From a point of security view, if a malicious node is present in the network, the user may obtain data with abnormal or invalid values. In this paper, we propose a mutual authentication scheme in ICSN to solve the security issues.

2. Motivation

If a malicious device is placed on ISCN, a sink node may connect with the malicious device and retrieve data indicating invalid or abnormal values. Also, it is possible that data indicating cached invalid or abnormal values may be circulated by subsequent Interests. To solve the problem, we propose a mutual authentication scheme in ICSN.

3. Mutual Authentication Scheme in ICSN

ICSN assumes a closed network with multiple sink nodes sensor nodes. Cluster head nodes (CH) are chosen from sensor nodes. The administrator manages them. The proposal method consists of two phases. The 1st phase is CH discovery and the 2nd phase is authentication and registration of the new sensor. As a prerequisite, the Key Manager (KM) and a sensor device shares 128-bit shared secret information. In the first phase, the new device broadcasts an Interest message to determine the CH to send the authentication request. The CH with the earliest data reply to Interest is determined as the destination of the authentication request. Figure 1 shows the second phase. New devices and the KM perform challenge-and-response authentication using shared secret information. At first, the ID of the new device is sent to the KM. When the KM receives the

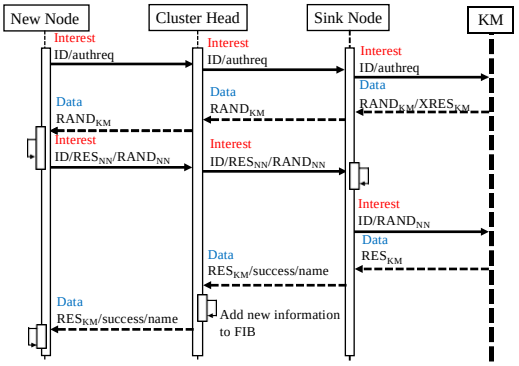

Fig.1.Mutual Authentication Scheme in ICSN.

Interest, it generates a random number and sends it back as Data. This data also contains random numbers and XRES (Predicted Response). XRES is cached in the Sink Node and only random number is sent to the new device. The new device calculates the RES (Response) with the random number generated by the KM and the shared secret information. It replies the RES and the random number to authenticate the KM to the KM. The Sink Node that receives the Interest compares XRES and RES and forwards the Interest. The KM calculates the RES and sends it as Data to the new device. The new device compares the RES of the KM with the XRES, and if the result is correct, sends Data to subsequent Interest.

4. Conclusion

In this paper, we proposed a mutual authentication scheme in ICSN to deal with malicious nodes in the network. In the future, we will implement and evaluate the proposed method.

Acknowledgements

Part of this research was funded by Japan Society for the Promotion of Science (JSPS) research grant JP22K12014.

References:

[1] K.Kimura and O.Mizuno, “Performance requirements evaluation of network functions in information-centric networking based wireless sensor network,” IEEJ Trans. Information and Systems (in Japanese), vol. 140, no. 6, pp. 583–584, June 2020.

Frequency Utilization Efficiency Improvement by Spectrum Suppressed Transmission with 16QAM

Teppei Kanke, Takatoshi Sugiyama

Graduate School of Engineering, Kogakuin University, Tokyo, Japan
E-mail: cm2104@ns.kogakuin.ac.jp

Abstract

We propose spectrum suppressed transmission using 16QAM for frequency utilization efficiency improvement. As a computer simulation result, at SNR = 15dB, frequency utilization efficiency can be increase up to 2.59bit/sec/Hz with suppression rate of 24%.

Introduction

In recent years, the frequency bands for assigning new wireless systems are exhausted. To solve this problem, spectrum suppressed transmission[1] has been proposed. It reduces its required bandwidth while maintaining throughput as possible to increase frequency utilization efficiency. However, conventional scheme has used QPSK only. In this paper, we propose spectrum suppressed transmission applied by 16QAM (Quadrature Amplitude Modulation) and its frequency utilization efficiency performances are evaluated quantitatively by computer simulations.

Simulation Configuration

The block diagram of the proposed scheme is shown in Fig. 1. The modulation is 10M symbol/sec single carrier 16QAM. The attenuation characteristics of the root roll-off filters are raised cosine function with the roll-off factor α = 0.2. The suppression filter's attenuation characteristic is same to the root roll-off filters, equivalent to $\alpha = 0.2$. The suppression rate r_s is defined by Eq. (1) using the Nyquist bandwidth f_N and the suppressed bandwidth $f_s$for 3dB bandwidth.

$$r_s = \frac{f_N - f_S}{f_N} \qquad (1)$$

The FEC (forward error correction) is LDPC coding[2] with coding rate of 1/2 and sum-product decoding[3] with maximum number of iterations of 10.

Simulation Results

Fig. 2 shows relationship between suppression rate $r_s$and frequency utilization efficiency at SNR = 15dB. In the case of 16QAM, frequency utilization efficiency is increased up to 2.59bit/sec/Hz by suppression with $r_s = 24\%$.

Conclusion

In this paper, we have proposed a new spectrum suppressed transmission scheme applied by 16QAM. As the result, it has been shown that the frequency utilization efficiency can be increased up to 2.59bit/sec/Hz with suppression rate of 24% at SNR = 15dB.

References:

[1] S. Omata, et al., "System Throughput Gain by New Channel Allocation Scheme for Spectrum Suppressed Transmission in Multi-Channel Environments over a Satellite Transponder," IEICE Trans. Commun., vol. E103-B, no. 10, pp. 1059-1068, Oct. 2020.

[2] R. Gallager, "Low density parity check codes," IRE Transactions on Information Theory, vol. 8, no. 1, pp. 21-28, Jan. 1962.

[3] Sae-Young Chung, et al., "Analysis of sum-product decoding of low-density parity-check using a Gaussian approximation," IEEE Trans. Information Theory, vol. 47, no. 2, pp. 657-670, Feb. 2001.

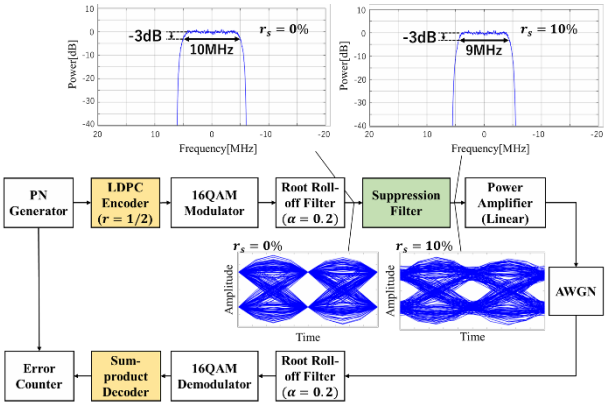

Fig. 1. The block diagram of the proposed scheme.

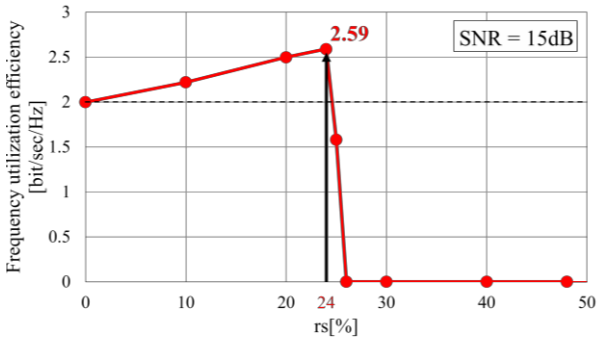

Fig. 2. Relationship between r_s and frequency utilization efficiency.

A Study on Performance of CPU Clock Rate Control Based on Application Monitoring

Kota Kumakura*, Takeshi Kamiyama, Masato Oguchi***, and Saneyasu Yamaguchi***

*Electrical Engineering and Electronics, Kogakuin University Graduate School
E-mail: {cm22022@ns, sane@cc}.kogakuin.ac.jp

** School of Information and Data Sciences Nagasaki University
E-mail:kami@nagasaki-u.ac.jp

*** Department of Information Sciences Ochanomizu University
E-mail:oguchi@is.ocha.ac.jp

Abstract

Android smartphones are an important platform with a market share of over 70% of all smartphones worldwide. The devices have a trade-off between power consumption and performance. The challenge is to improve application performance while reducing power consumption. This paper provides an analysis focusing on CPU utilization per function during application execution.

Introduction: Saving power consumption and improving performance are important themes in smartphones. Usually, both of these conflicting two things cannot be satisfied simultaneously. That is, an increase in CPU clock rate affects positively power saving and negatively the application performance. The reverse is also true. A decrease in the rate affects negatively and positively the performance and power consumption, respectively. Therefore, the CPU clock rate should be increased only when large CPU resources are required.

Related Work: In the work of [1], we proposed a concept of adjusting the CPU clock rate by predicting the CPU usage in the near future by monitoring method calls in the foreground application. The method increases and decreases the clock rate at beginning of CPU-consuming and non-CPU-consuming methods, respectively. The proposed method assumes that the CPU is intensively consumed in the executions of certain methods and it is rarely consumed in certain methods. In addition, these methods must be time-consuming because CPU clock rate changes for short method calls cause frequent CPU clock rate changes.

In the work of [2], we revealed the method calls of a practical smartphone application. We then showed that some method calls consumed intensive CPU resources and took a non-short time. In other words, the proposed concept is useful for these method calls in a practical application. However, these existing works have not evaluated whether such method calls are conducted frequently. In this paper, we investigate how frequently such method calls (i.e., calls with high CPU utilization and short execution time) are executed in an actual Android application and discuss whether the proposed concept is useful in many situations.

Evaluation: Table 1 shows detailed information on the top five method calls in evaluating consumed time [2]. The information is composed of the anonymized names of methods, the number of calls, the CPU usage during the calls, the execution times of the calls, the number of calls divided by the number of all calls, and the consumed time of these calls divided by the all consumed times.

The results in the table indicate that these method calls take a huge part in all the consumed time. Namely, optimizing the CPU clock rate for these method calls may significantly affect the device's total application performance and power consumption. In particular, method *a()* consume the time larger than half of all the consumed time.

Table 1. Detailed information on time-consuming method calls.

Method	num. of calls	CPU usage[%]	Execution time[s]	Call count / All Method [%]	Execution time / All time[%]
a()	7407	3.24	126.39	12.95	61.05
b()	109	3.19	9.47	0.19	4.57
c()	112	3.49	5.00	0.20	2.42
d()	1	0.95	0.88	0.00	0.43
e()	107	0.93	0.44	0.19	0.21

References:

[1] K. Kumakura, A. Sonoyama, T. Kamiyama, M. Oguchi and S. Yamaguchi, "Observation of Method Invocation in Application Runtime in Android for CPU Clock Rate Adjustment," 2021 Ninth International Symposium on Computing and Networking Workshops (CANDARW), 2021, pp. 481-483, doi: 10.1109/CANDARW53999.2021.00090.

[2] K. Kumakura, T. Kamiyama, M. Oguchi and S. Yamaguchi, "Stack-based Method Invocation and Return Monitoring in ART for CPU Clock Rate Adjustment," 2022 IEEE International Conference on Consumer Electronics - Taiwan, 2022, pp. 563-564, doi: 10.1109/ICCE-Taiwan55306.2022.9869064.

Acknowledge

This work was supported by JSPS KAKENHI Grant Numbers 21K11854 and 21K11874.

A Study on a Modified Vision Transformer Model for Image Processing

Tatsuhiko Ikeda* and Hidetoshi Saito

Graduate School of Engineering, Kogakuin University, Tokyo, Japan
E-mail: cm22005@ns.kogakuin.ac.jp

Abstract

Generative Adversarial Networks (GANs) are widely used in image, video and voice generation, etc. GANs belong to the family of Generative models and generate new synthetic data that resembles real data by pitting two neural networks, namely, the *Generator* and the *Discriminator* against each other. The quality and resolution of images produced by GANs are improving rapidly. Nowadays, *Vision Transformers*[1] (ViTs) are becoming more popular and dominating technique for various vision tasks. If we compare ViTs to *Convolutional Neural Networks* (CNNs), ViTs give more promising results and outperforms CNNs. In this research, we consider that improving the accuracy (correct response rate) of the Discriminator leads directly to generate a high-quality image with an appropriate resolution. Hence, we propose a modified ViT and introduce this modified ViT to improve the quality and resolution of GAN generated images.

1. Introduction

GANs attempt to learn a distribution of a probability density function (PDF) from a training data set and then GANs generate new samples that is drawn from the identical distribution of the PDF. GANs put in competition with the Generator and the Discriminator each other and generate new composite data that is analogous to original real data. The Generator (g) tries to capture the true data distribution for generating new samples. On the other hand, the Discriminator (d) is usually a binary classifier that tries to discern actual samples from fake generated samples as precisely as possible. However, it is known that tuning various GAN parameters are extremely difficult due to its instability and it is very prone to miss modes during the GAN training (learning) phase, which is called *Mode collapse*. Moreover, there exits the other problems for any GAN models such as non-convergence, diminished gradient, overfitting, etc.

2. Proposed GAN model

We propose a following modified ViT model. At first, we change the multi-head attention layers and to the self-attention layers in both of the encoder and decoder. Secondly, we replace two full connected convolution layers by a single CNN layer in all residual connections.

3. Simulation and Evaluation Methods

We use "102 Category Flower Dataset" consisting of 102 flower categories as real data set with 8,192 items of image data[2]. Then, our proposed Vit model (vit) is compared with the conventional Generative models as follows; the CNN model (cnn), the SE-block ("Squeeze-and-Excitation" block) model (se_block) and the SAGAN (Self-attention GAN) model (sa).

If we evaluate each GAN, the GAN output images are evaluated by using following evaluation indices as Fréchet Inception Distance (FID), image equality, and subjective visual inspection between low quality (1) and high quality (5). We get all evaluation values and loss functions for each model within 30 epochs and a batch size of 32. We select an optimum image based on subjective visual inspection which has best diversity and quality after 25 epochs. If we decide the optimum image, we can record the number of epochs, the FID score and the number of iterations every second at that time.

4. Simulation Results

Table 1. Evaluation results for various GAN models.

model	fid(epoch)	equality	subjective-evaluation	time(it/s)
d:cnn , g:cnn	96.96(26)	0.43	diversity: 2, quality:2	4.14
d:sa , g:sa	107.17(30)	0.63	diversity: 1, quality:1	3.78
d:se_block , g:cnn	105.30(30)	0.62	diversity: 2, quality:4	4.31
d:se_block , g:sa	111.66(30)	0.48	diversity: 4, quality:4	4.03
d:vit , g:cnn	112.25(30)	-0.19	diversity: 1, quality:1	1.65
d:vit , g:sa	124.09(27)	0.065	diversity: 4, quality:4	1.66

Table 1 shows the simulation results of each model at 30 epochs. As can be seen from Table 1, if we use a pair of the SAGAN and SE block models or the SAGAN and modified ViT models for the Generator and the Discriminator, both pairs of the Generator and the Discriminator attain the optimum image quality and diversity from a subjective point of view. If we compare objective indices between these two pairs of the Generator and the Discriminator, it is found that we get a remarkable lower equality value if we use the modified ViT model for the Discriminator.

5. Conclusion

In this report, we propose a modified ViT model. From the simulation results, we can generate high quality and diversity image which has an exceedingly small equality value if we use a pair of SAGAN and this ViT models for the Generator and Discriminator in the given Generative model.

References:

[1] A. Dosovitskiy, *et al*., "An image is worth 16×16 words: Transformers for image recognition at scale," ICLR 2021, 24 Jan 2021.
[2] 102 Category Flower Dataset, https://www.robots.ox.ac.uk/~vgg/data/flowers/102/.
[3] Squeeze-and-Excitation Networks, https://arxiv.org/abs/1709.01507.
[4] Self-attention Generative Adversarial Networks, https://arxiv.org/abs/1805.08318.

A Study on Deletion of SNIs for Service Identification

Ryo Asaoka*, Akihiro Nakao, Masato Oguchi***, and Saneyasu Yamaguchi***

*****Electrical Engineering and Electronics, Kogakuin University Graduate School
E-mail: {cm22002@ns, sane@cc}.kogakuin.ac.jp

******Interfaculty Initiative in Information Studies, The University of Tokyo
E-mail: nakao@nakao-lab.org

*******Department of Information Sciences, Ochanomizu University
E-mail: oguchi@is.ocha.ac.jp

Abstract

Service Identification is important for various purposes such as providing the zero-rating service. We proposed a method to improve identification accuracy by removing SNIs with low occurring probability. However, this study did not investigate the number of removed SNIs from the data for identification. In this paper, we focus on the method to improve service identification accuracy by removing SNIs with low occurring probability and discuss the number of removed SNIs.

Service identification is useful for a variety of purposes. For example, it enables the zero-rating service that does not charge communication fees for communications to specific services, or preferential forwarding of packets of important services in heavy congestion caused by a large-scale disaster.

However, since most of the recent communications are encrypted using TLS, it is not easy to identify services by analyzing the payload of packets. For these encrypted communications, a method to identify services by analyzing the unencrypted part of TLS communications was proposed [1]. In the preliminary learning phase, this method investigates the relationship between a service and the SNIs that occur in a set of TLS sessions established when connecting to the service. In the identification phase, the method compares the occurring SNIs with the SNIs investigated in the preliminary learning phase, and identifies the service based on the occurring SNIs and preliminary training data. However, some SNIs are not useful for identification. In the work of [2], a method was proposed to improve identification accuracy by removing SNIs with low occurring probability from the data used for identification. The performance evaluations showed that this improved identification accuracy. However, this study did not investigate the number of removed SNIs from the data for identification.

In this paper, we focus on a method to improve service identification accuracy by removing SNIs with low occurring probability and discuss the number of removed SNIs.

In the evaluation in the work of [2], service the identifications for Yahoo's ten services were conducted by the original method [1] and improved method [2]. The evaluation demonstrated that the accuracies of the identification of Yahoo Finance, Yahoo news, Yahoo Sports, and Yahoo style were significantly improved. Table 1 described the accuracies of both methods and the number of deleted SNIs by the improved method. Each method used 990 SNIs for identification.

The table shows that many of SNIs (around 90%) were deleted and the services were identified remarkably more accurately. This indicates that most of SNIs are not effective for identification and the information based on sets of SNs was highly redundant. In other words, we can expect that the accuracy of these methods can be largely improved by suitably choosing SNIs.

Table 1. Service Identification results (Accuracies, number of deleted SNIs)

Service	Accuracies[%]		Number of deleted SNIs
	Original	Improved	
Yahoo Finance	10	60	898.2
Yahoo News	10	90	878.4
Yahoo Sports	10	80	881.7
Yahoo Style	10	50	882.6

References:

[1] H. Yamauchi, A. Nakao, M. Oguchi, S. Yamamoto, and S. Yamaguchi, "Service Identification Based on SNI Analysis," IEEE Consumer Communications & Networking Conference (CCNC 2020), Work-in-progress paper, 2020.

[2] Ryo Asaoka, Akihiro Nakao, Masato Oguchi, Saneyasu Yamaguchi, "Accuracy Improvement by Occurrence Probability of Service Identification based on SNI," 2022 Ten International Symposium on Computing and Networking Workshops (CANDARW), 2022.

Acknowledge

This work was supported by JSPS KAKENHI Grant Numbers 21K11854 and 21K11874.

A Study on Mutual Interference with Islanding Detection Function in Inverters with Inertia Function

Dehui Li*, Yasuhiro Noro

Electrical Engineering and Electronics Program, Kogakuin University, Japan
E-mail: cm21059@g.kogakin.jp

Abstract

This paper verifies that changes in signals such as voltage and frequency occur under the islanding condition by active method islanding detection function. Compared to the results of an inverter with inertia function, the mutual interference of multiple units (two units) was confirmed.

Introduction

With the mass introduction of the renewable energy, the amount of those power generation cannot be controlled, and it cannot be possible to balance with demand, moreover, the irregular output change may cause frequency fluctuations. Thus, this time the inverter is equipped with an inertial function so that it can be controlled in the same way as a synchronous generator used in conventional power generation methods such as thermal power generation.

There is a concern that the signal of the islanding detection function, which may interfere with the inertial function and other functions of the inverter during islanding condition [1]. Therefore, it is of great practical significance to study how to detect islanding conditions when there are multiple inverters.

Target system

The inverter under consideration is a model with an inertia function that connects a storage device to the DC side as shown in *Fig. 1* and enables control equivalent to that of a synchronous generator.

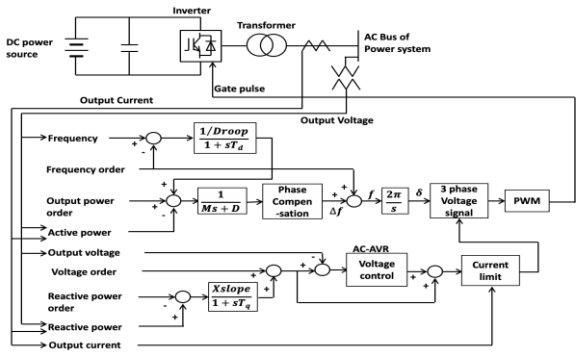

Fig. 1. Inverter with inertial function

The inverters capacity was set to 1MW, and conditions were set for a high-voltage (6.6kV) interconnection. Constant impedance was installed on the high-voltage bus bar so that both active and reactive power flows at the interconnection point with the grid would be almost zero[2]. Simulation of instantaneous values using EMTP (ATPDraw) was conducted to confirm the response of various quantities.

Simulation results

Reactive power fluctuation method: *Fig. 2* shows frequency change. Two inverters of this method are installed on the same system, If the inverters were disconnected from the system at 5.3 seconds, the frequency change exceeded 0.2 to 0.4 Hz [3], which is the criterion for islanding detection.

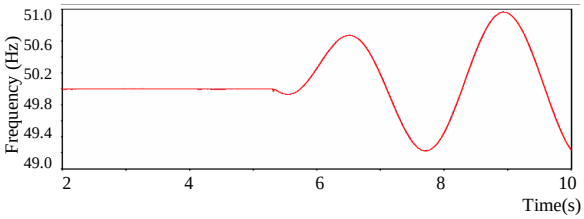

Fig. 2. Simulation result with reactive power fluctuation method

Q Control Mode Frequency Shift method: *Fig. 3* shows frequency change rates during the time variation. The inverters were disconnected from the system at 2 seconds. The criterion is 0.08~0.8 Hz/s [3], and it is considered to be detectable because it becomes larger than this value at about 0.5~1.5 seconds after the transition to islanding detection situation.

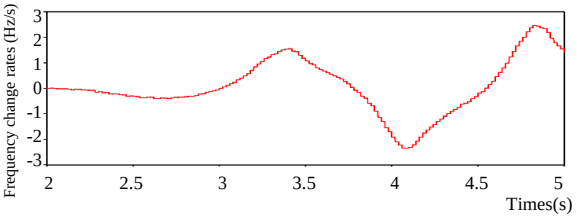

Fig. 3. simulation result with Q control mode frequency shift

Conclusion

By using two active methods which can detect if the system is in islanding condition where there are two inverters.

References

[1] Y. Noro, *IEEJ Transactions on Power and Energy*, **138**,11,854-861, 2018.

[2] T. Miyashiro, Y. Noro, *Annual Meeting of the Institute of Electrical engineering of Japan, 2020.*

[3] Grid Interconnection Expert Group, *Japan Electric Association System connection protocols*, 2019.

CO_2 Gas Sensing by In_2O_3-Based Thin-Film Transistors

Ayumu Nodera, Shun Mori and Shinya Aikawa

Department of Electrical and Electronic Engineering, Kogakuin University
2665-1 Nakano-machi, Hachioji, Tokyo 192-0015, Japan.
E-mail: aikawa@cc.kogakuin.ac.jp

Abstract

CO_2 gas sensors operating at relatively low temperature are demanded for many applications. In_2O_3 semiconductor is a promising candidate in terms of material processability and gas sensitivity. In this study, we fabricated In_2O_3-based thin-film transistors (TFT) and investigated their CO_2 sensitivities at 150 °C. Pure In_2O_3 and In_2O_3 co-sputtered with CaO (In_2O_3:Ca) films were prepared as an active channel. The In_2O_3:Ca TFT showed better CO_2 sensitivity, which the drain current was approximately 3 times higher compared to the initial N_2 environment. The In_2O_3:Ca films has a reactive (400) plane-rich crystal structure, thus, high CO_2 sensitivity was obtained compared to the In2O3 TFT with a stable (222) plane.

1. Introduction

Recently, CO_2 detection is strongly demanded for agricultural-, environmental-, and medical-uses, including daily life nowadays [1]. Although there are various kinds of CO_2 gas sensors, semiconductor type has some advantages in terms of miniaturization and cost-effectiveness. Because CO_2 is very stable, low sensitivity and high operation temperature above 300 °C are critical issue in a conventional resistive-type sensor [2]. To improve the sensor responses, basic oxides or alkaline earth oxides, which exhibit strong interaction with CO_2, have been utilized [3]. Typical thin-film transistor (TFT) is suitable for gas sensor application because of large surface area. In_2O_3-based materials are commonly used as a TFT channel and has unique features such as structural flexibility, which can incorporate impurities with different ionic radius into their matrix [4,5]. In addition, since they have active surfaces [6], high sensitive NO_x gas sensor operated at room temperature has been demonstrated [7]. However, there are still difficult to detect CO_2 gas with high sensitivity. In this study, we fabricated TFTs having pure-In_2O_3 or co-sputtered In_2O_3/CaO (In_2O_3:Ca) channel, and compared their I-V characteristics under CO_2 ambient. We found that crystal phase of the In_2O_3 co-sputtered with CaO has (400)-rich plane. Here, CO_2 sensitivity of the In_2O_3-based TFTs depending on the crystal plane will be discussed.

2. Experiments

A bottom-gate TFT was fabricated on a highly doped n^+-Si substrate (resistivity: 0.02 Ω cm) with a thermally grown oxide layer (SiO_2 thickness: 200 nm). Before the deposition of the In_2O_3 active channel, the substrate was ultrasonically cleaned in acetone and isopropyl alcohol and irradiated using an excimer lamp (wavelength: 172 nm) for 15 min to remove organic residue. The In_2O_3 and co-sputtered In_2O_3/CaO films were then deposited at room temperature by RF magnetron sputtering using the 4N purity, 3 inch diameter In_2O_3 ceramic target and CaO pellets. The $O_2/(Ar + O_2)$ ratio, RF power, and total pressure during sputtering deposition were fixed at 25%, 50 W and 0.24 Pa, respectively. The background pressure was evacuated below -4×10^{-4} Pa. By optimizing the deposition time, the thickness of the active channel formed through a stencil shadow mask was 20 nm. The channel width (W) was fixed at 1000 µm, while the channel length (L) varied between 50 and 350 µm. A schematic diagram of the TFT and an optical microscope image in top view are shown in Fig. 1(a). The fabricated TFTs were characterized in a vacuum prober in an inert N_2 and then the environment was replaced to CO_2 atmosphere. The TFT was heated at 150 °C during measurement, and all environments were atmospheric pressure during TFT characterization. The surface morphology of the films was observed by an atomic force microscopy (AFM, Olympus LEXT OLS4500). The crystalline structure of the In_2O_3 and In_2O_3:Ca films was determined using a X-ray diffractometer (XRD, Rigaku SmartLab) with a CuKα source at a power of 40 kV/30 mA

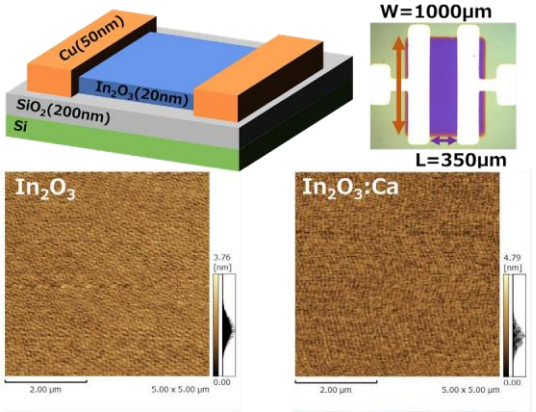

Fig. 1. (a) Schematic diagram of fabricated TFT, and the optical microscope image in top view. (b) and (c) AFM images of In_2O_3 and In_2O_3:Ca thin films, respectively.

3. Results and discussion

Figures 1(b) and (c) show AFM images of the In_2O_3 and In_2O_3:Ca films, respectively. The root mean square roughness for In_2O_3 and In_2O_3:Ca were 0.416 and 0.472 nm, respectively, which was no obvious morphological changes in both films. Figure 2 shows the I-V characteristics of the In_2O_3:Ca TFT under N_2 and CO_2 ambient. The maximum drain current ($I_{D,max}$) was 0.078 μA in the N_2 atmosphere, whereas it increased 2.8 times, 0.223 μA, in the CO_2 atmosphere. This means CO_2 gas was successfully detected. We suggest that increase in the $I_{D,max}$ under CO_2 ambient is due to the desorption of surface hydroxyl groups, which act as electron traps [9]. When CO_2 molecules reached on the surface, they react with OH^- and then become HCO_3^- as follows [10].

$$CO_{2(gas)} + OH^-_{(ads)} \rightarrow HCO_3^-_{(gas)} \quad (1)$$

Due to decrease in the trap species on the In_2O_3:Ca surface caused by the reaction with CO_2, thus, $I_{D,max}$ was increased.

To investigate the crystal structure of the channel, we performed XRD analysis. Figure 3 shows the XRD patterns of In_2O_3 and In_2O_3:Ca films. Usually, bixbyite In_2O_3 has (222) plane dominant structure, and the highest intensity at the (222) plane is obtained in most cases. As for the In_2O_3:Ca, the peak intensity at (400) was 1.2 times larger than that at (222), indicating that the (400) plane is majority in this film.

Figure 4 shows crystal structures of bixbyite In_2O_3 projected by the [121] and [010] directions. The (111) surface is a non-polar surface composed of both In cations and O anions. In contrast, (100) surface, which is a polar surface consisting only of In cations. This means that the (100) surface has higher ionicity than the (111) surface because of the cation polarization, resulting that more surrounding oxygen atoms can be chemisorbed on the (400) plane [11]. In addition, high surface energy of polar oxides can facilitate to remove hydroxyl groups in a reducing atmosphere [8]. The polar (100) surface has high surface energy, thus, adsorbed hydroxyl groups were easily desorbed again from the surface [12]. We suggest that the desorption of hydroxyl groups on the (400)-rich In_2O_3:Ca TFT surface exposure to reducing CO_2 atmosphere causes the current variation.

4. Conclusions

We fabricated TFTs with In_2O_3 and In_2O_3:Ca channels and compared their CO_2 sensitivities at 150 °C. The electrical properties showed that the $I_{D,max}$ of the In_2O_3:Ca TFT under the CO_2 environment increased 2.8 times higher than under N_2 ambient. This is due to the desorption of surface hydroxyl groups on the reactive In_2O_3(400) plane. The results showed that In_2O_3 co-sputtered with CaO is useful for fabrication of In_2O_3 thin-film with CO_2 sensitive (400)-rich surface.

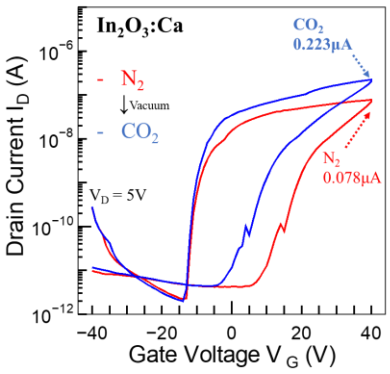

Fig. 2. Transfer characteristics of the fabricated In_2O_3:Ca TFT in N_2 and CO_2 environments. The electrical measurements were performed in the dark and atmospheric pressure conditions.

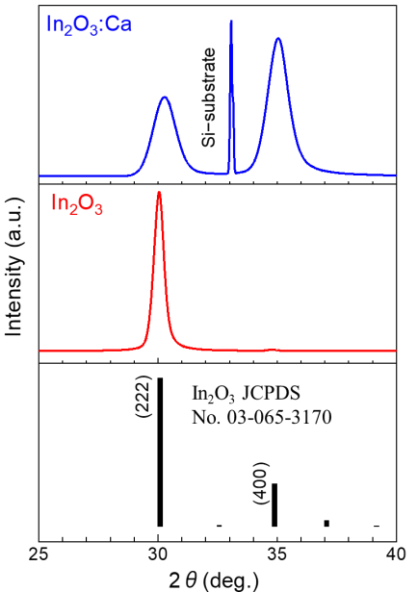

Fig. 3. X-ray diffraction pattern of the fabricated In_2O_3 and In_2O_3:Ca thin films.

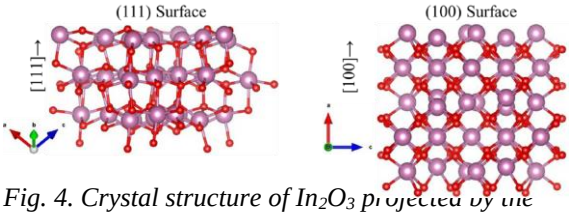

Fig. 4. Crystal structure of In_2O_3 projected by the [121] and [010] directions.

References:

[1] T. Ishihara, Electrochemistry. **69**, 3 (2001).
[2] P. Matheswaran, R. Sathyamoorthy, and K. Asokan, Sens.Actuators B Chem. **177**, (2013)
[3] A. Prim, E. Pellicer, E. Rossinyol, F. Peiro, A.

Cornet, and J. Morante, Adv. Funct. Mater. **17**, 15 (2007).
[4] S. Aikawa, T. Nabatame, and K. Tsukagoshi, Appl. Phys. Lett. **103**, 172105 (2013).
[5] F. Utsuno, H. Inoue, I. Yasui, Y. Shimane, S. Tomai, S. Matsuzaki, K. Inoue, I. Hirosawa, M. Sato, and T. Honma, Thin Solid Films. **496**, 1 (2006).
[6] G. Korotcenkov, V. Brinzari, J. Stetter, I. Blinov, and V. Blaja, Sens. Actuators, B. **128**, 1 (2007).
[7] M. Vijjapu, S. Surya, M. Zalte, S. Yuvaraja, M. Baghini, and K. Salama, Sens. Actuators, B. **331**, 129450 (2021).
[8] D. Cappus, M. Habel, E. Neuhaus, M. Heber, F. Rohr, and H. Freund, Surf. Sci. **337**, 3 (1995).
[9] D. Kim, S. Yoon, Y. Jeong, Y. Kim, B. Kim, and M. Hong, Appl. Phys. Express, **5**, 021101 (2012).
[10] S. Joshi, L. Jones, Y. Sabri, S. Bhargava, M. Sunkara, and S. Ippolito, J. Colloid Interface Sci. **558**, 15 (2020).
[11] H. Zhang, A. Walsh, R. Catlow, V. Lazarov, and R. Egdell, Nano Lett. **10**, 9 (2010).
[12] V. Brinzari, G. Korotcenkov, and V. Matolin, Appl. Surf. Sci. **243**, 1 (2005).

Electrical property and valence band offset in conductive MgNiO on sapphire substrates

M. Murayama[1*], A. Ishikawa[1], T. Yamaguchi[1], T. Honda[1],
K. Sasaki[2], A. Kuramata[2], and T. Onuma[1]

1. Department of Applied Physics, School of Advanced Engineering and Graduate School of Engineering, Kogakuin University, Tokyo, Japan
2. Novel Crystal Technology, Inc., Saitama, Japan
E-mail: cm21050@ns.kogakuin.ac.jp

Abstract

$Mg_xNi_{1-x}O$ (x=0~0.39) alloy films on c-sapphire were deposited by RF magnetron sputtering. The films for Mg composition below 32.1 mol% showed p-type conductivity having resistivity 20~2900 mΩ·cm. Valence band offset was determined to be 1.65±0.2 eV for the $Mg_{0.24}Ni_{0.76}O$/sapphire interface.

Ultra-wide bandgap semiconductors are recognized as novel materials for power electronics and deep UV LED. For further improvements on device performance, integration of ultra-widegap p-type layer is indispensable. NiO has a rocksalt structure with bandgap energy E_g of 3.7 eV. It shows p-type conductivity, intrinsically. MgO has the same crystal structure with E_g of 7.7 eV. MgNiO alloys are thus candidate materials to develop ultra-wide bandgap p-type layer. In this study, MgNiO films were deposited on sapphire substrates by RF magnetron sputtering, and their electrical property and band-offset were evaluated.

42-73-nm-thick $Mg_xNi_{1-x}O$ films were deposited by RF magnetron sputtering (Canon-Anelva: L-332-FH) at an ambient temperature. A 99.9 mol% purity NiO sintered target and c-plane sapphire substrate were set with a distance of 3 cm. To alloy with MgO, the NiO target was co-sputtered with 0 to 9 pieces of 10×10 mm^2 square-shaped 99.9% purity MgO substrates, which were placed on the target as shown in Fig. 1. RF power and oxygen flow rate were fixed with 150 W and 5 sccm, respectively. Sputtering pressure was fixed at 0.75 Pa. Resistivity ρ was determined by four-point probe method at room temperature. Mg composition was quantified by energy dispersive X-ray spectrometry. Carrier type was determined by the Seebeck effect measurement. The valence band offset (ΔEv) at the MgNiO/sapphire interface was determined by X-ray photoelectron spectroscopy (XPS).

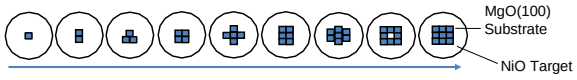

Fig. 1. Configuration of MgO substrates on the target.

Sputtering rate and ρ are plotted as a function of Mg composition x in $Mg_xNi_{1-x}O$ in Fig. 2. As shown, ρ increased monotonically in a range 20-2900 mΩ·cm with maintaining the sputtering rate around 400 nm/h. We confirmed a p-type conductivity except for x>32%. The XPS spectra for the sapphire substrate, 70-nm-thick $Mg_{0.24}Ni_{0.76}O$ film, and 1.5-nm-thick $Mg_{0.24}Ni_{0.76}O$/sapphire interface were measured. As schematically shown in Fig. 3, ΔEv at the $Mg_{0.24}Ni_{0.76}O$/sapphire interface was determined to be 1.65 eV. The value was smaller than ΔEv=2.31±0.2 eV for NiO/Sapphire interfaces [1]. The results indicate that the MgNiO alloys are good candidates for the ultra-wide bandgap p-type layer.

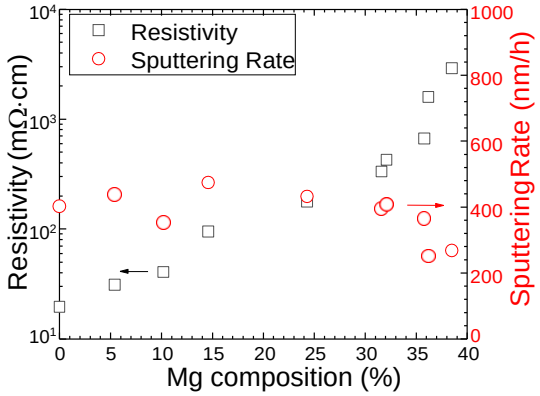

Fig. 2. Sputtering rate and resistivity ρ as a function of Mg composition x in MgxNi1-xO films.

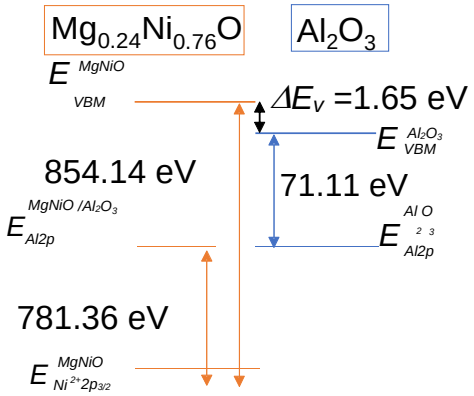

Fig. 3. Parameters used for determining the ΔEv.

The authors would like to thank Prof. S. Aikawa for his help with the sputtering equipment. This work was supported in part by the New Energy and Industrial Technology Development Organization (NEDO), subsidized by project No. 0624003.

References:

[1] S. D. Singh *et al.*, Appl. Surf. Sci. 389, 835839 (2016).

Growth and characterization of AlGaN and multiple quantum wells with varying III/V ratios by RF-MBE

Mahiro Hayasaki*, Tomoya Yamaguchi, Tomohiro Yamaguchi, Tohru Honda, and Takeyoshi Onuma

Department of Electrical Engineering and Electronics, Graduate School of Engineering,
Kogakuin University, Hachioji, Tokyo, Japan
*E-mail: cm21044@g.kogakuin.jp

Abstract

Recently, UV-C lights are getting explosive attention for UV sterilization. $Al_xGa_{1-x}N$ is the most promising material to realize semiconductor-based UV-C emitter. In this study, high Al composition $Al_xGa_{1-x}N$ films with varying III/V ratios and $Al_xGa_{1-x}N$/AlN (x>0.7) MQWs were grown on AlN templates by RF-MBE. III-rich condition was preferable to observe near-band-edge emission. However, observation of broad peaks and shoulders indicated that the composition fluctuation was considerable even in the ultra-thin well layers.

$Al_xGa_{1-x}N$ is the most promising material to realize semiconductor-based UV-C emitter. In RF-plasma-assisted molecular beam epitaxy (RF-MBE) of high Al composition $Al_xGa_{1-x}N$, III-rich growth is suffered from drawback due to the difference in the bonding energy of Ga-N and Al-N [1,2]. In this study, high Al composition $Al_xGa_{1-x}N$ films with varying Group III and Group V supply ratios and $Al_xGa_{1-x}N$/AlN (x>0.7) MQWs were grown by RF-MBE. Crystallinity and optical properties were evaluated, and the effect of composition distribution on emission properties was investigated.

75-555-nm-thick $Al_xGa_{1-x}N$ films were grown on 425-nm-thick c-plane AlN on Al$_2$O$_3$ templates [3]. A 100-200-nm-thick AlN buffer layer growth was followed by 5 or 10 periods of MQW growth. The barrier layer thickness was fixed at 10 nm, and the well layer was either 2 or 4 nm. RF power was fixed at 150 W. Nitrogen gas flow rate was 0.3 sccm. Substrate temperature was 775°C. The V/III ratio was varied by changing in the Group III supply. Photoluminescence (PL) spectra were measured at room temperature (RT) using a frequency-quintupled (213 nm) Q-switched YAG:Nd laser.

XRD θ-2θ patterns near the 0002 diffraction peak for Al$_x$Ga$_{1-x}$N films grown under near-stoichiometric (abbr. as near-stoichi.) and III-rich conditions are shown in the lower part of Fig. 1. The $Al_xGa_{1-x}N$ peaks of the films grown under III-rich conditions tend to be broad. Results for the MQW are shown in the upper part of Fig. 1. Satellite peaks were observed, and the peak separation reflect the change in the period. Fig. 2 shows the PL spectra. Note that the PL from the AlN template was observed as double peaks in the wavelength range above 300 nm. Near-band-edge emission (NBE) was observed in the wavelength range below 300 nm. For the $Al_xGa_{1-x}N$ films, a NBE peak was observed at 4.7 eV only for the III-rich film. The MQWs show similar trend, i.e., PL intensity was higher by employing the III-rich condition. However, observation of broad peaks and shoulders indicates that even in ultra-thin films, the composition is non-uniform under the III-rich conditions.

The authors grateful to Prof. A. Yoshikawa of Chiba University for his continuous encouragements.

References:

[1] D. Welch *et al.*, Sci. Rep. **8**, 2752 (2018). [2] E. Iliopoulos and T. D. Moustakas, Appl. Phys. Lett. **81**, 295 (2002). [3] H. Fujikura *et al.*, Appl. Phys. Express **13**, 025506 (2020).

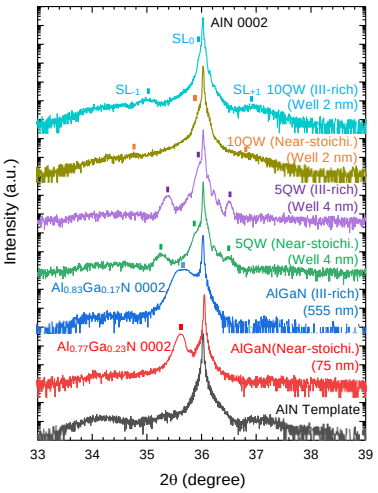

Fig. 1. XRD θ-2θ Patterns.

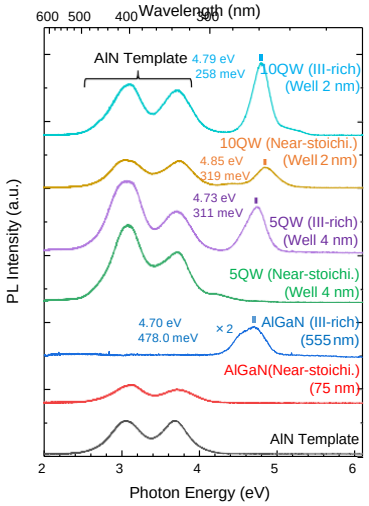

Fig. 2. PL spectra at RT.

Structural analysis in epitaxial growth of GaInN by RF-MBE using XRD-RSM

J. Takeuchi[1)], T. Sasaki[2)], H. Yokoyama[1)], T. Onuma[1)], T. Honda[1)], T. Yamaguchi[1)]

1) **Department of Electronic Engineering and Electronics, Kogakuin University, Tokyo, Japan**
2) **National Institutes for Quantum and Radiological Science and Technology (QST), Sayo, Hyogo, Japan**

E-mail: cm22030@ns.kogakuin.ac.jp

Abstract

Crystal strain and In composition during growth of GaInN on GaN at different growth temperatures were evaluated through *in situ* XRD-RSM measurements. Differences in In composition and relaxation ratio with growth temperature were confirmed.

GaInN is the material applied to visible light emitters of the light emitting diode (LED) and laser diode (LD) [1]. This material is also expected to be applied in the photovoltaic receiver responding to visible wavelength range. However, the growth of GaInN films generally requires heteroepitaxial growth on GaN substrates because there is no GaInN substrate. Since GaN and GaInN have different lattice constants and thermal expansion coefficients, fluctuations in In composition and crystal distortion occur in the grown GaInN crystal. These are greatly affected by the growth temperature [2]. To obtain high-quality GaInN heteroepitaxial films, it is necessary to understand the processes of In composition fluctuation and crystal strain variations.

In this study, GaInN was grown on GaN at different growth temperatures. The crystal strain and In composition during growth were evaluated by *in-situ* XRD-RSM measurements.

The experiment was performed using the MBE-XRD system, consisting of the MBE camber on the XRD stage [3]. GaInN films were grown under In-rich conditions with constant Ga/In flow ratio, nitrogen gas flow rate, and RF power. GaInN films were grown at different temperatures between 470 and 700°C with a growth time of 30 minutes. The growth ratio of GaInN is ~ 2 nm/min. *In-situ* XRD-RSM measurements on GaInN (10-11) plane were performed throughout the growth of GaInN. Peak positions were determined using a two-dimensional Gaussian fit. The relaxation rate and In composition were estimated from the obtained peak positions [4].

The time variation of the relaxation ratio for each sample is shown in Fig. 1. The lower the growth temperature, the higher the relaxation ratio, and differences in the relaxation rate can be observed from the initial growth stage. The relaxation ratio increased with increasing growth time. The amount of change in relaxation ratio with growth time varied depending on the growth temperature.

The time variation of the In composition for each sample is shown in Fig. 2. The In composition increased with increasing growth time, except for the sample grown at 470℃. Lattice relaxation is thought to enhance the In incorporation into GaInN. This would be one of the origins on the In composition fluctuations of GaInN films.

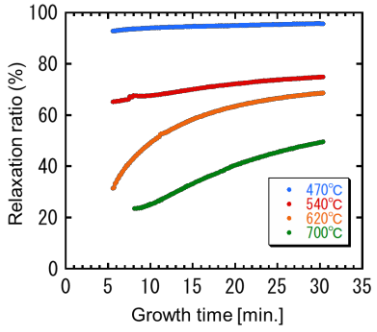

Fig. 1. Evolution of relaxation ratio during GaInN growth.

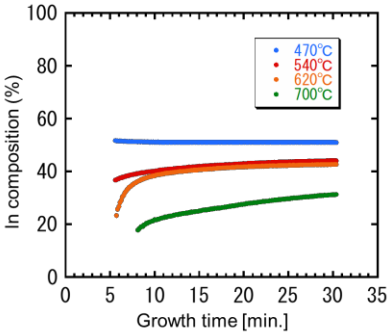

Fig. 2. Evolution of In composition during GaInN growth.

References:

[1] S. Valdueza-Felip *et al.*, Sol. Energy Mater. Sol. Cells **160**, 355 (2017).
[2] E. Papadomanolaki *et al.*, J. Cryst. Growth **437**, 20 (2016).
[3] T. Sasaki *et al.*, Jpn. Appl. Phys. **55**, O5FB05 (2016).
[4] S. Pereira *et al.*, Appl Phys. Lett. **80**, 3913 (2002).

Best Presentation Award

THIS CERTIFICATE IS PROUDLY PRESENTED TO

KAITO TADA, KAZUYA SEO, SHINICHIRO ITO, MASAKI HIRATSUKA

Aerodynamic Performance of Footballs with Different Complex Panel Surface Geometries

Danang, 25th November 2022

ASSOC. PROF. DOAN QUANG VINH

The University of Danang – University of Science and Technology


KOGAKUIN UNIVERSITY
Honorary Membership
We the undersigned do hereby proudly present this
Honorary Membership To
Prof. Lu Deng-Maw
For his support in organizing
The International Symposium on Advanced Technology
Honorary Membership
Assoc. Prof. Doan Quang Vinh
The University of Danang – University of Science and Technology

Edited by
The 21st International Symposium on Advanced Technology (ISAT-21)

Published by
Kogakuin University of Technology & Engineering,
Japan 1-24-2 Nishi-Shinjuku, Shinjuku, Tokyo, Japan
ISSN 2434-4273

Organized by
The University of Danang - University of Science and Technology, Vietnam
Co-Organized by
Kogakuin University of Technology & Engineering, Japan
Southern Taiwan University of Science and Technology, Taiwan
University of Philippines Los Baños, Philippines